DNA-copolymers structure formation: beyond self-assembly

Kedracki, Dawid

How to cite

KEDRACKI, Dawid. DNA-copolymers structure formation: beyond self-assembly. Doctoral Thesis, 2015. doi: 10.13097/archive-ouverte/unige:72905

This publication URL: https://archive-ouverte.unige.ch/unige:72905
Publication DOI: 10.13097/archive-ouverte/unige:72905

UNIVERSITÉ DE GENÈVE FACULTÉ DES SCIENCES

Section de chimie et biochimie Assist. Prof. Corinne Nardin

Département de chimie minérale et analytique

DNA-copolymers Structure Formation: Beyond Self-Assembly

THÈSE

présentée à la Faculté des sciences de l'Université de Genève
pour obtenir la grade de Docteur ès science, mention chimie

par
Dawid Kedracki
de
Gorlice (Pologne)

Thèse N° 4759
GENEVE
Atelier ReproMail
2015

Abstract

Nowadays, there is an undeniable demand for biologically active polymer based materials. Diagnostics, sensing, drug delivery, tissue engineering are just few examples of potential applications of such materials. Along this line, amphiphilic copolymers based on DNA, the functional molecule carrying the universal genetic information involved in a plethora of biological processes is one of the building blocks of a class of especially promising bioactive materials. In combination with spontaneous self-assembly the information stored in DNA-based macromolecules can result in the formation of well-defined structures in the nanometer and micrometer length scale. In depth understanding of nanostructures formation through conventional self-assembly as well as the investigation of alternative assembly modes along with examination of the functionality of the resulting structures are the key factors for introduction of DNA based molecules for real life applications. This is the scope of this thesis in which are described various synthetic strategies to generate DNA based amphiphilic copolymers which organized into functional structures. Scholar studies of the mechanism of structure formation were conducted considering the hydrophilic weight fraction as the key factor directing the self-assembly. Various modes of structure formation could be studied, inherent to that parameter i. e., crystallization assisted self-assembly, emulsification and nucleation polymerization. The functionality of the resulting structures as well as their potential application were eventually assessed.

Résumé

Il y a aujourd'hui une demande indéniable de matériaux polymère biologiquement actifs. Diagnostic, détection, administration de médicaments, ingénierie tissulaire sont quelques exemples d'applications potentielles de ces matériaux. Par conséquent, les copolymères amphiphiles à base d’ADN, molécule fonctionnelle par excellence, porteuse de l'information génétique universelle et impliquée dans une multitude de processus biologiques, sont les briques d'une classe unique de matériaux bioactifs particulièrement prometteurs.

En combinaison avec le processus d'auto-assemblage, les informations stockées dans les macromolécules d'ADN peuvent conduire à la formation de structures fonctionnelles à l'échelle nanométrique et micrométrique. Une compréhension approfondie de la formation de nanostructures fonctionnelles résultant de l'auto - assemblage, mais aussi l’induction de modes d’organisation fonctionnelle alternatifs sont les facteurs clés d’applications futures. Cette compréhension de l’auto-assemblage et d’organisations alternatives de structures fonctionnelles est l’objectif premier de cette thèse dans laquelle sont décrites diverses stratégies de synthèse pour générer des copolymères amphiphiles à base d'ADN, organisés en structures fonctionnelles par auto-association, polymérisation nucléaire et émulsion. Les études scientifiques de ces mécanismes de formation de structures fonctionnelles décrites dans cette thèse ont été effectuées en contrôlant la fraction hydrophile du copolymère-ADN, le facteur clé qui détermine le mode de structuration dépendamment des interactions macromoléculaires qui peuvent alors être engagées. La fonctionnalité des structures résultantes ainsi que leurs applications potentielles ont ainsi pu être évaluées.

Contents

1 Introduction

1.1 General introduction

Nature is a constant topic of wonder and source of inspiration for human kind. This inspiration gave birth to a new branch of chemistry based on Nature principles, called “biomimetic chemistry”, which is focused on developing ideas by mimicking Nature. Since the 1970s when the biomimetic chemistry was born, the dream of mimicking nature became realistic as it has never been before [1]. The essence of biomimetic chemistry consists in a creative transversal flow between biology and chemistry in order to broaden the breadth of this discipline [2]. The basic motivation of biomimetic chemistry is the understanding of key processes at the molecular level in biological systems, like for example, the molecular recognition of quickly targeting and highly selective artificial enzymes. The discipline which is highly associated with biomimetic chemistry is the field of polymer chemistry [3]. Synthetic polymers can be obtained from a plethora of different monomers in comparison to molecules present in nature which are based on a limited choice of construction units [4]. However, synthetic polymers have no biological activity per se. Taking into consideration the constant advances in polymer science it thus became clear that this discipline cannot just focus on the development of synthetic plastics but needs to expand, especially towards potential applications in biology. In this regard, Helmut Ringsdorf who described the first artificial membranes and who is regarded as the pioneer of this approach has also exploited the possibility of using polymers to simulate cellular processes like surface specific recognition and biomembrane stabilization. This work did set the background for the research at the material level like designing functional artificial biological systems, for example biomimetic photosynthetic systems using peptide nanotubes [5]. The branch of science that greatly expanded in the last 20 years along with biomimetic chemistry and which constitutes an integral part of biomimetic chemistry is nanotechnology [6].

Nanotechnology, which has drawn a remarkable attention due to the possibility to generate new materials and devices with outstanding physical and chemical properties [7, 8] is considered as the logical continuity in technological progress [9]. Despite great efforts made in design and development to ensure high performance devices, their implementation in real-application has faced many obstacles like reproducibility or scale feasibility for industrial production. A branch of nanotechnology called macromolecular self-assembly (MSA) appears to be promising and attractive, since it is an easily scalable and low-cost methodology which can overcome some of the obstacles mentioned above [9]. MSA results from the synergy between two major disciplines. The first relies on the organization of molecules by non-covalent interactions into so called supramolecular polymers, and the second one is the self-organization of macromolecules into multicompartment systems. Research on supramolecular polymer assembly is conducted with analogous approaches and tools as supramolecular chemistry. Hydrogen bonding, π-π interaction, van der Waals forces, hydrophobic effect, ionic and dipolar interactions are identified as basic non-covalent interactions leading to the formation of supramolecular structures [10]. These interactions together with forces that result from the repulsion between unlike blocks and cohesive interactions between like moieties, drive self-assembly [11]. Production of structures with tailored architecture, size, complexity as well as well-defined localization of functional groups, through a spontaneous bottom-up process of macromolecules organization is the main goal of MSA [12]. Both, top-down approaches through which the bulk material is modified to obtain desired products as well as bottom-up approaches with which materials are obtained from atoms/molecules assembly can provide well-defined nano-sized devices with unique chemical and physical properties [13, 14]. Properties such as mechanical strength and, elasticity as well as function of materials achieved by self-assembly result usually from the manipulation of pressure and pH under normal temperature in the liquid phase. However, reaching the suitable balance between repulsive and attractive forces is a fundamental condition of self-organization of various systems like colloidal suspensions, emulsions or biological systems. In order to be able to manipulate the alignment of particles in the desired manner the understanding of the nature and intricacy of these phenomenas is necessary [15]. The net relation between individuals can be isotropic or anisotropic relying on the type of synergy. In general, naturally occurring self-organized structures of non-biological systems are isotropic and result in non-hierarchically organized architectures. On the other hand, biomimetic (artificial amino acids, dendriticc polymers) and aggregating systems found in nature like deoxyribonucleic acid (DNA) or proteins are often remarkably anisotropic and results in well-defined, functional self-assemblies [9].

DNA is the amazing biological macromolecule evolved by Nature for billions of years [16] encoding the genetic information of the vast majority of living organisms [17]. DNA units/strands are composed of a sequence of the four nucleotides: purines, adenine (A) and guanine (G); and pyrimidines, cytosine (C) and thymidine (T) linked to phosphate–deoxyribose sugar [18]. The helical structure discovered by Watson and Crick, assembled by two hybridized complementary DNA strands is the simplest example of DNA organization [19]. Since that breakthrough work, interest raised DNA beyond its basic role, i. e. universal carrier of the genetic information. Owing to the highly programmable nature of DNA, current interests focus on the development of DNA based nanostructures [20]. DNA is considered as an ideal material for nanotechnology as its composition enables the production of nanoscale objects, with outstanding precision and intricacy in 1D, 2D and 3D [20, 21].

The versatility of polymers synthesis is the reason why they belong to the popular class of self-assembling building blocks, [12, 22]. In 1960s when the development of synthetic techniques allowed the production of well-defined block copolymers (BC) in terms of molecular weight, distribution as well as composition, the studies of self-assembling synthetic macromolecules were initiated. BCs undergo microphase separation into nanoscale periodic domains of chemically distinct covalently linked blocks [23]. The segregation of chemically unlike blocks and the cohesive interactions of like blocks can be considered as the driving force [24].Such a behavior has drawn the attention of the polymer community due to the fact that this phenomenon has never been noticed for any synthetic polymer before. In general block copolymers are depicted as macromolecules composed of at least two blocks of differing monomers with linear and/or radial alignment [25]. The whole family of block copolymers belongs to the wide category of soft condensed matter, which is characterized by fluid-like disorder on the molecular scale and a high degree of organization at wider length scales. The exceptional properties of BCs is a consequence of their complex structure resulting in their implementation in many industrial applications as thermoplastics elastomers, foams and adhesives [26]. Boosted toughness and surface properties for various applications in the microelectronic or biomedical industry can be achieved by selection of proper block copolymers. The highest input in polymer science originates from the development of controlled radical polymerization (CRP) in particular ATRP (Atom Transfer Radical Polymerization) and RAFT (Reversible Addition-Fragmentation chain Transfer) polymerization [27]. Sometimes combination of two or several polymerization strategies is used to achieve desired convoluted copolymers.

1.2 Introduction to DNA copolymers

1.2.1Polymers

Polymers and their basic properties are at first shortly introduced.

A polymer is defined as a macromolecule which consists of several monomer units. The words of the president of the Royal Society and 1957 Nobel Prize Laureate, Lord Todd, uttered almost 35 years ago –"I am inclined to think that the development of polymerization is perhaps the biggest thing chemistry has done, where it has had the biggest effect on everyday life. The world would be a totally different place without artificial fibers, plastics, elastomers, etc. Even in the field of electronics, what would you do without insulation? And there you come back to polymers again", seems to accurately present the importance of the polymer field in the technological progress [28]. Polymers are ubiquitous, they can be found in natural material such as wood or shellfish shell as well as in synthetic materials such as gels and plastics [29].

Depending on the type and repeating unit, polymers can be divided in [28, 30, 31] (*Figure 1-1)*;

1. Homopolymers, along which all monomer units are of the same composition (A being a monomer)

--A-A-A-A-A-A-A-A-A-A-A-A-

2) Copolymers, which are composed of a mixture of at least two monomers. In the class of copolymer, four classes can be distinguished;

a) Random (statistical), along which the sequence of polymer is incidental

-A-A-A-B-A-B-A-A-B-B-A-B-B-B-

Notation of such a polymer includes *stat* or *ran* between the monomer names, e.g. poly(A-*stat*-B) or poly(A-*ran*-B)

b) Alternating, a regular pattern of the monomers can be found in the sequence

-A-B-A-B-A-B-A-B-A-B-A-B-A-B-A-

Notation; poly(A-*alt*-B)

c) Block, when a continuous sequence of each monomer is implemented in the structure

--A-A-A-A-A-A-A-A-A-B-B-B-B-B-B-B-B-B-A-A-A-A-A-A-A-A-A-A-

Notation; poly(A-*block*-B-*block*-A)

d) Graft, when the copolymer is branched, being composed of different building blocks in the backbone and in the side chain

B-B-B-B-B-
--A-A-A-A-A-A-A-A-A-A-A-A-A-A-A-A-A-A-A-
B-B-B-B-B-
B-B-B-B-B-

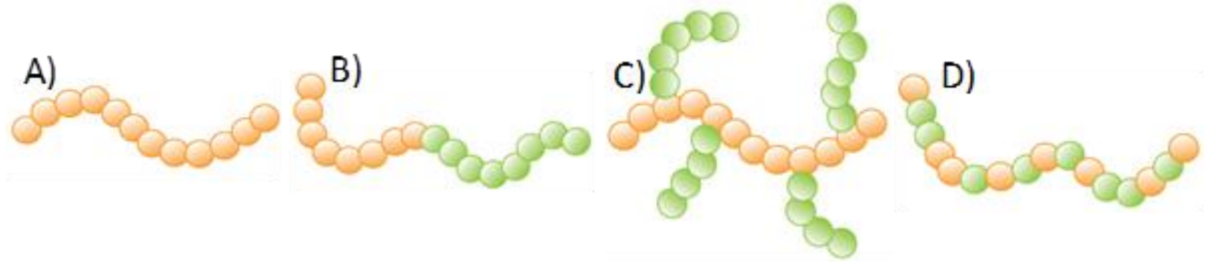

Figure 1-1. Polymer configurations A) homopolymer, B) block copolymer, C) graft copolymer, D) random/statistical copolymer [3]

As a consequence of the polymerization process throughout which the chain growth is controlled by the availability of monomers, polymers molecular mass vary greatly from the chemistry of low molecular mass molecules. Polymers are regarded as polydisperse. In order to define the molecular mass of polymers, two definitions are commonly used;

The number average molar mass;

$$M_n = \frac{\sum n_i M_i}{\sum n_i} \qquad \text{Equation 1}$$

The weight average molar mass;

$$M_w = \frac{\sum w_i M_i}{\sum w_i} \qquad \text{Equation 2}$$

Where, n_i is the number of molecules, w_i is the weight fraction of molecules with the molar mass M_i. Polydispersity of the polymer is described by the polydispersity index which is defined as the ratio of Mw/Mn. Ideally a monodisperse polymer would have a polydispersity index value equal to one [29]. Generally, molecular weights of polymers vary between 1000 and 10^6 Da.

The solvent choice is crucial. In a *good* solvent a chain expands to maximize interactions with solvent molecules. In this case the chain is swollen. In a *poor* solvent the chain minimizes the interactions with solvent molecules through chain contraction. In a so called *theta* solvent, these two effects are ideally balanced and polymer chains is in an unperturbed conformation [29, 32].

The conformation of solubilized chains depends on segment-segment and segment-solvent interactions. The *radius of gyration* (R_g) is the basic parameter which describes the polymer size. R_g averages the distance of a chain block from the center of mass of the coil [29, 33, 34];

$$R_g = \frac{R}{\sqrt{6}}$$ Equation 3

Where, R is the average end-to-end distance, related to the length (l) of independent subunits through the following equation;

$$R = l\sqrt{N}$$ Equation 4

Where, N is the total number of the monomer subunits.

Each independent subunit is composed of few monomers, exceeding the length l_o of a single monomer $l > l_o$. The parameter which is related to the length of independent subunits is the Kuhn's length l. In the example depicted in the figure below (*Figure 1-2*), the Kuhn's length is equal to 4 monomers. *Equation 3* is valid only in a theta solvent. The radius of gyration can be obtained from scattering measurements.

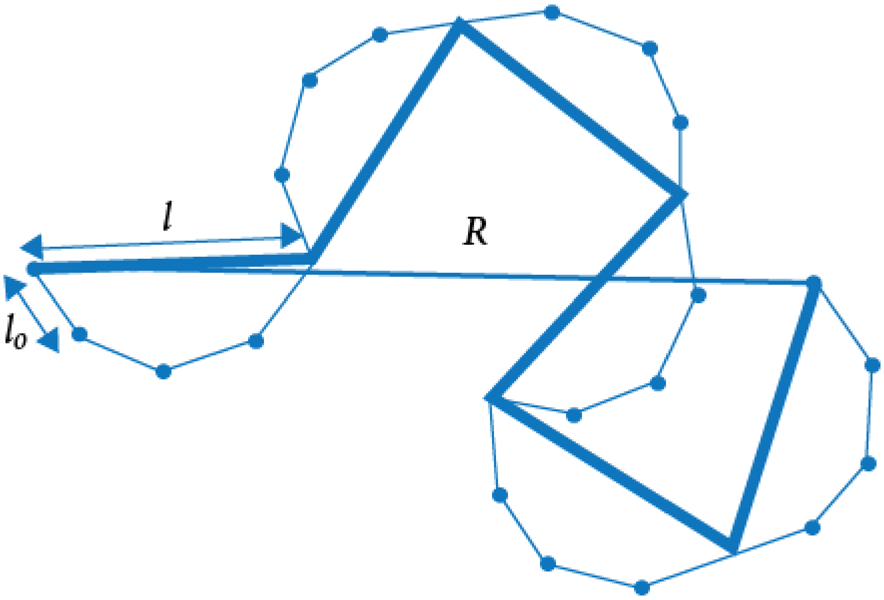

Figure 1-2. Difference between monomer length l_o and the Kuhn's length l

1.2.1.1 Block copolymers

Owing to constant developments in synthetic strategies, a broad library of block configurations has been achieved. *Figure 1-3* depicts representative macromolecular configurations which can be classified taking under consideration two parameters; a) the number of chemically different moieties and b) linear versus branched sequencing. Linear configuration A-B, where A monomer is covalently bounded to monomer B is considered as the most common and the most explored category of block copolymers. Due to thermodynamic incompatibility, segments A and segments B gather in A-B diblock self-assembly where the analogous blocks maximize the contact in contrary to the blocks which are dissimilar [24]. Nevertheless, macrophase separation is limited by entropic forces resulting from covalent linkage. As a consequence, the structure results from the equilibrium between repulsive and attractive forces. The free energy cost of contact between distinct segments is described by the temperature-dependent Flory-Huggins interaction parameter $\chi_{AB.}$ In bulk or solid state, constituent segments undergo self-assembly forming regularly-shaped and uniformly-sized compartments which are periodically distributed [35]. The degree of polymerization N and relative composition fractions f_A and f_B where $f_A=N_A/N$ and $f_A+f_B=1$ are two supplementary parameters which are determining the morphology of the system created by microphase separation [36]. Over a certain critical molecular weight usually polymers are incompatible if there is no strong intermolecular interaction like hydrogen bonding or electrostatic attraction, which illustrates the delicate minimization of the free-energy. *Figure 1-4* depicts equilibrium morphologies of diblock copolymers. The body-centered cubic spherical phase is formed when the content of the minority block reaches around 20%. At a volume fraction of ~30% of the minority block in a matrix of the majority block, hexagonally packed cylinders are formed. When the volume fraction of one segment reaches 38%, gyroid or perforated layers are formed depending on the incompatibility degree. Roughly equal volume fraction of two segments leads to alternating lamellae [35]. Morphological transitions mentioned above were obtained both experimentally [37-40] as well as by statistical thermodynamics theories [41-44].

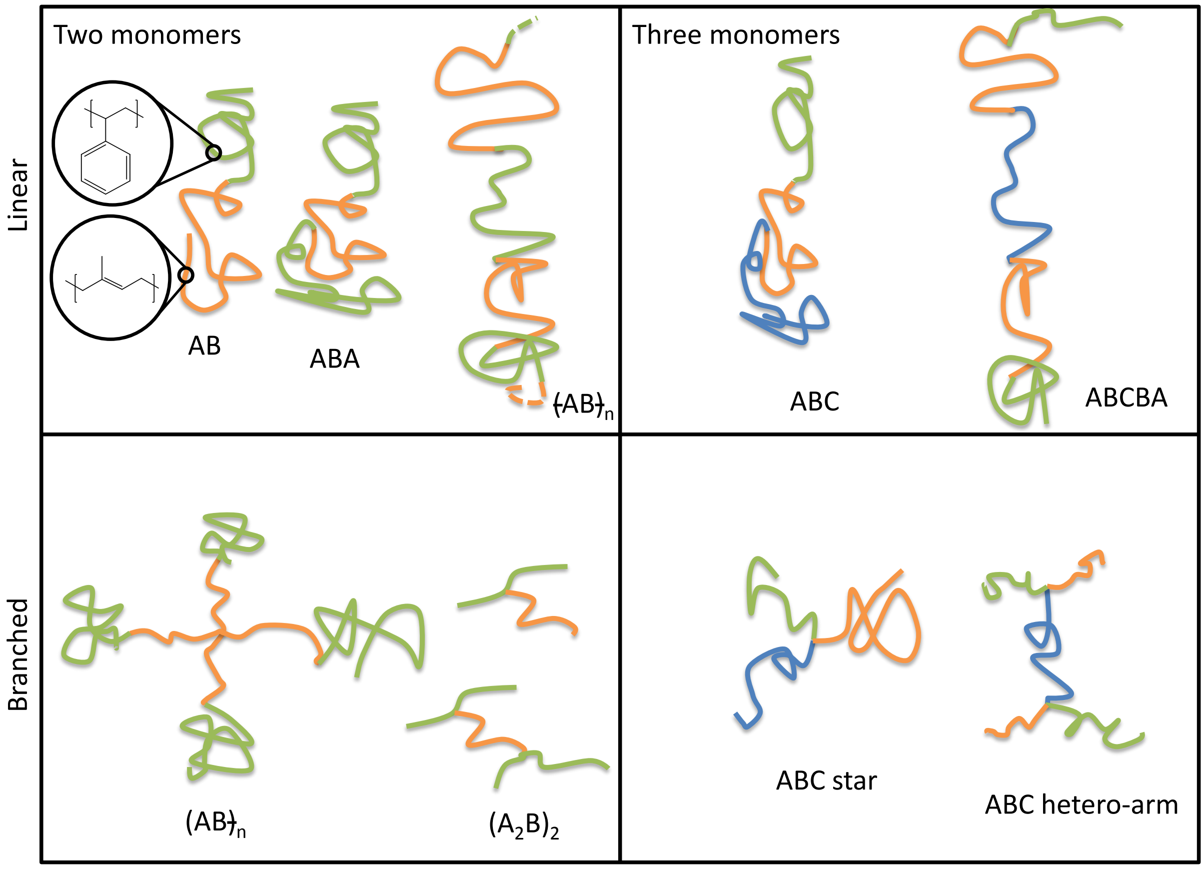

Figure 1-3. BCs can be arranged into almost countless number of molecular structures composed of two, three or more monomer types. In the picture above structures are divided according to monomer type and linear versus branched sequencing. Different colors (A, B and C shown as green, orange and blue, respectively) stand for the same monomer type. A copolymer is represented by a joined linear sequence of monomers. The colored strands are joined as shown to form the block copolymer macromolecule. Typical monomer length scale is sketched in the upper-left inset [24]

ABC or other multicomponent molecular systems are obtained when three or more monomers are used in the synthesis procedure. These numerous synthetic strategies allow arranging multiple monomers in branched architectures (*Figure 1-3*). Alterations in morphology as well as in properties might be induced by slight modifications in the molecular topology like for instance ACB instead of ABC or star-ABC (segments joined in the center). Triblock copolymers ABC can also self-assemble in the bulk state giving rise to even higher number of segregation patterns, being some of them visually wondrous and complex. Tetra and pentablocks self-assembled morphology patterns number should increase, however because of challenges in synthesis such structures were rarely reported [24].

In comparison to the bulk state, copolymers also self-assemble in a block-selective solvent, which is dissolving just one of the segments, giving birth to different morphologies, as will be discussed in the next subsection.

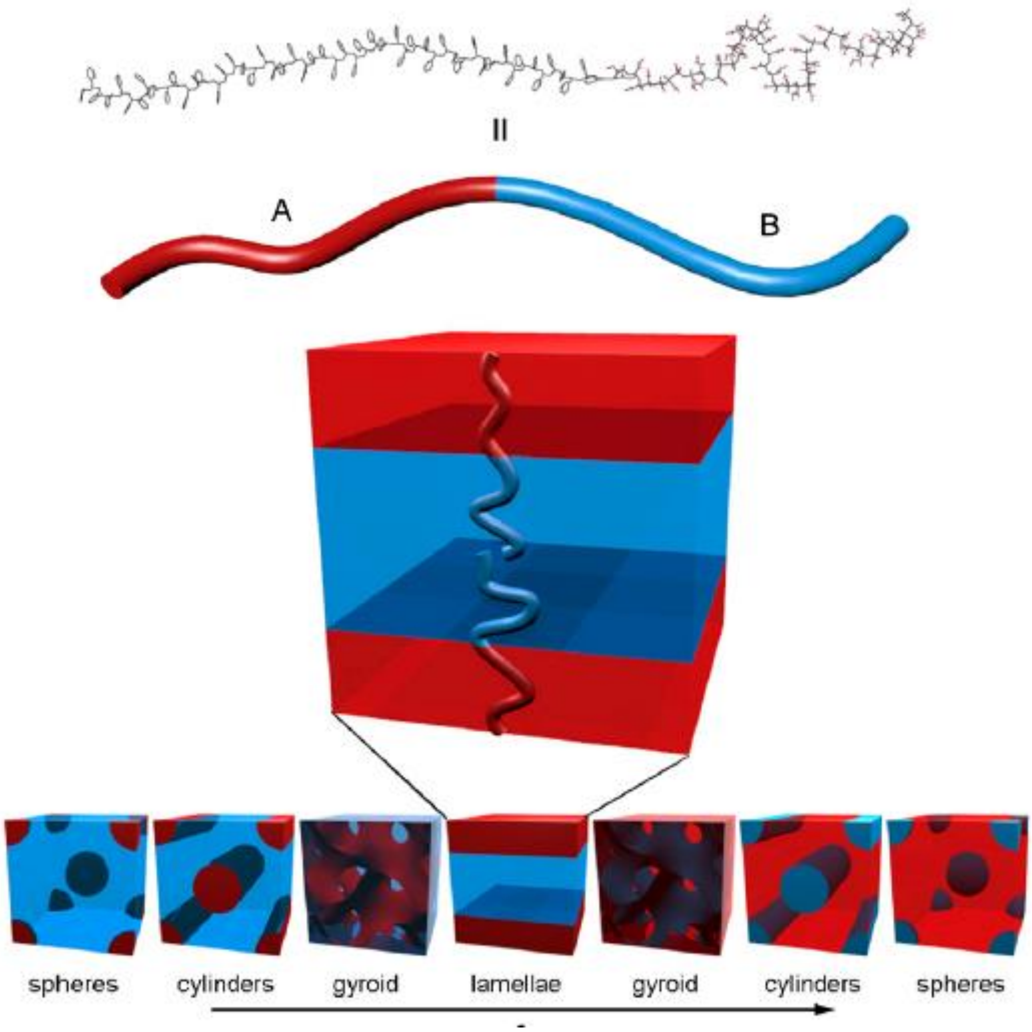

Figure 1-4.Thermodynamically stable segregation patterns .Two-color chain represents the A–B diblock copolymer. Structure is determined by the relative lengths of the two polymer blocks (f_A*)[26]. (Figure adapted with permission of Elsevier)*

1.3 The mechanism of Self-Assembly

Self-assembly (SA) is considered as the process through which building blocks spontaneously create well-defined and in numerous cases functional structures. Self-assembly is nowadays considered as attractive, cost effective and technologically feasible. Transition from disorder to order, resemblance of the SA process to the self-organization of living cells, practical ease of nanostructure production are just few of many factors which support this opinion [9, 45-47]. Self-assembly is omnipresent in nature from very low level of complexity as dimerization of two components to sophisticated functional cell membranes [48].

The features of individual elements e.g. shape, charge, mass, magnetic dipole and surface properties regulate interactions among them and thus self-assembly. The choice of building blocks is a crucial step, in order to obtain the desired pattern and adjust properties for potential application. Non-covalent or weak covalent interactions (van der Waals, electrostatic, hydrophobic, coordination and hydrogen bond) play the main role in macromolecular self-assembly while for self-organization of meso or macroscopic entities gravitational forces, external electromagnetic field, entropic and magnetic interactions are regarded as crucial [45].

From a thermodynamic point of view, two main types of self-assembly can be distinguished: static and dynamic. Static self-assembly (SSA) concerns systems that are either at global or local equilibrium and dissipate energy. SSA is a type of stable self-assembly which, however, may require energy to form an ordered structure. SSA is illustrated by the formation of lipid bilayers, protein folding as well as base pairing at the molecular level [49].

On the other hand, dynamic self-assembly (DSA) refers to stable non-equilibrated systems in a steady state preserved by constant energy supply. Biological cell processes and structures such as e.g. protein aggregates are examples of structures resulting from a dynamic self-assembly process. Generally speaking, DSA is mainly a feature of living organisms, although not exclusively. Most research in the self-assembly area is devoted to SSA while DSA is still poorly understood despite of several decades of research [45, 50].

1.3.1Amphiphiles

Amphiphiles contain both hydrophilic and hydrophobic parts, and the two parts are linked by covalent bonds. Amphiphiles are able to self-assemble in water to form various well-defined molecular assemblies, such as micelles and vesicles. Due to this chemical incompatibility this molecules self-organize in aqueous solution and at the air-liquid interface. The surfactant molecule which is composed of a hydrophobic tail and a hydrophilic or polar head is the basic example of an amphiphile. Self-assembly of amphiphilic molecules can be also defined as a delicate equilibrium between the attractive (driving force) and repulsive (opposition force) intermolecular forces. It is also noteworthy that there is no strong chemical bond like for example covalent bond involved in self-organization. Generally, the hydrophobic attraction is considered as the driving force, and electrostatic repulsion and/or solvation force as the opposition force. Firstly, the surfactant molecules are brought in close proximity to each other by the long-range hydrophobic forces and with the progression of the process, opposition forces like hydration forces (short-range repulsive interaction [51]) or electric double-layer repulsion begin to call in. Origin of these forces comes from the charge bearing hydrated head groups which are comparatively short-range forces in comparison to the hydrophobic interaction [15]. The variety of structures which can be generated by self-assembly is depending on slight modification of parameters such as concentration, polydispersity, molecular weight, hydrophilic weight fraction, charge, solvent, composition, water content and additives (ions, surfactants, and homopolymer) is enormous. Structures resulting from the organization of amphiphilic molecules are presented in *Figure 1-5*.

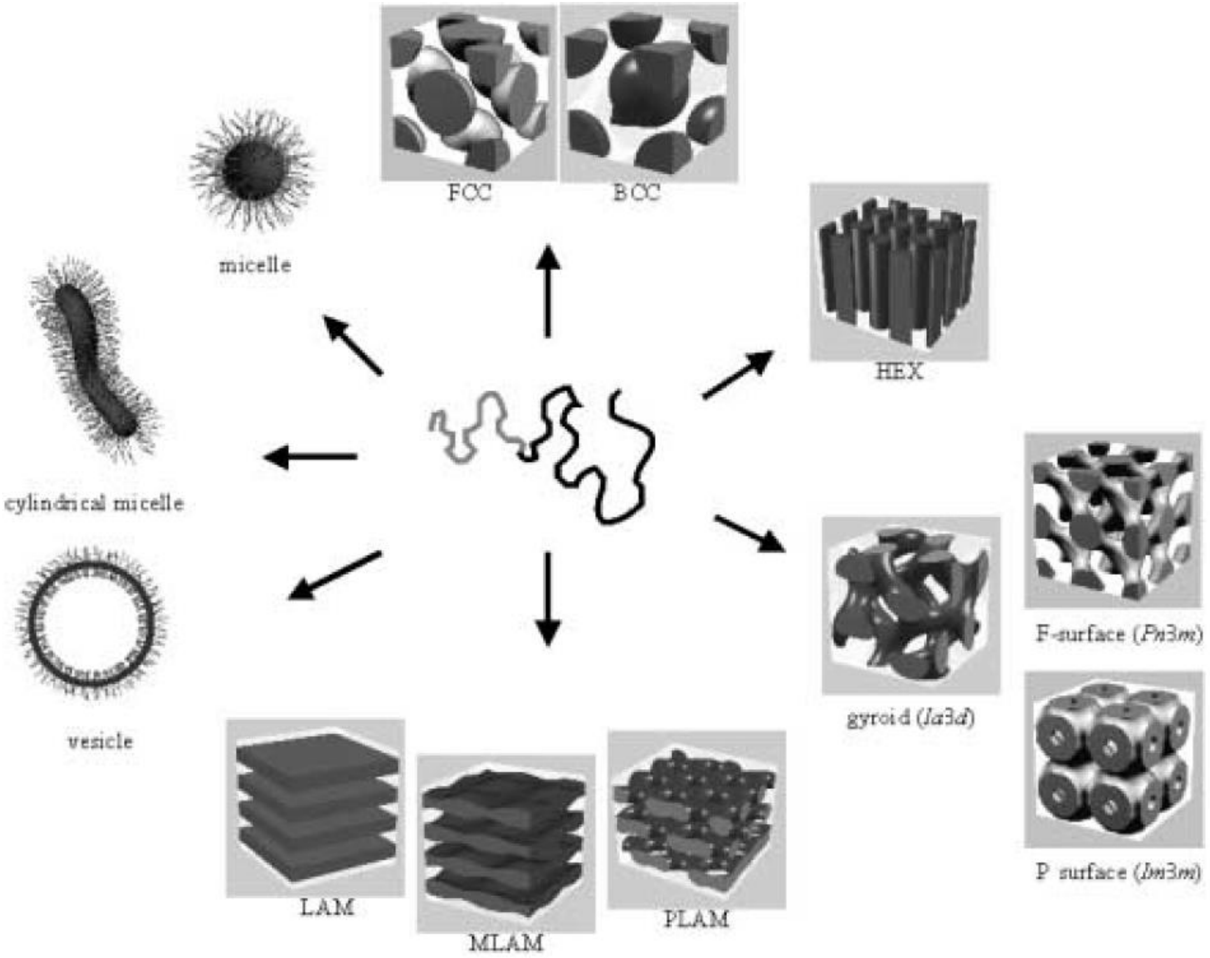

Figure 1-5. Self-organized structures of high molecular weight of diblock copolymer [52] (Figure adapted with permission of John Wiley and Sons)

The idea of taking advantage of the self-assembly process for biomedical applications was extensively exploited in the area of targeted and controlled drug delivery [53]. In dilute aqueous media, amphiphiles are soluble and embrace configurations of spherical or cylindrical core shell micelles as well as vesicles, being these architectures predominant for drug delivery [54, 55] to transport for example drugs or nucleic acids [56]. The formation of bilayers and closure into vesicular structures is depicted in *Figure 1-6*. Moreover, to make delivery more efficient, it is possible to tailor the vesicular properties in order to improve targeting and transport (*Figure 1-7*) [57]. Block copolymers are considered as promising alternative to lipids for drug delivery [58]. Indeed, there are limitations arising from the lipid nature for this application because of their low molecular weight [59], poor mechanical stability and short shelf-life in comparison to more stable block copolymer structures owing to their high molecular weight. However, block copolymers remain currently uncommon due to their lack of approval from the FDA (Federal Drug Administration) [60] in comparison to lipids which are extensively used. The immeasurable number of synthetic path to obtain self-organizing functional polymers is the key for their implementation in biomedical applications.

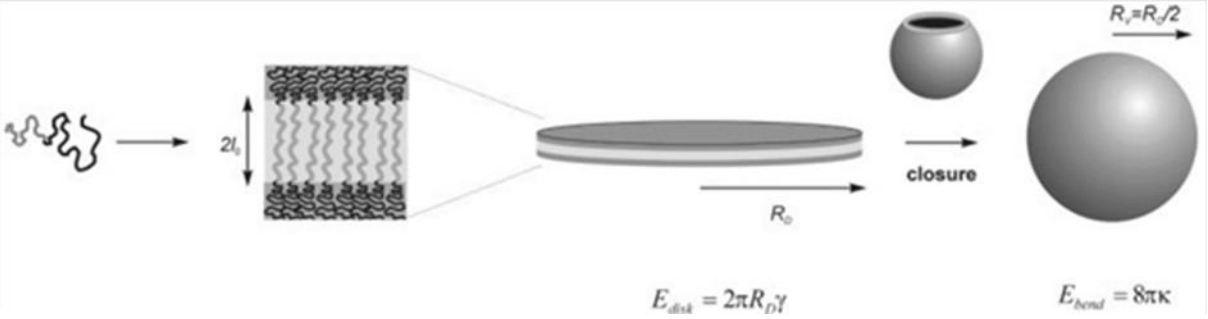

Figure 1-6. Schematic illustration of bilayer formation and its closure into vesicle(E_{disk}-line energy, γ-line tension, E_{bend}-bending energy, κ-bending modulus, R_D-disc radius, R_V-Vesicle radius) [61](Figure adapted with permission of John Wiley and Sons)

The need for forming such structures with tailored properties has drawn attention in various fields like enzymatic cascade reaction [62], drug delivery [63], amphiphilic copolymer nanocontainers [64] and nanoreactors [65].

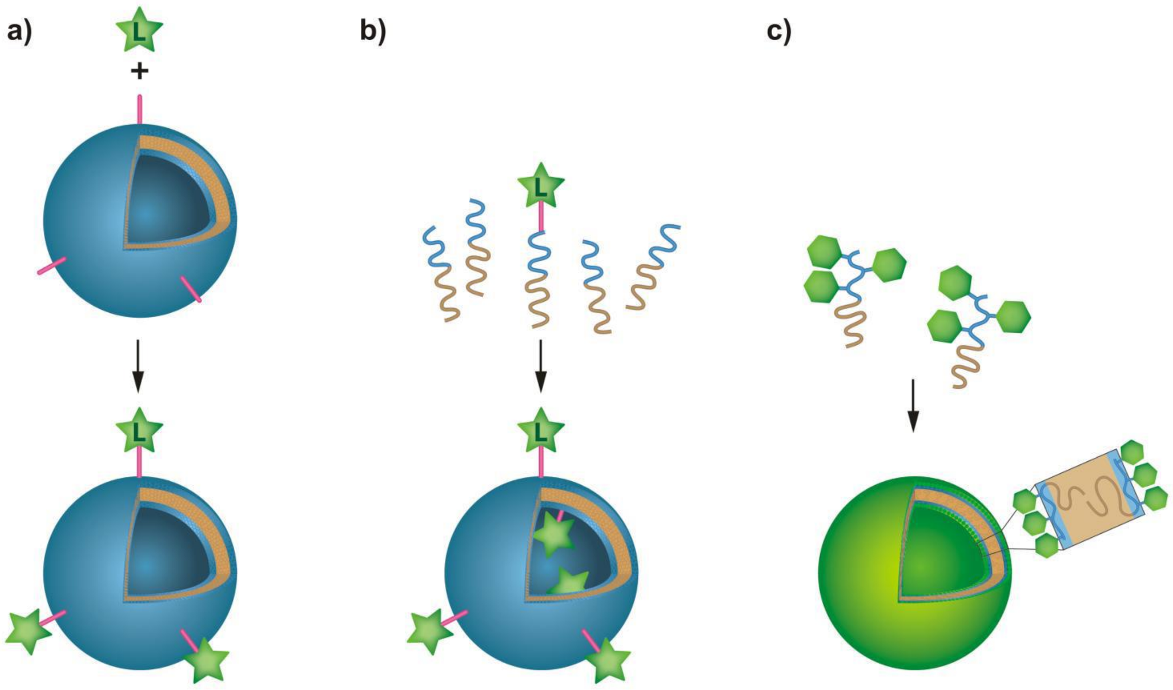

Figure 1-7. Strategies for polymersomes/liposomes functionalization. (a) Grafting of a functional ligand to the surface of vesicles (b-c) pre-functionalized and non-functionalized amphiphilic block copolymers organization: (b) functional entity attached as the end-group (c) functional ligand along the hydrophilic block. L = Functionalization molecule: fluorophore, biomolecules, polymer tentacle, etc.[57]

1.3.1.1 Packing parameter and interfacial tension.

In order to be able to predict the morphology of self-assembled structures Israelachvili, Mitchell and Ninham introduced a model that takes into account the geometric parameters of the surfactant molecules [66]. Following this approach in more detail it is possible to predict the expected morphology, micelle, vesicle, planar bilayer or other. This model is built on the idea of the so called *packing parameter p*, also named the *surfactant parameter*. In this classical representation the factor that controls the resulting self-assembled morphology is the size of the hydrophobic moiety in relation to the hydrophilic part. The curvature of the hydrophilic-hydrophobic interface is governed by its mean curvature H and its Gaussian curvature K, which are defined by the two radii of curvature R_1(interfacial) and R_2(mean)(*Figure 1-8*).

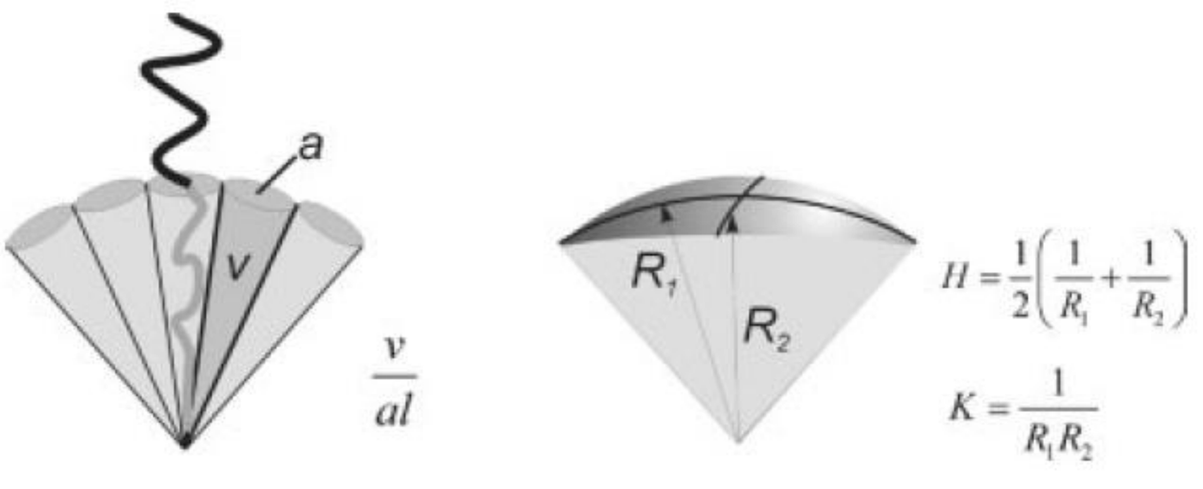

Figure 1-8. Depiction of amphiphile self-assembled morphology taking into account the packing parameter, interfacial curvature and Gaussian curvature[61]. (Figure adapted with permission of John Wiley and Sons)

The correlation between the packing parameter and the curvature is described by the following equation;

$$\frac{v}{al} = 1 + Hl + \frac{Kl^3}{3}$$ Equation 5

Where v is the volume of the hydrophobic part of the amphiphilic molecule, l is the chain length and a is the interfacial area. This approach has been successfully applied to predict and justify formation of structures dependent on surfactant volume fractions such as spherical micelles ($p \approx 1/3$), vesicles ($p \approx 1$), and cylindrical micelles ($p \approx 1/2$) [22](*Figure 1-9*).

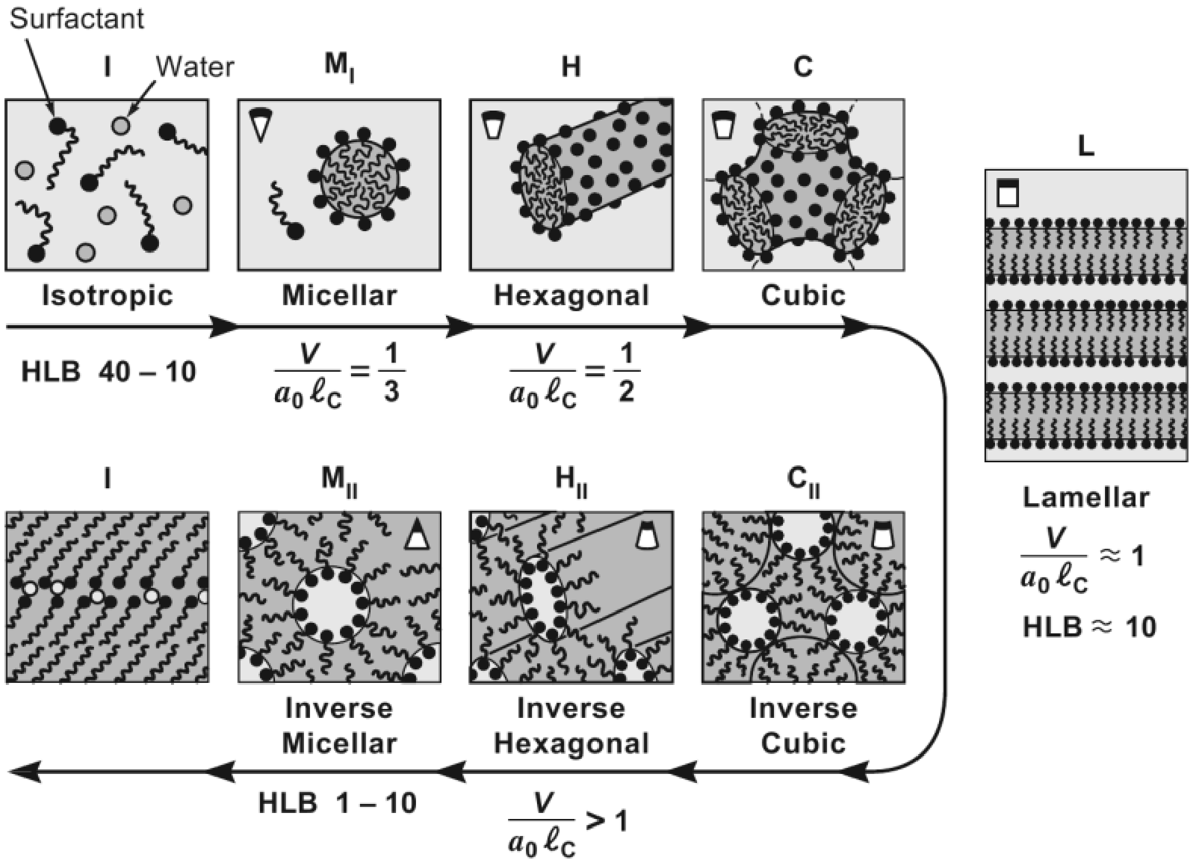

Figure 1-9. Examples of possible structures based on amphiphilic molecule geometry[67](V - volume of the hydrophobic part, l_c - chain length, a_o - the interfacial area. (Figure adapted with permission of Elsevier)

With the purpose of obtaining bilayers for a certain molecule characterized by volume v and length l, the interfacial area has to be tailored in a way to achieve the unity value of the packing parameter. Basically, the aggregates remain in a dynamic equilibrium with single solvated macromolecules when the glass transition temperature (T_g) (temperature at which amorphous materials undergo reversible transition from a hard and relatively brittle state into a molten or rubber-like state) of most hydrophobic blocks is lower than the ambient temperature of self-organization [22]. As a consequence, structure rearrange while molecules strive to reach their optimal thermodynamic equilibrium architecture [68]. Shape transition along with the decrease of the hydrophilic weight fraction was demonstrated for the poly(butadiene)-block-poly(ethylene oxide) copolymer (*Figure 1-10*) [69]. The model that is considered in this paragraph applies to molecules that can rearrange easily (such as surfactants, polymers or dendrons) and through these movements can fit the equilibrium shape and curvature.

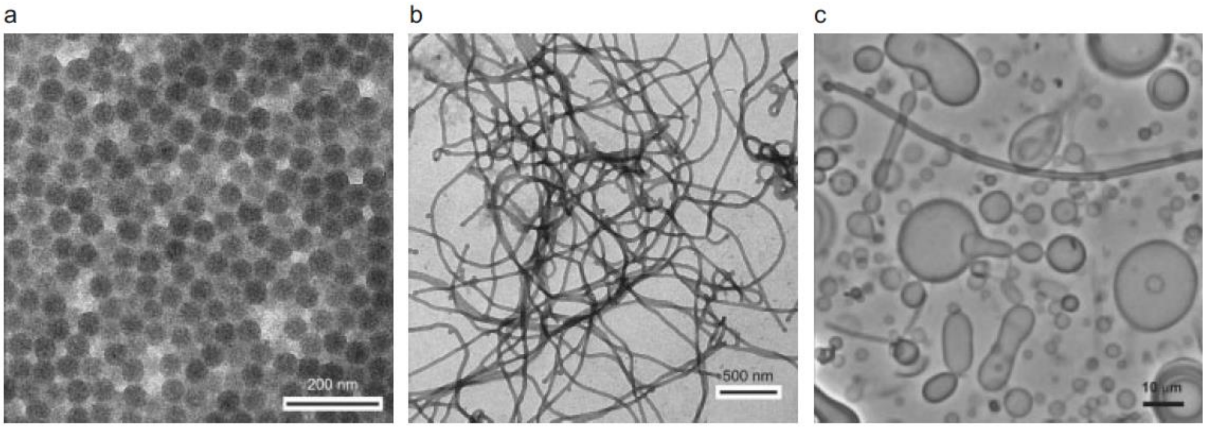

Figure 1-10. Various shapes of PB-PEO copolymer self-assembled structures, from: a)micelles, through b) cylindrical micelles to c) vesicles [61] (Figure adapted with permission of John Wiley and Sons)

The packing parameter does not describe sufficiently the laws governing the self-assembly process of high molecular weight polymer analogues of surfactants or lipids. With the purpose of elucidating the self-organization phenomenon the most important interaction are described in following subsection.

1.3.2 Interaction forces in self-assembly

The assembly process of nanocomponents into macroscopic structures depends on the interaction balance between different forces and especially on the free energy of the system to which enthalpic and entropic terms contribute. The nature of the main forces depends on many parameters e.g. concentration of the components, temperature, separation distance and others [9]. Moreover, the nature of the interactions, various interaction potentials and relative magnitudes are just few of many parameters engaged in the self-assembly process. As it was mentioned above a vast majority of processes lead to non-equilibrium conditions, which are thus competing with relaxation processes, which frequently results in formation of amorphous phases [70, 71]. Taking this under consideration, in order to form well-defined structure long-range interactions in comparison to the size of the building blocks are desirable. In addition, the majority of the attraction forces act exclusively at the molecular scale distance [70].

Usually, the weak and long-range forces play the major role in the self-assembly at all scales.

These forces belong to three classes 1) driving forces responsible for bringing the building blocks in close proximity, 2) opposing forces which are in equilibrium with the driving forces and 3) so called *functional forces* associated with the directionality and the functionality of self-assembled structures [15].

Following sub-chapters will be focused on origin and basic concepts of most common interactions. It has to be mentioned that depending on the self-assembly type there can be several kinds of interactions involved, not described below, which also contribute to the process, such as magnetic interactions, crosslinking interactions or DNA base pairing [70].

1.3.2.1 Van der Waals forces

Van der Waals (vdW) forces derive from the interactions at atomic and molecular levels between permanent or induced dipoles [9, 15]. Hence, there can be three potential configurations;

a) Keesom interaction, representing interactions between two permanent dipoles
b) Debye interaction, describing interactions of a permanent dipole with an induced dipole
c) London interaction which represents interactions between induced dipoles or polarizable objects

All above are classified as van der Waals interactions.

The van der Waals interaction potential is given by the following equation

$$U(r)_{vdW} = -\frac{C_{vdW}}{r^6} \qquad \text{Equation 6}$$

Where r is the separation between dipoles, and C_{vdW} is a proportionality constant that takes under consideration the three types of interaction mentioned above [67].

Inverse sixth-power dependence from *Equation 6* evidences that van der Waals interactions play a major role when the object are situated close to each other (usually less than 10 nm). Thus, vdW forces are classified as short-range interactions. The London interaction gives the highest input to Van der Waals attraction (aside from highly polar molecules) as it is always present since it can occur in the absence of permanent dipole or charge [15]. VdW interactions at the colloidal level and in specific conditions might be repulsive, however, at the molecular level are constantly attractive. The most significant conclusion is that despite of the reports of the dominant role of vdW forces in self-assembly [72, 73], it is problematic to differentiate the input of vdW interaction from others kinds of interactions in the self-assembly process [9].

1.3.2.2 Electrostatic forces

Electrostatic forces are another example of interactions, which frequently engage in the self-assembly process. Electrostatic interactions are the driving force for ionic, colloidal [74], macroparticles [75], diamond-like nanoparticle crystals [76], robust monolayer [77] and multilayer [78-80] surface coatings formation. In comparison to vdW forces which are mostly attractive, electrostatic interactions depending on the charge can be attractive or repulsive [9]. The choice of solvent, chemical nature and concentration of the counter ion can control the magnitude and the length scale of these interactions. These properties make the electrostatic interactions advantageous for particle stabilization in solution as well as to direct their self-organization into binary super architectures [70].

When ions, atoms or molecules interact in vacuum or other media, Coulomb interaction arises. Coulomb force is very strong (500-1000 kJ/mol) in comparison to vdW forces (~ 1 kJ) and long-range interaction (up to ~50 nm). Its potential energy is described by the following equation;

$$U(x) = \frac{Q_1 Q_2}{4\pi\epsilon_0 x} = \frac{z_1 z_2 e^2}{4\pi\epsilon_0 x} \qquad \text{Equation 7}$$

Where, Q_1 and Q_2 are two charges,, z_1 and z_2 are respective charge ionic valence, e is the elementary charge in vacuum, x is the distance between charges and ε_0 is the dielectric permittivity of vacuum [15].

Electrostatic forces are particularly relevant for polar systems. There is a number of ways that a surface can get charged, i. e. in contact or submerged in an aqueous medium for instance. The processes of dissociation, ionization, physisorption, chemisorption of ions are the most attainable. When the surface is positively charged, the negatively charged ions from solution will be attracted in proximity of the surface (*Figure 1-11*). Into the regions comparatively remote from the surface the positively charged ions will diffuse in, whereas the amount of negatively charged ions will decrease. The models established to describe this phenomena assume the formation of two layers (*Figure 1-11*), called; the Stern layer and the Gouy-Chapman double layer [15];

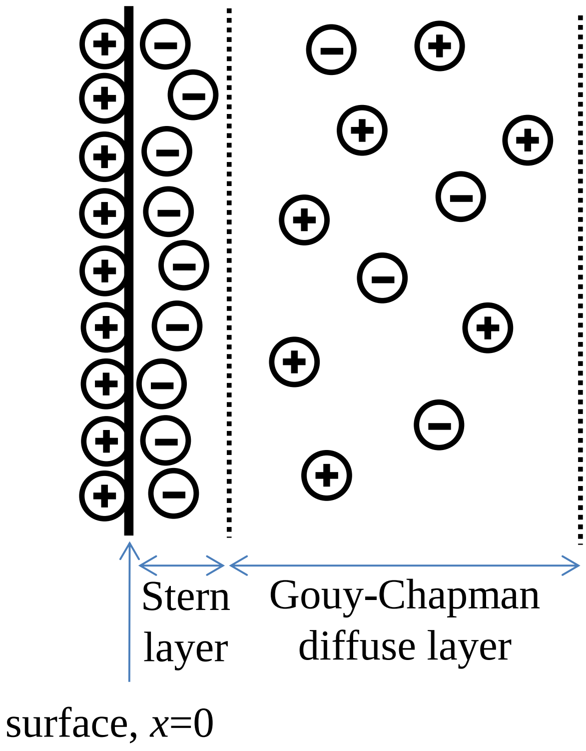

Figure 1-11. Schematic representation of the Stern layer and Gouy - Chapman diffuse layer

The medium distant from the surface is treated as neutral due to the equilibrium between number of oppositely charged ions which diffuse to the surface. The potential changes as a function of the distance from the surface and thickness of layers is immeasurable by any experimental technique. However, two theoretical models were developed to obtain a qualitative representation of the electric double-layer potential, namely; Debye-Hückel and Gouy-Chapman models. The potential according to the Debye-Hückel model is equal to;

$$U = U_0 e^{-\kappa x} \qquad \text{Equation 8}$$

Where, U is the potential at distance x, U_0 represents the potential at the distance approaching zero and κ^{-1} is defined as thickness of the double layer or screening length (Debye length).

Exponent in the *Equation 8* suggests that the potential decreases exponentially along with the distance. In the case when surfaces are coming closer to each other a repulsive force, called *electric double layer repulsion* is generated [81]. Electric double-layers electrostatic interactions dependence on surface roughness and uniformity of surface were well formulated by Duval [82].

To sum up, electrostatic interactions (along with vdW forces) play a crucial role in the self-assembly process and in many cases provide basis for structure formation as mentioned at the beginning of this paragraph. However, the impact of other forces (such as steric, hydrophobic and hydrogen bonding) on the formation of colloidal nanoparticles cannot be excluded.

1.3.2.3 The role of Entropy - steric and depletion forces

Steric forces are long-range interactions which in aqueous solution reach ~10R_g (R_{g}- radius of gyration). The magnitude of this force depends on the number of interactions which may occur in solution (e.g. polymer–polymer, polymer–solvent, polymer–colloid), parameters of the system or nature of charge. Steric forces induced by polymer interactions can be either repulsive or attractive depending on different experimental parameters as summarized below [15].

Repulsive interactions occur when;

a) Two polymer coated particles are in a *good* solvent. The interaction causes constrains to arrange the solvent molecules when the particles are close to each other. Repulsive force is greater than described by the Gouy-Chapman model owing to reduced dielectric constant of the medium [83].
b) Restriction on the molecular motion or orientation freedom of polymer which is caused by high density of the polymer chains, results in a loss of entropy and repulsive force.
c) Compression between two approaching surfaces is prevented due to high elasticity of polymer coils.

Polymeric brushes are often used to improve the stability of colloid dispersions through tethering of long-chain molecules, which are generating repulsive steric forces[84].

Attractive interactions occur when;

a) Polymer coated colloidal particles are placed in a *poor* solvent, which renders polymer-polymer attractive interactions preferred, in contrary to polymer-solvent interactions. The temperature is a significant parameter.

b) *Bridging attraction [85]* occurs, owing to high affinity between polymer chains tethered at the surface. The number density of the polymer chains is the relevant factor (along with temperature) as it regulates the availability of adsorption sites.

c) If a non-adsorbing polymer is present in the solution, attractive, so called depletion interaction may arise.

In the case of interaction between non-adsorbing polymers with colloidal particles, distribution of the amount of interacting polymer relative to that of particles will be equal if the distance between colloidal objects is sufficient. Polymer chains are evacuated from the area of colloid particle contact when distance between particles becomes smaller than the polymer size, which results in an increase of osmotic pressure in the depletion area and generation of a depletion attractive force [86]. This attraction force is generally weaker than vdW or electrostatic forces, however, its strength depends on factors like temperature or molecular weight of the polymer and intriguingly it does not rely on the size of colloidal particles. When the particles or polymer are charged, the net force leans on the polymer molecular weight as well as on the distance between particles, which is related to their concentration. Steric and depletion forces engage in e.g. DNA-mediated gold nanoparticle assembly [87], formation of tubular structures with use of DNA tiles and Au nanoparticles [87] as well as creation of 2D hexagonally close-packed monolayers from CdSe/CdS hydrophobic nanorods [88].

1.3.2.4 Hydrophobic effect

Hydrophobic interactions are crucial for the self-assembly of several macromolecules such as protein folding [89] or lipid membranes formation [90], and intense research is devoted to this issue. As it plays a central role, this interaction was already mentioned in this work and practical aspects on this topic are described in the subsection 1.2.2 *Amphiphiles*. Herein, rather theoretical aspects are described.

The hydrophobic effect arises from the aggregation of non-polar molecules in a aqueous solution with exclusion of water molecules [9]. When an apolar substance is added to the solution, dynamic hydrogen bonding between water molecules is disorganized due to the formation of a network like organization around the non-polar molecules according to the theory of iceberg formation [91-93]. The formation of an iceberg is not considered as an entropic effect. Transitional molecular motion restriction of water at iceberg cluster molecules (~10^3 times slower than in bulk water) [15] results in an entropy loss.

Simultaneously, water molecules motion increases due to aggregation of non-polar molecules which disorganize the iceberg structure. Because of aggregation, non-polar molecules decrease the contact surface with water which decreases their disruptive effect. Overall, the system assumes a considerable amount of entropy gain from motion of water molecules despite of the loss of entropy caused by confinement of the non-polar molecules. To sum up, hydrophobic effect originates from an entropy effect caused by the disruption of hydrogen bonds between water molecules [9, 15]. Moreover, formation of iceberg can explain the fact that low solubility of non-polar molecules in water originates from the unfavorable entropy.

Noteworthy, the role of iceberg formation in the hydrophobic effect was questioned by numerous scientists. Their work is mainly focused on explanation of the extremely long range hydrophobic interaction reaching even 100 nm from a non-polar surface. The evidences for the existence of iceberg like structures was presented by Yamaguchi *et al*., however their research did not uncover the relation between iceberg like structure formation and decreased mobility of water molecules [91]. Additionally, the presence of nanobubbles on the surface of hydrophobic molecules was reported, which could be linked with the strangely long-range nature of the hydrophobic interaction. It is believed that the exceptional strength of the hydrophobic interaction results from the capillary action between nanobubbles which occur subsequently to nanobubbles growth [94]. Data from AFM [95], X-ray reflectivity [96] and neutron scattering [97] support this hypothesis, which suggests that formation of gas-like water is more probable than ice-like water[98].

1.3.2.5 Hydrogen bonding

Hydrogen bond as in the case of dipolar interactions is widely electrostatic in nature [99, 100], whereby proton mediates the attraction of two larger electronegative atoms such as oxygen, nitrogen or fluorine [70]. These atoms attract the electron cloud of hydrogen atoms, thus causing their positive polarization. As a result, strong interaction between this positively charged hydrogen atom and nearby electronegative atoms can occur [15].

The strength of hydrogen bond ranges from 10 to 40 kJ/mol, which means that this force is weaker than a covalent bond (~ 500 kJ/mol), but stronger than vdW interactions (~1 kJ/mol). Generally, in protic solvents such as water, alcohol, the free energy of hydrogen bond formation is quite low (12-20 kJ/mol for water-water) [70]. A unique feature of hydrogen bonding is the possibility of bond formation only through specific binding sites like polarized hydrogen atoms and lone electron pairs. Structure formation such as linear chain, ring, dimer, layered sheet and three-dimensional network depends on the number of binding sites in the molecule [15]. The strength as well as directionality of the hydrogen bond are crucial for DNA double helix stability and integrity as well as for functionality of bio membranes and cellular transport [9]. As in supramolecular systems [47, 101], hydrogen bonding occurs frequently in the self-assembly of nanoparticles [102-105] or nanorods [106-108].

1.4 DNA molecular hybrids

Coupling of synthetic polymers with biological components can greatly increase the variety and complexity of structures originating from polymers. Block copolymers in which one of the building blocks is biological are referred as ‘polymer-bioconjugates’’ or ‘‘macromolecular chimeras’’ introduced by Schlaad *et al.* [109]. Selection of biological segment does not restrain to one class of molecules- it can be an amino acid or nucleic acid chain (DNA, RNA) as well as an oligo- or polysaccharide. Macromolecular chimeras was the first class of compounds combining convenience of synthetic polymers (e.g. protein repellency, temperature sensitivity) with the features of biological molecules (e.g. targeting-antibodies) [110].

In order to obtain well defined molecular chimeras, fine control over the synthesis is required. Synthetic strategies which can be used to obtain polymer bio-conjugates are summed up below.

1.4.1.1 DNA copolymers synthesis

(the following sub-section was adapted with Springer permission from *DNA-Polymer Conjugates: From Synthesis, Through Complex Formation and Self-assembly to Applications, Bio-Synthetic Polymer Conjugates* by D. Kedracki, I. Safir, N. Gour, N. Kien Xuan, C. Vebert-Nardin, , 253 (2013) 115-149 [111] and updated with the newest literature)

Modern synthetic chemistry allows currently the versatile synthesis of DNA-polymer conjugates through the large choice over the composition, length and architecture of both oligodeoxynucleotide (ODN) sequences and polymer segments. Conjugation of ODN can be conducted at the 2'-position of the ribose sugar, nucleobases and internucleotidic phosphodiester bonds. But the most common reactions take place at the 5'- or 3'-termini, due to high accessibility of these positions. It has been reported that this strategy has also another advantage, namely conjugation through the 3'-terminus enhances the exonuclease resistance of the nucleotide sequence[112] Conjugation of ODN is considered as quite challenging because even slight changes in the sequence structure may result in its properties change, which is crucial regarding the potential future application of the resulting DNA-polymer conjugates. Therefore, the specific sites for conjugation should be carefully selected. Another issue which has to be considered is that, conjugation sites may have limited access along the ODN fragment. Different stabilities of polymer and nucleotide sequence entities which can occur as the result of their exposure for specific reaction conditions should be also taken under account [113].

Synthetic strategies of DNA conjugation to polymers mainly rely on coupling terminal groups (grafting strategy), which is presently the most efficient and popular approach. Basically, there are two principal approaches for the binding of an ODN sequence with a polymer, which can be differentiated into solid-phase synthesis (SPS) and solution coupling. Solution coupling can be used for generation of both water soluble and amphiphilic DNA–polymer conjugates. However, carrying a solution reaction in order to obtain an amphiphilic product usually leads to low yields due to the chemical incompatibility of the two reactants [114]. These two types of DNA conjugation are based on the same types of reactions. However, despite of the slightly lower coupling efficiency in comparison to the solution coupling, SPS synthesis offers simplified purification and deals better with components solubility. In the last few years new methods of DNA conjugation with polymers have been reported, such as enzymatic reactions, which is not described here and the reader is referred to the following excellent reviews [114-117].

1.4.1.1.1 Solution coupling

Three main routes are used for DNA-polymer conjugation (*Figure 1-12*):

1) peptide bond formation

Amide bond is formed as a result of reaction between the amino group of one of the reactants (usually DNA) and the carbodiimide (e.g. 1-ethyl-3-(3-dimethylaminopropyl) carbodiimide (EDC)) activated carboxyl group of the second reactant (usually polymer) [118].

2) disulfide bond formation

This type of conjugation requires both elements modification with sulfhydryl groups, being one of these groups activated [119].

3) Michael addition

In the case of Michael addition sulfhydryl modification is required as well and this group subsequently reacts with maleimide or acrylic acid. The bond is formed through nucleophilic addition of thiol to an electron deficient carbon [119].

In the case of all reactions mentioned above the polymer reactant is usually used in slight excess [112]. High yields of DNA-polymer conjugates obtained by solution coupling have been widely reported [120-122]. Needless to say, solution strategies require purification subsequent to coupling.

The most important advantages of solution coupling, which could be accounted for, are that these reactions can be performed in laboratory conditions in a very straightforward way, without expensive automatic DNA synthesizer. Moreover, DNA sequences with various modifications are commercially available.

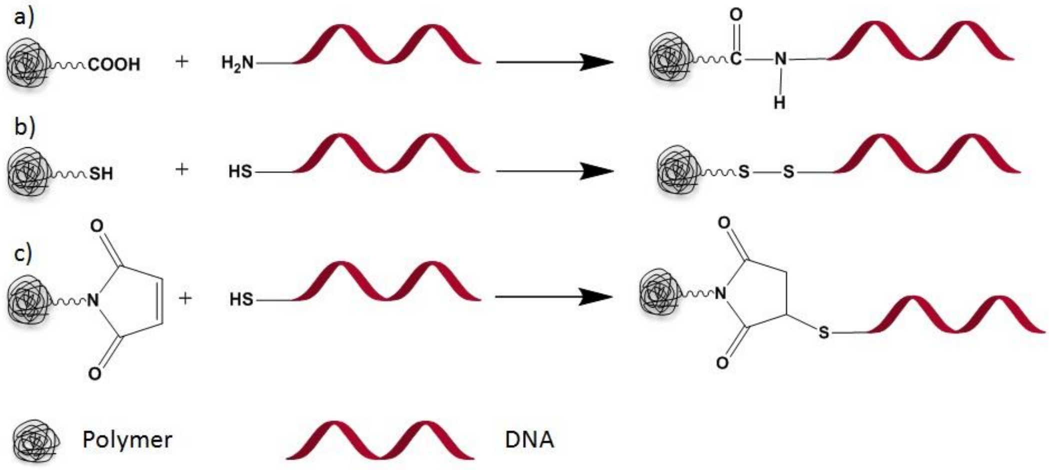

Figure 1-12. Solution coupling strategies of DNA conjugation with polymers. a) Amide bond formation. b) Formation of disulfide bridges between the thiol groups of both components. c) Michel addition of maleimide to ODNs fragment functionalized with a sulfhydryl terminal group [111](Figure adapted with permission of Springer)

1.4.1.1.2 Solid-phase synthesis (SPS)

As mentioned above this strategy prevents from performing tedious chemistry and purification steps [122]. It is also noteworthy that, over the course of the SPS reaction, potentially reactive groups along the ODN fragment are protected and thus potential side reactions are excluded. There are two kinds of SPS: programmed, fully automated sequencing in a DNA synthesizer and modified techniques taking advantage of simple tools like syringe filters. The advantages of automated synthesis are precise control over the reaction, large scale and fine reproducibility but the cost of using this approach is quite high. On the other hand, thanks to modified techniques, a product which matches perfectly special needs can be produced [119] .

Coupling to the 5’-end of ODNs using 2-cyanoethyl-N,Ndiisopropylphosphoramiditite (CEPA) reactive groups (*Figure 1-13* A) is the most fundamental method in automated DNA-polymer conjugate synthesis. CEPA modified polymers react with the detrityleted 5’-end of ODNs bound to a solid support, usually a Controlled Pore Glass (CPG) resin. To couple the polymer segment at the 3’-end of the DNA (*Figure 1-13* B), it is necessary to begin with the solid supported polymer or to carry out reverse synthesis, in which the desired compound is attached to the 3’-end of the sequence elongated in the 5’- to 3’-end direction. After cleavage from the resin and deprotection by liquid ammonia, ODN-based copolymers could be achieved [116].

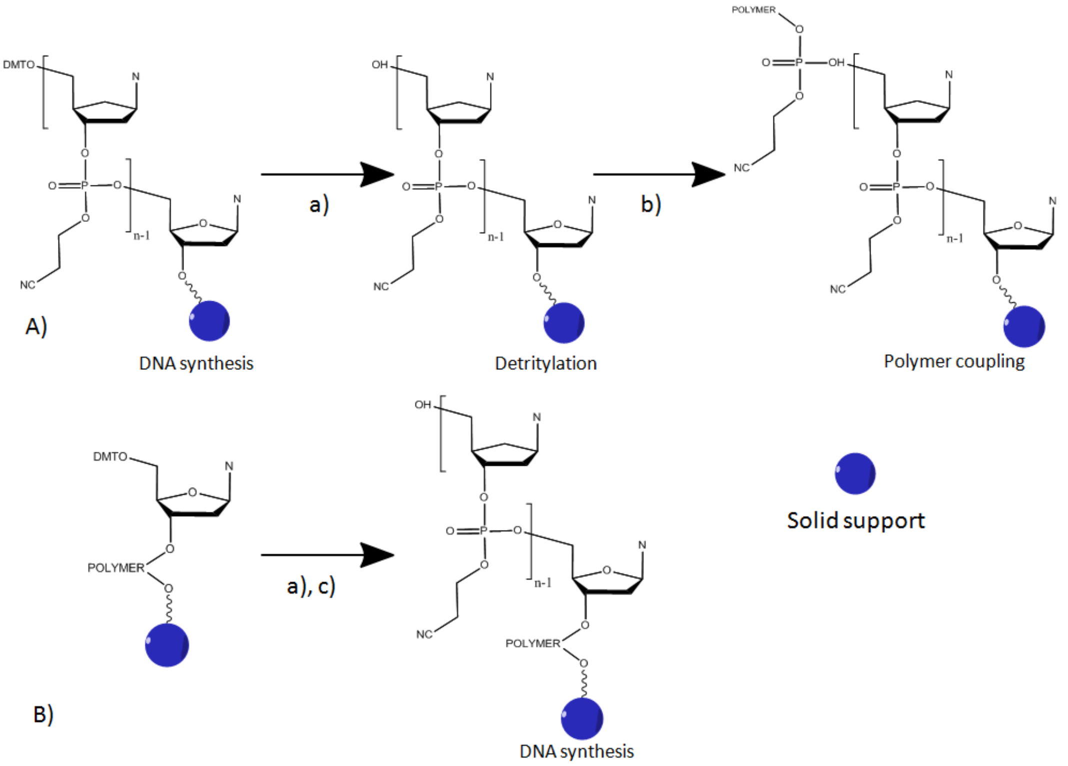

Figure 1-13. Synthetic scheme of the coupling of DNA with polymers at the (A) 5'- end and (B) 3'-end of the DNA; a) deblocking of DMT; b)coupling of activated CEPA to the 5'- end; c) standard synthesis with nucleoside phosphoramidite. Subsequently, in order to obtain the conjugate cleavage from the solid support is conducted prior to the washing out of the 2-cyjoanoethyl groups.[111] (Figure adapted with permission of Springer)

Disadvantages of the synthesis of DNA copolymers without a synthesizer are less convenience and time consumption but it is especially helpful in case of solvents or catalysts incompatibilities. The conditions of post-DNA synthesis indeed change depending on factors such as chemo-stability, catalyst and chemical structures. However, ex-situ approaches allow the preparation of linear and brush-type DNA-polymer conjugates [114]. We briefly present in here the different strategies for ex-situ synthesis on solid support. The mechanisms are the same as in the case of reactions conducted in aqueous solution [116, 123]. A Huisgen reaction occurs between an azide-modified oligonucleotide and an alkyl terminated component to form a 1,2,3-triazole (*Figure 1-14* d). This reaction is almost quantitative and can be conducted in aqueous solution. The efficiency of a Huisgen reaction is greatly increased when it is catalyzed by Cu^I [124, 125]. Sonogashira-Hagihara coupling is a reaction between terminal alkynes and aryl halide, catalyzed by palladium complexes. The reaction is conducted in the presence of catalytic amounts of Cu^I and an amine base (*Figure 1-14* e) [126, 127].

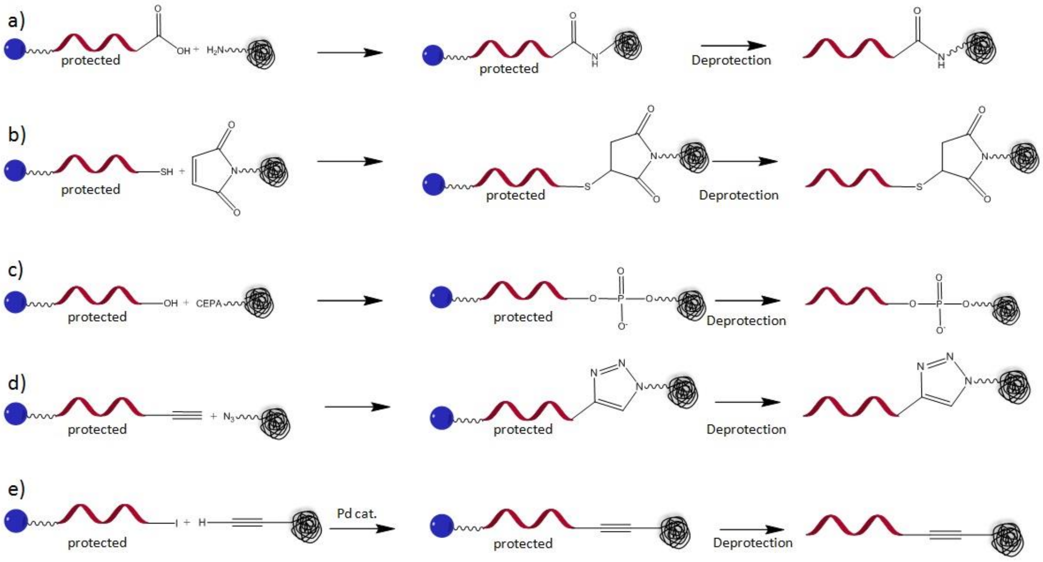

Figure 1-14. SPS strategies which can be employed for achieving DNA block copolymers (DBCs). a) amide bond formation, b) Michael addition, c) phosphodiester bonding, d) Huisgen reaction, e) Sonogashira-Hagihara reaction[111]. (Figure adapted with permission of Springer)

A recent promising strategy is the *"grafting-from"* ("*blocking-from*") approach which involves DNA chain modification with an initiator from which the polymer chain is grown. To the main benefits, which can be accounted for, is ease of unreacted species removal as well as purification and higher sterical availability which comes from the nature of the *"grafting-from"* approach which simply consists in monomer addition reactions [128]. The publications describing ATRP or RAFT polymerization approaches for the synthesis of DNA conjugates appeared already almost 10 years ago [129-131]. These reports depict the growth of the polymer from DNA chains immobilized at the surface modified with a suitable initiator. Noteworthy, to link the DNA with the appropriate initiator molecule, reactions which are described above are used (the most frequently peptide bond formation, mediated by NHS activation). In the case of the ATRP as well as RAFT polymerization from the DNA chain, an accelerated growth of the polymer chain was observed. This phenomenon was related to the presence of the highly charged phosphate group and complexation of copper by the nucleotide bases [129, 131]. However, analysis and characterization of the resulting DNA conjugates are problematic due to attachment of the copolymer to the surface. In 2014, Averick *et al.* proposed an even less complicated method to generate DNA linked initiators for synthesis of DNA based copolymers. The standard ATRP initiator is indeed converted to phosphoramidite. The subsequent polymerization occurs through *activators generated by electron transfer* (AGET) ATRP. This method was shown to provide high control over the molecular weight and narrow molecular weight distribution of the resulting copolymer [128]. It was also demonstrated through hybridization experiments that the nucleic acid sequence preserved its function. Authors evidenced that this strategy allows preparation of hydrophilic (*Figure 1-15*) as well as amphiphilic DNA based copolymers, which demonstrates the high versatility of this synthetic route. As the initiators were chosen in order to stay intact during the harsh condition of the cleavage from the resin, polymerization can be conducted subsequent or prior to the cleavage. The latter option offers accelerated preparation procedure and simplified purification processes which is especially relevant [128].

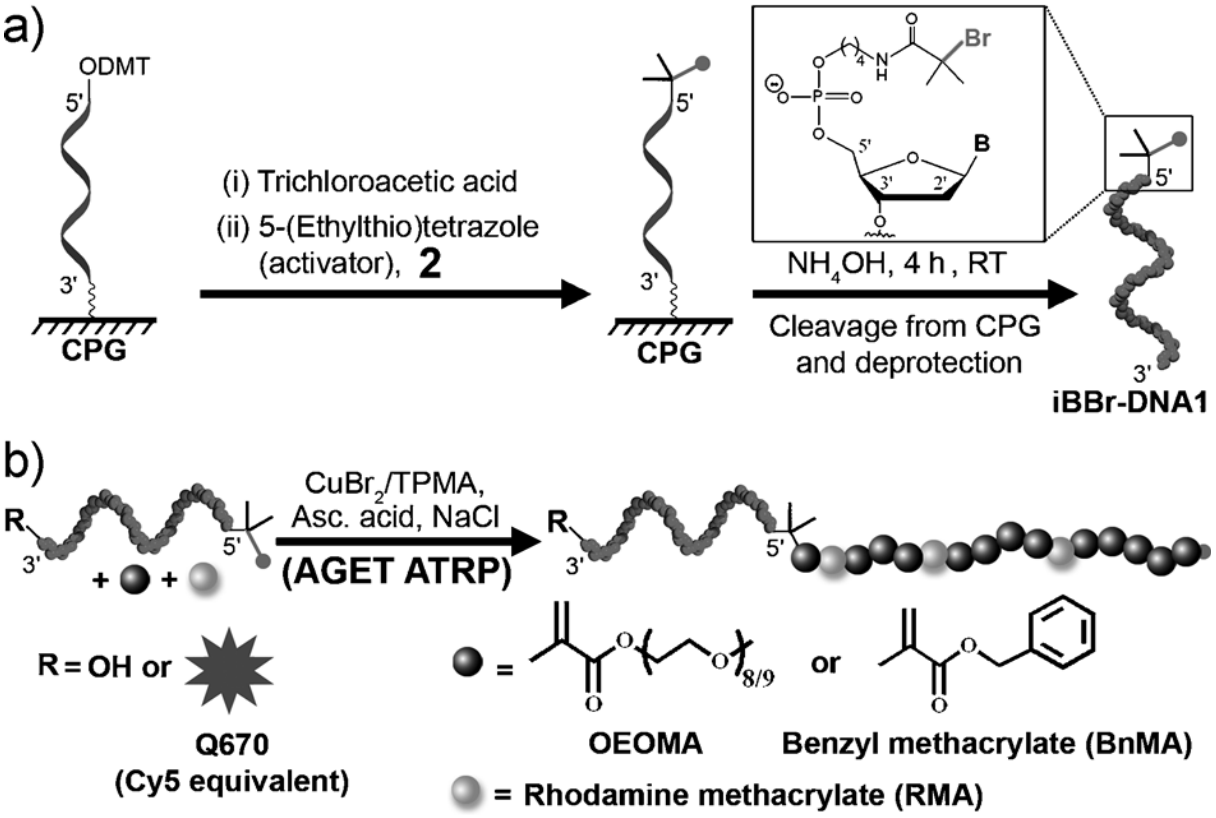

Figure 1-15. Synthesis of DNA based copolymer through AGET ATRP a)deprotection of ODN chain is followed by the addition of ATRP initiator to 5'-OH. Subsequent cleavage results in the deprotected DNA ATRP initiator, b) direct polymerization in solution with the use of two various monomers[128]. (Figure adapted with permission of John Wiley and Sons)

Scope of the thesis

DNA is a remarkable molecule carrying genetic information and involved in a plethora of significant biological processes. Nevertheless, cellular uptake, penetrability and plasma half-life of naked DNA is restricted. In order to overcome these limitations nucleotide sequences were conjugated to hydrophilic synthetic polymers. Coupling to the hydrophobic segments results in formation of nanostructures through self-assembly. This process might affect the properties of DNA involved in the assembly and hence opens new possibilities for carrier designing as well as means to establish the formation mechanism and interaction modes of organized DNA based copolymers. In order to provide such hybrids, synthetic strategies described in the section *Synthesis* were developed, from which peptide bond formation, maleimide coupling and disulfide bond formation are recognized as the most popular. Due to solubility incompatibility the synthesis of DNA hybrids has been so far evidenced for a finite number of polymer blocks like polystyrene (PS), propylene oxide (PPO), polyfluorene (PFO) and polybutadiene (PB) as the most popular hydrophobic moieties [114]. The structures achieved so far through self-assembly solely are spherical or cylindrical micelles and vesicles. The microphase separation of the hydrophobic and hydrophilic units was usually the driving force for structure formation [116].

The presented work deals with the development and characterization of novel DNA based copolymers to enlighten the several fundamental aspects involved in modes of structure formation and interaction. Herein, the others than ordinary ways to drive self-assembly are reported for the first time. Nucleation dependent polymerization as well as emulsification approaches are described. Former path resulted in the fibrillar morphology which is the first example of this particular assembly of DNA based copolymers and the latter produced micrometer size spherical capsules. To the best of our knowledge none of these two approaches was so far utilized in DNA based structure formation. Initially, polymer-DNA hybrids were prepared according to existing well described chemistry routes; however efforts to establish a novel straightforward strategy to couple DNA with higher efficiency were studied as well. Structures generated from copolymers according to various synthetic routes were investigated varying the hydrophilic weight fraction, and the architecture. Attempts were made to understand the principle of the structure formation of these molecules. In addition for the first time, the interesting bioinspired polymer, namely polyoxazoline was coupled with DNA. Polyoxazolines are regarded as pseudopeptides due to their structural resemblance to natural peptides, which represents their high potential for application in the field of biomedicine. Poly(2-ethyl-2-oxazoline) is an example of polymer of this class which is not toxic, biocompatible and approved by the Federal Drug Administration (FDA).

The thesis is divides into 4 chapters as described below.

3. Self-assembly: Synthesis and Self-assembly of a DNA Molecular Brush

In this chapter, we present a novel synthetic approach to generate of comb/graft DNA based copolymer through one step thiol click chemistry with a high coupling efficiency reaching 60% and high grafting density (67%). We demonstrate that the phenomenon of polymer crystallization can be used at first to simplify the further process of purification. Another important conclusion is that for this specific and high DNA grafting density the resulting copolymer self-assembles intro spherical structures which are stable against hydrogen bonding and as demonstrated by hybridization assays the nucleotide sequences remain functional, which paves the way for the use of this structures for speciation of nucleotide sequences.

4. Hydrogen bonding induced formation of DNA-copolymer fibrils through amyloid-like nucleation polymerization

This chapter describes the synthesis of PBOX-g- DNA copolymers according to conventional chemistry routes. In comparison to the results described in the chapter 3, the so synthesized polymer is of low grafting density, which induces another mode of structure formation. Low grafting density DNA copolymer self-assembles into fibers due to inter-and intramolecular interactions. Investigations of the fibers formation process suggest a nucleation dependent polymerization mechanism, which is very specific for amyloid protein and peptides. This work is of high importance, taking under consideration the association of amyloid fibers with several neurodegenerative diseases such as Alzheimer's disease.

5. Emulsions and emulsion templated self-assembly

5.1. Polymer-aptamer hybrid emulsion templating yields bio-responsive nanocapsules

It was demonstrated that a suitable DNA copolymer could efficiently stabilize a water-in-oil emulsion. Proven by AFM and reflectometry the functionality of the aptamer (oligonucleotide sequences which bind to a target molecule with very high affinity and specificity) is hindered neither by synthesis nor by the engagement of aptamer in the process of coupling and emulsion stabilization.

5.2. Hybrid Nanocapsules Targeting the Nucleolin Cancer Cells Surface Receptor

Poor solubility of many advanced and effective anticancer drugs is a reason of formulation issues. In order to make delivery of hydrophobic drugs efficient DNA-copolymer stabilized emulsions were further combined with the Layer-by-Layer (LbL) deposition methodology with novel strategy of functionalization with an aptamer. Emulsification would provide simple and highly efficient encapsulation of hydrophobic anticancer drugs.

2 Experimental techniques

2.1 UV-VIS Spectroscopy

The Beer-Lambert law, which relates the properties of the material to the absorption of the light passing through describes the fundamental principle of UV-Vis spectroscopy. The ratio between the intensity of the incident (I_o) and the transmitted (I) radiation defines the *transmittanc*e (T) or *absorbance* (A) [132].

$$T = \frac{I}{I_o} \qquad \text{Equation 9}$$

The transmitted intensity is dependent on the path length (*l*) and the molar concentration (*c*) of the sample as described by the following equation [133];

$$I = I_o 10^{-\varepsilon c l} \qquad \text{Equation 10}$$

Where ε is the molar absorption coefficient, also defined as *"extinction coefficient"*.

The molar absorption coefficient depends on the incident radiation and increases with the absorption.

Experimentally, the absorbance A is measured at a given wavelength.

$$A = -log\frac{I}{I_o} = -log\,T \qquad \text{Equation 11}$$

Thus, the Beer-Lambert law turns into;

$$A = \varepsilon c l \qquad \text{Equation 12}$$

The result described by Equation 4 is also defined as *optical density*.

2.2 Infrared Spectroscopy

Change of the molecules vibrational behavior like changing their vibrational and rotational modes through supply of energy by infrared radiation (IR) is the basic principle of infrared spectroscopy [134]. Thermal emission which is usually the source of infrared radiation causes vibrations of particular molecular groups, which is followed by changes of dipole moments. Molecules can absorb IR radiation when the energy of this radiation matches the molecule specific vibration frequency, namely the *resonance frequency*. The strength of the bond as well as the mass of the atoms is the factor which is determining the *resonance frequency*. The individual vibrational motion is normally followed by rotational motions even in the case when the absorption engages discrete quantized energy levels. The bending and stretching are the two main kinds of molecular vibrations. Many organic compounds can be characterized by IR spectroscopy due to unique vibrations of functional groups which do not spread on the whole molecule and are related to the absorption bands in the IR spectrum. Mid IR between 4000 and 400 cm^{-1} is the region of most favorable vibrational frequencies [135]. Spectral characterization is performed with the use of Fourier Transform techniques and of the *Michelson interferometer*, which enables extraction of frequencies within the composite signal. [133]. The most commonly used IR spectroscopy sampling technique is attenuated total reflection (ATR). The beam of IR light passes through an ATR crystal and is reflected at least once from the internal surface. Total Internal Reflection is a phenomenon on which ATR spectroscopy was built on. IR radiation propagating in an optically denser medium of refractive index n>1 is totally reflected at the interface of an adjacent medium of rarer optical medium (*Figure 2-1*). An evanescent field is generated in the medium of lower optical density despite of the fact that the light rays do not really propagate in this region. This evanescent field is absorbed by the sample molecules which interact with light at the interface between mediums with various optical density [136].

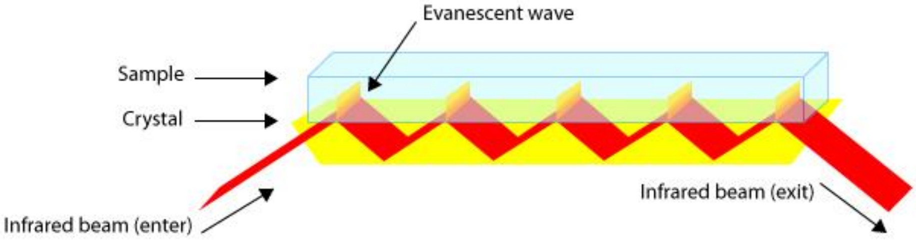

Figure 2-1. Schematic illustration of Total Internal Reflection in Attenuated Total Reflectance Spectroscopy[137]

2.3 Circular dichroism

Interactions of certain classes of molecules with left and right polarized light is the principle of circular dichroism. CD is considered to be one of the best methods to investigate the conformation of biological molecules. CD spectroscopy measurements are indeed straightforward, require rather small quantity of material and can be performed at various concentrations, pHs, temperatures and ionic strengths [138, 139]. Circularly polarized light is chiral. Chiral molecules are therefore required to distinguish interactions with both left and right polarized light [140]. UV and Vis light wavelengths are usually used in CD spectroscopy owing to high strength of CD signal and therefore short accumulation time. Moreover, the analysis of intra- and intermolecular interactions in self-assembled systems is enabled because of great sensitivity to long-distance electronic interactions. Below wavelengths of 180 nm the circular dichroism measurements are recognized as vacuum-ultraviolet circular dichroism, region in which most of the signal refers to $n \rightarrow \sigma^*$ band transitions of the lone-pair electrons of oxygen [141].

The difference in the absorbance of the left (A_L) and right (A_R) handed circularly polarized light is determined as CD;

$$\Delta A = A_L - A_R \qquad \text{Equation 13}$$

which is used to determine the CD extinction coefficient ($\Delta\varepsilon = \varepsilon_L - \varepsilon_R = \frac{A_L - A_R}{cl}$, where c is the concentration*(mol L^{-1})* and l the cell length *(cm)*) or the molar ellipticity ($[\theta^2]$, $[\theta] = 3298.2\Delta\varepsilon$)). The bands in the CD spectrum referred to as Cotton effect can take positive or negative absorbance value. For instance, the tertiary and quaternary structures of proteins can be characterized by near-UV CD (250-320 nm) spectra in which characteristic bands for amino acids such as cysteine and phenylalanine are detected. In the far-UV (below 250 nm) region, the signal of the peptide bond is the most prominent, with a characteristic transitions n→π* at around 220 nm and π→π* at around 190 nm. A CD spectrum in far-UV enables assessing the secondary structure (α-helix, β-sheet) of the protein [139].

2.4 MALDI-TOF

Nowadays, matrix assisted laser desorption/ionization time-of-flight spectrometry (MALDI-TOF) is considered as a versatile technique for macromolecules characterization. This relatively new in comparison with other mass spectrometry (MS) techniques found application in fields such as clinical chemistry, microbiology, genotyping and many others. Hence, it also enables analysis of the whole cell without need for separation, fractionation or cleanup. This method thus became very relevant for bacteria characterization. Due to capabilities such as high-molecular weight desorption of thermo labile molecules, fine accuracy as well as sensitiveness and wide range of analyzed mass (from 1 to 300 kDa) that can be detected with this method, MALDI-TOF is currently very popular. To the group of compound that were successfully analyzed can be accounted for peptides, proteins, oligosaccharides, oligonucleotides and lipids [142]. MALDI is a technique which is based on a non-destructive sample ionization and vaporization that allows avoiding significant decomposition of sensitive molecules and their transfer to a spectrometer in the form of ions [143]. The first step in MALDI analysis consists in the specimen co-crystallization with a significant excess of a matrix. This term usually refers to an UV absorbing weak organic acid. The matrix vaporized by laser irradiation carries the analyte molecules and thus is considered to play a crucial role by causing indirect analyte vaporization. Another role of the matrix is to serve as proton donor in the positive detection mode and receptor in the negative detection mode. The choice of mode depends whether positively or negatively ions are formed during ionization [144]. Various theories describe large molecules desorption such as the thermal-spike model [145] or the pressure pulse theory [146] . However ionization is generally recognized to occur via proton transfer between the matrix and the analyte ($MH^+ + A \leftrightarrow m + AH^+$ and $(m-H)^- + A \leftrightarrow m + (A-H)^-$) and cationization (primar ionization of a molecule by the formation of metal ion adducts, e.g. $mNa^{+} + A \leftrightarrow m + ANa^{+}$) [144]. Different types of analyzers exist, however due to simplicity, cost effectiveness, high sensitivity and unlimited mass range the time-of-flight (TOF) analyzer is the most widespread. In the TOF approach the set of ions is accelerated to the detector, where energy is distributed equally for all ions. As all have the same energy, but various masses, the ions arrive to the detector at various times.

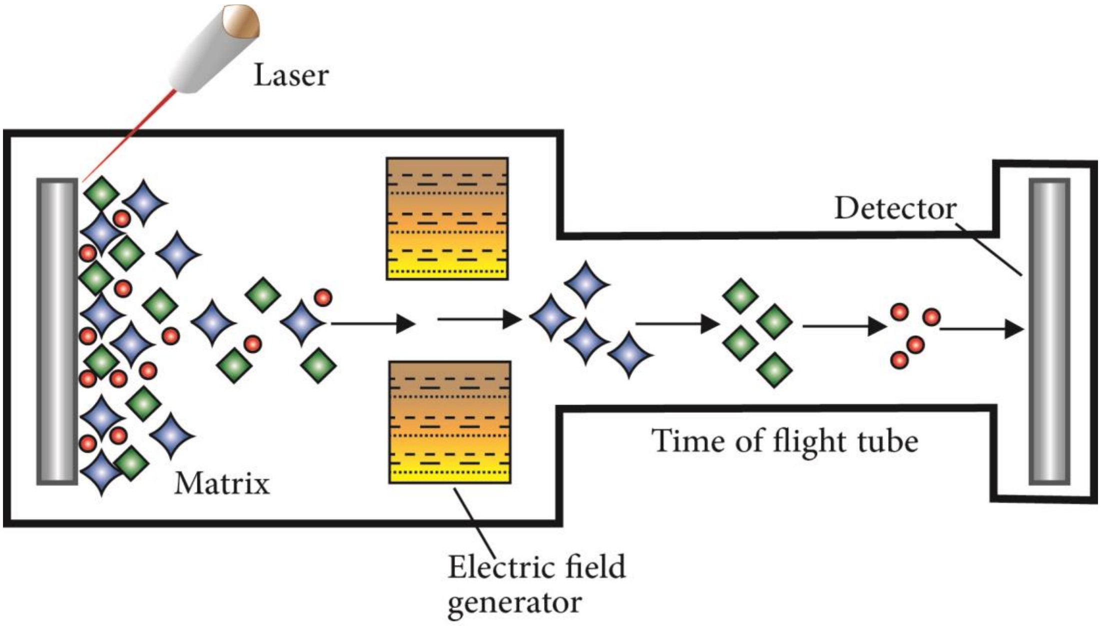

Figure 2-2. Schematic representation of MALDI-TOF working principle

Heavier ions need more time to reach the detector while lighter ions with the higher velocity arrive at first. The time of ions flight is used to determine the mass. The MALDI-TOF spectrometer operation principle is depicted in the *Figure 2-2*.

2.5 Reflectometry

Reflectometry can be regarded as a simplified version of ellipsometry. However, reflectometry is much cheaper and enables the continuous monitoring of adsorption events over short time-scales. Reflectometry is the perfectly suited tool for kinetics measurements of adsorption events on time scales from seconds to minutes. [147].The reflectometry has proven to be useful in biomolecular sensing with a sensitivity (0.32 pg/mL[148], 26 pg/mm^2[149]) comparable to suface plasmon resonance (SPR) [148]. A schematic representation of a reflectometry set-up is depicted in the *Figure 2-3*.

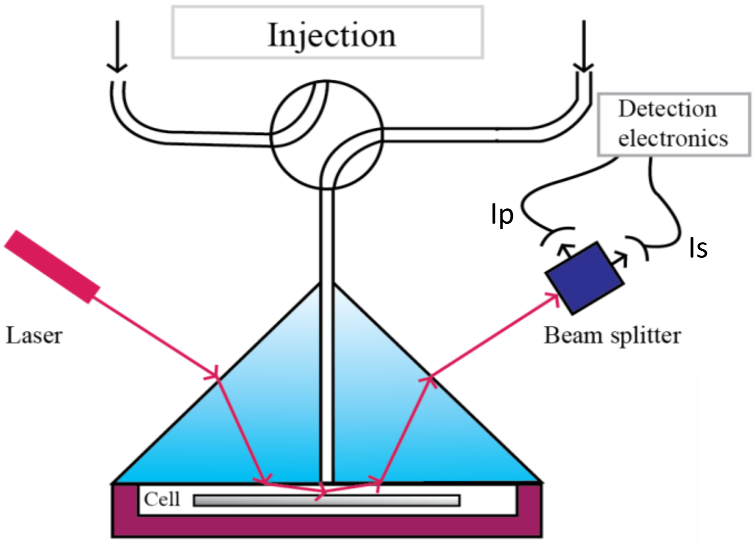

Figure 2-3. Reflectometry experimental set-up

The detection principle of this method is based on the reflectivity changes upon adsorption of the molecules at the interface. The optical prism usually made of fused silica focuses the linearly polarized light on the surface. The beam reflected from the surface passes through a beam splitter (Wollaston polarizer), which splits the beam into *parallel* (p) and *perpendicular* (s) components to the plane of the reflection. Two separate photodiodes measure continuously perpendicular (I_s) and parallel (I_p) intensities and thus the signal R is defined as [150];

$$R = \frac{I_p}{I_s} \qquad \text{Equation 14}$$

Adsorption on the substrate results in the formation of an additional layer which upon interaction with the incident light, changes its state of polarization. Change in the state of polarization is affecting the output signal R. I_p and I_s are proportional to *reflectance* (R_p and R_s) respectively and related to the output signal by the following equation [150];

$$R = C\frac{R_p}{R_s} \qquad \text{Equation 15}$$

Where C is an unknown instrumental constant, which can be eliminated by signal normalization;

$$S(t) = \frac{R(t) - R(0)}{R(0)} \qquad \text{Equation 16}$$

The reflectometry signal is proportional to the adsorbed mass, as described by the following equation;

$$S(t) = A\mathit{\Gamma}_{dry} \qquad \text{Equation 17}$$

Where, $\mathit{\Gamma}_{dry}$ is the adsorbed mass per unit area and A is a sensitivity constant which varies for every system. To quantify the sensitivity constant the impact of the adsorption on the refractivity signal value needs to be evaluated. This constant can be obtained from calculation with a homogenous four-slab model, in which the adsorbed polyelectrolyte layer is the topmost slab. The refractive index of this layer is calculated from mixing law [151];

$$n = n_s + \frac{\mathit{\Gamma}_{dry}}{L}\frac{dn}{dc} \qquad \text{Equation 18}$$

Where, n_s is the solvent refractive index, $\frac{dn}{dc}$ is the adsorbed material refractive index increment, L is the top layer thickness which can be obtained from an ellipsometric measurement(corresponding to adsorbed protein).

2.6 Light scattering

Light scattering can be understood as reemission of the electromagnetic wave upon interaction within a non-homogeneous medium in which the wave is propagating [28]. The electromagnetic wave electric field interacts with the electron cloud of the molecules. The electronic cloud is disturbed: the oscillating electrons reemit the radiation with the same frequency as the incident light. This phenomenon is named *light scattering* (LS).

Light scattering is an extremely useful tool for characterization of particles properties such as size, shape and molecular weight. Depending on how the intensity is monitored, light scattering can be divided into *static* (SLS) and *dynamic* (DLS). In the former the intensity is measured as a function of scattering angle, the latter measures the temporal variation of the intensity described by an autocorrelation function. *Static light scattering* might be used to obtain information about the positional correlations and the average spatial arrangement of the particles (concentrated systems) as well as the shape of individual particles (diluted systems). On the other hand *dynamic light scattering* provides information about the diffusion coefficient, size as well as size distribution. The combination of SLS with DLS can provide additional information such as molecular weight and shape [152, 153].

Static light scattering (SLS)

A schematic representation of a light scattering set-up is presented below;

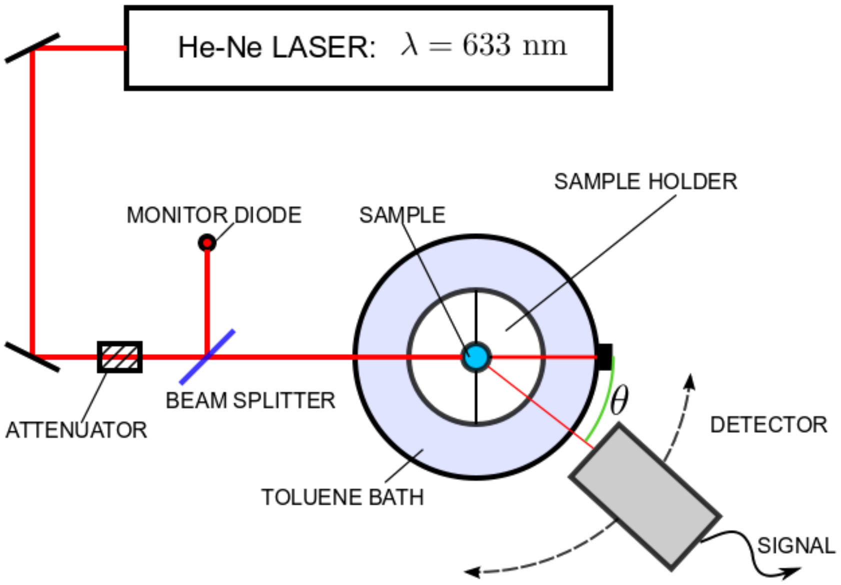

Figure 2-4. Schematic representation of an LS experimental set-up.[154]

The laser emits light of wavelength λ_i and wave vector $\vec{\kappa}_i$ which upon propagation through a polarizer is characterized by a determined polarization. The part of incident light that undergoes scattering is characterized by a wave factor $\vec{\kappa}_s$. When the light arrives at detector the intensity of the light is monitored at the angle θ and distance R. The volume at the intersection of the incident and scattered light comprising a number N of particles is known as scattering volume V_s [155].

The difference between the incident and scattered wave factors is defined as *scattering vector*;

$$\vec{q} = \vec{\kappa}_i - \vec{\kappa}_s \qquad \text{Equation 19}$$

In a case of elastic scattering, the wave factors of incident and scattered light have the magnitude $\frac{2\pi}{\lambda} = \frac{2\pi n}{\lambda_o}$, the magnitude of scattering vector is given by (n is the solution refractive index);

$$|\vec{q}| = \frac{4\pi}{\lambda} sin\left(\frac{\theta}{2}\right) \qquad \text{Equation 20}$$

The reverse dependence of scattering vector is defined as *spatial resolution*. *The form factor*, P(θ) is a parameter that is defined as the ratio of scattered intensity at angle θ and at angle θ=0, and illustrates the strong angular dependence of scattered intensity by large particles [155].

Quantitative analysis requires reduced scattered intensity represented by the *excess Rayleigh ratio*;

$$\Delta R(\theta) = \frac{\Delta I_s(\theta)}{I_o}\frac{R^2}{V_s} \qquad \text{Equation 21}$$

Where, $I_o$is the incident light intensity and ΔI_s is the difference between intensity of the scattered light by a specimen and the pure solvent monitored at distance *R*.

In the case of identical particle *excess Rayleigh ratio* is described by;

$$\Delta R(\theta) = KcMP(q)S(q) \qquad \text{Equation 22}$$

Where, $K = 4\pi^2 n^2 \left(\frac{dn}{dc}\right)^2 / (N_A \lambda_o^4)$, $\frac{dn}{dc}$ refractive index increment, *c* particle concentration, *M* molar mass of particles, *P(q)* particle *form factor* and $S(q)$ *structure factor* (inter-particle interaction potential). In the dilute regime and in the limit of low scattering angles, the *form factor* can be presented as;

$$P(Q) = 1 - \frac{q^2 R_g^2}{3} + \cdots \qquad \text{Equation 23}$$

Where R_g is the *radius of gyration*. Thus the Rayleigh ratio can be presented as[28];

$$\frac{Kc}{\Delta R(\theta)} = \frac{1}{M}\left(1 + \frac{q^2 R_g^2}{3} + \cdots\right)(1 + 2BcM + \cdots) \qquad \text{Equation 24}$$

Where *B* stands for the second virial coefficient. This equation provides the basis for *Zimm plot* analysis. An example of this approach is given in Figure 4. It requires conduction of two extrapolations, one to the zero scattering angle and the second to the zero concentration. The result of this extrapolation provides the $1/M_w$ value. The values of R_g and B can be obtained from the slopes of the angle and concentration extrapolations. The $sin^2\left(\frac{\theta}{2}\right)$ is proportional to q^2 , in a case of plotting $\frac{Kc}{\Delta R}$ versus $sin^2\left(\frac{\theta}{2}\right) + \gamma c$ (γ being an arbitrary constant used to spread the data).

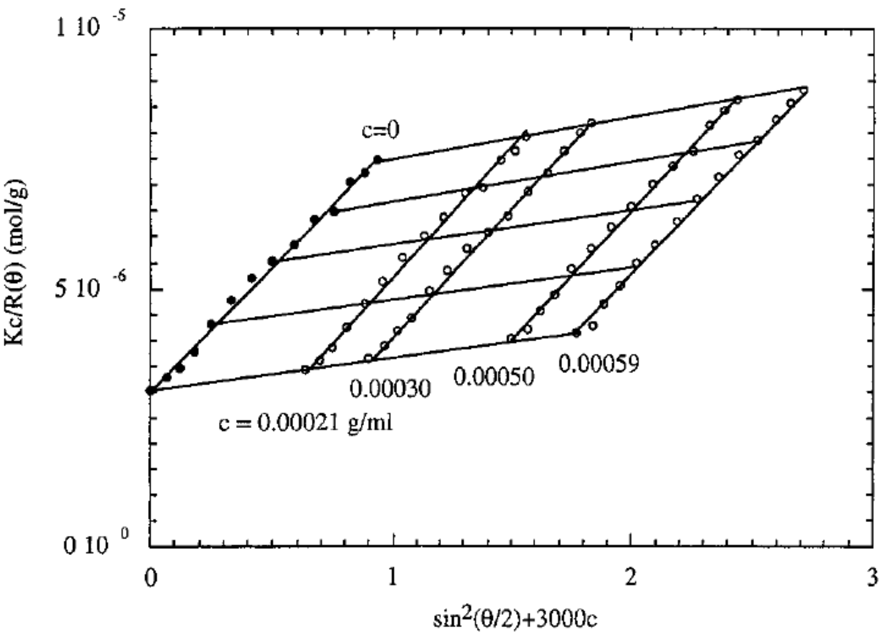

Figure 2-5. Zimm plot of methylcellulose in water[156]. (Figure adapted with permission of American Chemical Society)

One possible choice for the γ value is to set it around $1/\Delta c$, where Δc is the interval in the concentration series. Subsequently, linear regression of each concentration data set should be performed, 1) $\frac{Kc}{R_\theta}$ fitted against $sin^2\left(\frac{\theta}{2}\right)$, at zero angle intercept recorded, 2) $\frac{Kc}{R_\theta}$ fitted against c, at zero concentration intercept recorded. Subsequently, by fitting of the zero angle intercepts versus concentration and the zero concentration versus $sin^2\left(\frac{\theta}{2}\right)$ has to be performed. From these two slopes the values of R_g and B can be determined. The value of $1/M_w$ is indicated at the point of $\frac{Kc}{R_\theta}$ axis where the both lines intersect [28].

Dynamic light scattering (DLS)

The working principle of DLS relies on two phenomena, the Tyndal effect and Brownian motion. Two main factors namely *scattering angle (θ)* and the *monitoring time (t)* determine the scattered light intensity. In case of SLS, just particles with the size comparable to the incident light wavelength can be reliably characterized (the minimum condition is $\lambda/20$), while in the DLS experiment, particles can be significantly smaller than the light wavelength. Due to the Brownian motion of particles the scattered intensity is time dependent. All particles encountered by the light beam can be treated as secondary light sources and due to their constant movement; the distance which light has to pass to enter the detector varies with time. The intensity fluctuates in time, due to particle motion, which appears as “speckles” in space. To ensure that these fluctuations are monitored, the photo detector spatial resolution must be suitable. The single speckle is known as the “coherence area” (A_{coh}) and is dependent on the separation between detector and object (R) as well as on the wavelength (λ)[157];

$$A_{coh} = \frac{\lambda^2 R^2}{\pi x^2} \qquad \text{Equation 25}$$

Where x stands for the radius of the scattering volume. To ensure high resolution of the measurement it is necessary to provide high value of the scattering vector, which can be achieved by decreasing the size of the detector aperture. The time of fluctuations rely on the diffusion coefficient. Needless to say that the large particles will diffuse slower than smaller, which is reflected in the slowly fluctuating intensity signal in comparison to the small particle which moves faster. *Autocorrelation,* known also as *the photon correlation spectroscopy* (PCS), provides the quantitative information about the fluctuations time scale. The scattered intensity is described by a time dependent signal, *I(t)* measured at various time intervals. When the scattered intensity is considered at the arbitrary time t $I(t)$ and subsequently at delayed time t + τ presented as $I(t+\tau)$, the normalized autocorrelation function is given by[157];

$$g^2(\tau) = \frac{\langle I(t)I(t+\tau)\rangle}{\langle I(t)\rangle^2} \qquad \text{Equation 26}$$

For $\tau = \infty$ the signal is ideally uncorrelated and the result of the above equation is equal to $\langle I\rangle^2$. On the other hand when $\tau = 0$ the equation yields $\langle I^2\rangle$ and the signal is ideally correlated. The normalized autocorrelation function for a photo count complying with a Gaussian function is associated with the first-order correlation function of the electric field $g^1(\tau)$ by the following relation [157];

$$g^1(\tau) = [g^1(\tau) - 1]^{0.5} \qquad \text{Equation 27}$$

The DLS basic principle concerns the analysis of the autocorrelation function in order to retrieve information about particle size. Autocorrelation function decays exponentially with the delay time for a monodisperese suspension of spherical particles subject to a Brownian motion and is represented by the following equation;

$$g^1(\tau) = A \cdot e^{-Dq^2\tau} + B \qquad \text{Equation 28}$$

Where A is the correlation function amplitude, B stands for the baseline, D is defined as the particle translational diffusion coefficient and q is the magnitude of the scattering vector. The hydrodynamic radius of spherical particles can be calculated from the Stokes-Einstein equation;

$$D = kT/(6\pi\eta R_h) \qquad \text{Equation 29}$$

Where k is the Boltzmann constant, T is the temperature and η is the viscosity of the solvent [157]. Noteworthy, this equation is applicable for spherical particles in diluted systems with the size that does not induce angle dependence of the scattered intensity.

2.7 Small angle X-ray scattering (SAXS)

Small angle X-ray scattering is an elemental technique for structural analysis of condensed matter as well as to probe the interactions of biological molecules and their complexes in solutions [158-160]. The area of application is very wide and covers fields such as metal alloys, synthetic polymers, porous materials, nanoparticles etc. As SAXS enables measurements in the high range of conditions from physiological to denaturing it is a perfectly suited tool for investigating nucleic acids and proteins. Moreover, in comparison to the techniques such as NMR there is no restriction regarding molecular weight of the examined molecule [159]. In general, conventional SAXS analysis is dedicated to relatively big structures, whereas wide angle X-ray diffraction probes at atomic levels of crystals organization. Needless to say, SAXS analysis is not restricted just to large lattice spacing diffraction but also amorphous and mesomorphic materials [158]. The advent of high flux synchrotron sources provides spatial (nanometric range) and time (milliseconds) resolution which is unreachable by other techniques [153]. In this approach the synchrotron beam can be focused to micro and nanometer size due to sufficient range of divergence and photon flux. The advantage of microfocused SAXS is that it enables the examination of small entities and provides immensely clustered data from the investigation of thin samples with the real space resolution of micro and submicrometers [153]. Combined SAXS and wide-angle X-ray scattering enables to obtain structural information about investigated systems in the range between 0.3 and 100 nm in the time scale from microsecond to months for both diluted and concentrated samples.

Elastic scattering of X-ray photons of molecules as the function of the angle is the general principle of this method. Standard SAXS measurement is depicted in the *Figure 2-6*.

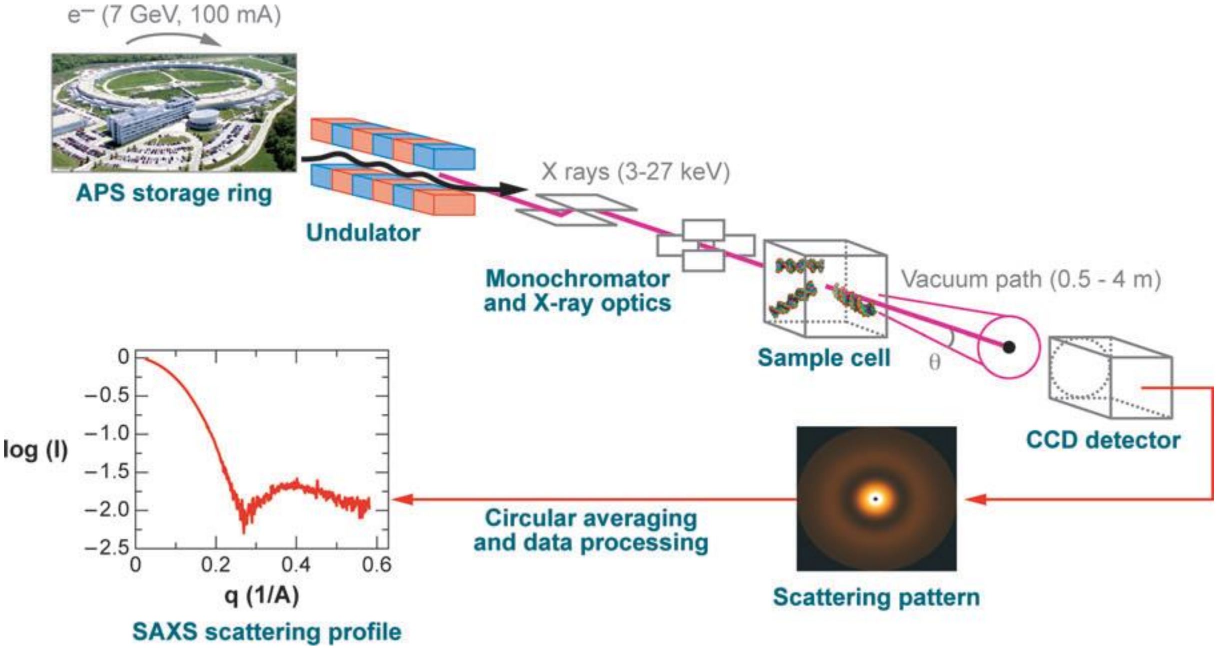

Figure 2-6. Schematic representation of small-angle X-ray scattering setup for beam line 12-ID at the Advanced Photon Source (APS).[159]

Global structure and conformation information about examined molecules are extracted from the scattering profile. Parameters such as M_w, radius of gyration (R_g) and intramolecular distance (D_{max}) are achievable through SAXS analysis [159]. In a case of appropriately dilute solutions of biomolecules in which interactions between particles are negligible, parameters such as radius of gyration (R_g) and scattering intensity $I(0)$ can be obtained from the Guinier approximation for small momentum transfers q[153];

$$I(q) \approx I(0)exp(\frac{-q^2R_g^2}{3}) \qquad \text{Equation 30}$$

The molecular weight can be obtained from;

$$I(0) = \kappa c(\Delta\rho)^2 M_w^2 \qquad \text{Equation 31}$$

Where c is the concentration, $\Delta\rho$ is the molecule average density contrast and κ proportionality constant. $\Delta\rho$ is also known as scattering length density and it is defined as the difference in electron density between that of the macromolecule ($\Delta\rho_1$) and that of the solvent

($\Delta\rho_0$)[158](with the assumption that the solvent is a featureless matrix with a constant scattering density[160]).

Moreover, Svergun and coworkers[161-163] have created the software that for (partially) known structures of the individual components can model molecular complexes [153].

2.8 Size exclusion chromatography/Gel permeation chromatography (SEC/GPC)

Characterization of the *molar mass distribution* (MMD) which is an intrinsic property of a polymer is the extremely relevant information. *Gel permeation chromatography* (GPC) or *size exclusion chromatography* (SEC) is recognized as a fast, reliable, mild and powerful technique which can provide information about MMD, throughout hydrodynamic volume based separation [164, 165]. This technique takes advantage of cross-linked mechanically stable gels of various sizes which through sieving action and depending on the difference in the molecular weight separates specimen into different fractions. Polystyrene and silica particles are the most widespread non-ionic stationary phases. The choice of the pore size range is essential in order to achieve successful separation. This segregation is governed by two processes; (1) more important simple size exclusion and (2) molecular diffusion regulated dispersion process [164]. The mechanism of the first process can be drawn as follows - large molecules which take over most of the solution effective volume are removed from the column at first as their size exceeds the pore size of beads and travel rapidly between the beads of the gel. On the other hand, distance of smaller molecules through the gel is elongated due their diffusion through pores. Thus, both hydrodynamic volume and shape of the molecule determine accessibility of the pore for a polymer chain.

2.9 Confocal laser scanning microscopy (CLSM)

Imaging of thick samples, for example rounded cells or tissues with the use of traditional wide field optical microscopy might be challenging due to the strong background signal generated from the objects located out of the focal plane by the fluorescence of the labeled structures present in the volume of sample or because of auto-fluorescence. Confocal imaging provides the means to overcome this issue by eliminating the signals which are not coming from the plane of interest.

However, the first concept of the confocal microscope was proposed in the mid-1950. The era of CLSM did begin in 1980 when the first microscope of this kind for standard imaging of fluorescently labelled species was presented. This breakthrough was possible because of the bursting progress in the laser and computer technology as well as the preparation of the fluorescent dyes that were suited for particular laser excitation lines. CLSM generates the optical section by illuminating the specimen optically with the laser beam and scanning point-by-point. A spatial filter (pinhole) which is placed in the image plane in front of the detector eliminates undesired fluorescence coming from above and below the plane of interest. This crucial solution enabled discrete levels imaging of the intact biological specimen. Additionally, CLSM overcomes the other issues related to standard epifluorescent (excitation of the fluorophore and detection of the fluorescence are conducted through the same light path) microscopy imaging which is of very limited z resolution. In the case of the 1.4 numerical aperture (NA) lens the vertical resolution is equal to 0.23 μm and lateral resolution to 0.14 μm. Fine resolution as well as high contrast provided by confocal imaging can help to obtain several information such as precise localization as well as 3D structure of the specimen [166, 167]

Working Principle

However the CLSM is an integrated system constructed around a typical light microscope [168], instead of a lamp as a light source a laser is used (usually few light sources). Computer and scanning head containing devices such as, filters, galvanometer-based raster scanning mechanism, pinhole apertures and photomultiplier tube (PMT) detectors are other components necessary for an efficiently working CLSM set-up [166](*Figure 2-7*).

Figure 2-7. CLSM set-up[166]. (Figure adapted with permission of John Wiley & Sons)

Illumination as well as detection in CLSM focuses on a single point in the sample. Subsequently this point is scanned across the sample in a raster pattern, from side to side and top-down (point-scanning). The scanning raster pattern is achieved by vibrating mirrors controlled by a galvanometer. The light source and the objective are isolated from each other by the objective and located at the same side of the sample plane. The essential part of a confocal microscope is the pinhole aperture. The light returning from the sample is received by a pinhole which is situated at the confocal position in front of the detector, however, it eliminates the fluorescence signal from the individuals which are not in the focal plane as well as plenty of the stray light (*Figure 2-8*) [166, 169]. The signal from the intensity of fluorescent photons arrives at PMT detector which generates a corresponding voltage converted by the digital imaging system into an image. The thickness and resolution are depending on few factors such as diameter of the pinhole aperture, numerical aperture of the objective lens and imaging light wavelength (higher resolution is achieved with a shorter wavelength)

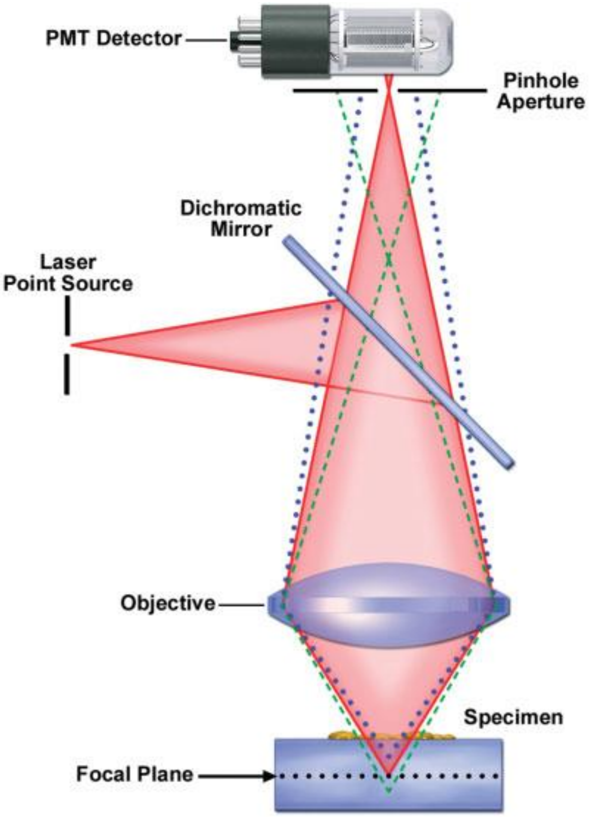

Figure 2-8. The principle of CLSM microscopy

2.10 Electron microscopy

Getting insight into the structure of macro and nano meter size objects is the aim of *Electron microscopy* (EM). In comparison to optical microscopy with which the light is used to obtain the information about morphology, in EM this role belongs to the electron beam [170]. Its wavelength is significantly smaller than the UV-VIS light range, which is the origin of considerably improved resolution. Owing to the fact that sample-electrons interactions are much stronger than sample- light interactions, imaging in vacuum conditions is required. The probing area is small, however, it does not affect strongly the intensity of the signal, which is very advantageous in a case of nanobjects imaging. Moreover, due to the charge of electrons, it is straightforward to focus them and scan with the use of an electrostatic field. Formation of an electron beam by an electron gun, its acceleration by electric potential, subsequent focusing through a metal aperture and magnetic lenses into a monochromatic beam and final projection onto the sample is the common working order in all electron microscopes [171].

The electron beam can be generated through thermionic emission or by field emission. A tungsten filament is usually used as typical thermionic electron gun. In order to provide electrons with adequate energy to overcome the work function of the metal, filament is heated to 2800 K in vacuum.

The *brightness of the source* β is a relevant electron gun parameter. Source brightness can be increased by use of lanthanum hexaboride (LaB_6) which is a smaller source size of lower work function than tungsten. This manipulation enables the use of higher currents, which relates with better image contrast sensitivity or decrease in probing area, which improves the spatial resolution. Another possibility is to use a *field emission gun* (FEG), which can provide an electron beam with a size of 5 nm and significantly improved brightness (10^4 improvement in comparison to a tungsten gun).

Electron–specimen interactions

Figure 2-9 depicts volumes and penetration depths which are the source of different signals, originating from the beam-sample interactions. The area of electron-specimen interaction has a teardrop shape. Sample composed of the element with high atomic number are characterized by lower penetration depth compared to the materials with low atomic number. The different types of electrons resulting from sample-specimen interaction are described below.

Secondary electron (SE) - is a low-energy electron (usually less than 50 eV), which is most frequently emitted from the atoms located close to the surface of the material. Secondary electrons originate not exclusively from inelastic scattering but it can be also electrons from the primary beam which have lost most of their energy as a result of scattering, nevertheless able to reach the surface. The amount of secondary electrons is very high, compared with backscattered electrons. The electron yield strongly depends on the accelerating voltage. The lateral resolution in secondary electron imaging is of the order of 1 to 5 nm for regular samples, however will change according to the probe size and signal-to-noise factors.

Backscattered electrons (BSE) - are high-energy electrons which are elastically scattered and escape from the surface of material without loss in kinetic energy. The number of backscattered electrons is much smaller than secondary electrons and does not depend on accelerating voltage. However, the backscattered electron yield significantly depends on the atomic number (Z). Along with increasing Z the number of emitted backscattered electrons also increases. Considerable worst resolution of backscattered electrons imaging (commonly in the range of 25 to 100 nm), compared to secondary electron imaging results from the larger penetration depth and –therefore sampling volume.

Auger electrons and *X-rays* – Relaxation of the electron beam ionized atoms results in the liberation of the excess energy between the levels involved in the transition, generating Auger electrons, X-rays or visible photons. Emission of Auger electrons is competitive for X-rays and occurs frequently with soft materials, which is very profitable for their surface analysis. Emitted X-rays are useful for elemental analysis [171].

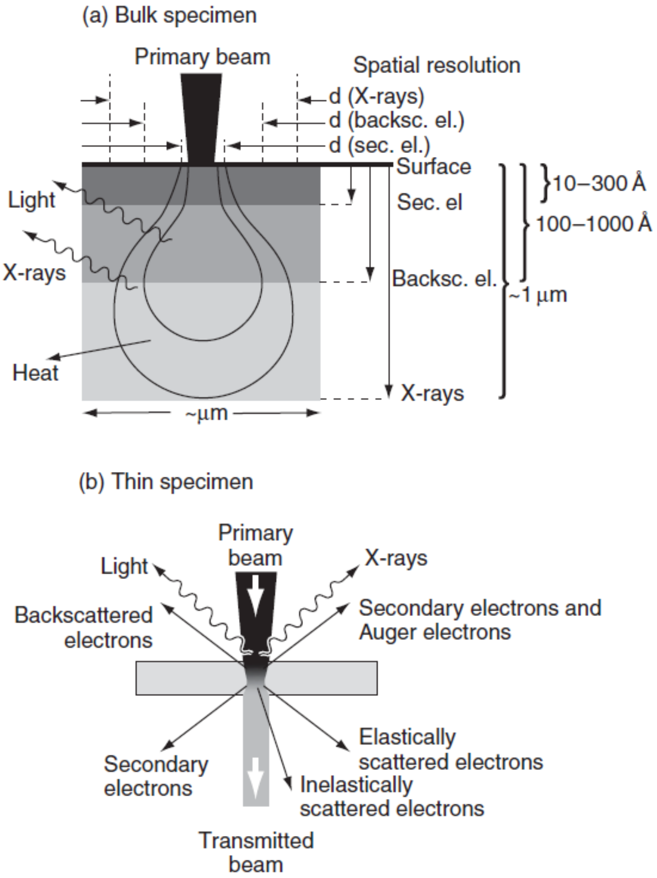

Figure 2-9. Scheme of electron-specimen interactions for a) thick sample, b) thin sample [171] (Figure adopted with permission of John Wiley and Sons)

Scanning electron microscopy

The schematic representation of a SEM device is presented in *Figure 2-10*. The role of objective lens in the case of SEM is the focusing of the electron beam (which size ranges between 2 and 10 nm) on the sample. The beam gets through the optical axis of the objective lens. The signal originating from secondary electrons, backscattered electrons or X-rays emitted from every place on the sample surface is monitored by the detector when the specimen is scanned in a two-dimensional raster (as well as across the sample). Amplified detector output controls the intensity of each pixel and thus emission intensity The monitored raster size to the specimen raster size ratio determines the magnification [171]. To the advantages of using SEM can be accounted for high availability, low cost, narrow electron beam and high resolution (500000 times magnification), successive magnification rates, significant depth of focus resulting in 3D images. Surface charge buildup might change the trajectory of SE and in order to avoid that, the sample should be conductive. Electro-conductive samples such as gold nanoparticles can be measured straight away; however for non-conductive specimens the shadowing technique has proved to be successful to coat the sample with a thin layer of metal.

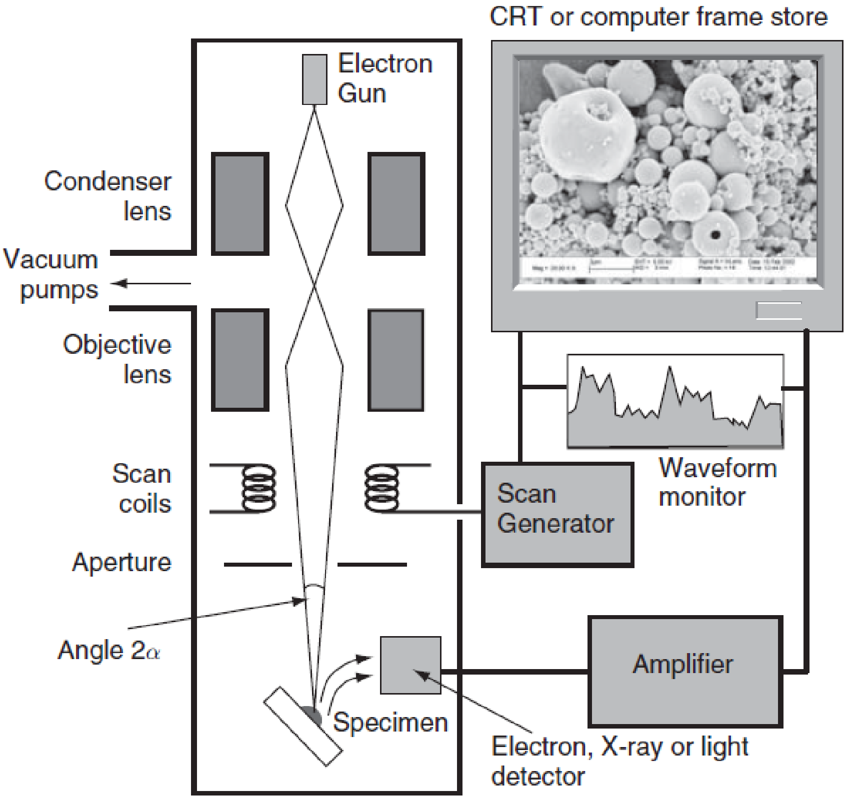

Figure 2-10. Schematic representation of an SEM set-up[171]. (Figure adopted with permission of John Wiley and Sons)

Transmission electron microscopy

The conventional transmission electron microscope of construction similar to a regular optical microscope is a powerful way for imaging objects of size in the micro- and nanometer range. TEM devices are usually composed of the following components on the optical path; electron gun, condenser lens, specimen stage, objective lens, intermediate lens, projector lens and data acquisition unit (*Figure 2-11*). Similar to SEM, high vacuum is required in order to avoid collision of electrons with molecules in air. In comparison to optical microscopy glass lenses are substituted for electromagnetic ones [153]. The TEM microscope accelerating voltage is significantly higher than in the case of SEM and in standard cases varies between 100 and 400 kV, which is very advantageous for imaging of thick samples because of deeper penetration depth and decreased electron wavelength and increased resolution [171]. Nevertheless, one should consider that increasing the accelerating voltage may result in sample damage. The condenser system (C1, C2) controls the demagnification of the spot size and regulates the size and convergence of the spot size at the sample [171]. The sample is deposited on a copper grid of 3 nm diameter to create a thin film with thickness that should not exceed few hundreds of nanometers. Magnification in TEM imagining can reach 10^6. The immediate sample observation is provided because of a fluorescent screen at the bottom of the column. Electron density is a source of contrast in TEM imaging. The specimen which have less contrast have to be prepared for imaging by techniques such as negative staining, freeze fracture or cryogenic methods [153].

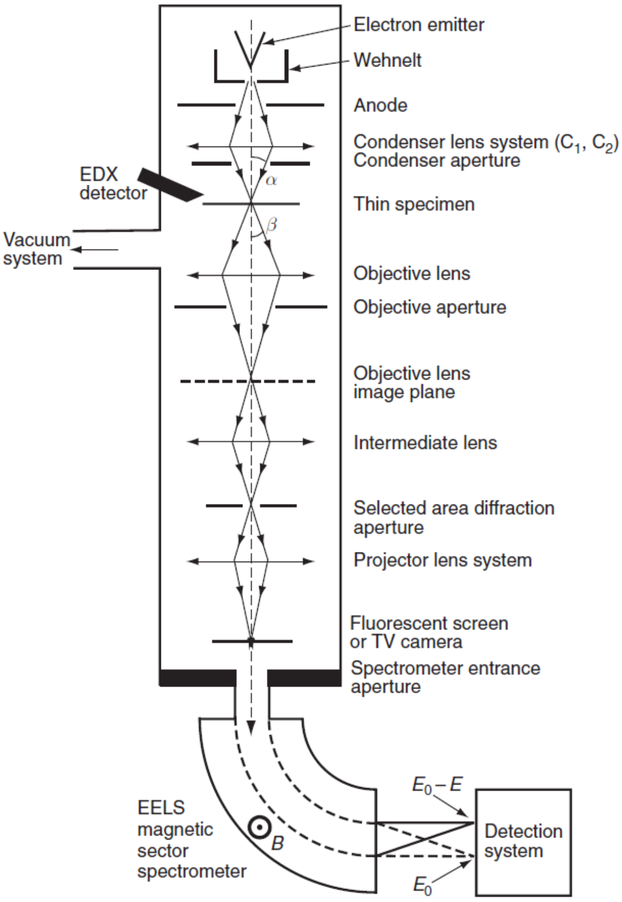

Figure 2-11. Schematic representation of TEM set-up [171]. (Figure adopted with permission of John Wiley and Sons)

2.11 Atomic Force Microscopy

Atomic force microscopy (AFM) was developed 5 years after the Scanning Tunneling Microscope STM technique to overcome its limitations, namely in order to enable imaging of samples which are non-conductive, like for example proteins. The nanometer-scale tip is the most relevant part of an AFM set-up [171]. The tip can be also replaced with a probe which is attached to the end of an extremely sensitive “spring-board” like cantilever. This sharp tip is scanning in the vicinity of the surface, attractive and repulsive forces which cause the cantilever bending and thus probing nanoscale phenomena. In comparison to STM in which tunneling currents are measured in AFM the magnitudes of atomic forces is a function of probe position on the surface of the specimen. The resolution of AFM set-up allows obtaining topographical images of single molecules even with atomic resolution. Moreover, AFM can be performed in UHV, ambient air and even in liquid which is especially important for biological systems. Aside imaging, it is possible to evaluate the intra- and intermolecular forces, e.g. between functionalized particles. Sample surface or/and tip surface modification with specific supramolecular assemblies (e.g. polymers, proteins) enables engagement of the molecules into contact and subsequent separation (pushing and pulling) and thereby measurements of the forces of interactions. Overall, AFM is a tool perfectly suited to study local properties at material surfaces with excellent spatial resolution as well as force sensitivity [153].

Basic principles

The AFM tip is located at the end of the cantilever and has a radius of few nanometers. While the AFM scans over the sample, the position sensitive detector (PSD) registers the cantilever deflection (vertical and horizontal) which is subsequently converted into voltage signals and thus the topographical map is drawn.

Ability to control with high precision the relative positions of the cantilever and specimen is a source of high spatial resolution in AFM. The lateral (X, Y) and vertical (Z) position control with sub-nanometer resolution is achieved by implementation of piezoelectric crystals, which are able to expand or contract along desired axis upon bias voltage application. Thus, few nanometers in the lateral and less than 1 nm in vertical directions of image resolution are achieved. Schematic representation of a scanning action is presented in *Figure 2-12*.

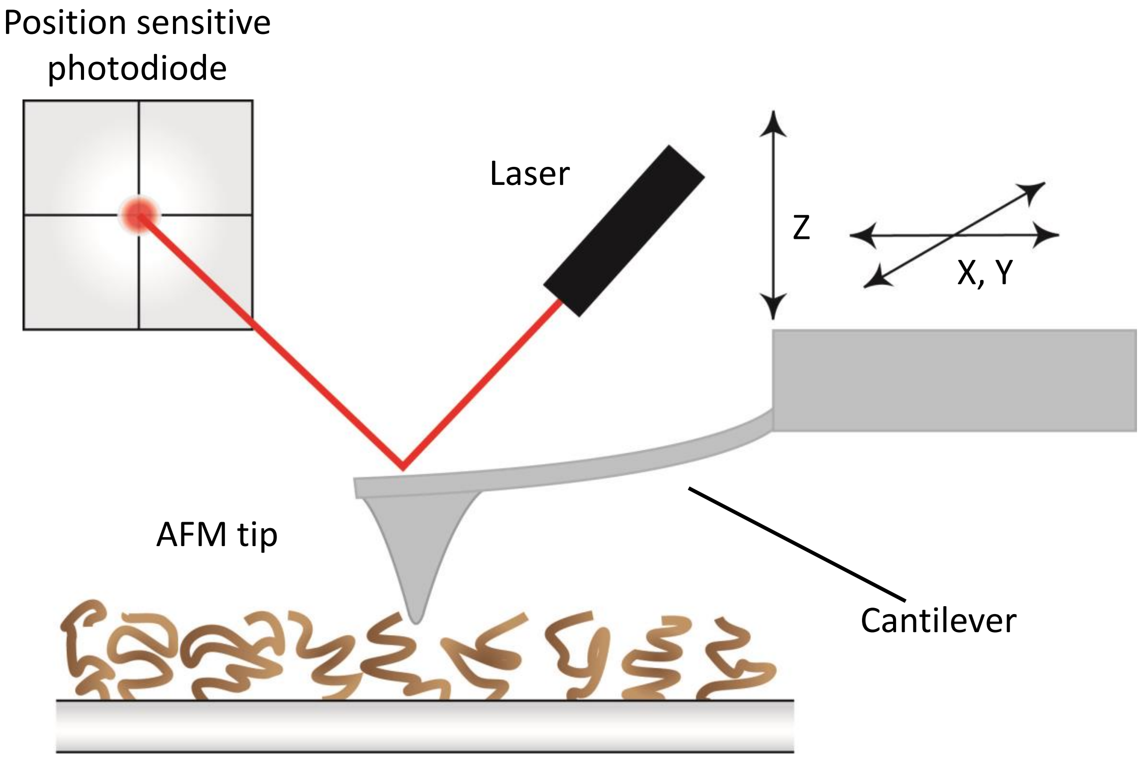

Figure 2-12. Schematic representation of AFM operation

Two main AFM modes are described below;

Contact mode

While imaging in this mode the tip is in constant contact with the surface. The vertical deflection is maintained at a constant set point by feeding the vertical cantilever deflection with the feedback loop in the Z of piezo (material, which expands and contracts proportionally to an applied voltage) scanner and thus the topographical map is drawn. Constant contact of the tip and surface during scan is guaranteed by feedback loop which steadily adjusts the tip position along the Z axis. Z position of the piezo at each point is registered and converted into topographic data. Noteworthy, this operation mode is considered as destructive for soft samples and not recommended for their imaging. However, due to high scan speed it is very often used for recording real-time images.

Tapping mode

This mode is known as well as *intermittent contact* mode. In this mode the tip makes soft contact with the specimen while oscillating near its resonance frequency. The PSD registers the amplitude of the oscillation which is established as a function of the tip-sample distance. The phase shift in the oscillating cantilever resulting from interaction forces between the tip and the specimen such as electrostatic repulsive force, attractive capillary force and the force exerted by the cantilever is relative to the driving signal. In contrary to the contact mode, in tapping mode the danger of damaging sample is minimized. To differentiate particular materials from blends the phase shift can be used.

3 Self-assembly

3.1 Synthesis and Self-assembly of a DNA Molecular Brush

(the following subsection was adapted with ACS permission from "*Synthesis and Self-assemmbly of a DNA Molecuar Brush*" by D. Kedracki, Ch. Mahshid, P. Maroni, H. Schlaad and C. Nardin, Biomacromolecules 2014 , 15 (9), pp 3375–3382, Supporting Information with the figures mentioned in the text are placed at the end of this subsection)

ABSTRACT. We report herein on the polymer crystallization assisted thiol-ene photosynthesis of an amphiphilic comb/graft DNA copolymer, or molecular brush, composed of a hydrophobic poly(2-oxazoline) backbone and hydrophilic short single stranded nucleic acid grafts. Coupling efficiencies are above 60% and thus higher as compared to the straight solid phase supported synthesis of amphiphilic DNA block copolymers. The DNA molecular brushes self-assemble into submicron sized spherical structures in water as evidenced by light scattering as well as atomic force and electron microscopy imaging. The nucleotide sequences remain functional as assessed by UV and fluorescence spectroscopy subsequent to isoindol synthesis at the surface of the structures. The determination of a vesicular morphology is supported by encapsulation and subsequent spectroscopy monitoring of the release of a water soluble dye and spectroscopic quantification of the hybridization efficiency (30% in average) of the functional nucleic acid strands engaged in structure formation: about one half of the nucleotide sequences are available for hybridization whereas the other half is hindered within the self-assembled structure. Since speciation between complementary and non-complementary sequences in the medium could be ascertained by confocal laser scanning

microscopy, the stable self-assembled molecular brushes demonstrate potential for sensing applications.

1. INTRODUCTION

Copolymer self-assembly is an elegant route to form structures with sizes in the sub-micrometer range in solution and on surfaces [172-177]. Of high interest though is the propagation of the macromolecular properties to the ensemble inherent to this process. Copolymers organize into functional nanostructured materials with potential applications in various fields such as biomedicine, biomaterials engineering or catalysis [178, 179]. Keeping in mind future developments in biology and medicine, copolymers have thus been designed to assemble structures that might eventually enable the manipulation and comprehension of a biochemical mechanism to solve biological or medical issues in the future.

Along this line, the synthesis and self-assembly of copolymers constituted of a segment composed of a polypeptide, a polysaccharide or a nucleotide sequence have been reported [111, 115, 117, 180-184]. The synthesis of linear self-assembling DNA copolymers is usually achieved according to either conventional organic routes or molecular biology techniques by solid phase supported synthesis [111, 115, 117]. To advance the understanding of the molecular self-assembly of DNA copolymers and achieve highly versatile self-assembling macromolecules, we report herein the synthesis of an amphiphilic comb/graft DNA copolymer composed of a hydrophobic poly(2-oxazoline) backbone and hydrophilic short single stranded nucleic acid grafts. This macromolecular architecture is of high interest since the formation of structures of higher order might be induced in a bottom-up approach from the molecular scale to the third dimension [185].

Poly(2-oxazoline)s in general, are considered for usage in biomedical applications [186]. Poly[2-(3-butenyl)-2-oxazoline] (PBOX) is particularly interesting because of its low glass transition temperature (~10 °C) and vinyl double bonds which are susceptible to functionalization via thiol-ene photochemistry [187-190]. Like poly(2-isobutyl-2-oxazoline) and poly(2-nonyl-2-oxazoline)[191], PBOX exhibits an upper critical solution temperature (UCST) solution behavior in ethanol-water mixtures. The polymer is soluble in a mixture of ethanol-water 55:45 w/w at above 44 °C, whereas below this temperature phase separation and crystallization occurs with the spontaneous formation of insoluble microspheres (see *Scheme 3-1*).

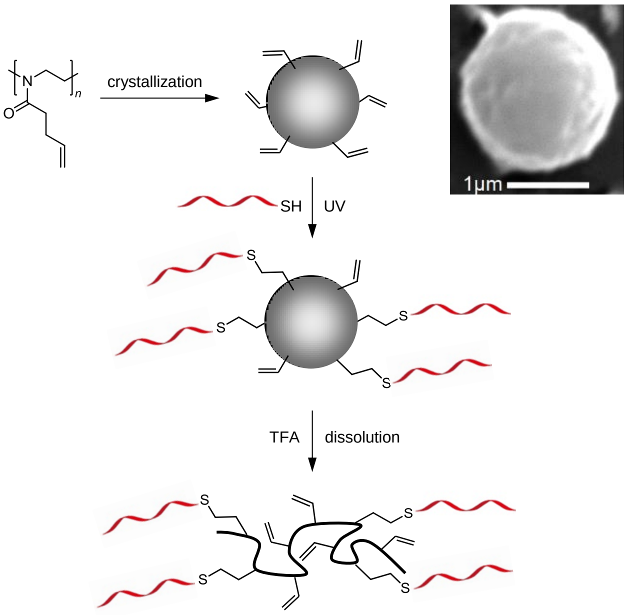

Scheme 3-1. Synthesis of PBOX-g-DNA molecular brush through thiol-ene modification of poly[2-(3-butenyl)-2-oxazoline] crystallites in water

The crystallites are physically cross-linked polymer chains, which dissolve upon exposure to acid, e.g. trifluoroacetic acid (TFA), without chain scission [191]. Here, we took advantage of this crystallization process in combination with the possibility to perform thiol-ene photochemistry[192] to graft DNA chains onto the PBOX and synthesize a DNA molecular brush. Since the nucleic acid strands are modified at the 5'-end through a hexyl spacer by a thiol group, these are grafted onto the PBOX microspheres though a one-step reaction prior to dissolution in trifluoroacetic acid (TFA). As demonstrated in the following, the grafting efficiency reached 67% in agreement with steric hindrance owing to molecular crowding of single stranded nucleic acid strands grafted to the polymer backbone. The molecular brushes (released from the microspheres by treatment with TFA) organize in aqueous solution into spherical structures with sizes of about ~300 nm. The nucleic acid strands remain functional subsequent to coupling and stable structure formation enables speciation between complementary and non-complementary nucleotide sequences present in the surrounding.

2. MATERIALS AND METHODS

Materials

Sodium chloride (>99.5%) and magnesium chloride (99.9%) were purchased from Acros Organics (Geel, Belgium), sulphuric acid (96%) was purchased from Fisher Scientific SA (Wohlen, Switzerland). 5'-CTCTCTCTCTTT-3' (5'-$(CT)_5T_2$-3',"DNA") modified at the 5'-end through a C_6 hexyl spacer with a thiol group, 5'-AAAGAGAGAGAG-3' (5'-$A_2(AG)_5$-3'," complementary DNA"), Cy5-5'-$(CT)_5T_2$-3 and FITC-5'- $A_2(AG)_5$-3' were purchased from Microsynth Laboratory (Balgash, Switzerland). C stands for cytosine, T for thymine, G for guanine and A for adenine. Poly(ethylene imine) (PEI, nominally 40,000 gmol^{-1}) was purchased from Polysciences (Eppelheim, Germany). TCEP (tris(2-carboxyethyl)phosphine) was purchased from Roth AG (Arlesheim, Switzerland). Ethanol (98%), trifluoroacetic acid (≥99 %), tetrahydrofuran (≥99.9%), hydrogen peroxide (50%, diluted prior to usage) and dialysis tubing were ordered from Sigma Aldrich (Buchs, Switzerland). Poly[2-(3-butenyl)-2-oxazoline] (PBOX) was prepared by cationic ring-opening isomerization polymerization of 2-(3-butenyl)-2-oxazoline as described in the literature.[6c] The isolated PBOX chains had an average length of 43 repeat units, corresponding to a number-average molar mass (M_n) of 5380 g mol^{-1}, by ^{1}H NMR end group analysis, and a dispersity index (ratio of weight- over number average molar mass, M_w/M_n) of 1.05, by size exclusion chromatography (SEC). LCR 0.22 µm pore size syringe filters were purchased from Merck Millipore (Zug, Switzerland). Zeta cells were provided by Instrumat SA (Lausanne, Switzerland). Silicon wafers single side polished, orientation N/Phos < 100 >, (625±25) µm thickness, 1-50 Ohm cm resistivity were purchased from Silchem (Freiburg, Germany). Mica was purchased from Plano (Wetzlar, Germany). The uranyl acetate staining solution and Mesh Copper Grids for transmission electron microscopy were purchased from Electron Microscopy Sciences (Hatfield, US). Milli-Q water was used in all cases.

Synthesis of the DNA molecular brush

A 0.5 wt% polymer solution (0.12 mg) in an ethanol/water mixture (55:45, w/w) was dissolved at 60 °C prior to be cooled down below the UCST, and stirred at room temperature for 3 days. Subsequently ethanol is allowed to evaporate overnight. Thiol modification was then conducted in the same manner as reported elsewhere [192]. Briefly, 1 mg of thiol DNA is added to the solution of microspheres ($[SH]_0/[C=C]_0 = 0.28$) together with 75 µg of tris(2-carboxyethyl)phosphine (TCEP). TCEP was added in order to reduce DNA-S-S-DNA to 2 DNA-SH. Subsequent to degassing by bubbling argon for 5 minutes, the solution was exposed to UV light ($\lambda = 305$ nm, 24 h). The product was then purified by dialysis (MWCO 14000 Da) and SEC chromatography. Self-assembly was induced by direct dissolution of the product in water.

Analytical instrumentation and methods

^{1}H NMR measurements were carried out at room temperature using a Bruker DPX-400 spectrometer operating at 400.1 MHz. ATR-IR spectra were recorded on a Bruker VERTEX 80v spectrometer with a liquid nitrogen cooled narrow-band mercury cadmium telluride (MCT) detector; 1 mg mL^{-1} sample solutions were spread on a Germanium plate and left for drying for 30 min. The germanium background was recorded prior to sample analysis. X-ray diffraction measurements were peformed on the SuperNova equipment (Oxford Diffraction, UK) using the Cu Kα radiation source ($\lambda_{CuK\alpha} = 1.5418$ Å). An Abbemat Reflectometer WR MW (Anton Paar, Germany) was used to determine the refractive index increment (d*n*/d*c*) of the PBOX-g-DNA copolymer. UV-Vis spectra were registered on a Varian Cary-50 in a quartz cuvette of 1 cm path length for all measurements, in the same manner as reported previously.[193] Size exclusion chromatography (SEC) of PBOX was performed on a system with simultaneous UV (λ = 270 nm) and RI detection using *N*-methyl-2-pyrrolidone (NMP + 0.5 wt % LiBr) as the eluent at +70 °C, flow rate: 0.8 mL min^{-1}, and a column set of two 300 x 8 mm^2 PSS-GRAM 7 μm spherical polyester particles with porosities of 10^2 and 10^3 Å. Calibration was done with polystyrene standards. Aqueous SEC with PBOX-g-DNA was performed on a Viscotek GPCmax system (Viscotek, Houston, TX, USA) with differential refractive index, right angle light scattering (RALS) and low angle light scattering (LALS) detectors. A 0.3% aqueous solution of sodium azide was used as the eluent at 35 °C, flow rate: 1.0 mL min^{-1}. Separation was achieved using two Viscotek columns (ViscoGEL column, TSK-GEL® GMRW XL Products 300 x 7.8 mm^2). Calibration was done with polystyrene sulfonate standards (Polymer Standards Service GmbH, Mainz, Germany). Concentration and angle dependent light scattering studies were conducted on the multi-angle ALV-CGS-8 goniometer (Langen, Germany). This device is equipped with eight detectors and a solid-state laser operating at λ = 532 nm (VerdiV2, Coherent). For all measurements, low volume borosilicate quartz cuvettes were used, which were cleaned in a mixture of H_2SO_4-30% aqueous H_2O_2 3:1 v/v prior to any measurement. Dilution series were prepared by sequential dilution of the initial 1 mg mL^{-1} aqueous solutions of the copolymer. All experiments were carried out at a temperature of 25 °C. The apparent hydrodynamic radius (Cumulant analysis) and apparent radius of gyration (Berry analysis) were evaluated according to conventional routes.[194, 195] For atomic force microscopy (AFM), 20 μL of sample was drop casted on a mica surface, gently washed with ethanol and dried under nitrogen. For single molecule imaging of the copolymer, mica surfaces were dipped overnight in $MgCl_2$ (30 mM) and afterwards extensively washed in order to allow attachment of DNA molecules to the surface by double charged ions subsequent to spin coating.[196] The self-assembled structures were dissolved in a small volume of trifluoroacetic acid and subsequently diluted in THF/EtOH (1:1) mixture in order to obtain 5 10^{-8} g L^{-1} final concentration of copolymer. 20 μL of sample was drop casted on the mica surface, gently washed with ethanol and dried under nitrogen. AFM images were acquired with a Cypher AFM (Asylum Research, Santa Barbara, CA) operating in the AC-mode. Biolever mini AC40TS cantilevers (Olympus, Japan) with a nominal tip radius smaller than 9 nm were used for recording images in liquid. These probes have spring constants of around 0.1 N m^{-1} and resonance frequencies in liquid of around 25 kHz. The free oscillation amplitude (FOA) and the scan rate were set to 40 nm and 4.88 Hz respectively. The set point used varied between 60-70% of the FOA. The data acquisition and analysis were operated with the Asylum Research software, delivered with the AFM instrument. For transmission electron microscopy (TEM), grids were glow discharged for 30 s prior to imaging in order to render the grids surface more hydrophilic. Later on, 2 droplets of 2% uranyl acetate solution were prepared on a parafilm foil. 5 µL of fresh sample was dropped on a carbon coated 400-mesh copper grid and after 30s of adsorption liquid was blot off on filter paper by holding it vertically. Afterwards the grid was placed on the first uranyl acetate droplet for 1s and then stained on the second for 30s. Remaining liquid was again blot off on the filter paper prior to imaging with a Tecnai G2 electron microscope operating at 120 kV. For scanning electron microscopy (SEM), 10 µL of a 1 mg mL^{-1} aqueous solution was placed on silicon wafers and after one minute drying with nitrogen, samples were coated with gold for 20 s in a Jeol JFC-1200 Fine coater. Subsequently, SEM images were acquired on a Jeol 6510LV microscope, equipped with a tungsten filament gun, operating at 10.6 mm WD and 10 kV.

Sample preparation

For quantification of the hybridization efficiency, the concentration of self-assembled structures was adjusted to obtain an absorbance value of about 0.1 (absorbance unit) which corresponds to 1 µM of DNA (in a 50 mM NaCl solution). Subsequently 0.1 nmol of the complementary sequence (0.75 µL, 5’-$A_2(AG)_5$-3’ 0.5 mg ml^{-1}) was added and the mixture was left for hybridization at 4 °C for 30 minutes. Subsequently, the UV spectrum (λ = 240-320 nm) of this solution was recorded in order to monitor the hybridization efficiency, estimated from maximum absorbance values at 268 nm wavelength. The procedure was sequentially repeated until no decrease of the absorbance was detected. All measurements were conducted in a quartz cuvette of 1 cm light path on a Varian Cary-50 Instrument (Zug, Switzerland).

To assess the speciation of nucleic acid sequences by confocal laser scanning microscopy (CLSM) to a solution of 20 nmol of 5'-$(CT)_5T_2$-g-PBOX sequence, 20 μL of FITC-5'-$A_2(AG)_5$-3' (complementary, 100 μM concentration, 1 eq.) and Cy5-5'-$T_2(CT)_5$'-3 (non-complementary, 100 μM concentration ,1eq) were added. The mixture was stirred and placed at 4 °C for 1 h. To enable imaging, immobilization on glass slides was achieved by modification of the glass surface with positively charged poly(ethylene imine) (PEI) ($5\ 10^{-3}$ g L^{-1}) since the outer layer of the self-assembled structures is composed of the negatively charged DNA sequences. In brief, the solution of PEI was spread on the microscopy glass slide and left for adsorption for 5 minutes. Afterwards, the glass surface was extensively washed with Milli-Q water and 10 μL of the solution containing the mixture of stained nucleotide sequences was spread on the glass slide, covered by the cover glass and observed simultaneously by confocal laser scanning microscopy (Zeiss LSM 700 confocal microscope; lens 100x 1.4 NA) at two different excitation wavelengths with suitable filters (FITC ex. 488 nm, em. 520 nm, Cy5 ex. 639 nm, em. 679 nm). Subsequently, the remaining solution was centrifuged (15 min, 14000 rpm) and the supernatant was removed in order to get rid of the sequences that did not hybridize. The self-assembled structures were subsequently suspended again and washed with water three times (by centrifugation). 10 μL of this solution was dropped on a glass slide and covered with a cover glass for imaging by CLSM. To quantify the speciation, fluorescence spectroscopy was conducted with sample prepared in the same manner as for CLSM. Fluorescence intensities of FITC (ex. 485 nm) and Cy5(ex. 639 nm) were registered keeping the same slits aperture for all measurements. For all solutions, a 50 mM NaCl aqueous solution was used. In parallel, encapsulation and release of a fluorescent dye was monitored by fluorescence spectroscopy. The water soluble fluorescein dye was selected to assess the hollow sphere morphology of the self-assembled PBOX-g-DNA. Imaging was performed by CLSM before and subsequent to the dye release which was triggered by addition of 2% aqueous solution of sodium azide. The release time course was recorded by fluorescence spectroscopy. Briefly, 1 mg of PBOX-g-DNA copolymer was dissolved in 50 μg mL^{-1} fluorescein aqueous solution, in order to encapsulate the fluorescent dye during the spheres formation. The free dye was removed by 4 days dialysis against water (MWCO 14000). The time course of dye release was recorded with a Horiba Jobin Yvon Fluoromax 2 (New York, USA). Towards this end, 90 μL of sample was placed in a quartz cell (QS 3.0 mm, Hellma Analytics) to which10 μL of 2% sodium azide was added during the measurement to induce disassembly of the spheres and monitor the release time course (485/512 with an integration time of 0.5 s, standard error of 1 %, for a duration of 900 s). For the control measurement, 1 mg of PBOX-g-DNA was added to 1 mL of 0.5 mg mL^{-1} Nile Red solution dissolved in methanol. The resulting solution was dialyzed against methanol/water mixture and water for 5 days in order to induce self-assembly as well as to remove the free dye. Samples were as well imaged by CLSM prior and subsequent to disassembly by addition of sodium azide subsequent to dye encapsulation at a concentration of 2 μg mL^{-1}.

For isoindol synthesis, 20 nmol of 5'- $A_2(AG)_5$-3'-SH (200 uL, 100 uM) and 20 nmol of 5'-$A_2(AG)_5$-3'-NH_2 (200 μL, 100 μM) were added to a solution of the self-assembled molecular brush (containing 40 nmol of 5'- $T_2(CT)_5$-3') mixed and incubated at 4 °C for 30 min (total volume 1 mL, 50 mM NaCl solution). Afterwards 40 nmol (1.3 mg) of o-phthalaldehyde were added to the solution and left in a light protected place under stirring for 24 h. Fluorescence spectra were recorded after 30 min and 24 hours. Hellma Ultra micro cuvettes 3 x 3 mm^2 were used for all fluorescence spectroscopy measurements. All spectra were recorded on a Horiba Jobin Yvon Fluoromax 2 (New York, USA).

3. RESULTS

The nucleotide sequences are purchased desalted of HPLC purity grade. The nucleic acid strand is a model linear sequence of melting temperature (34°C in 50 mM NaCl) higher than the working temperature (20°C) which does not self-hybridize and assemble a thermodynamically stable double helix with its complementary sequence. Like poly(2-isobutyl-2-oxazoline) and poly(2-nonyl-2-oxazoline),[191] PBOX (average number of repeat units, 43) is soluble in a mixture of ethanol-water 55:45 w/w above 44 °C, whereas below this temperature phase separation and crystallization occurs with the spontaneous formation of insoluble microspheres (*Scheme 3-1*). The crystallinity of the freeze-dried sample was verified by X ray diffraction (*Figure S1*), which shows two predominant sharp peaks at $2\theta \sim 12$ ° (d spacing 7.4 Å) and $2\theta \sim 23$ ° (d spacing 3.8 Å), peaks of lower intensity at $2\theta \sim 14$ ° (d spacing 6.3 Å), $2\theta \sim 28$ ° (d spacing 3.1 Å) and $2\theta \sim 31$ ° (d spacing 2.8 Å) and a broader peak at $2\theta \sim 19$ ° (d spacing 4.6 Å).

Thiol-terminated nucleotide sequences were added to a solution of the crystalline PBOX microspheres (($[SH]_0/[C{=}C]_0 = 0.28$) in degassed water and irradiated with UV light ($\lambda = 305$ nm) over 24 hours.[191, 192] Chemical characterization was performed subsequent to dialysis and size exclusion chromatography to remove any non-reacted product, in particular DNA fragments.

The success of the coupling reaction and the purity of the PBOX-g-DNA brush copolymer product (absence of PBOX or DNA fragments) could be confirmed by FT-IR and SEC analyses (*Figure 3-1, Table S1*). As compared to the pristine PBOX, the intensity of the band at 912 cm^{-1}, attributable to the stretching of vinyl groups, is much lower in the PBOX-g-DNA copolymer. In addition, a peak at 1060 cm^{-1} appears in the spectrum of the copolymer, which corresponds to the C-N stretching of the amines present along the nucleotide sequence. Quantitative analysis of the PBOX-g-DNA copolymer by UV-vis spectroscopy (brief description in SI as reported in reference 9) evidences a reaction efficiency of 67%. Since the PBOX chain comprises 43 repeat units, the grafting density is ~20% or, in other words, in average every 6th unit along the PBOX backbone carries a nucleotide sequence. SEC further reveals a copolymer of low polydispersity (23000 Mn, 24800 Mw, 1.08 PDI).

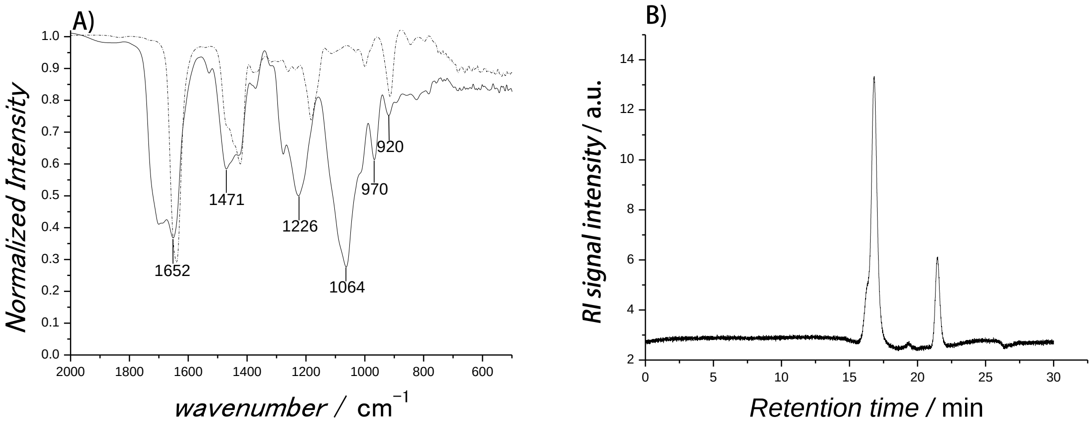

Figure 3-1. Chemical characterization. A) FT-IR spectra of pristine PBOX (dashed line) and PBOX-g-DNA copolymer brush (solid line). B) SEC RI trace of the PBOX-g-DNA copolymer brush (peak at 22 mL refers to the flow marker).

Structure formation of the resulting PBOX-g-DNA molecular brushes into spherical structures takes place in aqueous solution. Both scanning and transmission electron microscopy reveal the formation of spheres of sizes between 100 and 400 nm (*Figure 3-2*). Structure formation is induced by direct dissolution in aqueous solution under stirring. This method usually leads to the formation of structures of wide size distribution, which is reduced by sequential extrusion through membrane filters to perform light scattering investigations [197].

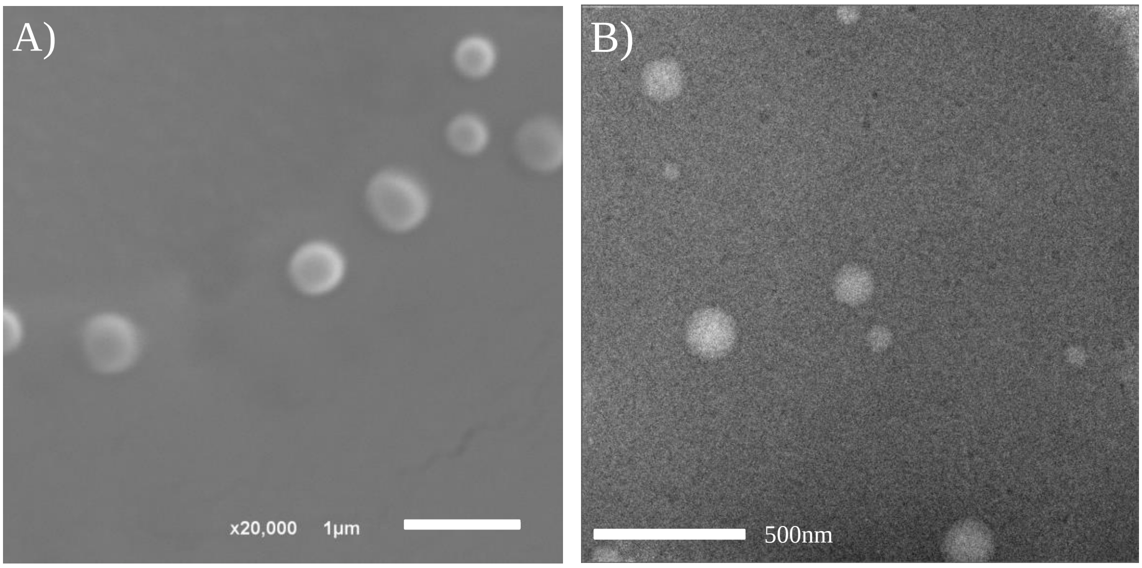

Figure 3-2. Morphological characterization of the PBOX-g-DNA self-assembled structures by A) SEM (only the largest structures are observed) and B) TEM.

To achieve both sizing and refine the morphological determination, we combined multi-angle dynamic and static light scattering (*Figure S2, Figure S3 and Figure S4*) (DLS and SLS respectively). DLS yields an apparent hydrodynamic radius R_H of (117 ± 3) nm whereas SLS reveals a radius of gyration R_G of (146 ± 4) nm. SLS analysis further indicates that the self-assembled PBOX-g-DNA hybrid structures are built of about 20000 macromolecules.

We eventually resorted to dye encapsulation and release assays to elucidate the morphology of the self-assembled structures. Unlike the non-water soluble Nile Red dye, which could not be encapsulated (*data not shown*), encapsulation of the water soluble fluorescein could be imaged by fluorescence microscopy (*Figure 3-3*) and the release monitored by fluorescence spectroscopy (*Figure S5*) subsequent to encapsulation at a concentration at which self-quenching occurs. Upon disassembly of the structures, the fluorescence intensity increases owing to dilution of the dye in the medium.

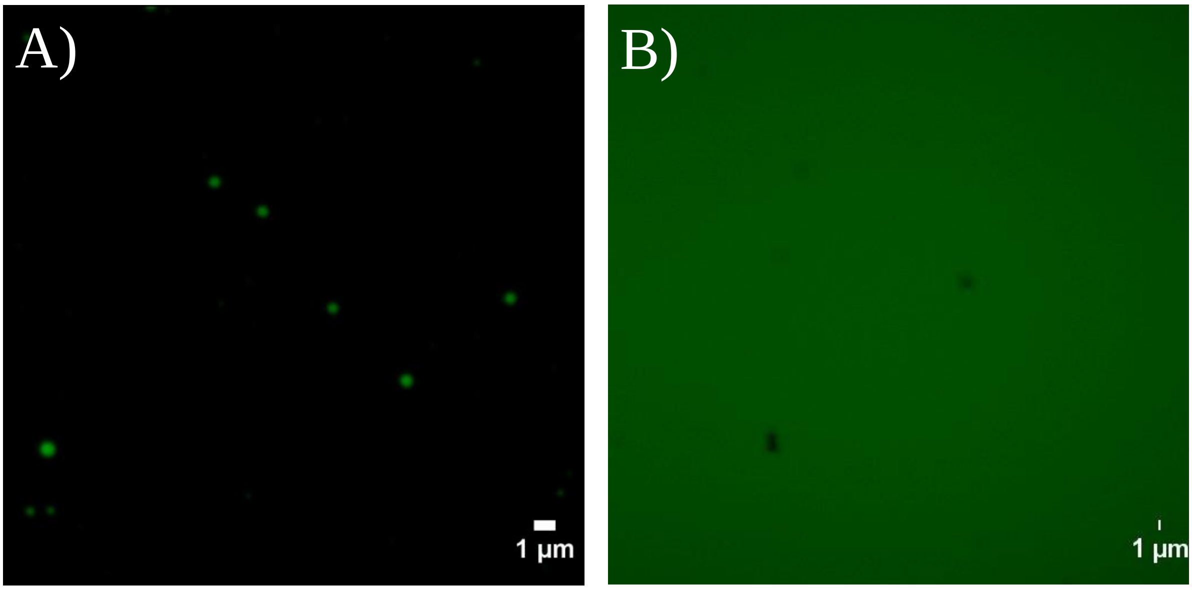

Figure 3-3. A) Encapsulation of the fluorescent water soluble fluorescein dye B) dye release subsequent to disassemble of the PBOX-g-DNA structures as observed by fluorescence microscopy

If the nucleotide sequences remain functional subsequent to polymer modification and self-assembly can simply be assessed by quantifying the hybridization efficiency of the nucleic acid grafts engaged in structure formation with their complementary sequence by UV-vis spectroscopy (*Figure S6A*). Upon hybridization the absorbance indeed decreases to a value which is about half of that of the single stranded nucleotide sequence. Scattering does not hamper this measurement since the system under investigation is dilute and this of low refractive index increment. A representative spectrum is displaced in *Figure S6B*. Around 30% of the nucleotide sequences engaged in the structure formation remain available for hybridization (*Figure S6C*) whereas 100% hybridization efficiency was monitored between the pristine complementary sequences in solution (*Figure S6D*). With the nucleic acid strands under investigation, no self-hybridization could be observed (*data not shown*). Further evidence that the nucleic acid strands involved in structure formation are functional is gathered by the fact that the PBOX-g-DNA structures could be used as three dimensional scaffolds to carry out organic reactions. We resorted to an approach reported previously.[198] Briefly, hybridization between the nucleic acid strands involved in the PBOX-g-DNA self-assembly and complementary sequences modified either with an amine or a thiol group is induced to produce isoindol by addition of free *o*-phthalaldehyde (*Figure S7A*). As can be seen on *Figure S7B*, the fluorescence of the reaction product could be monitored by spectroscopy. The intensity increases with reaction time what corresponds to the formation of the compound with higher fluorescence quantum yield. This outcome further confirms that the nucleic acid sequences, subsequent to grafting and structure formation, remain functional at the interface between the aqueous surrounding and the self-assembled structures.

Since the hydrophilic weight fraction, the charge as well as the rigidity of the macromolecule is increased upon hybridization, structures of larger size (949 ±70 nm) are observed upon the formation of the double helix between the complementary sequences (*Figure 3-4*). However, no morphological transition has been observed.

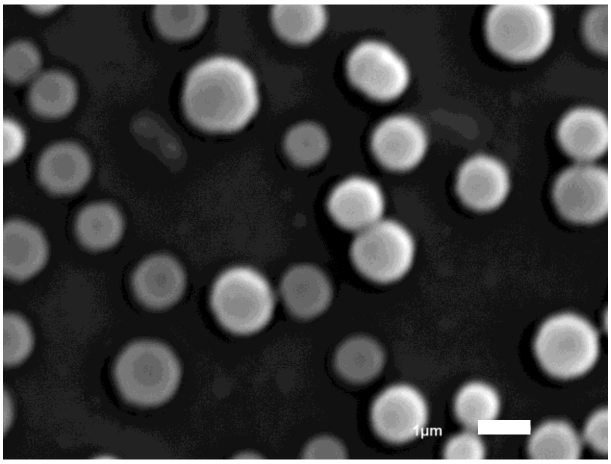

Figure 3-4. PBOX-g-DNA morphology as observed by SEM subsequent to hybridization (130% complementary sequences).

The stability of the self-assembled structures upon hybridization further enabled the assessment of the potential of these sub micrometer size spheres as sensing tools for nucleic acid strands speciation, which was carried out through the combination of laser scanning confocal microscopy (CLSM) and fluorescence spectroscopy. A solution containing two kinds of nucleotide sequences stained with fluorescent dyes emitting at different wavelengths have been incubated with the PBOX-g-DNA self-assembled structures. The complementary sequence is labeled with FITC whereas the non-complementary strand is labeled with Cy5. After sample incubation at 4°C, the mixture was imaged under CLSM and the fluorescence intensity monitored (*Figure S8*). As can be seen on *Figure 5A and 5C*, the complementary sequences engaged in the PBOX-g-DNA structure formation do hybridize (green glow) whereas the non-complementary sequences remained in the background, which shines in red. These could be simply separated by centrifugation and washing steps (*Figure 3-5 B and D, Scheme S1*). The green labeled spherical structures subsequent to hybridization solely remain.

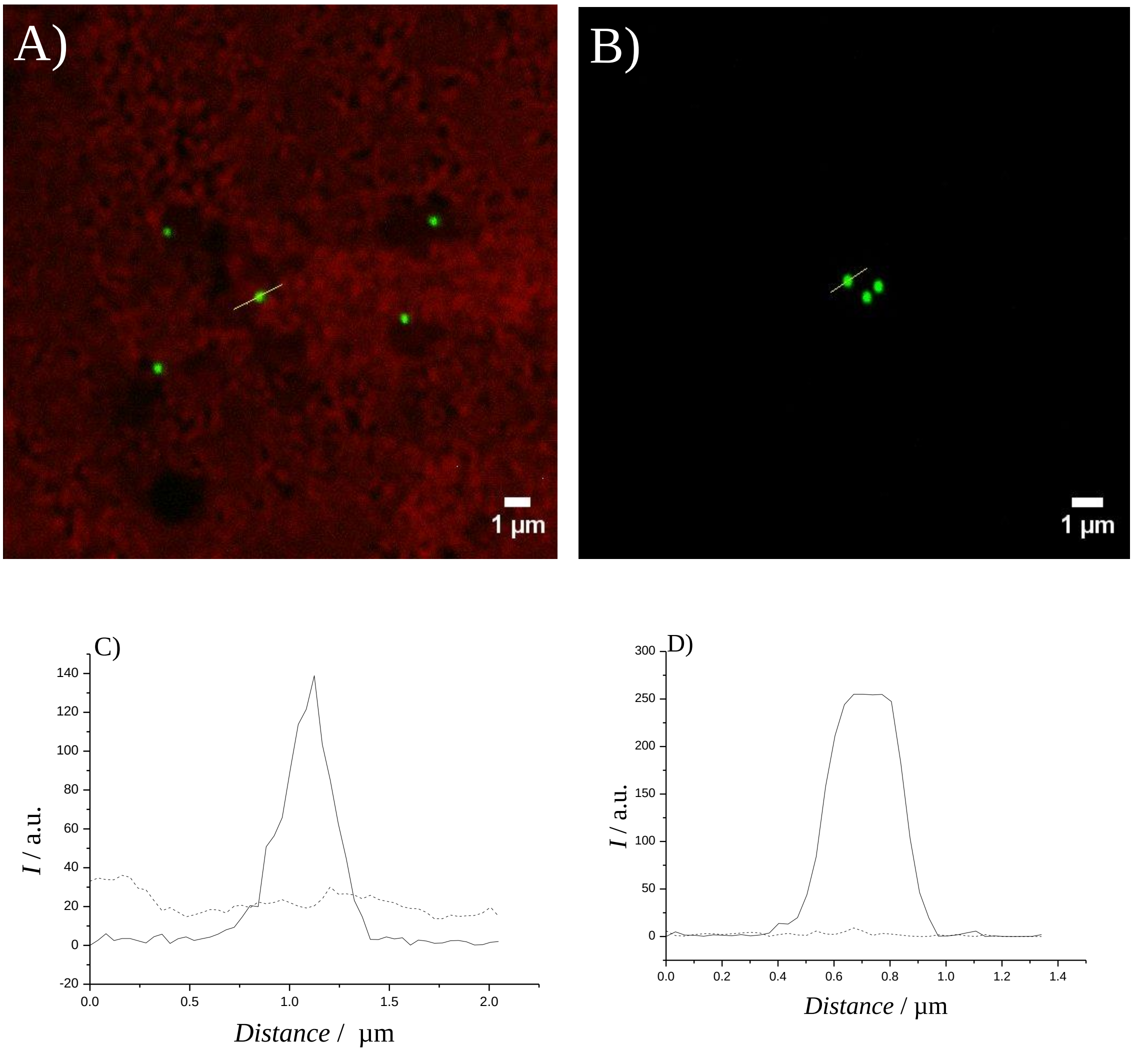

Figure 3-5. Confocal laser scanning microscopy images of A) Solution of PBOX-g-DNA self-assembled structures incubated with the complementary sequence stained with FITC which hybridizes with the nucleic acid grafts engaged in self-assembly and the non-complementary sequence labeled with Cy5 which remains in solution (background) B) Subsequent to washing, the complementary sequence stained with FITC hybridized with the PBOX-g-DNA composing the self-assembled structure, being the non-complementary sequence removed during the washing process (no background). Corresponding fluorescence intensity profile for FITC-5'- $A_2(AG)_5$-3'(solid line), Cy5-5'-$T_2(CT)_5$'-3 (dashed line) C) before washing and D) after washing. Only the largest structures are visible by optical microscopy.

4. DISCUSSION

Amphiphilic DNA block copolymers are usually achieved by grafting to nucleic acids synthesized by solid phase supported synthesis (SPS) on Controlled pore Glass (CpG) .[3f] To prevent tedious synthesis and purification steps, coupling is performed prior to cleavage of the amphiphilic block copolymer from the porous phosphoramidite CpG resin. However limited diffusion of the macromolecules through the pore of the phosphoramidite solid phase hampers both the efficiency of the reaction up to about 30% and the choice of the polymer to molecular weights up to about 5000 Da [199]. The polymer crystallization assisted thiol-ene synthesis of a polymer-*graft*-DNA molecular brush described herein enables achieving reaction efficiencies above 60% without tedious synthesis routes or purification steps. The polymer crystallites are of smaller size than the conventional beads used in automated synthesis. The interfacial area available for reaction is therefore higher in comparison to structures of larger size. In addition to the inherent efficiency of thiol-ene photosynthesis, the reactive vinyl groups might be located at the outer surface of the crystallites and the diffusion of the short single stranded synthetic nucleotide sequences through the physically cross-linked polymer structures might be less limited than through the pores of a phosphoramidite solid support [200]. The latter hypothesis is strongly supported by the degree of grafting of nucleic acid strands to the PBOX backbone. According to steric hindrance 8 nucleotide sequences of about 3 nm Flory radius[201] at best could be grafted along a 24 nm long PBOX polymer backbone, which is in agreement with the grafting density we quantified through UV spectroscopy.

Subsequent to coupling of the nucleic acid grafts to the PBOX backbone, crystallization could no more be induced. The resulting macromolecule is a nonlinear comb/grafted amphiphilic macromolecule (Scheme *3-2*). Unfortunately, high resolution AFM did not enable imaging single molecular brushes, which have the tendency to collapse on the surface (*Figure S9B*). This macromolecule self-assembles into 150 nm radius spherical structures in aqueous solution. Although the hydrophilic weight fraction (about 90%) is high, the ρ-factor ratio R_G/R_H = (1.25 ±0.07) is above one, which is indicative of the formation of hollow spheres or elongated structures[194]. The formation of compound micelles or dispersion of the polymer cannot be ruled out. However, several indirect evidences point towards the formation of vesicular structures. Imaging shows the formation of spherical particles. Light scattering investigations enables sizing of particles of low size distribution and assessing an aggregation number of about 20000 PBOX-g-DNA molecules within each spheres, which points toward the formation of vesicular structures. Indeed the molecular area occupied by a DNA molecule within a bilayer as estimated experimentally, 8 nm^2 is in close agreement with the theoretical value[201]. These results indicate that about half of the nucleotide sequences are pointing toward the aqueous surrounding and the other half is hindered within the vesicular structure. This hypothesis is further supported by the hybridization efficiency, estimated to 30%. Solely the nucleotide sequences that are pointing towards the surrounding are available for hybridization, about 50% statistically. It may be that some nucleotide sequences are not accessible for hybridization because of steric hindrance upon structure formation. A molecular area above 7 nm^2 is indeed needed for optimal hybridization efficiency [201]. Nevertheless, the vesicular morphology is supported by TEM which shows the presence of spheres characterized by a lighter inner core than the background and successful encapsulation and release of a water soluble fluorescent dye, not possible with a hydrophobic probe.

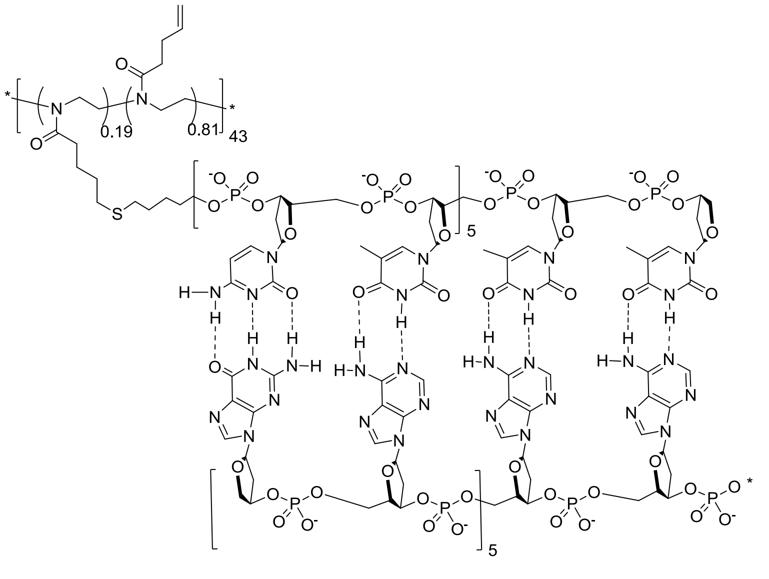

Scheme 3-2. Chemical structure of the PBOX-g-DNA molecular bottle brush and hybridization with its complementary sequence

Since the structures are composed of a PBOX membrane-like layer surrounded by a corona of the nucleic acid strands that point toward the inner aqueous pool and the surrounding medium of the vesicular structure, upon hybridization, the size increases. Self-assembly does not take place when the process is induced in a solution of the complementary sequence. No morphological transition or disassembly could be observed up to the addition of 130% of complementary sequences in the surrounding (*Figure 3-4*). The large molecular weight of the copolymer (30000 Da) infers mechanical stability to the self-assembled structures owing to the low chain mobility of the copolymer [202]. The stability might be further supported by intra-and intermolecular hydrogen bonds between the constitutive nucleic acid grafts. Upon hybridization, only the nucleotide sequences pointing towards the aqueous surrounding are solicited. The ones pointing towards the inner aqueous pool might maintain their reinforcing interaction to preserve the structures. Hybridization occurs through hydrogen bonding as well (*see Scheme 2*), which although the hydrophilic weight fraction and the physical incompatibility is modified, supports the stability of the structure.

5. CONCLUSIONS

Overall, these experimental results demonstrate that the ability of the polymer to crystallize into microspheres could be used to carry out the straight synthesis of a PBOX-g-DNA molecular brush and induce structure formation into sub-micrometer size spherical structures that are stable against hydrogen bonding as evidenced by demonstrating the stability of the structures in presence of nucleic acid strands in the surrounding. These could therefore be used for the speciation of complementary and non-complementary strands both present in the surrounding. Although the formation of compound micelles cannot be ruled out, some indirect evidence points toward the formation of vesicular structures.

Funding Sources

The University of Geneva and the Swiss National Science Foundation for Research (PPOOP2-12838) are acknowledged for financial support

ACKNOWLEDGMENT

We would like to especially thank Annelies Sels for her experimental support as well as to Msc Anna Polomska and Dr Ander Estella for SEC analysis. Dr. Nidhi Gour, Dr. Kien. X. Ngo, Dr. Jancy Nixon Abraham and Ilyès Safir are thanked for useful discussions. Nora Fiedler is thanked for the synthesis of PBOX.

ABBREVIATIONS

A, adenine; AFM, atomic force microscopy; ATR-IR, Attenuated Total Reflectance, Infrared spectroscopy; AUC, Analytical ultracentrifugation; C, cytosine; CLSM , confocal laser scanning microscopy ; DNA, Deoxyribonucleic acid; FITC, Fluorescein isothiocyanate; FOA, free oscillation amplitude; G, guanine; ^{1}H NMR, Proton Nuclear Magnetic Resonance; LCR, low compound retention; M_n, Number average molar mass; M_w, weight average molar mass;

MWCO, Molecular Weight Cut Off; NMP, N,methyl,2,pyrrolidon; PBOX, poly(2-(3-butenyl) oxazoline); PEI, poly(ethyleneimine); RI, Refractive Index; SEC, Size-Exclusion Chromatography; SEM, scanning electron microscopy; TEM, transmission electron microscopy; TCEP, (tris(2,carboxyethyl)phosphine); T, thymine; TFA, trifluoroacetic acid; UCST, upper critical solution temperaturȩ; UV, Ultraviolet; UV-Vis, Ultraviolet–visible spectroscopy; WAXS, Wide-angle X-ray scattering.

Supporting Information

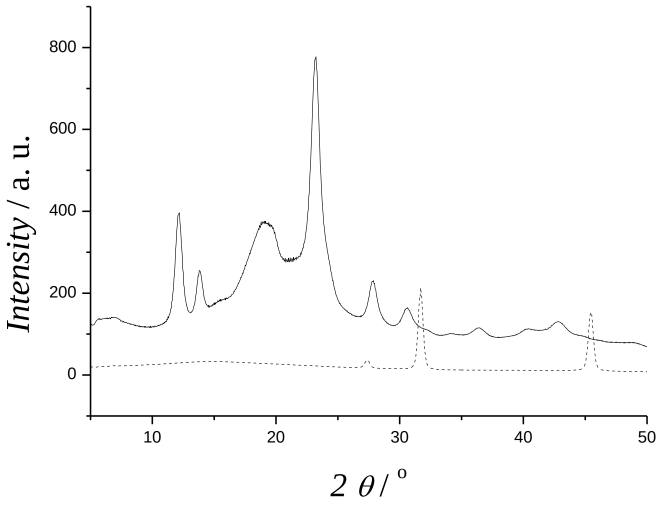

Figure S1. X-ray diffraction curve of freeze-dried precipitate of PBOX, prior to (dashed line) and subsequent to crystallization (solid line) of a 1 wt% polymer solution in ethanol–water 55:45 (w/w) at room temperature

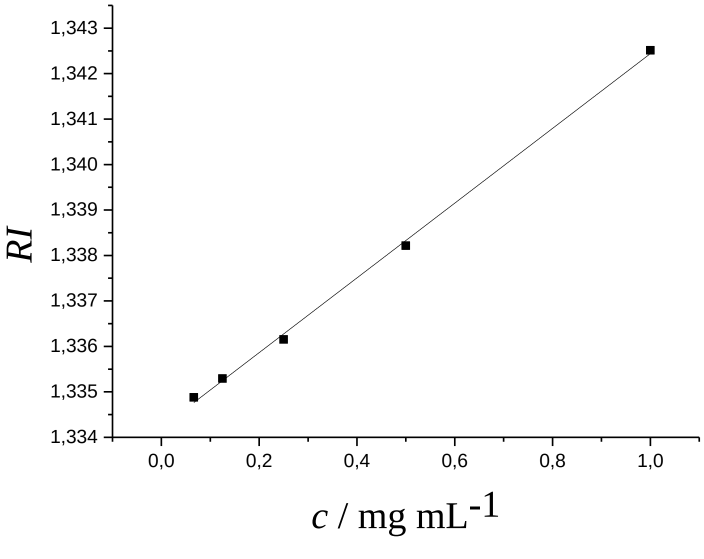

Figure S2. Refractive index (RI) dependence on concentration (c): $\frac{\mathrm{dn}}{\mathrm{dc}} = 0.0082\ \mathrm{cm}^3 g^{-1}$

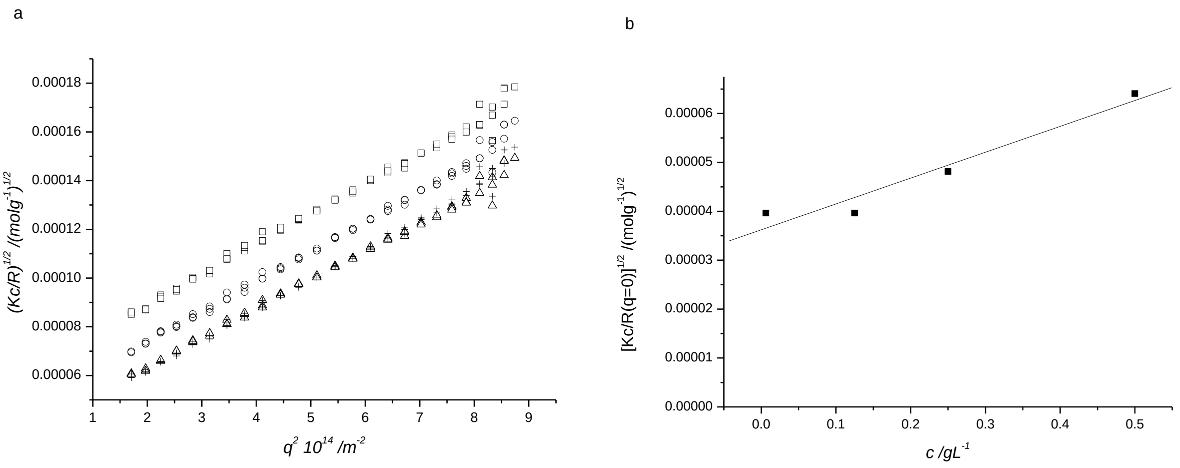

Figure S3. Berry analysis of the scattered intensity as assessed by static light scattering a) angle dependence for □) 0.5, ○) 0.25, Δ) 0.125 et +) 0.00625 gL^{-1}; b) concentration dependence subsequent to 0 angle extrapolation

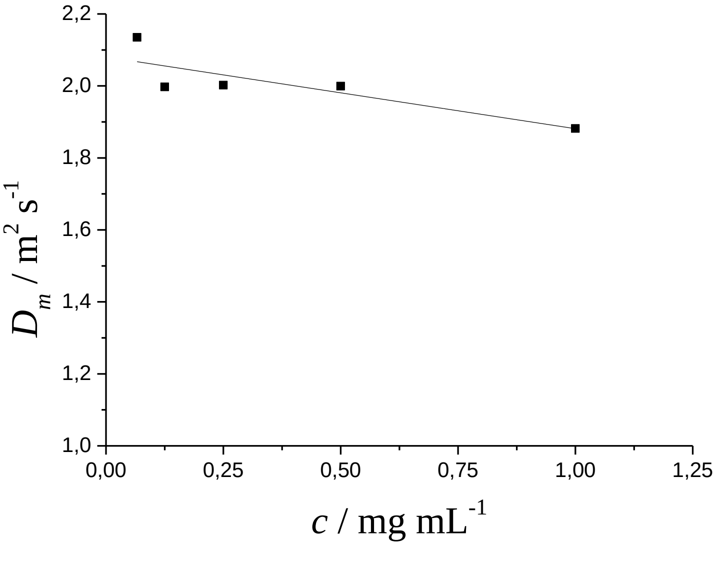

Figure S4. Concentration dependence of the mutual diffusion coefficient as measured by dynamic light scattering

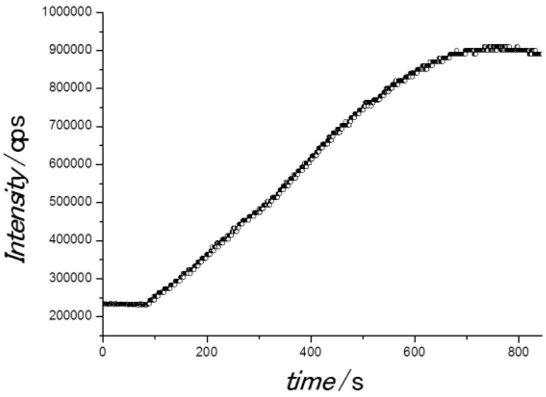

Figure S5. Time course of the fluorescein fluorescence intensity subsequent to encapsulation (concentration) and release by addition of sodium azide.

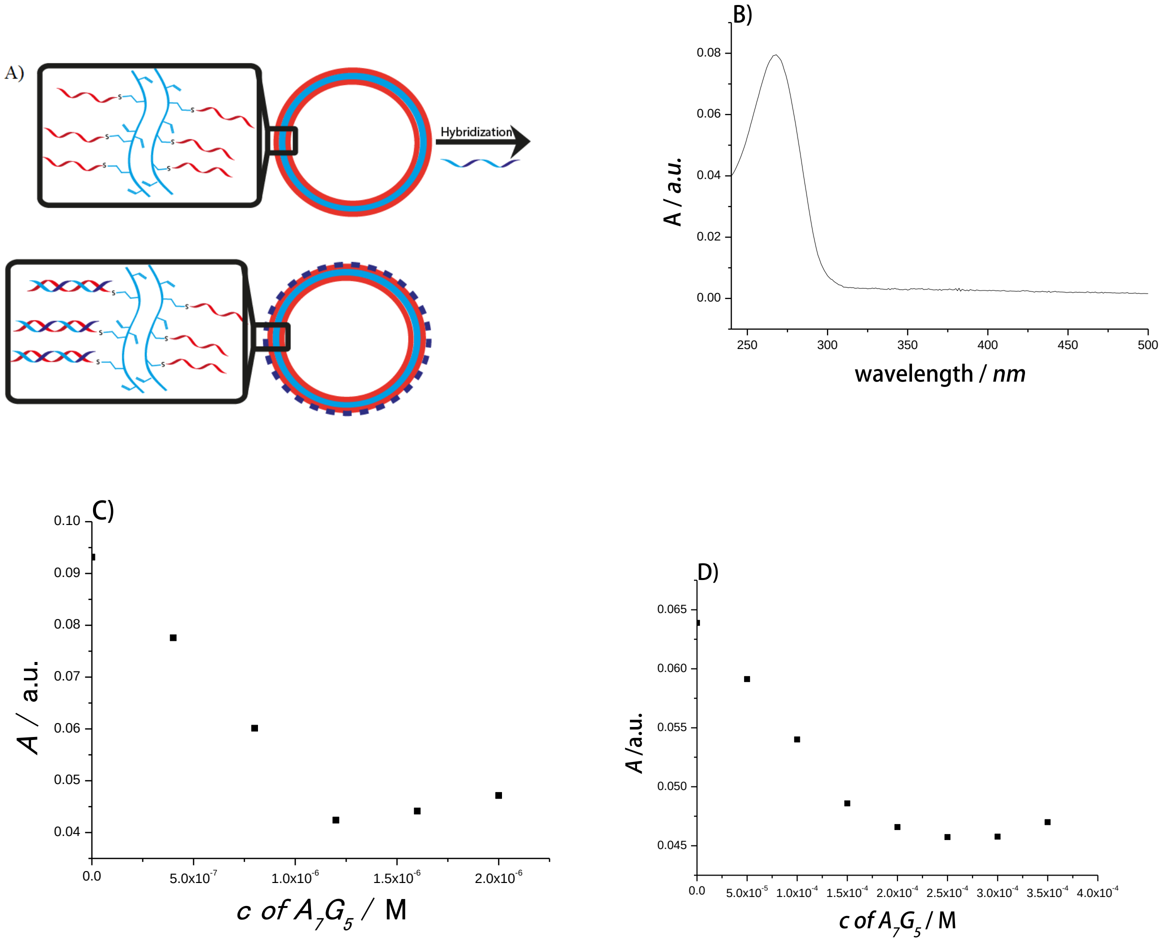

Figure S6. A) Schematic representation of hybridization. B) Representative spectrum which rules out hindrance owing to scattering C) Titration upon hybridization D) Control hybridization of free C_5T_7 with A_7G_5. Efficiency 100%.

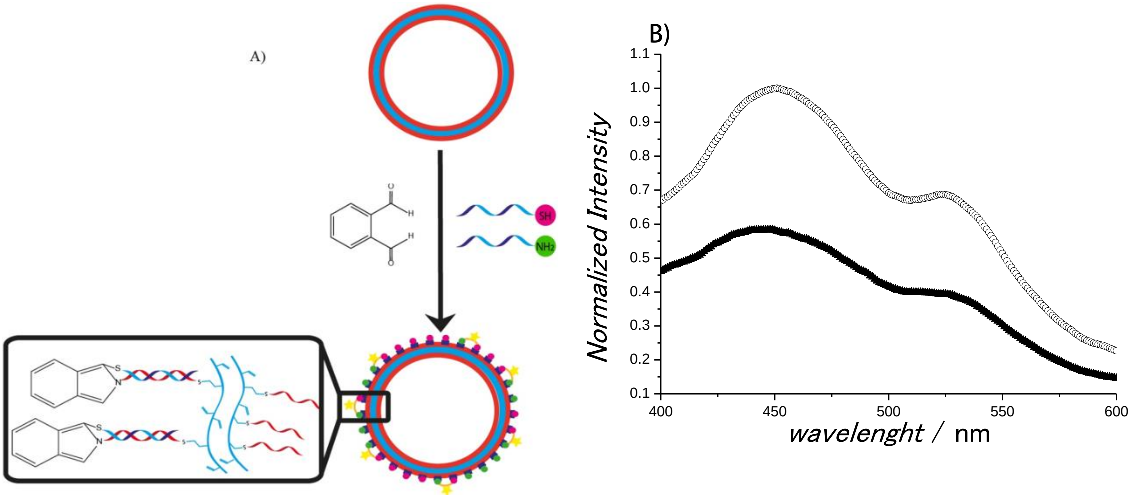

Figure S7. A) Schematic representation of isoindol reaction ,B)Fluorescence spectroscopy upon isoindol formation at the surface of PBOX spheres, ▲) initial stage of reaction , ○) reaction completed

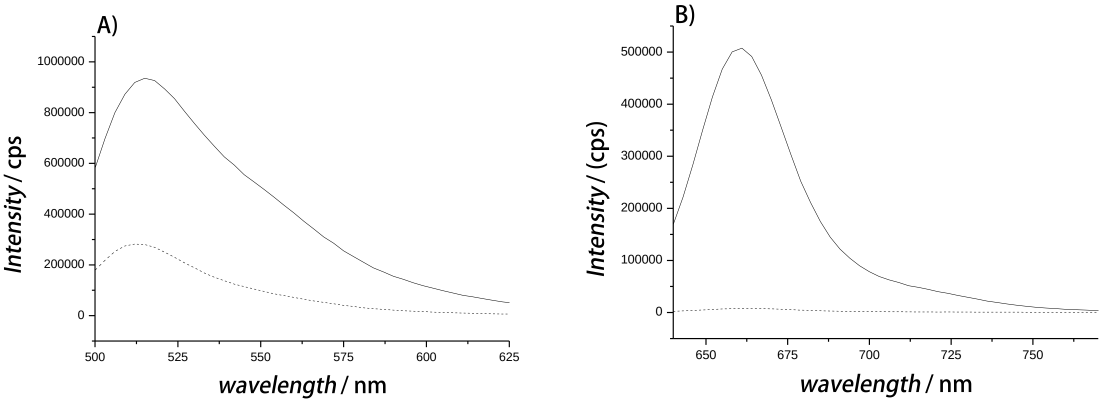

Figure S8. Fluorescence intensity spectra upon speciation (solid line: before washing; dotted line: after washing) of a solution of PBOX-g-DNA self-assembled structures incubated with the complementary sequence stained with A) FITC which hybridizes with the nucleic acid grafts engaged in self-assembly and B) the non-complementary sequence labeled with Cye5 which remains in solution before washing (background). Subsequent to washing, the complementary sequence stained with FITC hybridized with the PBOX-g-DNA composing the self-assembled structure, being the non-complementary sequence is removed during the washing process (no background).

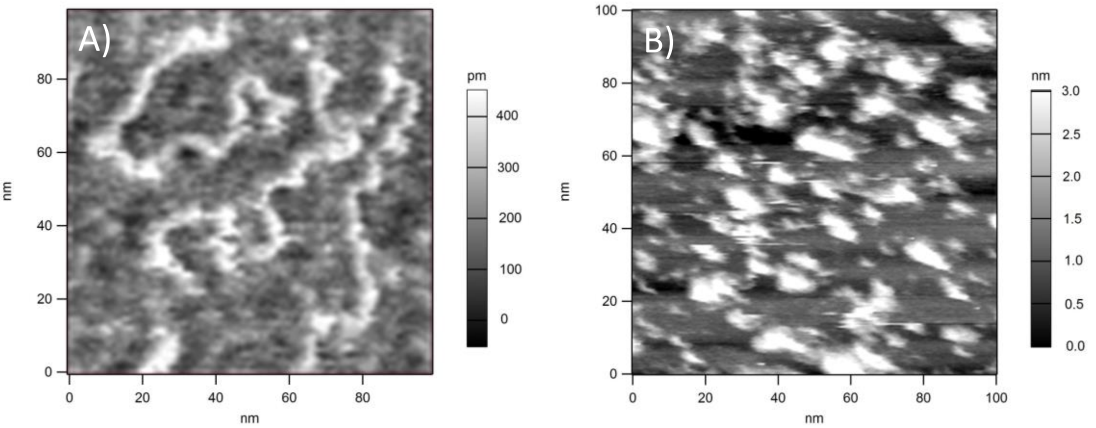

Figure S9. Atomic force microscopy imaging of A)molecularly dissolve PBOX polymer chains adsorbed on micaB) PBOX-g-DNA copolymer adsorbed on mica

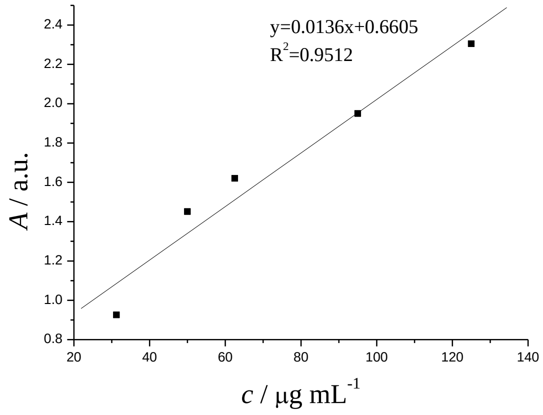

Figure S10. Absorbance calibration curve of the aptamer at 268 nm.

UV-Vis grafting density estimation. In order to estimate the grafting density of DNA along the PBOX chain we have utilized UV-Vis spetrocopy. Poly(oxazoline) absorbance at 268 nm is negligible what made this estimation possible. With in mind to find out the number of DNA strands per PBOX chain, the calibration curve with various concentration of 5'-(CT)$_5$T$_2$-3' (**Figure S10**).

For a representative quantification of the grafting density: absorbance value at 268;

A_{268}= 1.809

Thus, concentration is equal to;

x= (1.809-0.6605)/0.0136= 84.5 μg mL^{-1}

Concentration for measurement; 0.1 mg mL^{-1}, volume; 1mL

m_{DNA}=84.5 μg

M_{PBOX} = 5381.45 g mol^{-1}

M_{DNA}=3709.9 g mol^{-1}

m_{PBOX} = 100-84.5 =15.5 μg

n_{PBOX} =15.5*10^{-6}/ 5381.45 = 2.9 nmol

m_{DNA} =84.5μg

n_{DNA} = 84.5*10^{-6}/3709.9 = 22.8 nmol

n_{DNA} / n_{PBOX} = 7.86 ≈ **8** DNA strands for one PBOX chain

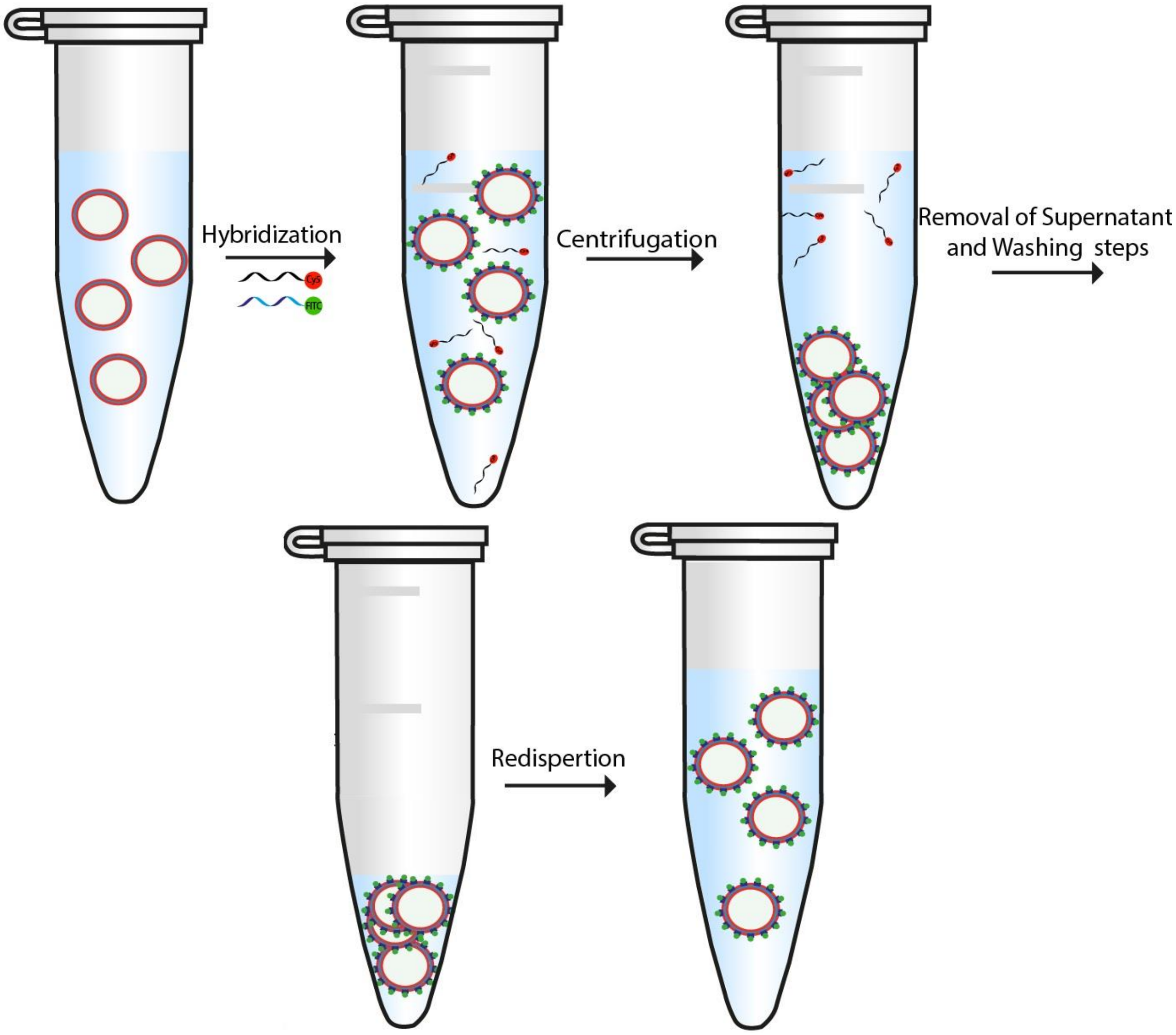

Scheme S1. Procedure for sorting out nucleotides sequences with the use of PBOX-g-DNA spheres.

Wavenumber (cm^{-1})	Assignments
920	Vinyl C=CH2
970	P-O in (R-O)2-PO2 upper band
1064	P=O in $(R\text{-}O)_2\text{-}PO_2$ lower band
1226	P=O in (R-O)2-PO2 upper band
1471	N-H streching
1652	C=O amide I

Table S1: Significant FTIR vibration bands and their corresponding wavenumbers

4 Controlled Aggregation in Amyloid like Systems-introduction

Fibril formation of amyloids into ordered linear arrays is suspected of initiating neurodegeneration in vivo. It is therefore of great importance to elucidate the mechanism of their aggregation [203-206]. Formation of fibers draws attention not just to solve biological and medical issues, but it is also important from the perspective of potential applications in nanotechnology (scaffolding for tissue engineering), food processing or treatment of eye cataract diseases [203, 207, 208]. Amyloid are referred to proteins and peptides which exhibit a cross β-sheet structure in which the peptide backbone run perpendicularly to the axis of the fiber, which are generally long with a diameter ranging from 40 to 120 Å [208]. Self-organization of β-sheet into protofibers is followed by their further packing which leads to formation of amyloid fibers (*Figure 4-1*). The formation of amyloid structures was identified for at least 16 various protein and peptides [209], which share the same core structure regardless of having different composition and configuration [208]. It thus seems to be a generic feature of peptides and proteins [210].

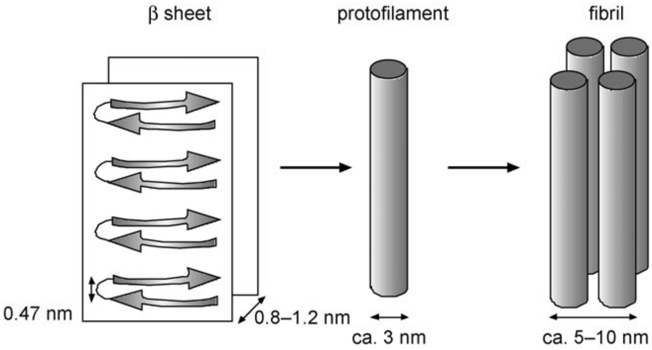

Figure 4-1. Amyloid fibers structure[203] (figure adopted with permission of John Wiley and Sons).

Nucleation dependent polymerization- The mechanism of fiber formation

Numerous various highly characterized processes are recognized to occur through nucleation dependent polymerization, including microtubule formation [211], sickle-cell fibril formation

[212], flagellum assembly [213] and others [214]. Frequent observation of a lag phase suggested that amyloid fibers formation also occurs according to a nucleation and growth process [205, 206, 214]. Characteristic features of these processes are (*Figure 4-2*) 1) revealed by a nucleation phase, which goes through series of thermodynamically unfavorable association steps (K_n<<1) to form oligomeric nuclei 2) subsequent thermodynamically favorable (K_g>>1) growth phase and 3) steady state phase in which the monomer and aggregate are in equilibrium [214].

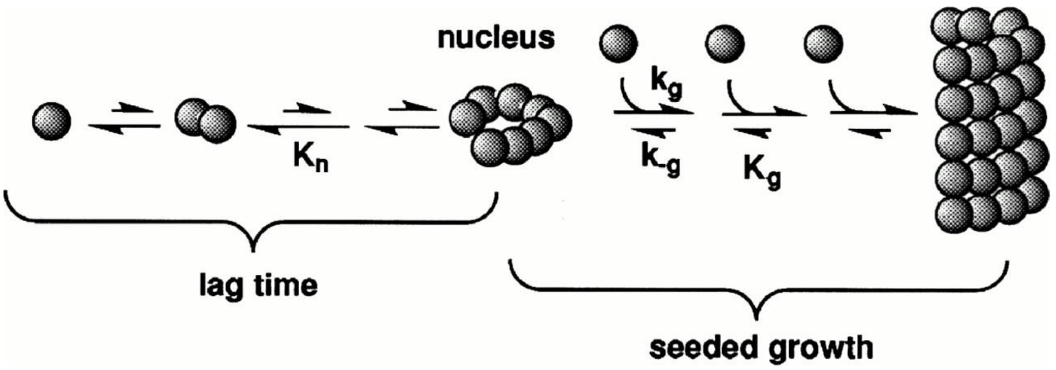

Figure 4-2. Nucleation-dependent polymerization simple mechanism [206]. Equilibrium constants for each step are small and equal, while growth steps equilibrium constants K_g are large and equal [211].

The following properties are characteristic for the nucleation polymerization; a) larger aggregates can be formed just above a critical concentration, which is analogous to a critical micelle concentration (cmc) (*Figure 4-3*), b) lag phase after which aggregates are noticeable, c) addition of seeds help to reduce the lag time (*Figure 4-4*) [203, 206, 214].

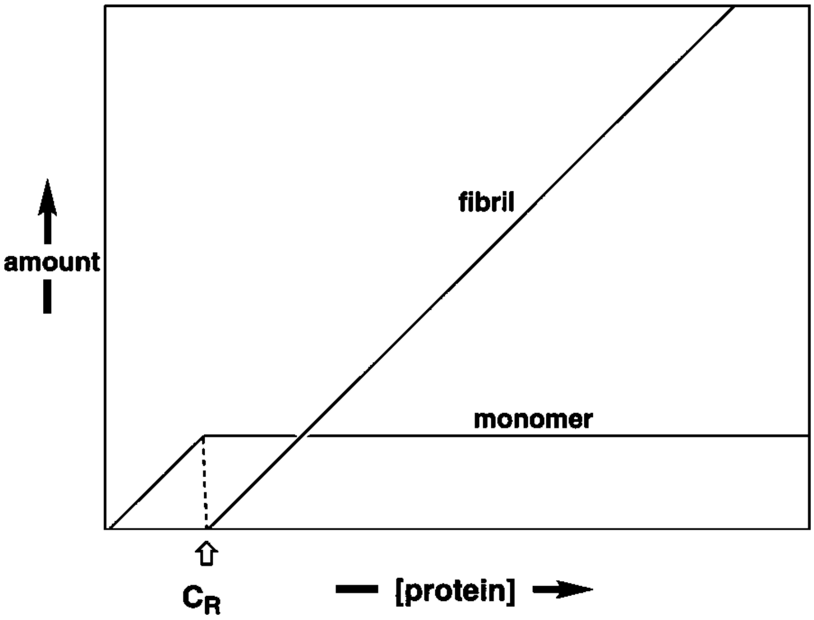

Figure 4-3. Concentration dependent fibers formation. C_r *stands for critical concentration [206].*

In the common nucleation dependent assembly, polymers are formed when the concentration of monomer will reach a threshold value, which is defined as critical concentration (*Figure 4-3*). If the concentration does not reach this level, monomers are in majority. The critical concentration is characterized by the growth equilibrium constant K_g which is inherent to the protein solubility during the steady-state phase [211, 214]. Micelle generation is as well characterized by a critical concentration. However their formation is much faster than amyloid fibers due to a larger entropic barrier to fibers formation. As a result the supersaturated protein solution is referred as metastable or kinetically soluble [206].

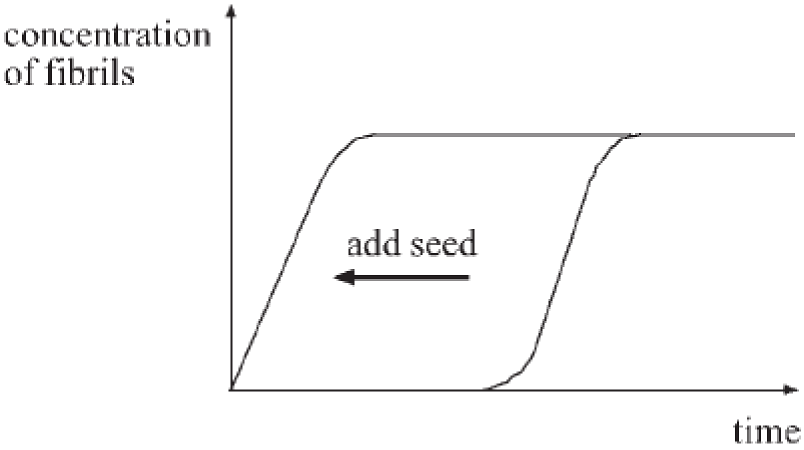

Figure 4-4.Elimination of lag time by seed addition [203] (figure adopted with permission of John Wiley and Sons).

The time during which the nucleus forms and solution is kinetically soluble before formation of fibers is known as lag time *(Figure 4-5)* [206, 214]. Formation of prenucleus oligomers during the lag phase occurs in a quantity that might be difficult to detect (detectability in a narrow concentration range) [214]. Slow rate of this process is a consequence of non-favorability of the association. Protein concentration is the main factor which regulates the time of lag phase [215].

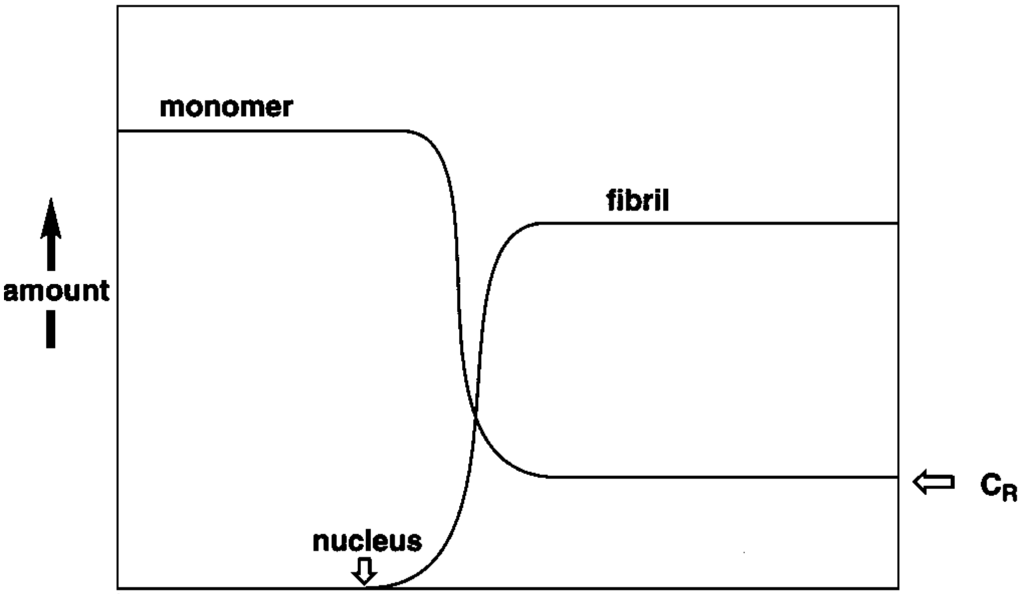

Figure 4-5.Simplified scheme presenting kinetic curve of amyloid formation [206]

Addition of exogenous seeds or nuclei results in intermediate polymerization together with reduction up to elimination of the lag time [216]. Subsequent growth occurs according to first-order kinetics [217, 218]. Seeding depends on complementarity of the fibril seed growth phase and the substrate, which makes seeding highly discriminating [219]. Nevertheless, various constitution seed can serve as heterogeneous seed and supply complementarity between seed growth and native substrate, exactly as in the case of the growth of inorganic crystals [206]. Heterogeneous as well as homogenous seeds can play a relevant role in supporting the amyloid fiber formation in Alzheimer’s disease.

4.1 Formation of DNA-copolymer fibrils through an amyloid-like nucleation polymerization mechanism

(the following subsection was adapted from “*Formation of DNA-copolymer fibrils through an amyloid-like nucleation polymerization mechanism*” by Dawid Kedracki, Sergey K. Fillipov, Nidhi Gour, Helmut Schlaad and Corinne Nardin, Macrolomolecular Rapid Communications-DOI 10.1002/marc.201400728, Supporting Information with the figures mentioned in the text are placed at the end of this subsection)

ABSTRACT. Conjugation of a hydrophobic poly(2-oxazoline) bearing tertiary amide groups along its backbone with a short single stranded nucleotide sequence results in an amphiphilic comb/graft copolymer which organizes in fibrils upon direct dissolution in water. Supported by CD, AFM, TEM, and scattering data, fibrils are formed through inter- and intra-molecular hydrogen bonding between hydrogen accepting amide groups along the polymer backbone and hydrogen donating nucleic acid grafts leading to the formation of β-sheet layers which close into hollow tubes.

1. INTRODUCTION

Soft materials based on self-assembling copolymers hold great promises for applications in the biomedical field as well as for the development of future technologies based on the design of advanced functional materials resulting from their hierarchical organization at several length scales [220]. Self-assembling copolymers organize into sophisticated functional structures through non-covalent interactions such as hydrophobic, electrostatic, π-π stacking and hydrogen bonding [110]. Bio-inspired polymers belong to a particular class of polymers which form such subtle superstructures through non-covalent interactions [221]. Moreover, coupling of biological components with synthetic polymers could greatly improve the biocompatibility of the resulting material. Such block copolymers are referred to as “polymer-bioconjugates”, biohybrids”, or “macromolecular chimeras” [109]. Molecular chimeras are constitutive of the first class of compounds combining the suitable properties of synthetic polymers such as protein repellency, temperature sensitivity with the features of biological molecules (e.g. targeting-antibodies) [110]. Biopolymer assemblies are thus obviously attractive for healthcare and pharmaceutical applications. Nevertheless, the selection of the biological segment is not restricted to one class of molecules and it could be either an amino acid chain (peptide) or nucleic acid chain (DNA, RNA) as well as an oligo- or a polysaccharide.

Molecular chimeras in which the biological component is a single stranded DNA fragment belong to a particularly interesting class. Owing to DNA involvement in a plethora of vital biological mechanisms in addition to the transfer of the universal genetic information, the conjugation of DNA with biocompatible polymers has recently become a subject of intensive studies [222-224]. Conjugation is for instance expected to overcome issues such as limited plasma half-life as well as cellular penetrability [225, 226]. Besides, coupling with non-water soluble synthetic polymers results in the formation of self-assembled structures revealing the remarkable properties of the constitutive DNA fragment [113, 227-230].

An intriguing synthetic polymer species is poly(2-alkyl-2-oxazoline) (POX), which due to their structural resemblance to polypeptides are also regarded as pseudopeptides [186]. In comparison to amino acid sequences, poly(2-oxazoline)s contain tertiary amide groups without any chirality center (or tacticity) that may disturb or prevent the formation of higher order structures. However, chirality as well as control over polymer hydrophobicity can be easily achieved through modification with side chain substituents, which further opens the opportunity for construction of complex and hierarchical biomimetic self-assemblies [188].

Generally, self-assembly occurs due to microphase separation of chemically distinct blocks into nanoscale periodic domains [23] in which segregation of chemically unlike blocks as well as cohesive interactions of like blocks can be considered as the driving force [24]. Self-assembly of amphiphilic molecules in aqueous solution can thus be defined as a process of seeking for the delicate equilibrium between the attractive and repulsive intermolecular interactions.

The synthesis of β-sheet-mimicking copolymers is of high interest as well to both develop new classes of materials for biomedical applications and to understand the basic rules of nanoscale assembly [231]. Reports provided up to date describe block copolymers composed of either peptide sequences able to form β-sheets or cyclic peptides forming fibrillar superstructures or nanotubes in aqueous solutions [110, 203, 231]. This self-assembly has drawn much attention because of its association with neurodegenerative diseases such as Alzheimer's, Parkinson's, Huntington's diseases, type II diabetes or Creutzfeldt-Jacob disease [232, 233]. The accumulation of misfolded protein aggregates called amyloid fibers is the typical hallmark of these diseases. These amyloid fibril formation proceeds by a nucleation dependent polymerization process seeded by initial globular structures which assemble into protofilaments and bundles of twisted β-sheets [203].

Herein we report the self-assembly behavior of an amphiphilic POX-*graft*-DNA copolymer, obtained by solid phase coupling between the poly[2-(3-butenyl)-2-oxazoline] backbone carrying *N*-protected amino acid side chains and a water soluble (DNA) nucleotide sequence. Structure formation results from inter- and/or intra-molecular hydrogen bonding. To the best of our knowledge this is the first report in which self-assembly formation of a hybrid composed of a pseudo peptide and a DNA sequence occurs through a nucleation polymerization mechanism. Structures assembled in aqueous solution were characterized by circular dichroism (CD) spectroscopy, transmission and scanning electron microscopy (TEM and SEM), atomic force microscopy (AFM) as well as small-angle X-ray scattering experiments (SAXS).

2. EXPERIMENTAL SECTION

Copolymer Synthesis

Poly[2-(3-butenyl)-2-oxazoline] (POX) was obtained by cationic ring-opening isomerization polymerization of 2-(3-butenyl)-2-oxazoline as reported earlier.[189] The isolated PBOX chains had an average length of 43 repeat units, corresponding to a number-average molar mass (M_n) of 5380 g mol^{-1}, by ^{1}H NMR end group analysis and a dispersity index (M_w/M_n) of 1.05 (SEC). The alkenyl groups of POX were modified with *N*-(tert-butyloxycarbonyl)-L-cysteine (BocCys) (Merck) by thio-click chemistry [189]. As revealed by ^{1}H NMR analysis (Figure S1) of the purified product POX/BocCys, 76% of the unsaturated units were functionalized with the *N*-protected amino acid (~33 units per chain) and 24% remained unreacted (~10 units) (chemical structure in *Scheme S1* (top left)). The POX-*graft*-DNA polymer hybrid was obtained by solid phase synthesis following synthetic strategies reported earlier [111, 193, 234]. Briefly, a 12 nucleotide-long sequence (5'-CTCTCTCTCTTT-3', 5'-$(CT)_5T_2$-3'), modified with an amino group through an hexyl spacer at the 5'-end and bound to the controlled pore glass (CpG) phosphoramidite solid support at the 3'-end (Scheme S1) was reacted with the carboxylic acid group of the POX/BocCys activated by *N*,*N*'-diisopropylcarbodiimide (DIC). After the coupling reaction, the resin was washed thoroughly with DCM and DMF, filtered out prior to cleavage with liquid ammonia. The copolymer was purified by dialysis against water for 5 days (molecular weight cut-off 7500 Da) and finally freeze-dried.

Analytical Instrumentation and Methods

^{1}H NMR measurements were carried out at room temperature using a Bruker DPX-400 spectrometer operating at 400.1 MHz. UV/vis absorption spectra were recorded on a Lambda 25 spectrometer (Perkin Elmer, Singapore) in a quartz cuvette of 1 mm path length. The FTIR spectra were taken on a Spectrum One, Perkin Elmer instrument; samples were measured in solid state using a Single Reflection Diamond ATR. CD measurements were carried out on a JASCO J-815 spectrometer (Sand Diego, USA). Preliminary synchrotron SAXS experiments were performed on the BM26B beam line (ESRF, Grenoble, France) using a pixel detector (1M PILATUS). The X-ray scattering images were recorded using a monochromatic incident X-ray beam (λ = 0.154 nm) covering the $0.023\ \mathrm{nm}^{-1} < q < 1.65\ \mathrm{nm}^{-1}$ range of momentum transfer ($q = 4\pi/\lambda \sin\theta$), with 2θ the scattering angle). Further measurements were performed on the B21 beam line (Diamond Light Sourse, Didcot, UK) in the $0.025\ \mathrm{nm}^{-1} < q < 4.00\ \mathrm{nm}^{-1}$ range. In all cases reported in here, the two-dimensional scattering patterns were isotropic. They were azimuthally averaged to yield the dependence of the scattered intensity I_s(q) on the momentum transfer q. Prior to fitting analysis, the solvent scattering has been subtracted. All data manipulations were performed using the BH plot and Data Tools software implemented in SAXS utilities. For SAXS measurements the POX-graft-DNA copolymer was dissolved in water at neutral pH to obtain the final concentration of 1mg mL^{-1}. Subsequently the sample was vortexed thoroughly and left for equilibration at least for 24 h. Prior to transmission electron microscopy (TEM) imaging, 400-mesh copper grids were glow discharged for 30 s to render the grids surface more hydrophilic. TEM images were recorded on a Tecnai G2 electron microscope (Tokyo, Japan) operating at 120 kV. 5 μL of sample (1 mg mL^{-1}) was deposited on a carbon coated 400-mesh copper grid and after 30s of adsorption liquid was blot off on filter paper by holding it vertically. After preparation, the sample was imaged without staining. AFM images were acquired using an MFP-3D microscope (Asylum Research, Santa

Barbara, CA) in the non-contact mode at room temperature. For all AFM measurements, cantilevers (Pointprobe NSC, MikroMasch, Tallin, Estonia) with an elastic constant of $K_c = 4.28\ Nm^{-1}$, and resonance frequency of 137 kHz were used. SEM images were acquired on a Jeol 6510LV microscope (München, Germany), equipped with a tungsten filament gun, operating at 10.6 mm WD and 10 kV.

3. RESULTS AND DISCUSSION

POX-*graft*-DNA is an amphiphilic copolymer with the chemical structure shown in *Scheme 4-1*. Analysis by analytical ultracentrifugation (AUC) sedimentation-velocity (*Figure S2*) reveals distinct sedimentation profiles of the starting materials and the final product which supports the success of the solid phase synthesis route (see Experimental Section). Estimation of the grafting density by UV/vis spectroscopy [193] (*Figure S3*) indicates that every polymer chain carries in average one DNA graft, hence POX-*graft*-DNA is a actually an AA′B hetero three-arm star polymer with a molar mass of ~16.3 kDa and hydrophilic weight fraction of 67%.

The CD spectrum of the pristine nucleic acid sequence is displayed in *Figure S4*. The positive large wavelength band at $\lambda = 280$ nm and negative Cotton effect at about $\lambda = 245$ nm is characteristic of the DNA B-form [235]. Comparing with the spectrum of POX-*graft*-DNA, the characteristic minimum of β-sheet structures appears at $\lambda = 218$ nm [203]. It can be concluded that conjugation of the polymer and the nucleotide sequence and subsequent dissolution in aqueous solution results in the formation of a structure of higher order.

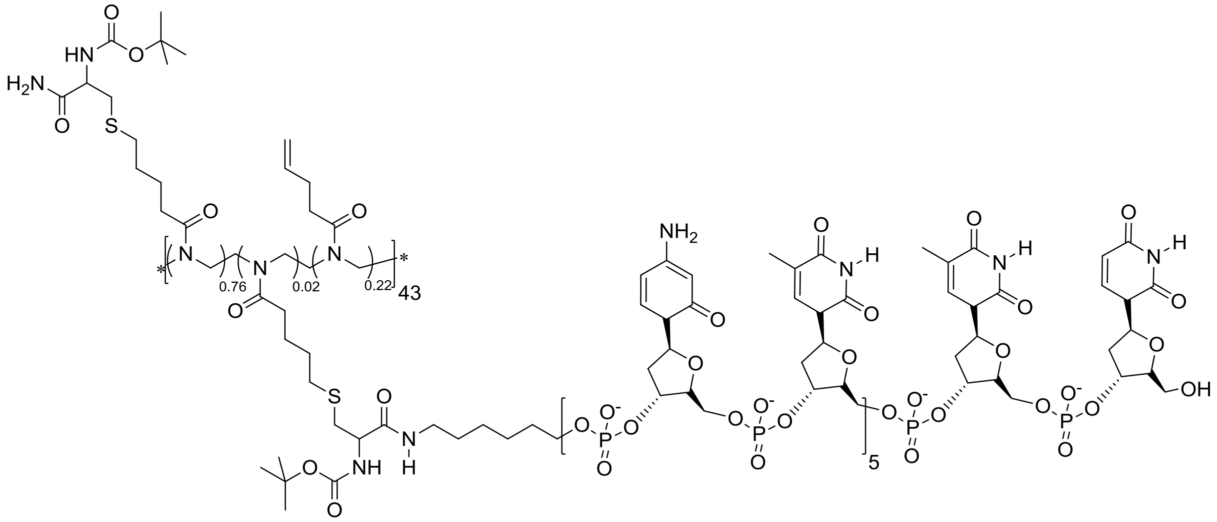

*Scheme 4-1. Chemical structure of POX-*graft*-DNA*

Direct dissolution of the final product in water at a concentration of 1 mg mL^{-1} results indeed in the formation of large structures due to both chemical and physical incompatibility between the non-water soluble polymer segment and the hydrophilic nucleic acid grafts. Morphological characterizations performed by atomic force microscopy (AFM) revealed the presence of spherical aggregates of (1.8±0.4) µm average diameter (*Figure S5A and S5B*) along with fibrillar structures of (1.60±0.30) µm diameter and length in the range of few tens of microns (*Figure 4-6 A*). Cross-sectional analysis (*Figure S5C*) allowed obtaining information about the height of the aggregates which is of about (184±50) nm. The difference between diameter and height suggests that fibers probably collapsed upon interaction with the surface and shrinkage occurs by measurement in the dry state, which could be an indication of their hollowness. Due to presence of the electron dense phosphate groups along the nucleotide sequence, which are natural enhancers of the contrast in transmission electron microscopy (TEM) imaging could be conducted without staining. TEM revealed the presence of tubular structures with a light inner core and dark periphery which could indicate that POX-*graft*-DNA copolymers compose the walls of hollow fibrils (*Figure 4-6 B*).

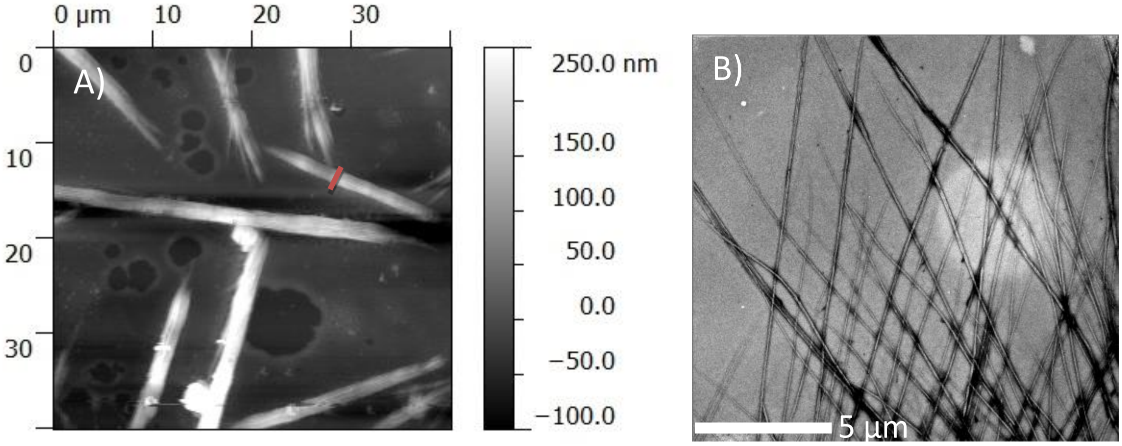

*Figure 4-6. Fibers morphology assembled by that POX-*graft*-DNA as assessed by A) AFM and B) TEM imaging*

SEM imaging could however be conducted at different time intervals after product dissolution to provide information about the kinetics of fibers formation. Imaging conducted within hours (*Figure 4-7 A*) after dissolution reveals the formation of globular structures and protofibers which over tens of hours aggregated (*Figure 4-7 B*) to form highly organized filaments (*Figure 4-7 C*). Such as behavior is comparable to the process of nucleation polymerization characteristic of the formation of polypeptide fibrillar structures [203]. Initial globular structures, assembled owing to the chemical incompatibility between the polymer and the nucleic acid sequence, might play the role of seeds for the fibrillation process to occur [203, 236]. According to research outcomes reported by Hamley and coworkers, the formation of polypeptide fibrils arises from co-action between polypeptide backbones, while folding occurs as a result of highly specific interaction of the side chains. Since the fibril length is related to the rate of aggregation,[237] the significant dimensions of fully formed fibers could be due to the slow process of aggregation.

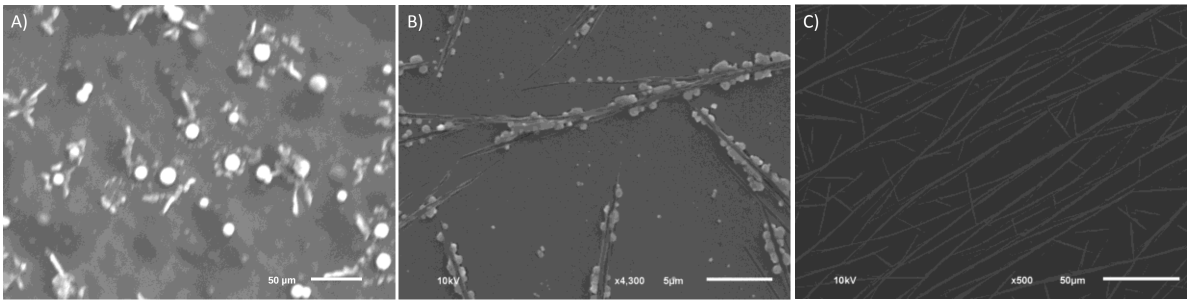

Figure 4-7.SEM imaging A) initial state-globular and protofibers structures B) intermediate aggregation C) fully formed fibers

To examine the impact of hydrogen bonding in the process of structure formation, POX-*graft*-DNA fibers were co-incubated with urea which is inhibiting hydrogen bonding. In the presence of 0.1 M urea fibers were completely disorganized after 24 hours (*Figure S6*), which thus evidences the key role of hydrogen bonding in fibrillar structures formation.

In order to obtain more detailed information about the morphology of POX-*graft*-DNA fibers, characterization through small-angle X-ray scattering (SAXS) was eventually performed. SAXS curves (*Figure 4-8*) could be analyzed with the form factor of a hollow cylinder of finite length in the micrometer range (8600 nm) in combination with that of a Gaussian coil. The best possible fit was achieved with structures of 17 nm inner radius and outer radius of 76 nm, in close agreement with the results obtained by imaging.

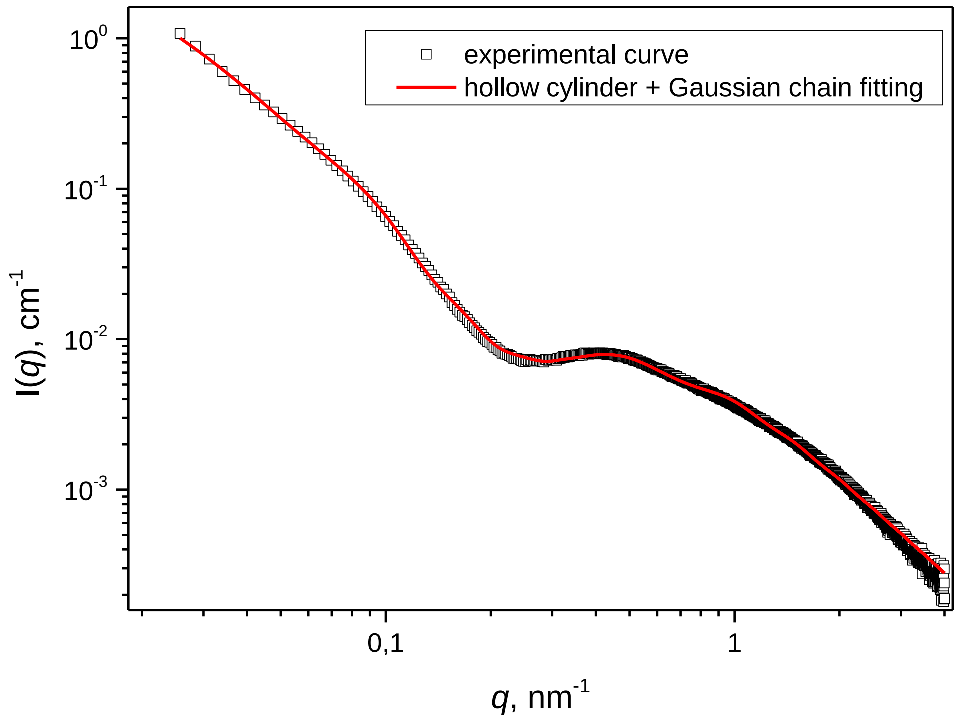

Figure 4-8. SAXS outcomes of fibers assembled by POX-graft-DNA at 1 mgmL^{-1} in aqueous solution

Following the reports on copolymer with structural resemblance to POX-*graft*-DNA [190, 221] we can hypothesize that initial globular structures are formed due to microphase separation of the incompatible blocks which are subsequently stabilized by intra- and inter-molecular hydrogen bonding between the POX tertiary amides and the nucleic acid strands involved in the structure formation through nucleation dependent polymerization [236]. It can be assumed that chains are oriented parallel to the long axis of the microfiber and linked together via hydrogen bonding. Needless to say, intermolecular hydrogen bonding is probably determining but not the only factor for formation of this specific architecture. In addition to the role of the hydrophilic weight fraction, which drives the formation of the globular structures[61], intramolecular interactions might play a role. This hypothesis is supported by experimental results reported previously [238]. The grafting of a larger number of nucleic acid sequences along the POX backbone results in the self-assembly of micelles. In that case, intramolecular hydrogen bonding is prevented, being the self-assembly supported by chemical incompatibility and intermolecular interactions solely.

Based on these experimental results one can however conclude that the wall of the fibers is constructed of a sheet of POX-*graft*-DNA chains organized as schematized in *Figure 4-9*.

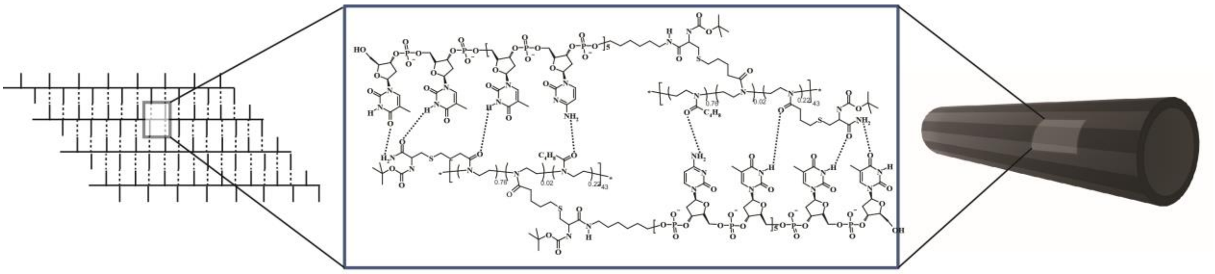

Figure 4-9.Provisional structure of hollow tube composed of PBOX-g-DNA

4. CONCLUSIONS

The direct dissolution of the POX-*graft*-DNA amphiphilic copolymer in water results in the formation of fibrillar structures. It is assumed that fibers are hollow tubes with cross sectional radius of ~20 nm and length of few tens of microns. Based on the slow kinetics, fibrils are formed according to a nucleation dependent polymerization mechanism. The walls of the tubes are composed of POX-*graft*-DNA layers formed through intra- and inter-molecular hydrogen bonding.

Supporting Information

Materials: Dichloromethane (DCM) (extra dry, 99.8%), *N,N*-dimethylformamide (DMF) (99.8%), sodium chloride (>99.5%), triethylamine (99%) were purchased from Acros Organics (Geel, Belgium). Acridine orange,*N,N′*-diisopropylocarbodiimide (>98%), dialysis cassettes (molecular weight cut-off 7.5kDa), were supplied by Sigma Aldrich (Buchs, Switzerland). The ammonia solution 35% was purchased from Fisher Scientific SA (Wohlen, Switzerland). 5’-CTCTCTCTCTTT-3’ modified at the 5’ end througha hexyllinker by an amino group and 5’-FITC labelled complementary DNA sequence 5’-AAAGAGAGAGAG-3’ were purchased from Microsynth Laboratory (Balgash, Switzerland). Silicon wafers single side polished, orientation N/Phos< 100 >, (625±25) µm thickness, 1-50 Ohm cm resistivity were purchased from Silchem (Freiburg, Germany). DMSO

Synthesis and characterization:

In brief, N,N′-diisopropylocarbodiimide was used to activate the carboxylic group of Boc-cysteine modified poly[2-(3-butenyl)-2-oxazoline] according to a protocol reported earlier.[234] The activated ester was exposed to a nucleophilic attack at the free 5‘-amino group of a 12-mer (sequence 5’-CTCTCTCTCTTT-3’) modified at the 5’ end by an amine group through a hexyl C_6 linker whereas the 3’ end remains bound to the controlled pore glass (CPG) solid support. Solid phase synthesis was selected in order to avoid tedious steps of chemistry or purification. Treatment with liquid ammonia enabled to cleave the product from the resin and remove protecting groups. The final product was characterised by UV/VIS spectroscopy, and analytical ultracentrifugation.

Conjugation of amino modified DNA to N-Boc-cysteine modified poly[2-(3-butenyl)-2-oxazoline]. Poly[2-(3-butenyl)-2-oxazoline)modified with boc-cysteine (2 μmol, 25.8 mg, 1 eq), was dissolved in 1.5 mL of dry DCM and placed in a 2 mL reactor. Subsequently 11.3 μL of DIC (68 μmol, 8.5 mg, 1 eq-in respect to the number of PBOX side chains modified with cystein) was added. Later on, the reactor was mounted on a mechanical shaker for 1h at room temperature, 250 mg of solid cpg-resin bound 5'-CTCTCTCTCTTT -3' modified at the 5' end with an amine group through a C_6 amino linker (10 μmol, 250 mg, 5 eq) was appended together with 40 μL of triethylamine. Closedreactor was shaked at room temperature overnight. Filtration is possible due to the filter located at the bottom of the reactor. All residual solution was thus removed from the reactor and the resin washed thoroughly with DCM and DMF and subsequently again with DCM to get rid off any unreacted species and other side products using syringe pressure filtration. Finally the resin was dried in presence of nitrogen and weighed in an eppendorf tube.

Removal of the cpg solid support. In order to cleave the product from the resin, beads were transferred together with 1.5 mL ofammonia solution. Mixture was kept in a thermoshaker at 40 ^{o}C for 24 h. Afterwards the resin was separated from solution. Subsequently, in order to remove unreacted species, salts and protecting groups this solution contaning product was transferred to a dialysis membrane (7500 MWCO, against milli-Q water for 5 days). Subsequently the solution was filtered through 0.45 micron filter membranes and lyophilized. Yield 8 mg (31% reaction yield). The resulting compound was characterised by UV-VIS AUC, and FTIR.

UV-Vis grafting density estimation. To find out the grafting density of DNA along the PBOX chain, UV-Vis spetroscopy was used as reported earlier.[238] Poly(oxazoline)absorbance at 260 nm is negligible, which enables this estimation. In order to estimate the number of DNA strands per PBOX chain, the calibration curve with various concentration of 5’-(CT)$_5$T$_2$-3’ was established (Figure S3).

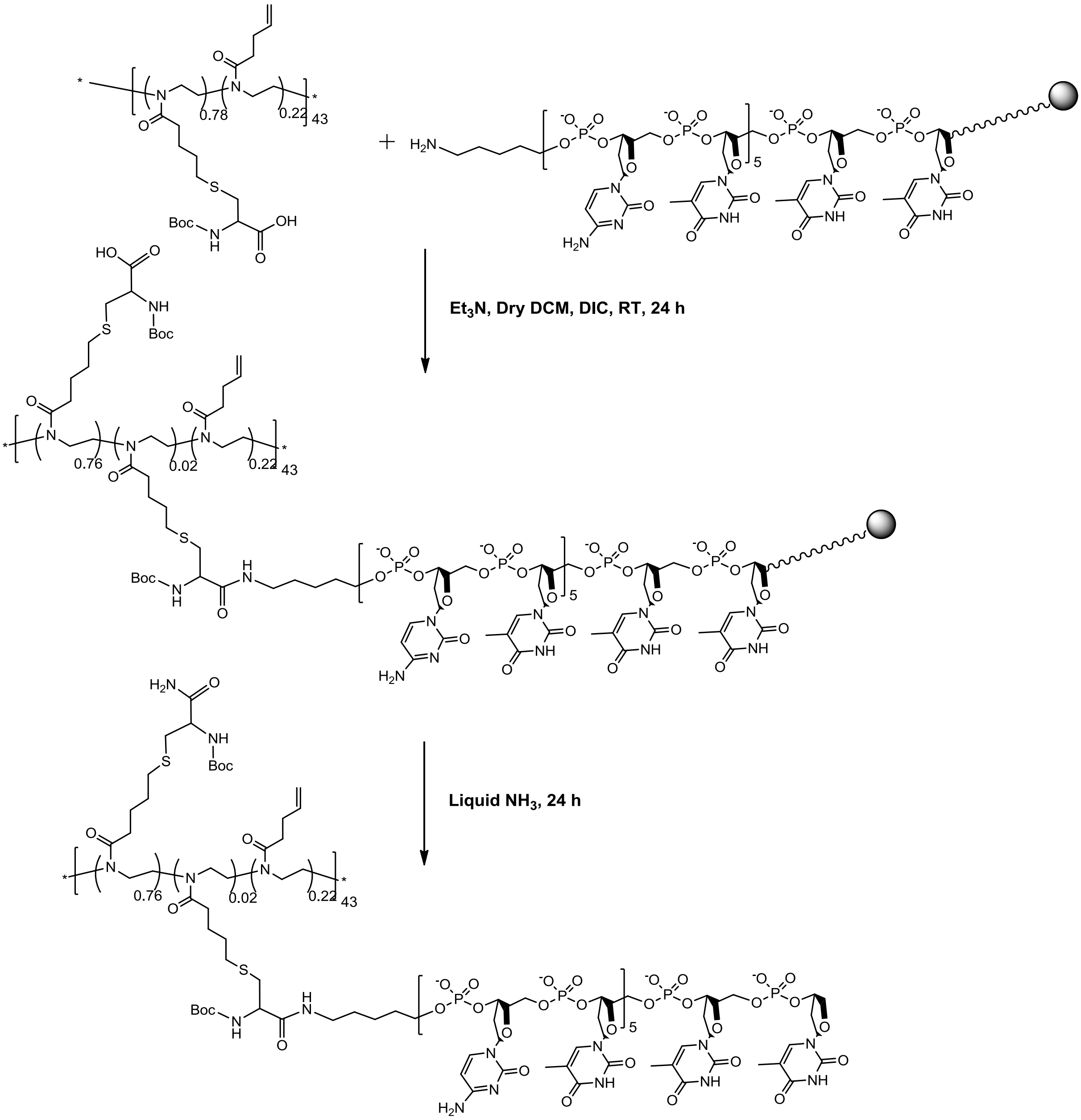

Scheme S1. Synthesis of PBOX-g-DNA

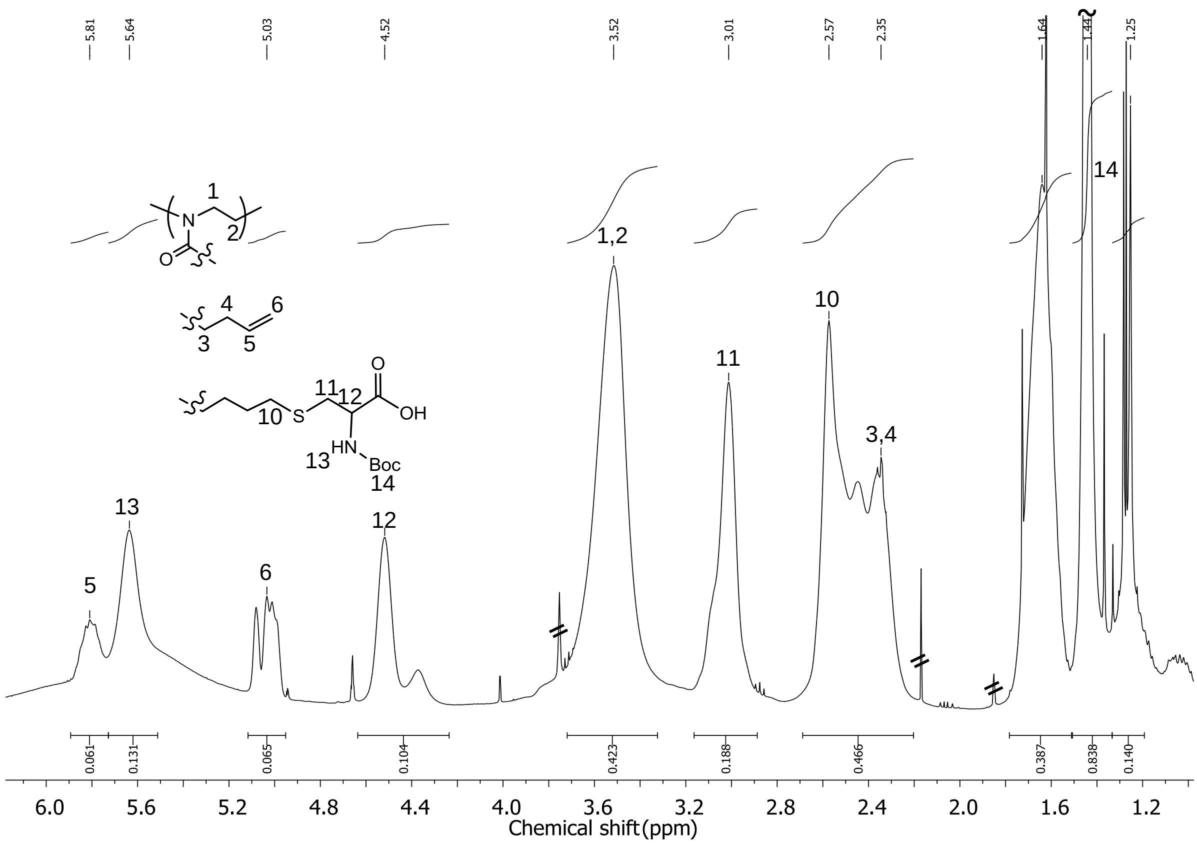

Figure S1. ^{1}H-NMR spectrum (400.1 MHz, CDCl$_3$, r.t.) of the PBOX/BocCys precursor

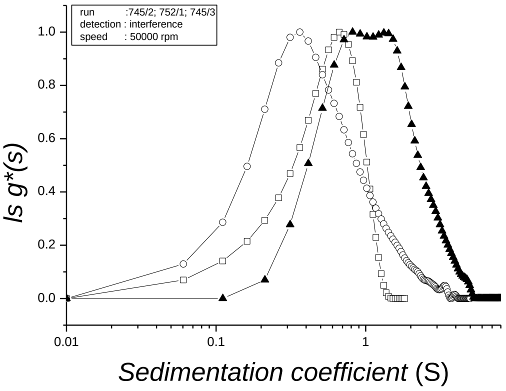

Figure S2. AUC sedimation coefficient distributions of PBOX/BocCys (□), DNA (○), and PBOX-g-DNA (▲) in water-ethanol 1:1 (v/v).

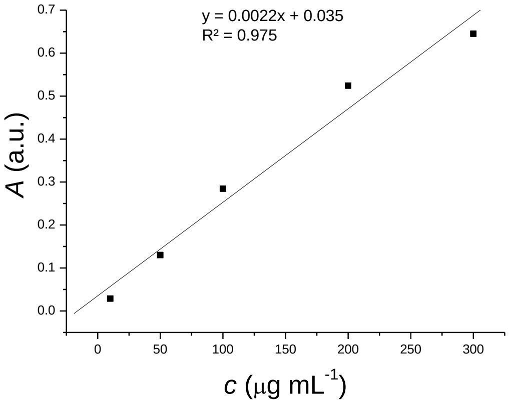

Figure S3. Absorbance calibration curve of the DNAat 260 nm.

For a representative quantification of the grafting density: absorbance value at 260; A_{260}= 0.101

Thus, concentration is equal to;

x= (0.101-0.0353)/0.0022= 29.9µg mL^{-1}

Concentration for measurement;0.1 $mgmL^{-1}$, volume; 1mL

m_{DNA}=29.9µg

$M_{PBOX/BocCys}$ =12612.5$gmol^{-1}$

M_{DNA}=3692.9 $gmol^{-1}$

$m_{PBOX/BocCys}$ = 100-29.9 =70.1µg

$n_{PBOX/BocCys}$=$70.1*10^{-6}$/12612.5= 5.56nmol

m_{DNA} =30.1µg

n_{DNA} = $30.1*10^{-6}$/3692.9 = 8.15 nmol

n_{DNA} /$n_{PBOX/BocCys}$ = 1.47 ≈ **1**DNA strand for one PBOX chain

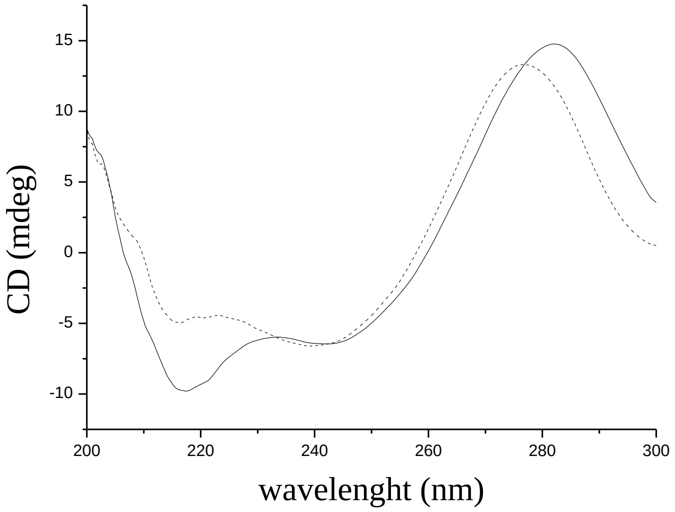

*Figure S4.*CD spectrum of DNA (dashed line) and PBOX-g-DNA (solid line)

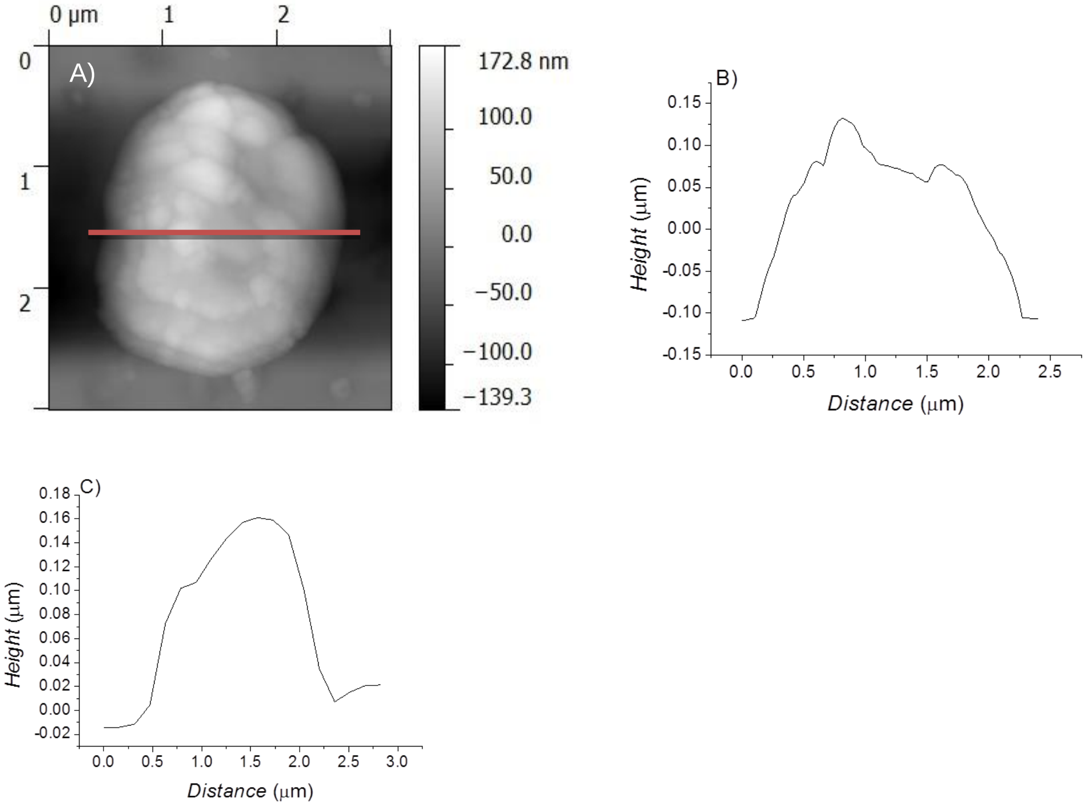

Figure S5. A) AFM imaging of initial globular structure and B) corresponding cross-sectional analysis, C) Fiber cross-sectional analysis

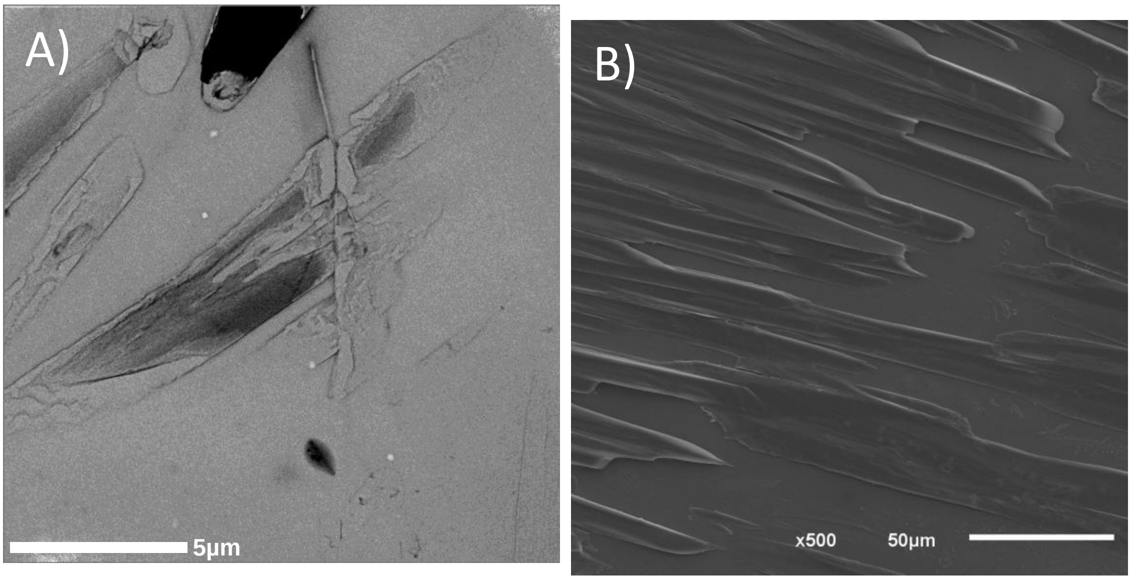

*Figure S6.*Imagingof fibers incubated with 0.1 M urea. A)TEM B)SEM shows disruption of fibrils.

5 Emulsions and emulsion templated self-assembly

5.1 Fundamentals

Blending two immiscible liquids with an emulsifier and addition of energy has been a topic of research for decades. In the early 90s this research area was explored extensively, which resulted in various theories and methods of preparation [239]. Emulsions have found applications in industry (especially in the food industry [29]) and medicine owing to their potential for encapsulation and delivery of active agents, alteration of rheological features; modification of optical characteristic, lubrication, ease of organoleptic properties adjustments [240, 241]. Generally, oil and aqueous phases are the two immiscible liquids used to obtain an emulsion. However, occasionally other immiscible liquids might be used. Three types of emulsion can be distinguished; macroemulsions, microemulsions and nanoemulsions (*Table 1*) [241]. The basic equation that describes the free energy necessary to disperse a liquid of volume V into droplets of radius R is given below [29];

$$\Delta G = \gamma \frac{3V}{R} \qquad \text{Equation 32}$$

Where, γ is the interfacial tension. From this equation, it can be concluded that reducing the interfacial tension, lowers the free energy and thus relative stabilization of the emulsion is achieved.

The droplet size of conventional emulsions is in a range from 100 nm to 100 μm and covered by a single layer of emulsifier (surface active agent) to prevent aggregation (*Figure 5-1*) [242]. Usually, macroemulsions are not thermodynamically stable due to the relatively high positive Gibbs free energy resulting from the contact between oil and water and they phase separate over time exposed to processes as Ostwald ripening, flocculation, coalescence and phase separation [242].

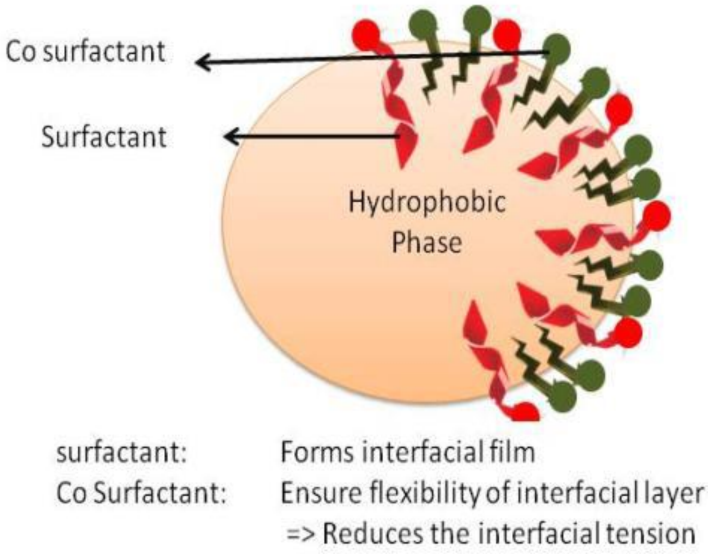

Figure 5-1 .Emulsion droplet [243]

Micro and macroemulsions can be formed in polymer blends as well. In that case, where block copolymer is used as a high molecular weight analogue of a surfactant to reduce the interfacial tension. In the ideal case, the interfacial tension is reduced to zero, which results in formation of thermodynamically stable emulsions [29].

Table 1. The characteristics of nano-, macro- and microemulsions [241].

Emulsion	**Radius range**	**Stability**	**Surface-to-mass ratio/m^2 g^{-1}**	**Appearance**
Emulsion	100 nm to 100 mm	Metastable	0.07–70	Turbid/opaque
Nanoemulsion	10–100 nm	Metastable	70–330	Clear/turbid
Microemulsion	2–50 nm	Stable	130–1300	Clear

5.1.1Theory of emulsion formation

Comparison between the free energy of an emulsion and an undispersed system can yield information about emulsion thermodynamic stability. The total free energy of an undispersed system (I) is equal to (*Figure 5-2*)[29];

$$G^I = G_1^I + G_2^I + G_{12}^I \qquad \text{Equation 33}$$

Where, G_1^I and G_2^I are free energies of liquid 1 and 2 and G_{12}^I is the excess of free energy related to the existence of a liquid-liquid interface, which is described by the following equation.

$$G_{12}^I = \gamma_{12} A^I \qquad \text{Equation 34}$$

Where, γ_{12} stands for interfacial tension and A^I is interfacial area.

The free energy term which describes the increase of configurational entropy resulting from droplets formation when liquid 2 is dispersed in the liquid by mechanical work is defined by following equation;

$$G^{II} = G_1^{II} + G_2^{II} + G_{12}^{II} - TS^{II\,conf} \qquad \text{Equation 35}$$

Expansion of the interfacial area requires free energy, which is partially offset by the $-TS^{II\,conf}$ entropic term. The configurational entropy can be approximately expressed as [244];

$$S^{II\,conf} = -Nk_B\left[ln\emptyset_2 + \left(\frac{1-\emptyset_2}{\emptyset_2}\right)ln(1-\emptyset_2)\right] \qquad \text{Equation 36}$$

Where *N* is the number of droplets, k_B is the Boltzmann constant and $\emptyset$ is the volume of the fraction of liquid 2. The bulk free energies of G_{12}^{II} and G_{12}^{I}do not change during the dispersion, hence the change of the free energy caused by emulsification is given by the following equation;

$$\Delta G^{dispersion} = G_{12}^{II} - G_{12}^{I} - TS^{II\,conf} = \gamma_{12}\Delta A - TS^{II\,conf} \qquad \text{Equation 37}$$

$$\approx \gamma_{12}A^{II} - TS^{II\,conf}$$

Where, ΔA is the increase in the surface area. Emulsion may be thermodynamically or kinetically stable, which is related to usually a positive free energy change in pure liquid systems. The minimal values of interfacial tension where emulsification arise is defined by ΔG=0, or

$$\gamma_{12}{}^{crit} = -\frac{k_B T}{4\pi r^2}\left[ln\emptyset_2 + \left(\frac{1-\emptyset_2}{\emptyset_2}\right) ln(1-\emptyset_2)\right] \qquad \text{Equation 38}$$

Where, r is the average radius of the drop. Addition of surfactant reduces the interfacial tension and hence the free energy to break up the emulsion. There are many kinds of emulsion with ΔG (dispersion)≤0, which form spontaneously.

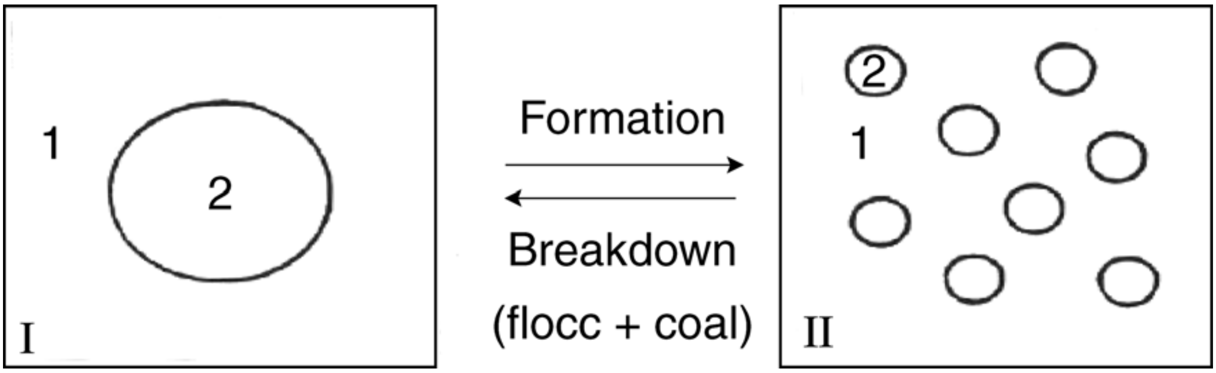

Figure 5-2. Emulsion formation and breakdown [245]

5.1.2Conventional emulsion

The list of the ways according to which emulsion droplet characteristics (*Figure 5-3*) (stability rheology, delivery, encapsulation and optical properties) can be adjusted is narrow;

- <u>Droplet properties</u>: Cautious choice of components and conditions of formation determine features of the droplet such as composition, concentration, physical state and the size distribution
- <u>Interfacial properties</u>; Careful selection of surface active components control thickness, electric charge, polarity rheology, responsiveness and permeability
- <u>Phase properties</u>; Selection of suitable oils and/or supplementation with additives of the oil or water phase like gelling agents, thickening agents, salts determine density, viscosity, refractive index of both phases.

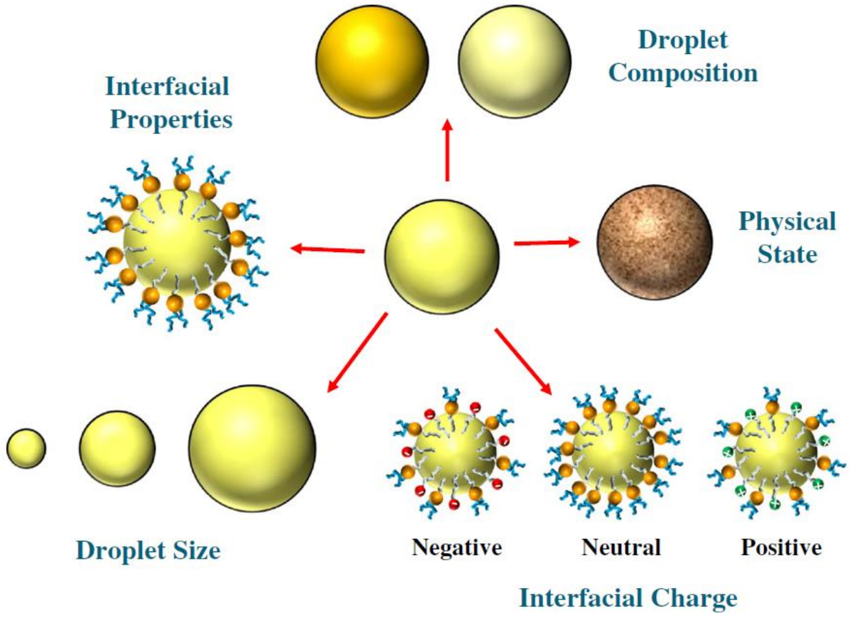

Figure 5-3. Size, charge and the droplet composition can be modified to obtain building moieties with various properties [242]. (Figure adapted with permission of Elsevier)

Use of the strategies mentioned above in order to tailor emulsion properties to specific applications is simple and economically beneficial, what is vital for industrial applications.

However, it has to be mentioned that not all modifications can be performed by use of these approaches [242].

5.1.3 Structured emulsion designing

In order to generate emulsions with original functional features, major advances were introduced.

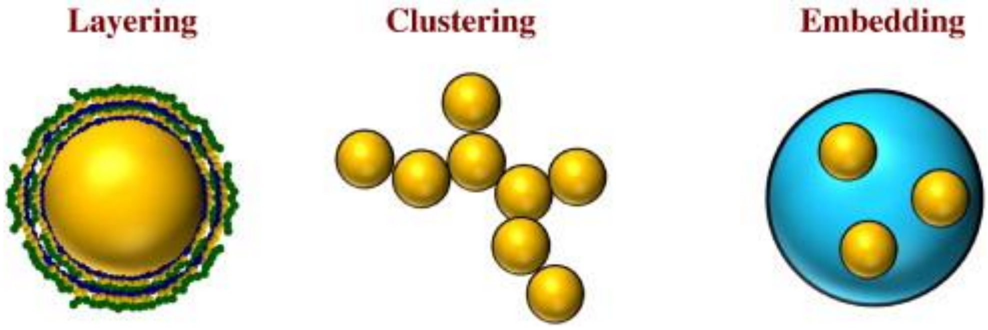

Figure 5-4. Strategies allowing emulsion with novel properties generation[242]. (Figure adapted with permission of Elsevier)

These methodologies can be divided as follows (*Figure 5-4*) [242];

5.1.3.1 Layering

Laminating coating such as oil droplets, solid particles or polymers can be used to tailor the functional features of emulsion based systems. Sequential deposition of oppositely charged polyelectrolytes, the so called Layer-by-Layer method provides an example of laminated coating [246].

5.1.3.1.1 Layer-by-Layer technique

Starting from 1992 when the LbL technique was introduced by Decher [247] this assembly of polyions or other charged molecular or colloidal object oppositely charged has attracted much attention due to its high potential in multilayered thin film formation with a wide range of electrical, magnetic and optical properties [248-251]. Polyelectrolytes [252, 253], proteins [254, 255], enzymes [256-258], charged organic molecules [259, 260] and nanoparticles [261, 262] are examples of the charged species which can used in the layer-by-layer deposition.

Polyelectrolyte multilayers are the most deeply and intensively studied examples of LbL assembly [263], which can be prepared either by dipping the surface in the solution [247] or spraying the compounds onto the substrate [264]. The general procedure for this technique is depicted in *Figure 5-5* below.

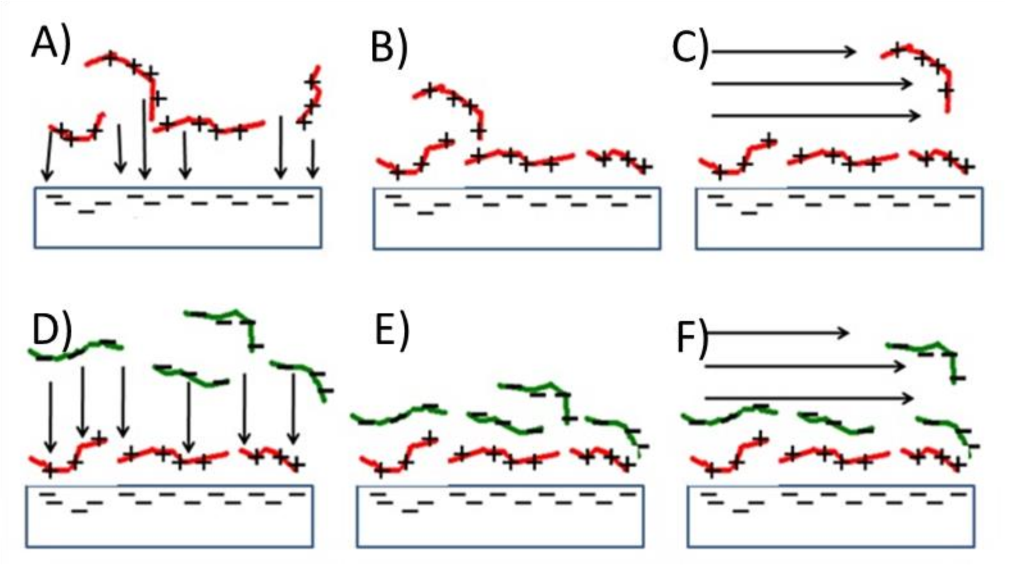

Figure 5-5. LbL thin film formation: Substrate placed in a solution coating oppositely charged species is A),B)covered by 1st electrolyte to form a 1st layer C) excess of electrolyte is removed throughout washing D)Substrate with one adsorbed layer is placed in the 2nd solution containing species oppositely charged to the 1st solution E) thus second layer is adsorbed F) excess of 2nd electrolyte is removed throughout washing. This cycle can be repeated until a layer of desired thickness is formed.

This template assisted assembly technique is much reliable and fast [265]. Spatial organization of the layers as well as characteristic of components determine the properties of multilayered composites, which can be tailored for many applications such as microchannel flow control [266], chemical or bio sensing [267-269], antireflective coatings [270], corrosion protection [271], batteries [272]. Environmentally friendly and ultra-low-cost are the few important advantages of this technique [265]. The LbL method can also be used for preparation of core-shell particles with tailored size and properties. The colloidal particle serves as a template onto which multilayers are assembled. Hollow capsules can be generated by subsequent removal of the core material (*Figure 5-6*). This versatile and simple technique allows the formation of multilayer films with a thickness which can be fine controlled by varying the total number of deposited layers [263].

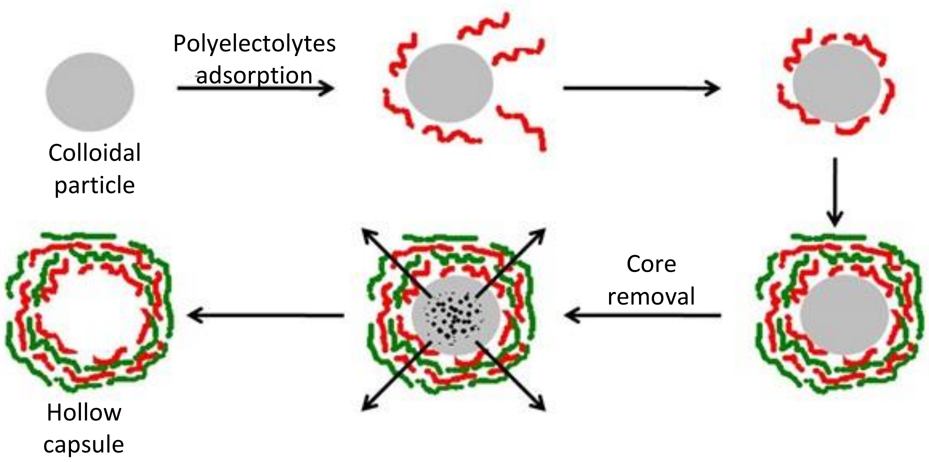

Figure 5-6. Schematic representation of hollow multilayered capsule formation with the use of LbL technique

5.1.4 Copolymers in the emulsification process

Directing the block copolymer self-assembly through combination with emulsification can result in a library of original architectures in which emulsion droplets serve as template. Emulsification provides a wide pool of possibilities to control the self-assembly process with the help of solvent evaporation (which causes the collapse of the block copolymer within the droplet or at its rim) and various parameters arising from emulsification such as confinement effects, interfacial tension etc. [35]

5.1.4.1 Emulsification in preparation of BCs based vesicles and capsules

Capsules originating from block copolymers is a topic which draws much attention due to possible medical applications [273]. Vesicles mainly composed of block copolymers and prepared in like liposomes are often called polymersomes. In addition to traditional methodologies such as film rehydration [274] or electroformation [275], polymersomes might be also formed through emulsification strategies like double emulsions or microfluidics [276-278]. Zehng and Liu [279] reported an example of a polymersomes-like preparation route with the use of an emulsion stabilized with the triblock copolymer poly(glyceryl methacrylate)-block-poly(2-cinnamoyloxyethyl methacrylate)-block-poly(tert-butyl acrylate). (*Figure 5-7*).

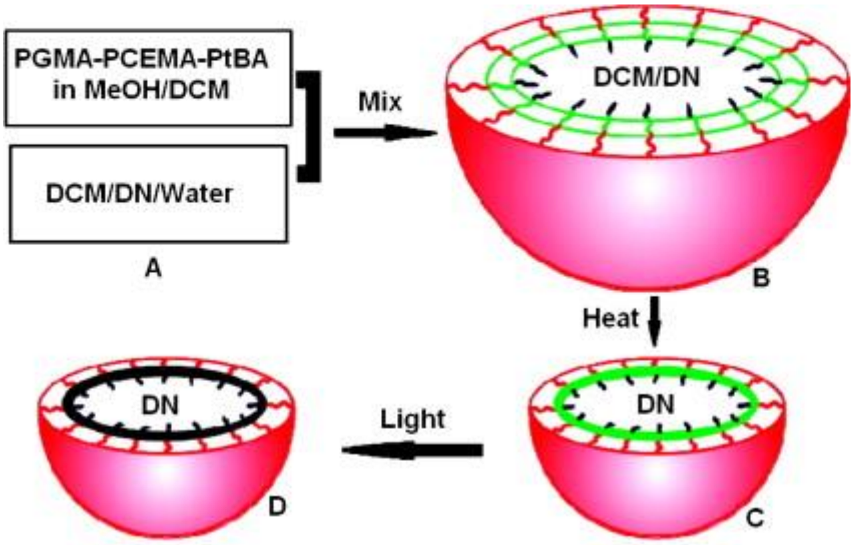

Figure 5-7. Vesicle preparation from PGMA-b-PCEMA-b-*PtBA triblock copolymer[279]. (Figure adapted with permission of ACS)*

In brief, solubilized copolymer (in the methanol/dichloromethane (DCM) mixture) was added to the oil/water mixture containing decahydronaphthalene (DN), DCM, and water. Due to the solubility properties of each block (PGMA-water soluble, PCEMA and PtBA water insoluble) the triblock copolymers organized at the oil/water interface and thus provide droplets stabilization. Subsequent DCM evaporation led to droplets containing only DN which further resulted in the collapse of the PCEMA block which was eventually photo-cross-linked entrapping the DN. Such nanocapsules are used to encapsulate hydrophobic molecules, while polymeric vesicles might incorporate aqueous species [280]. Needless to say, this structure is able to immobilize simultaneously hydrophobic as well hydrophilic agents (hydrophobic located within the polymersome wall and hydrophilic in the aqueous core) [281].

Thereof double emulsions are another strategy to obtain block copolymer vesicles. First step of this methodology concerns solubilization of the block copolymer in the volatile solvent followed by addition of water in order to form W/O emulsion. Further, the W/O emulsion is added to an aqueous phase, to generate a (W/O)/W emulsion. Eventually, the organic solvent is evaporated which leads to the collapse of the hydrophobic block (*Figure 5-8*). The assembled water-filled capsules with the walls composed of block copolymers have outward and inward hydrophilic corona exposed towards the aqueous phase [35].

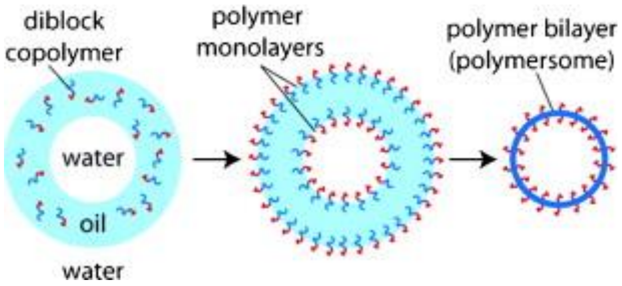

Figure 5-8. Schematic demonstration of polymersomes formation from a double emulsion [278].

5.2 Polymer-aptamer hybrid emulsion templating yields bio-responsive nanocapsules

(**the following subsection was adapted with John Wiley and Sons permission from "*Polymer-aptamer hybrid emulsion templating yields bio-responsive nanocapsules*" by D. Kedracki, P. Maroni, H. Schlaad and C. Nardin**, ***Advanced Functional Materials*** **(2014), 24(8), 1133-1139, Supporting Information with the figures mentioned in the text are placed at the end of this subsection**)

ABSTRACT. This article describes the synthesis of a DNA-polymer, being the nucleotide sequence an aptamer selected in vitro to target specifically the immunoglobulin E (IgE) protein, an allergy biomarker. Subsequent to coupling to poly(2-alkyl-2-oxazoline) with *N*-protected amino acid side chains, the resulting amphiphilic DNA-polymer hybrid composed of the water soluble DNA fragment grafted to the hydrophobic polymer segment can be regarded as a high molecular weight analogue of a surfactant. We demonstrate that the copolymer-aptamer stabilizes efficiently sub-micrometer size oil-in-water and water-in-oil emulsions, by dynamic light scattering (DLS), microscopy, and reflectometry. Particularly interesting is that the aptamer remains functional after coupling to a polymer backbone, stabilization of the emulsion droplets and locking of the structure subsequent to cross-linking polymerization. The resulting nanocapsules still target specifically the IgE protein. The biological-stimulus responsiveness of the structures is of high potential for future developments of carriers for sustained and targeted delivery.

1. INTRODUCTION

DNA-copolymers composed of either water soluble or hydrophobic polymer segments of various compositions are nowadays available through both organic and molecular biotechnology routes [111, 115, 117]. Amphiphilic DNA-polymer can self-assemble in aqueous solution into micelles of various shapes such as spherical core shell micelles [115, 117] or vesicles [111], which are closed spherical copolymer shells. Sizes in the sub-micrometer range could be achieved by this mechanism of micro-phase separation [111, 115, 117]. Of particular interest is Watson-Crick base pairing between complementary nucleotide sequences, which assemble to form a double helix through hybridization to enable further either structure manipulations such as stimulation of morphological transitions from spherical to rod-like micelles,[115, 117] immobilization of self-assembled structures on surfaces [282, 283] as well as chemical functionalization using a labeled complementary sequence to target cell surface receptors for instance [115, 117].

Besides hybridization, nucleotide sequences might however interact specifically with a target moiety. We ourselves observed a positive response of bacteria to surface-tethered nucleotide sequences and self-assembled structures thereof [282, 283]. Although no specificity of the nucleotide sequences towards *Escherichia Coli* could be expected, the bacteria produced curli, which are organelles of adhesion expressed upon interaction with surfaces coated with nucleotide sequences. Aptamers however are synthetic single stranded nucleotide sequences that undergo remarkable molecular recognition properties [284-287]. Binding affinities are comparable to those achieved with antibodies due to an efficient in vitro combinatorial strategy of selection called systematic evolution of ligands by exponential enrichment (SELEX), a major advantage over production of antibodies [284]. The specific and complex 3D shape of aptamers, which are short single-stranded nucleotide sequences (ssDNA or RNA) enables binding with high specificity to a wide variety of targets from single molecules to complex mixtures or whole organisms. We therefore describe herein the grafting of the aptamer against the immunoglobulin E (IgE), an allergy biomarker, to a hydrophobic polymer segment. Anti-IgE aptamers have been shown to block interactions with the IgE receptor with high affinity to inhibit IgE-mediated serotonin release from cells in tissue culture [284]. Anti IgE-apatmers might therefore prove to be useful for blocking local inflammatory responses mediated by IgE. With future biomedical applications in mind and the possibility to use methods developed in polymer science to investigate the system under consideration, we thus report in here the grafting of the IgE-aptamer to a poly(2-alkyl-2-oxazoline) with *N*-Boc protected amino acid and alkenyl side chains. This synthetic macromolecule is a bioinspired amphiphilic copolymer with a structural relation to polypeptides, which therefore reveals high potential for biomedical applications [187, 189, 190, 288]. Applying emulsification methodology to prepare liquid oil cores creates opportunity to encapsulate in an easy way active agents. High applicability of this technique to many different active agents makes it widely used in various fields like pharmacy, food and cosmetics [289]. Along this line, capsules resulting from the process of emulsification are of high interest since the resulting structures might enable the carriage of either water soluble or hydrophobic drugs respectively [290-293]. Moreover, emulsification is a technique which in combination with copolymer self-assembly can generate variety of structures with tunable shape, internal morphology as well as size by mean of controlling factors such as confinement effects, interfacial tension and others [35]. Towards this end, pickering emulsions have been prepared using ferritin-polymer conjugates that can undergo UV cross-linkage stabilization to enable the transfer of the soft protein-polymer capsules to media of equal polarity as the inside of the capsules [294]. Monodisperse poly(dopamine) polymer capsules could be prepared by one-step interfacial polymerization on dimethyldiethoxysilane emulsion droplets, being the template removed in a subsequent step [292]. Nucleotide sequences have been used for capsules preparation based on DNA hybridization as well [295]. To infer targeting properties to particles or capsules prepared by emulsification, such structures were functionalized with antibodies to target cancer cells.[296] In this context, the polyoxazoline-aptamer hybrid described herein is an amphiphilic grafted copolymer, which enables the stabilization of sub-micrometer size emulsions and the preparation of biological-stimulus responsive nanocapsules according to the definition given in a recent review [297]. The system described in here could indeed enable specific targeting owing to IgE biding in a ligand-receptor recognition mode.

2. RESULT AND DISCUSSION

The IgE-aptamer polymer hybrid has been synthesized by solid phase synthesis according to chemistry routes published previously.[1] Briefly, poly(2-alkyl-2-oxazoline) with pendant *N*-Boc protected amino acid and alkenyl side chains (PBOX/BocCys) (^{1}H NMR in *Figure S1*) was grafted to the 37 nucleotide-long aptamer sequence (5’-GGGGCACGTTTATCCGTCCCTCCTAGTGGCGTGCCCC-3’), which is modified at the 5’ end with an amine group by a hexyl spacer and linked to the controlled pore glass (CpG) phosphoramidite solid support at the 3’ end **(***Scheme 5-1***)**. The carboxylic acid group at the PBOX/BocCys was first activated by *N,N*'-diisopropylcarbodiimide (DIC) to react with the aptamer. After the coupling reaction, the resin is washed thoroughly with DCM and DMF, filtered out prior to cleavage with liquid ammonia to yield the final product further purified by dialysis (MWCO 14 kDa) and finally lyophilized.

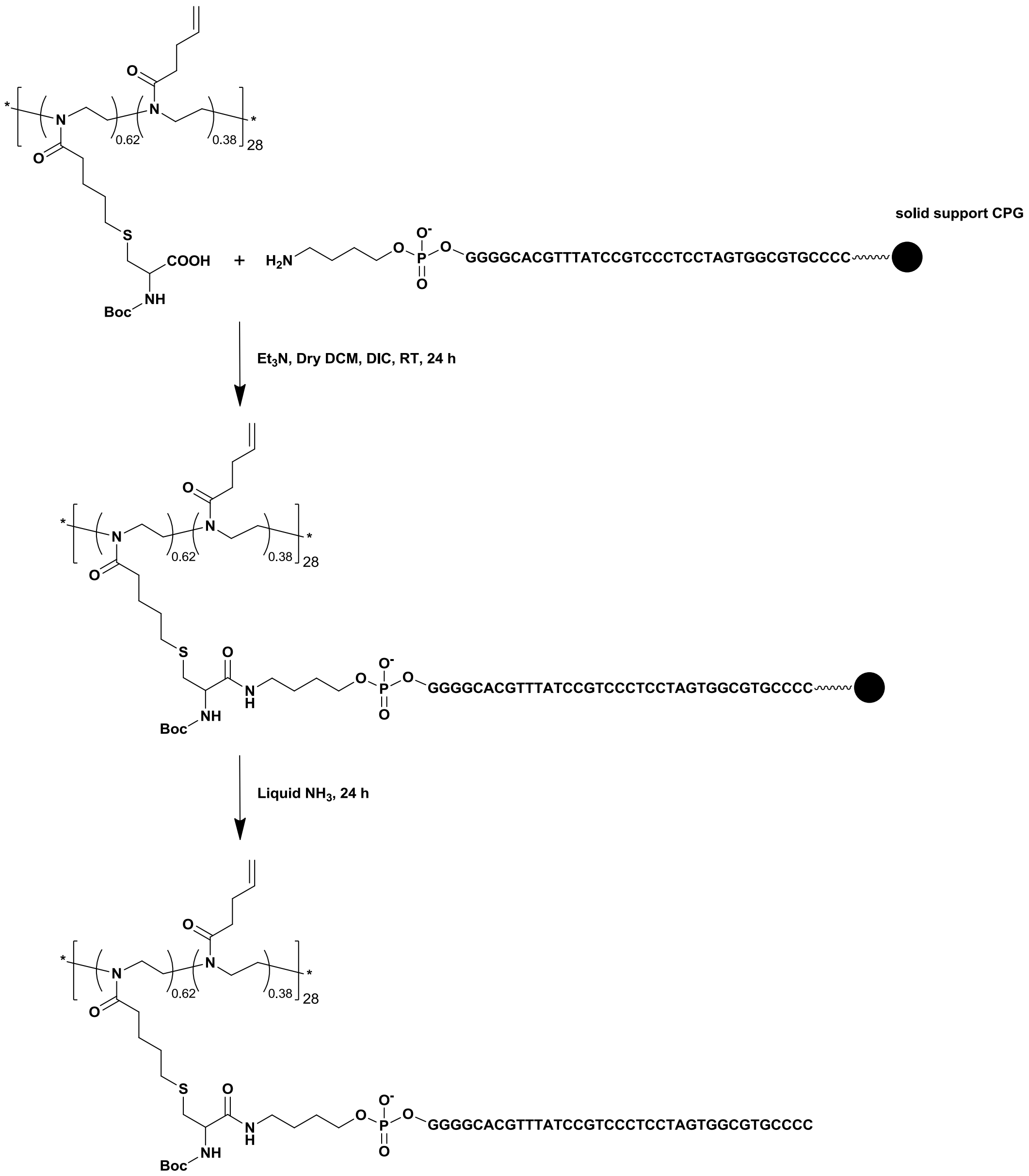

Scheme 5-1. Synthesis of the PBOX-aptamer hybrid by solid phase synthesis.

Analyses by analytical ultracentrifugation (AUC sedimentation-velocity, *Figure S2*) support the success of the solid phase synthesis route, in particular that of the purification stage. UV-Vis spectroscopy (*Figure S3*) indicates that every polymer chain carries in average two aptamer sequences, hence the PBOX-aptamer is a macromolecule of ~30.2 kDa with a hydrophilic weight fraction of 75%. It is worth being mentioned that, due to the high hydrophilic weight fraction, the PBOX-DNA does not exhibit temperature sensitivity, as indicated by the absence of turbidity change in the temperature range of 20-60 °C.

Although of high hydrophilic weight fraction, the PBOX-aptamer is composed of a hydrophobic PBOX backbone along which are grafted the water soluble aptamers. The macromolecule can thus be regarded as a high molecular weight analogue of a surfactant with the major advantage of being constituted of a bioinspired biocompatible synthetic polymer segment coupled to a biological stimulus-responsive nucleotide sequence. The surface activity of the PBOX-aptamer could indeed be assessed by monitoring surface pressure isotherms (*Figure S4***)**. This surface activity of the PBOX-aptamer thus enables the stabilization of both oil-in-water (o/w) and water in oil (w/o) emulsions to design biological stimulus responsive nanocapsules.

100 μL of a 10% dodecane solution of the copolymer-aptamer was added dropwise to 20 mL of water and subsequently exposed to ultrasounds (ultrasonic probe, time 5 min, amplitude 35%) in order to break the continuous phase. The resulting droplets were imaged by confocal laser scanning microscopy (CLSM) subsequent to encapsulation of a hydrophobic dye (Nile red) dissolved in dodecane along with the PBOX-aptamer (*Figure S5*). Imaging demonstrates the formation of oil-in-water droplets. The emulsion was further filtered through 0.2 μm pore-size LCR filter membranes to decrease both the size and the size distribution, to subsequently perform dynamic light scattering (DLS) in order to quantify the size and the stability of the emulsion prior and subsequent to stabilization with the PBOX-aptamer. The emulsion is stable in time as assessed by DLS. An aggregation rate of -1.2×10^{-19} m^3s^{-1} clearly evidences that the 100 nm average size droplets are stabilized by the PBOX-aptamer hybrid. At high ionic strength (1 M KCl) this aggregation rate is of 9.4×10^{-20} m^3s^{-1} to be compared to the 1.2×10^{-17} m^3s^{-1} theoretical value of the fast or diffusion controlled aggregation of an unstable, rapidly aggregating system [298, 299]. Stability is further supported by the value of the surface charge. Zeta potential value of –56.5 mV is suitable to induce repulsion between the negatively charged copolymer stabilized capsules and prevent aggregation [300]. At this

stage, the question that is raised is whether this aptamer remains functional subsequent to coupling to the polymer and emulsification. Since the chosen aptamer has been selected against immunoglobulin E (IgE), a first set of experiments were conducted with fluorescently labeled proteins. Oil-in-water emulsions were therefore at first stabilized with the copolymer-aptamer and incubated for one hour with fluorescein isocyanate (FITC) labeled IgE prior to CLSM (*Figure 5-9, Figure S6A and B*). As can be observed, IgE is localized at the rim of the dodecane droplets in water. However, in the case of water-in-oil emulsion, the aptamer points towards the inner core of the structure (*Figure S6C*), which is fluorescent subsequent to binding to the FITC-labeled IgE protein.

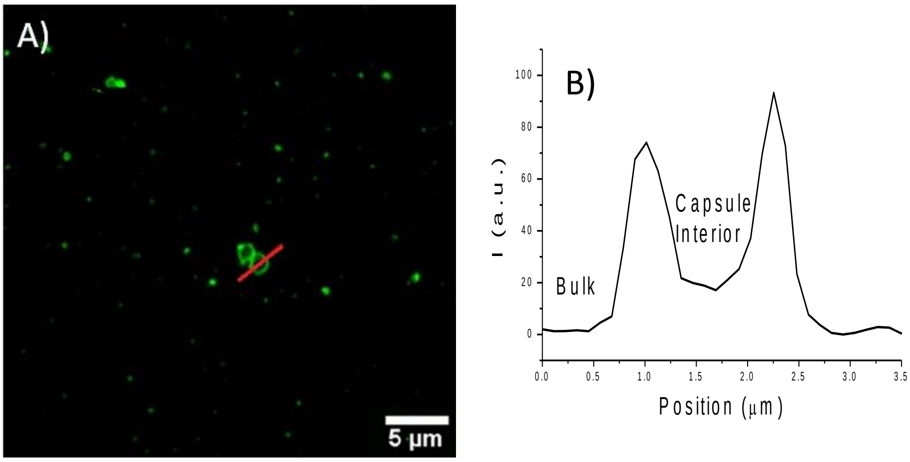

Figure 5-9. Confocal laser scanning microscopy of the A) Oil-in-water emulsion stabilized by the PBOX-aptamer, incubated with FITC labeled IgE and B) corresponding fluorescence intensity profile, which evidences that the IgE protein is located at the rim of the droplet.

These primary results evidence that the aptamer remains functional subsequent to coupling to the polymer and engagement in the stabilization of the emulsion. Nevertheless, efficiency of binding might be hindered by intermolecular interactions owing to steric hindrance upon organization at the interface. To overcome this limitation, we further resorted to a method we established to achieve optimal functionality of surface tethered nucleotide sequences [201]. Briefly, the PBOX-aptamer is incubated with its target, the IgE protein, prior to emulsion stabilization. Fluorescence of the outer rim of the droplets could also be observed by CLSM (*Figure S6D*).

To assess the specificity of binding of the PBOX-aptamer engaged in the emulsification process, reflectometry was eventually combined to atomic force microscopy (AFM) imaging. Emulsions stabilized with either the PBOX-aptamer or a non-specific PBOX-DNA were incubated with a surface modified with either IgE or BSA. As it can be seen on the time course monitoring of the adsorption of the emulsion (*Figure 5-10 A*), mass increase is detected when the emulsion is stabilized by the PBOX-aptamer and the surface-coated with IgE up to an average value of 1.01 mg m^{-2} whereas on a BSA coating, no adsorption occurs (*Figure 5-10 A*). Similarly, with a nucleotide sequence which has no specificity of binding to IgE, no adsorption could be detected (*Figure 5-10 B*).

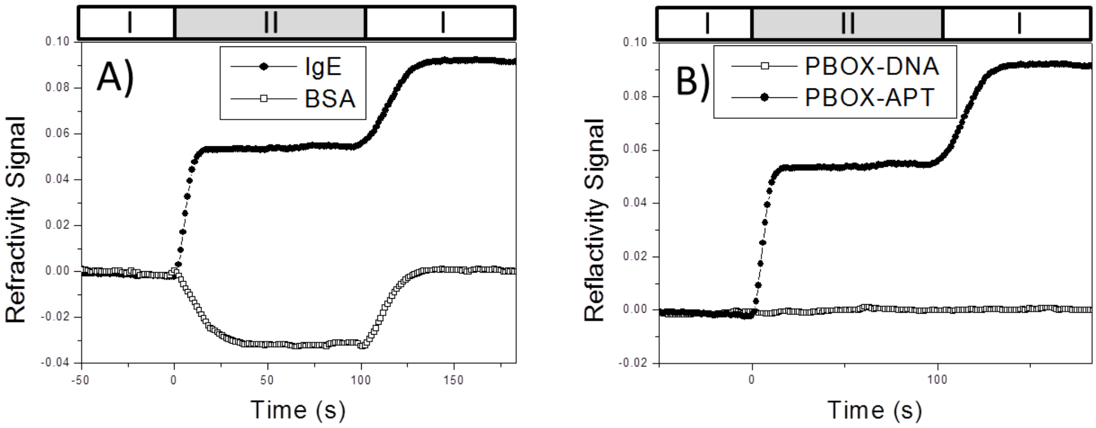

Figure 5-10. Representative time course of the refractive index as measured by reflectometry upon adsorption of the PBOX-aptamer stabilized emulsion adsorption on A) silica modified with □) BSA (non-target protein of the aptamer), ●) IgE aptamer target. B) Adsorption of emulsion droplets on IgE modified silica stabilized by □) PBOX-DNA (the sequence is not specific to the IgE protein), ●) PBOX-aptamer. The surface is initially flushed with a 15 mM NaCl buffer solution (I). At time zero, a 10 times diluted filtered emulsion solution in 15 mM NaCl is introduced (II) and eventually, the surface is again flushed with the buffer solution (solution I).

This specificity of binding has been further assessed by AFM. As can be observed in Fig. 3, the PBOX-aptamer stabilized emulsions could be located on a surface coated with the IgE protein whereas no structures could be detected when the emulsion is stabilized with a PBOX-DNA that has no specificity to IgE (*Figure S7*). Imaging by AFM further evidences the robustness of the emulsion stabilization by the PBOX-aptamer. The droplets collapse without disruption as evidenced by a 40 nm height as compared to the 100 nm size of the structure in solution as quantified by DLS (*Figure S8*). Although specific interaction occurs between the surface and the droplets, the emulsion droplets immobilized on the surface shrink but are not disrupted (*Figure 5-11 B, C*).

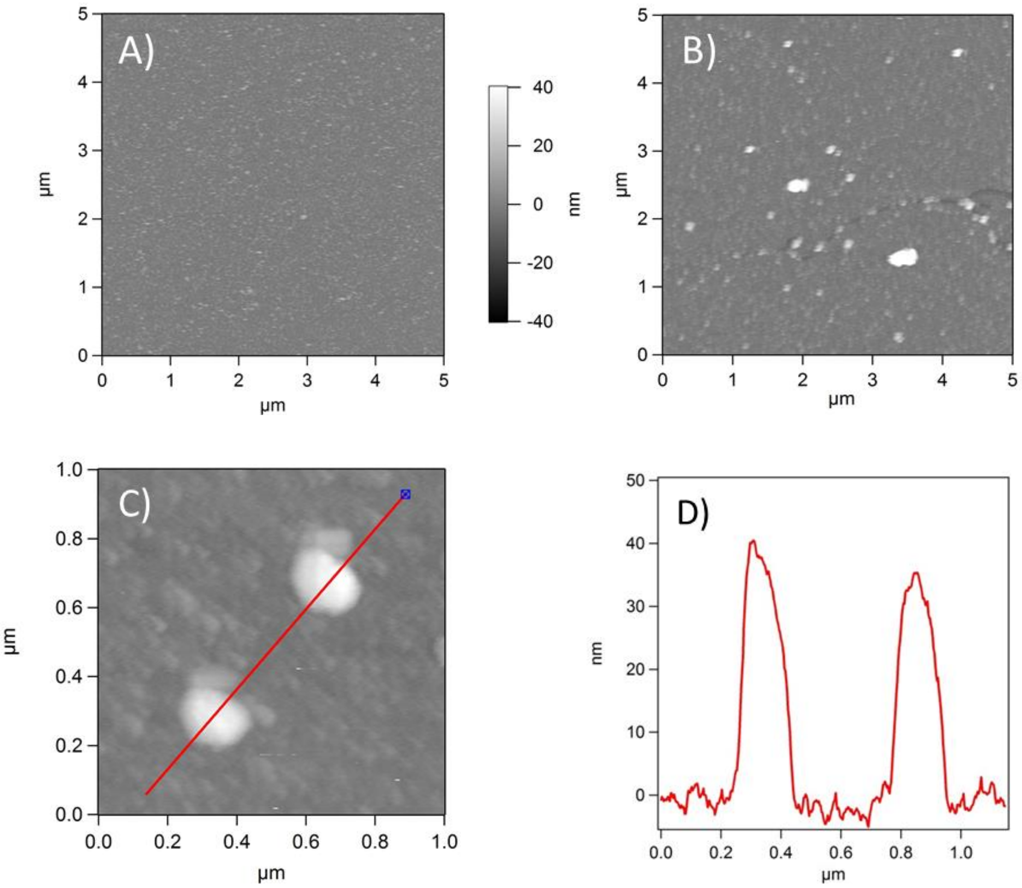

Figure 5-11. Adsorption of the PBOX-aptamer stabilized emulsion as observed by atomic force microscopy. A) IgE coated silica B) PBOX-aptamer stabilized emulsion adsorption on IgE modified silica, C) soft emulsion droplets of the PBOX-aptamer are stable. D) Corresponding height profile (same height scale for all micrographs).

Further stabilization could be achieved by UV-irradiation of the cross-linkable pendant groups which were not modified with cysteine for subsequent grafting to the aptamer sequences. 11 vinyl pendant groups are therefore available in average per PBOX backbone for an eventual cross-linking polymerization step. As it can be seen in *Figure 5-12 A, B* and *Figure 5-13*, this final stabilization step enables imaging by both scanning and transmission electron microscopy (SEM and TEM respectively) which is otherwise not possible with the pristine soft emulsion.

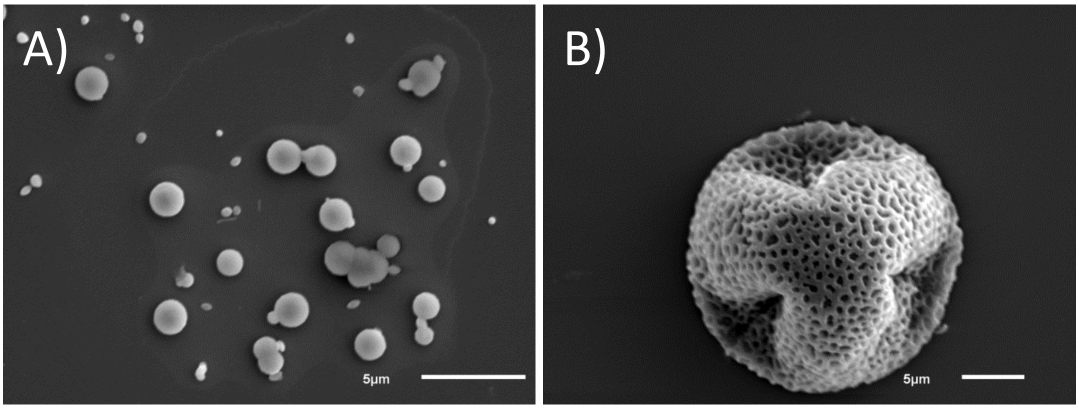

Figure 5-12. Scanning electron micrographs of PBOX-aptamer capsules after cross-linking by irradiation with UV light A) Cross-linkage is performed subsequent to filtration B) large porous structures are observed (owing to the organic solvent evaporation in the vacuum of SEM) when no extrusion is performed to reduce the size and fusion of the droplets might occur.

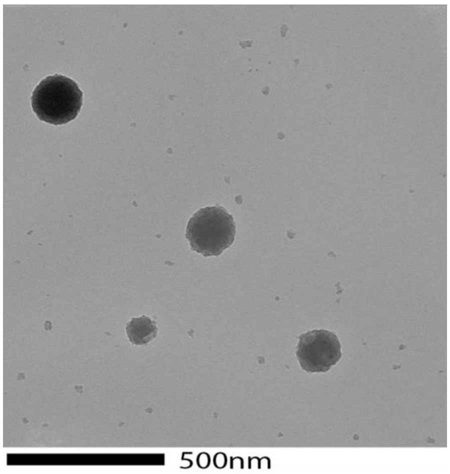

*Figure 5-13**.** Transmission Electron microscopy image of cross-linked PBOX-aptamer spheres (filtered before cross-linking polymerization).*

Since this cross-linking step occurs at the oil water interface, the function of the aptamer is not affected. The cross-linked structures could be located on a surface modified with the IgE aptamer target (*Figure 5-14*), which indicates that the aptamer remains functional and binds to the protein subsequent to sequential grafting to the polymer, emulsion stabilization and cross-linkage to achieve stable biological stimulus responsive capsules. In vivo, this stabilization is crucial since it would slow down the degradation of the capsules by nucleases and proteinases, which would leave either structure of small size or polymer backbones of low molecular weight that could be cleared out by the renal system. Cross-linkage might occur between the droplets, inducing their fusion into large microspheres at the surface of which one can observe porosity probably induced by the evaporation of the organic solvent (*Figure 5-12 B).*

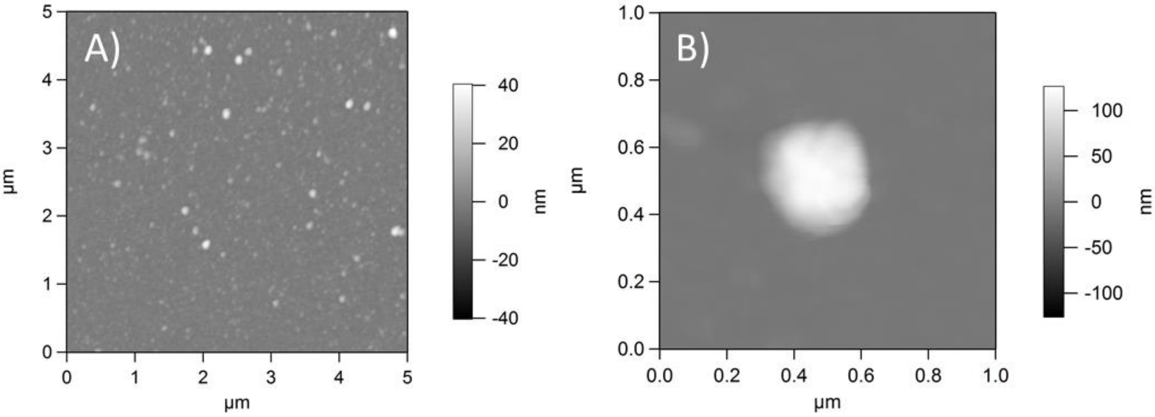

Figure 5-14. Adsorption of the cross-linked emulsion on IgE coated silica A) 5x5 µm, B) 1x1 µm micrographs obtained by atomic force microscopy.

3. CONCLUSIONS

Coupling of the IgE aptamer to PBOX has been conducted through solid phase synthesis. The resulting amphiphilic copolymer-aptamer efficiently stabilizes oil-in-water and water-in-oil emulsions. Further stabilization could be demonstrated subsequent to an UV induced crosslinking polymerization step. Engagement of the aptamer in the emulsion stabilization does not hinder its specificity of binding to its target, which paves the way for further developments of capsules for sustained and targeted delivery through the synergistic combination of site specific aptamer recognition of the encapsulated load. The quantification of the aptamer binding kinetics and affinity to its target subsequent to polymer coupling and emulsion stabilization is currently under investigation.

Experimental

Materials: Dichloromethane (DCM) (extra dry, 99.8%), *N,N*-dimethylformamide (DMF) (99.8%), sodium chloride (>99.5%), triethylamine (99%) were purchased from Acros Organics (Geel, Belgium). *N,N′*-diisopropylocarbodiimide (>98%), dialysis tube (molecular weight cut-off , MWCO 14 kDa), dimethoxy(methyl)octyl silane were supplied by Sigma Aldrich (Buchs, Switzerland). The ammonia solution 35% was purchased from Fisher Scientific SA (Wohlen, Switzerland). Dodecane (99%) was provided by Alfa Aesar (Zürich, Switzerland). 5’-GGGGCACGTTTATCCGTCCCTCCTAGTGGCGTGCCCC-3’ (5’-G11C14A3T9-3’,”Aptamer”) and 5’-CTCTCTCTCTTT-3’ (5’-C_5T_7-3’,”DNA”) modified at the 5’ end through a C_6 hexyl spacer with an amine group was purchased from Microsynth Laboratory (Balgash, Switzerland). Immunoglobulin E (IgE) labelled with FITC and albumin from bovine serum (BSA) were supplied by Invitrogen (Zug, Switzerland). Poly(ethylene imine) (PEI, nominally 40,000 $gmol^{-1}$) was purchased from Polysciences (Eppelheim, Germany). LCR 0.22 μm pore size syringe filters were purchased from Merck Millipore (Zug, Switzerland). Zeta cells were provided by Instrumat SA (Lausanne, Switzerland). Silicon wafers single side polished, orientation N/Phos < 100 >, (625±25) μm thickness, 1-50 Ohm cm resistivity were purchased from Silchem (Freiburg, Germany).

Poly[2-(3-butenyl)-2-oxazoline] (PBOX) was prepared by cationic ring-opening isomerization polymerization of 2-(3-butenyl)-2-oxazoline as described in the literature.[4a] The isolated PBOX sample had a number-average molecular weight (M_n) of 3.5 kDa (corresponding to an average number of 28 repeat units) (^{1}H NMR) and a dispersity index (M_w/M_n) of 1.05 (SEC). *N*-(*tert*-butyloxycarbonyl)-L-cysteine (BocCys) (Merck) was then partially added to the alkenyl groups of PBOX via thiol-ene photochemical reaction.[4a] ^{1}H NMR analysis (**Fig. S1**) of the purified product, PBOX/BocCys, revealed that 62% of the unsaturated units were functionalized with the *N*-protected amino acid (~17 units per chain) and 38% remained unreacted (~11 units); see the chemical structure in *Scheme 5-1*(top left).

The syntheses of PBOX-aptamer and PBOX-DNA are described in the supporting information section. Milli-Q water was used in all cases.

Methods

Analytical Instrumentation. ^{1}H NMR measurements were carried out at room temperature using a Bruker DPX-400 spectrometer operating at 400.1 MHz. Reflectometer Abbemat WR MW(Anton Paar, Germany) was used to determine the refractive index increment (dn/dc) of the PBOX-aptamer. UV-Vis spectra were registered on a Perkin Elmer Lambda 900 in a quartz cuvette of 1 cm path length for all measurements. Size exclusion chromatography (SEC) with simultaneous UV and RI detection was performed in *N*-methyl-2-pyrrolidon (NMP + 0.5 wt % LiBr) at +70 °C, flow rate: 0.8 mL min^{-1}, column set: two 300 × 8 mm^2 PSS-GRAM (7 μm spherical polyester particles) columns with porosities of 10^2 and 10^3 Å. Calibration was done with polystyrene standards. Analytical ultracentrifugation (AUC) was performed on an Optima XL-I ultracentrifuge (Beckmann-Coulter, Palo Alto, CA) equipped with Rayleigh interference optics. Sedimentation-velocity experiments were done with 1 mg mL^{-1} solutions of polymer in water/ethanol 1:1 (v/v) at a rotational speed of 50 krpm at 25 °C. Hydrodynamic sizes (diameter) of the emulsion droplets were assessed by dynamic light scattering (DLS) at 25 °C using a Zetasizer Nano Series from Malvern Instruments with the backscattered angle detection at 173° in optically homogeneous square polystyrene cells. The zeta potential of emulsion droplets was measured by the micro electrophoretic method using a Malvern Zetasizer Nano ZS apparatus. Surface pressure isotherms were conducted on an R&K Langmuir Through (Freiburg, Germany). For this measurement, a 1 mg mL^{-1} copolymer solution in chloroform was prepared. All measurements were carried out at 292 K.

Emulsion Preparation; 4 mg of PBOX-aptamer was dissolved in 100 μL of dodecane and left under stirring for 24 h. Subsequently, the copolymer solution was added to 20 mL of a 15 mM NaCl solution and exposed to ultrasounds in order to break the organic phase (Branson Sonifier Digital 450, Zurich, Switzerland) during 2 min, amplitude 35%, max temp; 40 °C, impulse on; 1 s, impulse off; 1 s. The resulting emulsion was filtered through 0.2 μm pore size LCR non-protein binding filters in order to decrease the size and size distribution prior to the determination of the hydrodynamic radius and zeta potential of the droplets.

Reflectometry; 5 10^{-3} g L^{-1} protein (IgE) solution was prepared in 15 mM NaCl buffer solution. All substrates (silicon pieces with dimensions of 1.2 x 0.5 cm) were cleaned in a 3:1 solution of concentrated sulphuric acid and 30% hydrogen peroxide for 30 min, washed with Milli-Q water and dried under nitrogen. Afterwards, the precise thickness of the native silica layer (average thickness = 1.2 nm) was determined by null ellipsometry (Multiskop, Optrel, Berlin, Germany).[301] Subsequently, to induce physical adsorption of proteins on the substrates, plates were placed in an IgE solution for 24 h. Later on, substrates were extensively washed with a buffer solution (15 mM NaCl aqueous solution) in order to remove the excess of protein. Subsequently, ellipsometry was again performed to measure the thickness of the adsorbed protein layer (average thickness = 3.82 nm). In order to determine the thickness of the protein layer, a fixed value of refractive index was used, equal to the SiO_2 refractive index. Binding of the PBOX-aptamer stabilized emulsion to protein was quantitatively assessed by reflectometry measurements, conducted on a home-built fixed-angle reflectometer which allows determination of the adsorbed dry mass.[150, 151] The average sensitivity value was equal to 0.054 m2 mg-1 with a dn/dc value of the PBOX-aptamer of 0.075 ml g^{-1}. In brief, after IgE adsorption, the silicon, plate was placed in the cell and the system washed with a buffer solution (solution I). Subsequent to signal stabilization, the solution of filtered dodecane emulsion stabilized by the PBOX-aptamer copolymer (solution II) was pumped into the cell and the change of refractivity signal (which is proportional to the adsorbed mass) was measured. After signal stabilization, buffer solution was again pumped into the cell (solution I), in order to verify if mass desorption would occur. The refractivity signal indeed increased due to the high refractive index difference between the emulsion and buffer solutions. The real adsorption value is thus obtained after buffer washing. Detailed description of the set up and analysis is given elsewhere [150, 151].

Blank experiments, with substrates modified with BSA instead of the IgE protein and dodecane emulsion stabilized by PBOX-C_5T_7 instead of PBOX-aptamer, were conducted in the same manner. All solutions were degassed under vacuum.

Atomic Force Microscopy (AFM); Samples for AFM were prepared by the same procedure as for reflectometry. However, in order to adsorb emulsion droplets, substrates were dipped in the emulsion solution for 5 min and subsequently gently washed with the buffer solution. AFM images were acquired with a Cypher AFM (Asylum Research, Santa Barbara, CA) operating in the AC-mode. Biolever mini AC40TS cantilevers (Olympus, Japan) with a nominal tip radius smaller than 9 nm were used for recording images in liquid. These probes have spring constants of around 0.1 N m^{-1} and resonance frequencies in liquid of around 25 kHz. The free oscillation amplitude (FOA) and the scan rate were set to 40 nm and 4.88 Hz respectively. The set point used varied between 60 and 70% of FOA. The data acquisition and analysis were operated with the Asylum Research software, delivered with the AFM instrument.

Scanning electron microscopy (SEM); A 10 μL of the fresh crosslinked emulsion solution was dried at room temperature on silicon wafers. Dried samples were coated with gold for 20 s in a Jeol JFC-1200 Fine coater. Subsequently, SEM images were acquired on a Jeol 6510LV microscope, equipped with a tungsten filament gun, operating at WD 10.6 mm and 10 kV.

Transmission Electron Microscope (TEM); For TEM, 5 µL of fresh sample was placed on a carbon coated 400-mesh copper grid. After sample drying, the sample was imaged without staining directly with a Tecnai G2 electron microscope operating at 120 kV.

Confocal laser scanning microscopy(CLSM); In order to visualize protein interaction with oil-in-water emulsions stabilized by the PBOX-aptamer, 250 µL of FITC-IgE solution was directly added to 250 µL of the original non filtered PBOX-aptamer emulsion (100 times diluted), stirred on vortex and co-incubated for 1 h at 4°C (**Scheme S1A)**. To enable imaging, immobilization of the emulsion droplets on glass slides was ensured by modification of the glass surface with positively charged poly(ethylene imine) (PEI) ($5 \cdot 10^{-3}$ g L^{-1}) since the outer layer of droplets is composed of the negatively charged aptamer. In brief, the solution of PEI was spread on the microscopy glass slide and left for adsorption for 5 minutes. Afterwards, the glass surface was extensively washed with Milli-Q water and 10 µL of the PBOX-aptamer stabilized emulsion incubated with FITC-IgE was spread on the glass slide, covered by the cover glass and observed by microscopy. In order to observe reverse emulsions, a 5% solution of PBOX-aptamer copolymer was prepared in a protein solution and incubated at 4°C for 1 h. Subsequently, the mixture was added to 2 mL of dodecane and stirred vigorously (1500 rpm) to induce emulsification. In this case, the hydrophobic PBOX is located at the outer rim of the droplet (**Scheme S1B)**. To enable immobilization of the droplets, microscopic glass slides were silanized with dimethoxy(methyl)octyl silane. Briefly, glass slides along with 100 µL of dimethoxy(methyl)octyl silane were kept in a petri dish for 3 h under vacuum. Consecutively 10 µL of the reverse emulsion with FITC-IgE was spread on a modified glass slide, covered with a cover glass and imaged under a Zeiss LSM 700 confocal microscope (with laser excitation at 488 nm, lens 100x 1.4NA).

Acknowledgements

The Swiss National Science Foundation (SNSF PPOP2-128380) and the University of Geneva are greatly acknowledged for the financial support. We are thankful for the experimental support of Prof. Michal Borkovec, Dr. Bauer (Bioimaging platform from the University of Geneva), Prof. A. Zumbuehl (University of Fribourg), Dr. N. Gour, Dr. K. X. Ngo, Dr. J. Nixon, BSc F. Chevasson, MSc Mahshid Chekini and MSc I. Safir .

The authors are as well thankful for the scientific support of Nora Fiedler (polymer synthesis and NMR), Marlies Gräwert (SEC), and Antje Völkel (AUC) (MPI-KG).

Supporting Information
Synthesis and characterization:

In brief, the carboxylic group of Boc-cysteine modified poly[2-(3-butenyl)-2-oxazoline] was activated by N,N′-diisopropylocarbodiimide, according to a procedure reported earlier.[234] The activated ester is subjected to a nucleophilic attack at the free 5‘-amino group of a 37-mer aptamer (sequence 5’-GGGGCACGTTTATCCGTCCCTCCTAGTGGCGTGCCCC-3’) modified at the 5’ end by an amine group through a hexyl C_6 linker whereas the 3’ end remains bound to the controlled pore glass (CPG) solid support. Solid phase synthesis was chosen to avoid tedious steps of chemistry or purification. Finally the solid support and protecting groups were removed by treatment with liquid ammonia. The resulting compound was characterised by UV/VIS spectroscopy, and analytical ultracentrifugation.

Conjugation of amino modified 5’-GGGGCACGTTTATCCGTCCCTCCTAGTGGCGTGCCCC-3’ to N-Boc-cysteine modified poly[2-(3-butenyl)-2-oxazoline]. Boc-cysteine modified poly[2-(3-butenyl)-2-oxazoline) (2 µmol, 14.5 mg, 1 eq), was dissolved in 1.5 mL of dry DCM and transfered to a 2 mL reactor, prior to addition of 6.8 µL of DIC (40.8 µmol, 5.1 mg, 1.2 eq in respect to the number of PBOX side chains modified with cystein). The reactor was placed in a mechanical shaker for 1h at room temperature Subsequently, 250 mg of solid cpg-resin bound aptamer 5’-GGGGCACGTTTATCCGTCCCTCCTAGTGGCGTGCCCC-3’ modified at the 5’ end with an amine group through a C_6 amino linker (250 mg, 10 µM, 5 eq) was added to the reactor. To this, 40 µL of triethylamine were appended. The reactor was closed and shaked at room temperatur overnight. The 2 mL reactor is fixed to a filter at the bottom which prevents filtration of the resin out but enabling that of solvents. All residual solution was thus drained out from the reactor and the resin washed thoroughly with DCM and DMF and subsequently again with DCM to remove any unreacted species and other side products using syringe pressure filtration. Finally the resin was dried in presence of nitrogen and weighed in an eppendorf tube.

Removal of the cpg solid support. The oligonucleotide bound to the solid support obtained in the previous step was transferred to an eppendorf tube and subsequently 1.5 mL of ammonia solution was added and the resulting mixture kept in a shaker maintained at 40 ^oC for 24 h. The solution was then filtered to remove the resin and the supernatant collected. Subsequently this solution was transferred to a dialysis membrane (14000 MWCO) to remove unreacted species, salts and protecting groups. The dialysis membrane was slowly stirred against milli-Q water for 3 days. Subsequently the solution was filtered through 0.45 micron filter membranes and lyophilized. Yield 6.5 mg (45% reaction yield). The resulting compound was characterised by UV-VIS and AUC.

UV-Vis grafting density estimation. We resorted to UV-Vis spetrocopy to estimate the grafting density of aptamer along the PBOX backbone. This estimation was possible due to the fact that the poly(oxazoline) absorbance is negligible at 287 nm. With in mind the estimation of the grafting density, the calibration curve with various concentration of the aptamer was established at first (**Figure S3**).

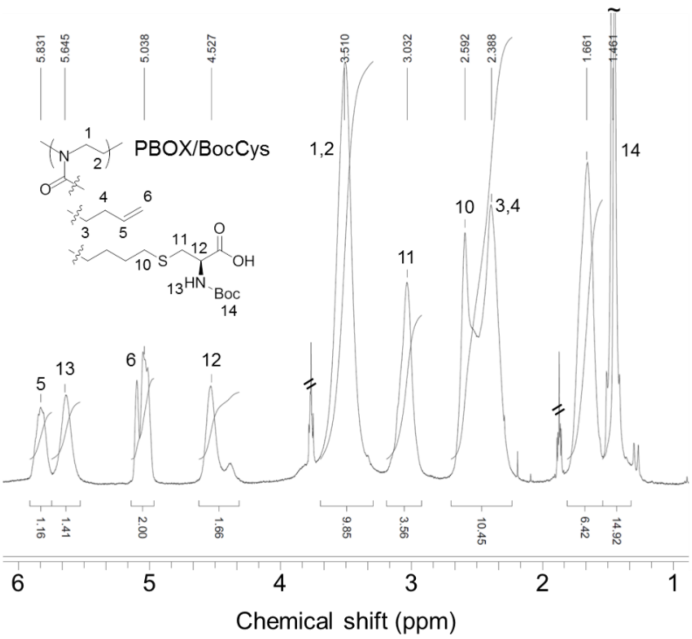

Figure S1: ^{1}H-NMR spectrum (400.1 MHz, $CDCl_3$, r.t.) of the PBOX/BocCys precursor.

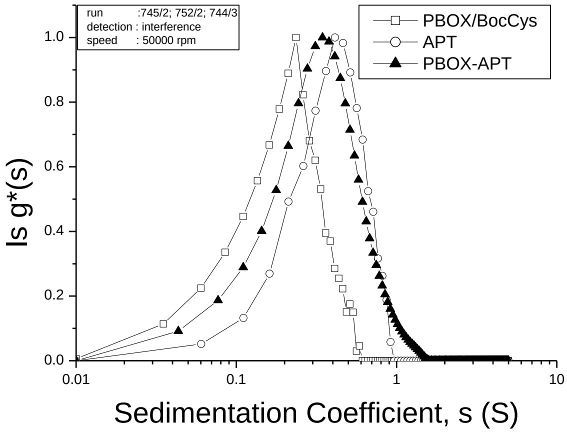

Figure S2: AUC sedimation coefficient distributions of PBOX/BocCys (□), aptamer ATP (○), and PBOX-aptamer (▲) in water-ethanol 1:1 (v/v).

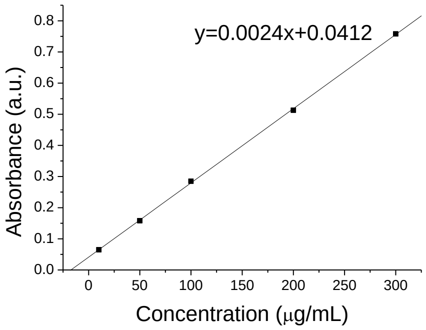

Figure S3. Absorbance calibration curve of the aptamer at 287 nm.

For a representative quantification of the grafting density: absorbance value at 287; A_{287}= 1,858

Thus, concentration is equal to;

x= (1.858-0.0412)/0.0024= 753 μg mL^{-1}

Concentration for measurement; 1 mg mL^{-1}, volume; 1mL, mass of copolymer 1mg

m_{APT}=753 μg

$M_{PBOX/BocCys}$= 7250 g mol^{-1}

M_{APT}=11462.6 g/mol

$m_{PBOX/BocCys}$ = 1-0,753=0,247 mg

$n_{PBOX/BocCys}$=0.000247/ 7250 = 34 nmol

m_{APT} =753 μg

n_{APT} = 0.000753/11462.6 = 65.7 nmol

n_{APT} / $n_{PBOX/BocCys}$ = 1,93 ≈ **2** aptamer strands for one PBOX chain

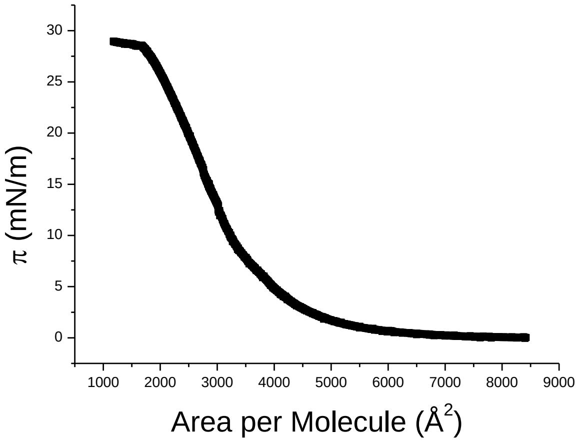

*Figure S4***.** Surface pressure isotherm of the surface active PBOX-aptamer

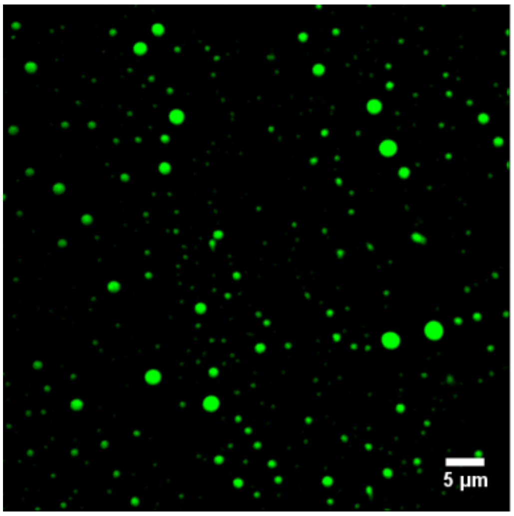

Figure S5. Confocal laser scanning microscopy of non extruded PBOX-aptamer copolymer stabilized oil-in-water emulsion subsequent to encapsulation of the hydrophobic Nile Red dye.

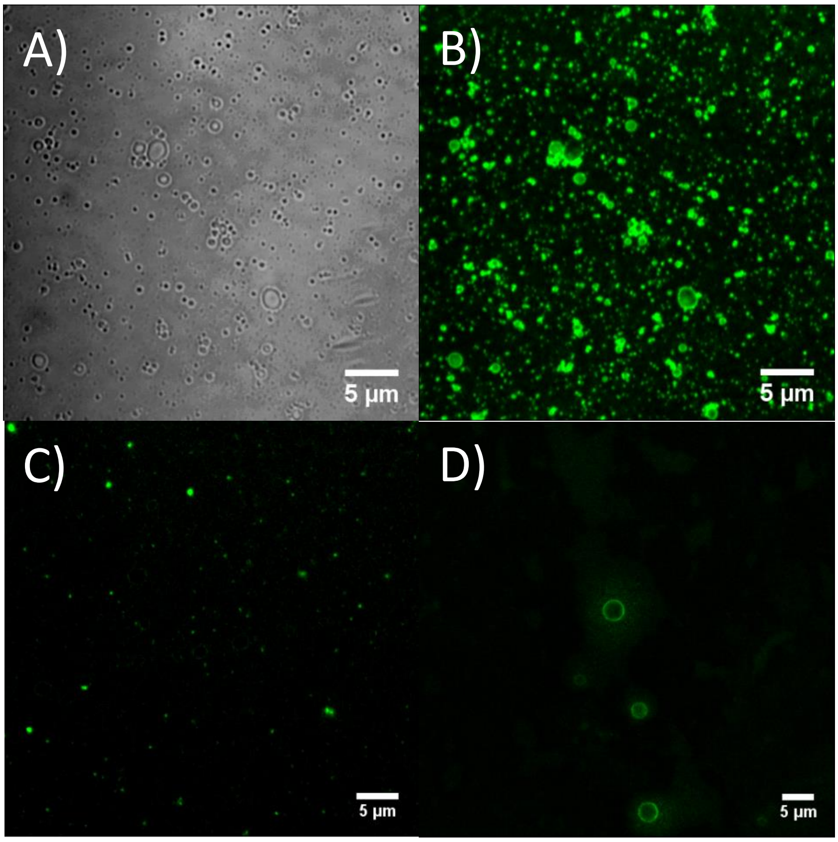

Figure S6. Confocal laser scanning microscopy images taken in the A) transmission channel and in the B) fluorescence channel of the initial, non-filtered emulsion stabilized by the PBOX-aptamer and incubated with FITC labeled IgE; C) Reverse oil in water emulsion stabilized by the copolymer-aptamer and incubated with FITC labeled IgE and D) emulsion stabilization subsequent to PBOX-aptamer stabilization, being the copolymer incubated with the protein prior to emulsion stabilization.

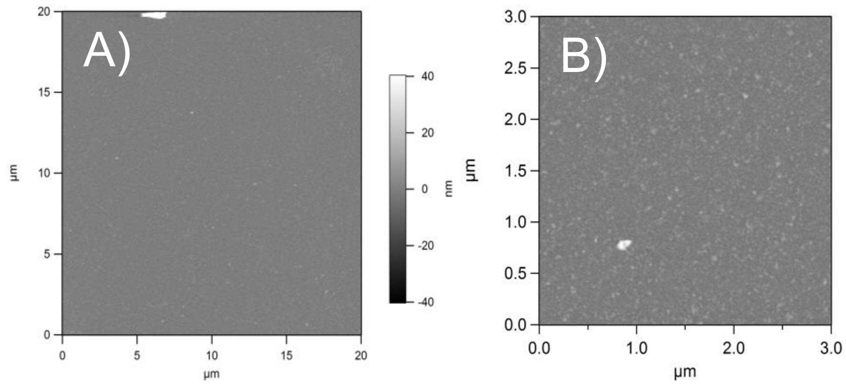

Figure S7. Atomic force microscopy height images of A) IgE coated silica and B) subsequent immobilization of an emulsion stabilized with a non IgE specific PBOX-DNA (same height scale for all micrographs).

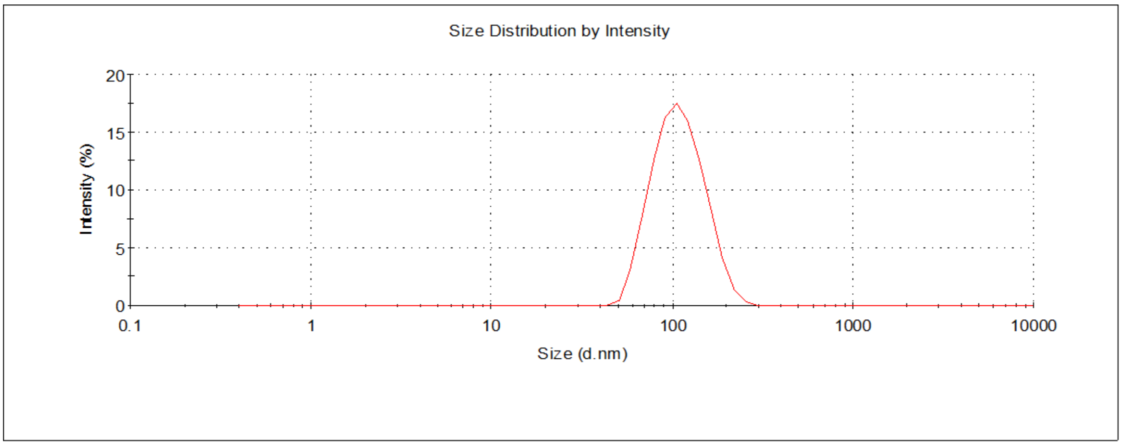

*Figure S8***.** Size of emulsion droplets after 0.22 µm filtration, PDI=0.054 (average of 3 measurements).

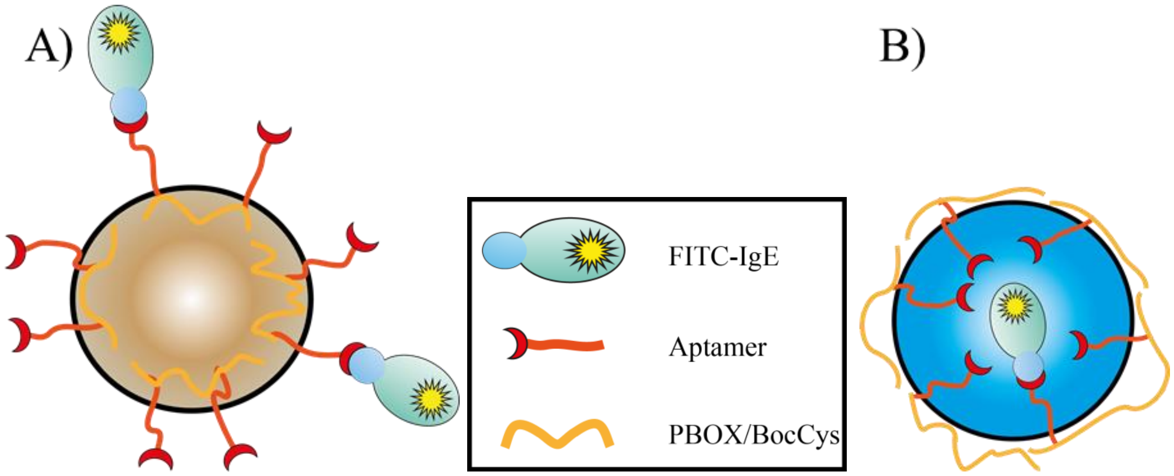

Scheme S1. Schematic representation of A) oil in water emulsion and B) reversed emulsion.

5.3 Hybrid Nanocapsules Targeting the Nucleolin Cancer Cells Surface Receptor

(This subsection is a continuation of the research described in the chapter 5.2. and herein efforts to transform the described system into drug delivery vehicle are described, Supporting Information with the figures mentioned in the text are placed at the end of this subsection)

ABSTRACT. Safe and efficient delivery of many poorly soluble potent anticancer drugs is a severe issue in the field of pharmacology. Herein, we report on a high loading efficiency drug delivery system for such drugs based on emulsion droplets. Stabilization of the droplets by multiple layers of polyelectrolytes results in controlled release of the drug from the core. Decoration of the outermost layer with the DNA aptamer AS1411 could enable specific interactions of the capsule with nucleolin, which is overexpressed on many types of cancer cells.

1. INTRODUCTION

Several strategies like radiation, surgery or biotherapy have been proposed to treat different types of cancer, among which the systematic chemotherapy still persist as frontline treatment [302]. Indeed, drugs used in chemotherapy such as doxorubicin, have high potential of killing cancer cells. However, because of non-specificity which significantly affects healthy cells, rapid clearance of chemotherapeutic agent from the circulation system, strong chemoresistance, poor tissue selectivity and low drug accumulation in tissue as well as the poor aqueous solubility of many anticancer drugs, chemotherapy is considered as imperfect [303, 304] [305, 306]. Nanotechnology has been contributing significantly to provide the improvement of pharmacokinetic features as well as therapeutic indices of plethora of various drugs [307]. Additionally, biodegradable nanocarriers such as polyelectrolyte microcapsules (PMCs), emulsion based carriers and liposomes are of high interest since the systems are of size in the nanometer range, which enables ease of specific delivery, protection of payload, multiple drugs delivery, reduction of toxicity and drug high-loading efficiency [303, 308, 309]. The layer-by-layer (LbL) method is a convenient strategy to induce controlled release of a capsule cargo over an extended period of time in order to maintain the drug concentration at the therapeutic level over time. This environmentally friendly and ultra-low cost sequential adsorption of oppositely charged polyelectrolytes, originally designed for planar substrates, is feasible on any charged template and was successfully applied for coating of colloids [242]. In order to obtain the defined thickness and the desired delay of cargo release the adsorption cycles can be repeated and the composition of the polyelectrolyte layers can be modified [308]. Since a large spectrum of biocompatible and biodegradable polyelectrolytes is commercially available to induce the release upon pH or temperature trigger, implementation of this methodology in the field of pharmaceutics could thus be envisioned [310-314].

Many of the drug delivery vehicles take advantage of passive targeting through the enhanced permeability and retention (EPR) effect. Leaky vasculature and lack of proper lymphatic clearance system of the tumour tissue result in higher intratumoural therapeutic agent accumulation and increased retention times in the tumour interstitium in comparison with healthy tissues [315, 316]. Coating of the nanocarriers with the hydrophilic, inert and biocompatible polyethylene glycol (PEG), decreases the rate of opsonisation leading to the reduced clearance by the mononuclear phagocytic system (MPS) resulting in prolonged circulation time and increased delivery efficiency via the EPR effect. Nevertheless still only a fraction of the drug enters the tumour cells [305]. In order to make drug delivery more efficient and specific to the intended location, reduce toxicity, increase uptake and accumulation of the therapeutic agent in the tumour without damage of the normal cells, active delivery strategies are being devised. To provide active targeting, the outer surface of the nanodevices could be functionalized with ligands that bind specifically to the molecules which are overexpressed on the surface of cancer cells. The nanocarriers could thus be internalized by the cell by receptor-mediated endocytosis [304, 307]. The most popular ligands that could be accounted for are peptides, antibodies, small molecules and aptamers [317]. Small size, low or no immunogenicity, high temperature resistance, chemical stability, high specificity and affinity, make the aptamers ideal candidates for targeted delivery [287]. Aptamers ("defined also as chemical antibodies") are short DNA or RNA fragments produced by chemical synthesis which are folding into specific 3D structures to bind the target with dissociation constants in the pico and nanomolar range [287]. Paclitaxel (PTX) is one of the most popular antiproliferative drugs which has been used for the treatment of various types of solid tumours. Due to the poor aqueous solubility of paclitaxel (>0.001 mg/mL), a mixture of Cremophor® EL and ethanol is used for its solubilization, which causes many serious side effects related to this excipients [318-320]. It was demonstrated that the cytotoxicity of the excipients and the toxicity of the drug via systemic exposure can be reduced when the drug is delivered in a form of a nanoparticle system [319, 321]. In this work, we describe the hierarchical organization of a hybrid nanodelivery capsule system build up on a liquid core. Oil-in-water emulsion was stabilized by amphiphilic polyoxazoline-aptamer copolymer (PBOX-AS1411).

Copolymer stabilization of an oil-in-water emulsion enables straightforward and efficient encapsulation of PTX. Subsequently, in order to further stabilize the droplet and control the release of the drug the liquid core was coated with biocompatible polyelectrolytes, namely poly(l-lysine) and poly(l-glutamic acid) (PLL/PLGA). The molecular weight of the polyelectrolytes was chosen to be in the range between 10-20 kDa to ensure ease of biodegradation. In order to increase hydrophilicity as well as prevent the uptake by MPS the outer layer of the capsules is PEGylated. To introduce targeting, the capsules were eventually decorated with the AS1411 aptamer which enables the efficient recognition of nucleolin. AS1411 is a 26-nucleotide guanine rich DNA aptamer which binds specifically the nucleolin protein overexpressed on the tumour cells surface. Moreover, this protein is playing a crucial role in biochemical processes such as packing and transport, rRNA, transcription, replication and recombination of DNA [322]. Various studies demonstrated enhanced uptake of AS1411 aptamer functionalized nanocarriers by the tumour cells in comparison to the normal cells which express nucleolin at much lower levels than tumour cells [303]. Thus, the AS1411 aptamer could be used to target the delivery of PTX filled nanodevices to the cancer cells which are overexpressing nucleolin.

2. RESULTS

PBOX-AS1411(*Figure 5-15*) hybrid was obtained as a result of coupling between the poly(2-alkyl-2-oxazoline) with pendant N-Boc protected amino acid and alkenyl side chains (PBOX/BocCys) (^{1}H NMR in *Figure S1*) with an amine modified AS1411 according to a procedure given in ESI (*Figure S2*). Distinct sedimentation profiles of the starting materials as well as of the final product were revealed by analytical ultracentrifugation analyses (AUC sedimentation-velocity, *Figure S3*) and support the success of the conjugation. According to UV-Vis spectroscopy (ESI) every polymer chain was coupled with one aptamer strand.

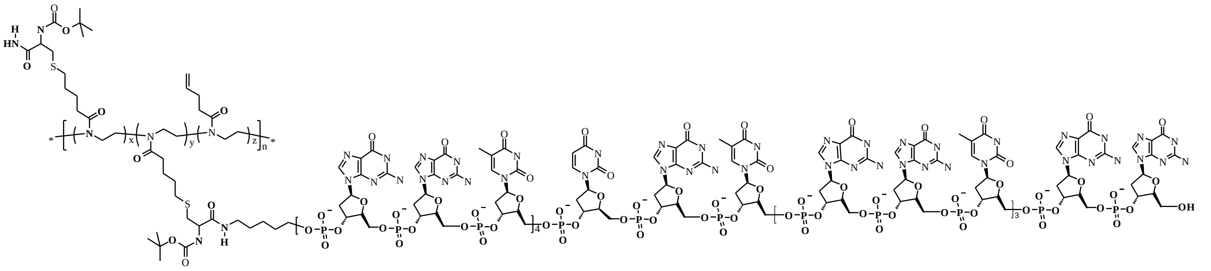

Figure 5-15. Macromolecular structure of the PBOX-AS1411(x=0.58,y=0.04,z=0.38)

The resulting amphiphilic copolymer can be used as emulsifier in the emulsification process [111]. Emulsion droplets filled with PTX were prepared as described in ESI. Chloroform was selected as the organic phase due to its low boiling point which facilitates subsequent solvent removal and PTX high solubility in this solvent. Following the extrusion through 0.22µm LCR non-protein binding filter, the emulsion droplets were characterized by transmission electron microscopy (*Figure 5-16 b*), dynamic light scattering (DLS) and zeta potential measurements revealing spherical structures with a diameter of about 80 nm (*Figure S4, S5*) in average and surface charge of -34 mV, which provides enough repulsion between droplets to avoid aggregation as well as indicates that aptamer copolymer stabilized droplets can be used as a substrate for layer-by-layer deposition [242, 246].

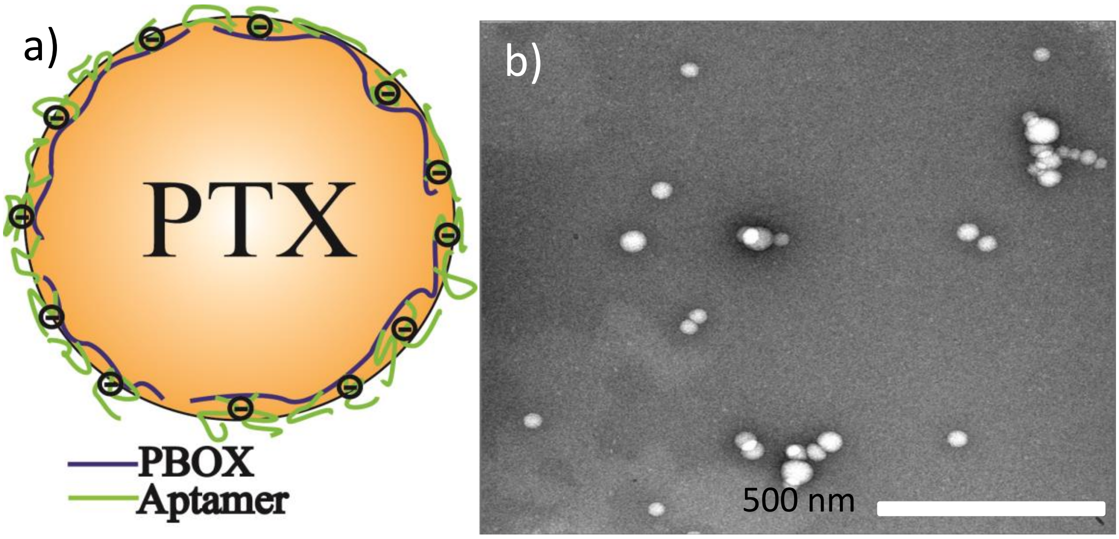

Figure 5-16. a) schematic representation of an emulsion droplet b) TEM imaging of PBOX-AS1411 copolymer stabilized emulsion

Sequential deposition of oppositely charged polymers onto the colloidal particles further grants capsule stabilization [323] and enables the formation of a shell of desired thickness around the core [324]. Multilayer coating would protect the load and enable sustained release [325]. In order to simplify the process of multilayer assembly, the so called “dynamic” layer-by-layer process with the use of a home-build ultrafiltration cell was used (*Figure S6*) [326, 327]. This technique enables convenient removal of the polyelectrolyte excess through straightforward washing steps. The details of the multilayer build-up are described in the ESI. Zeta potential measurements are used to monitor the sequential deposition of layers and revealed the characteristic zig-zag dependence resulting from the adsorption of oppositely charged PLL and PLGA (*Figure 5-17 b*).

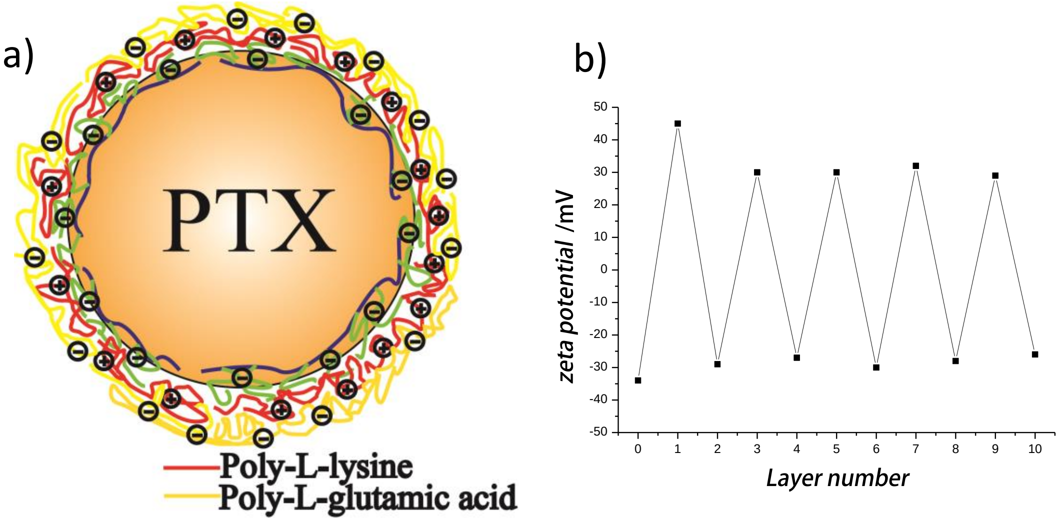

Figure 5-17. a) Schematic representation of a multilayer covered capsule b) representative zeta potential monitored upon polyelectrolyte deposition cycles

After formation of few layers chloroform was removed by mild heating, which led to a slight size decrease (20 nm). LbL deposition at different stages was also monitored by TEM imaging (*Figure 5-18*). Electron imaging demonstrated that polyelectrolyte adsorption does not affect the size of the capsule significantly.

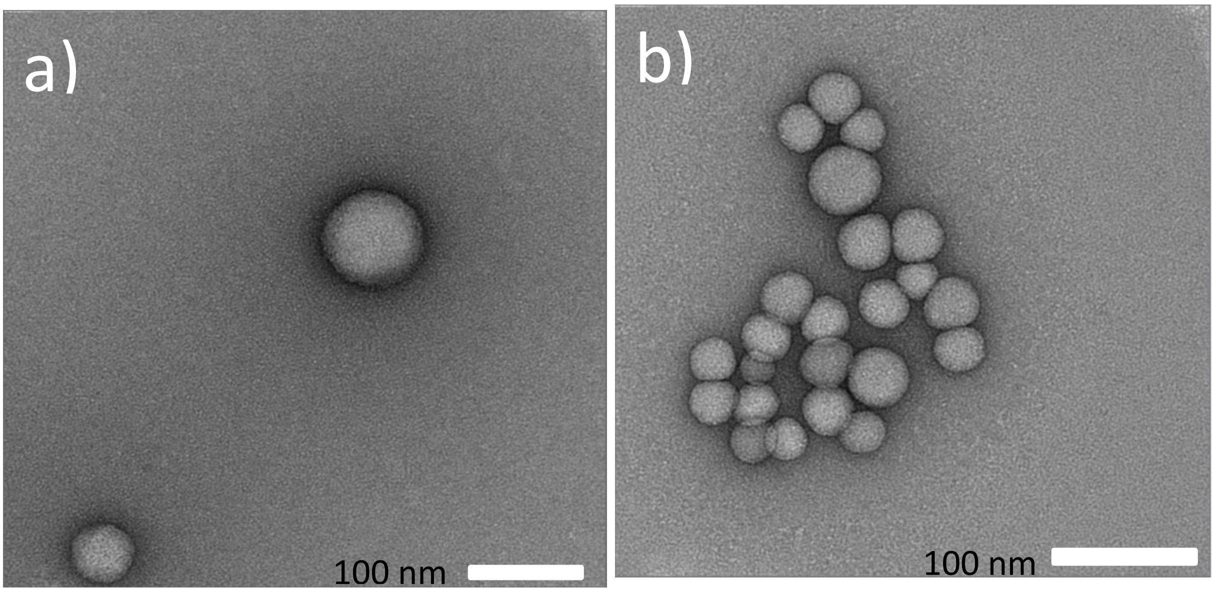

Figure 5-18. TEM imaging a) 1 layer deposited b) 5 layers deposited (uranyl acetate staining)

Incorporating the drug which crystalizes upon the solvent removal helps to preserve the spherical morphology of the droplets even when the structures are exposed to high vacuum condition for imaging by both scanning and transmission electron microscopy (*Figure 5-18, Figure S7*) in contrary to empty pristine soft emulsions. To obtain further evidences for the multilayer formation Confocal Laser Scanning Microscopy (CLSM) was used. The core and 3rd layer were stained by coumarin 6 and DyLight633 respectively (procedure in ESI). Simultaneous imaging it two different channels enabled to localize both the interior and the shell of the capsules which is an additional conformation of shell formation (*Figure 5-19*).

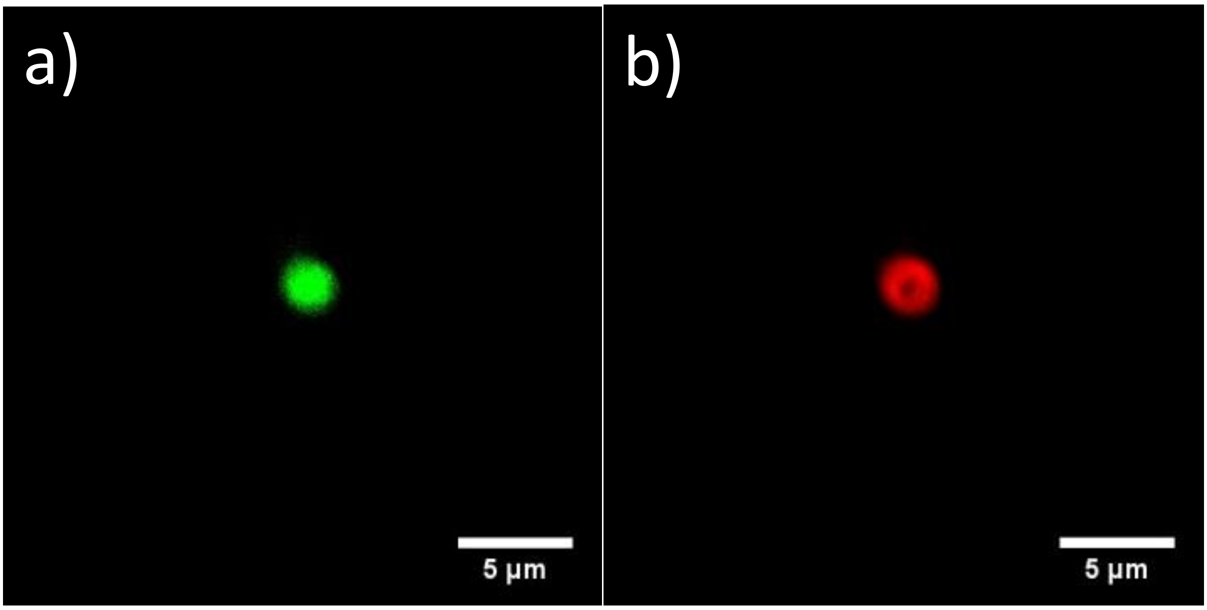

Figure 5-19. CLSM imaging of 3 layers covered capsules composed of a a), chloroform core stained with Coumarin 6 and b) outer PLL layer conjugated with DyLight633

In order to determine the delay of the drug release from the capsules covered with the varying number of polyelectrolytes layers release kinetics experiments were performed by fluorescence spectroscopy (protocol in ESI). This data revealed the release slowdown of capsules covered with 6 and 3 bilayers in comparison to the capsules with just one bilayer of adsorbed polyelectrolyte (*Figure S8*). However in general the time of release from the capsules with these bilayer numbers is too short for the drug delivery application and improvement has to be implemented. One strategy would be to increase the number of polyelectrolyte layers, another possibility would be to achieve crosslinking of the polyelectrolyte layers through EDC/NHS chemistry [328] (or cross-linking mediated increased stabilization of the core through polymerization of PBOX pendant vinyl group) [193].

In order to render the surface of the capsules more hydrophilic, inert and thus reduce the systemic clearance rates and increase the retention time the mPEGylated PLGA(methoxy-poly(ethylene glycol)-block-poly(L-glutamic acid sodium salt)) copolymer was adsorbed on the outer layer of the capsule. Success of the PEGylation was confirmed by the zeta potential measurement. Upon the adsorption of the PEG copolymer the zeta potential decreased from 30 to 2 mV.

With the objective of achieving active delivery, capsules were tagged with AS1411 aptamer. Highly specific and efficient DBCO click chemistry was employed to reach this goal. In comparison to the azide-alkyne cycloaddition (CuAAC) for which the presence of copper is required to catalyze the reaction but which could hinder bioorthogonal conjugation in living cells the DBCO click chemistry is conducted without the copper addition. In the first step the amino terminated AS1411 aptamer was reacted with DBCO NHS ester in order to introduce the functional group at the nucleic acid sequence terminus (protocol in the ESI, *Figure S9*). MALDI TOF spectrometry revealed the peak corresponding to the DBCO modified aptamer, which supports the success of this conjugation (*Figure S10*). To implement azide group at the rim of the capsules, the mPEG-PLGA was mixed with the azido functionalized PEG-PLGA (Azido-poly(ethylene glycol)-block-poly(L-glutamic acid sodium salt)) in a 95:5 ratio prior to the PEGylation. To provide the steric availability of azide groups for aptamer tagging, azide modified PEG-PLGA copolymer was selected longer than the methoxy-PEG-PLGA (~13 kDa and ~9 kDa respectively). Afterwards, stoichiometric amount of DBCO-AS1411 was appended to the solution of azido functionalized capsules (*Figure S11, S12*). The solution was stirred for 1 hour and subsequently the excess of DBCO-AS1411 was removed by dialysis (Float-A-Lyzer G2 100kDa MWCO). Upon grafting of the negatively charged aptamer the zeta potential decreased from 2 to -8 mV.

To evaluate the specificity of binding of the AS1411 aptamer tagged polymeric nanocapules, reflectometry and atomic force microscopy (AFM) imaging were combined. Capsules functionalized with the AS1411 aptamer as well as non-functional PEGylated capsules were incubated with a surface modified with either the AS1411 target nucleolin protein or BSA. From the time course monitoring of the adsorption of the capsules (*Figure 5-20 a*), it can be noticed that the detected adsorbed mass increases when the nanocarriers modified with the AS1411 aptamer are brought onto the surface coated with the nucleolin (NCL) protein up to an average value of 2.93 mg m^{-2}. Nevertheless, a significant adsorption was detected also on the BSA coating (5.16 mg m^{-2}) which could be associated with the nonspecific electrostatic interaction between negatively charged BSA and partially positive capsules surface (*Figure 5-20 b*).

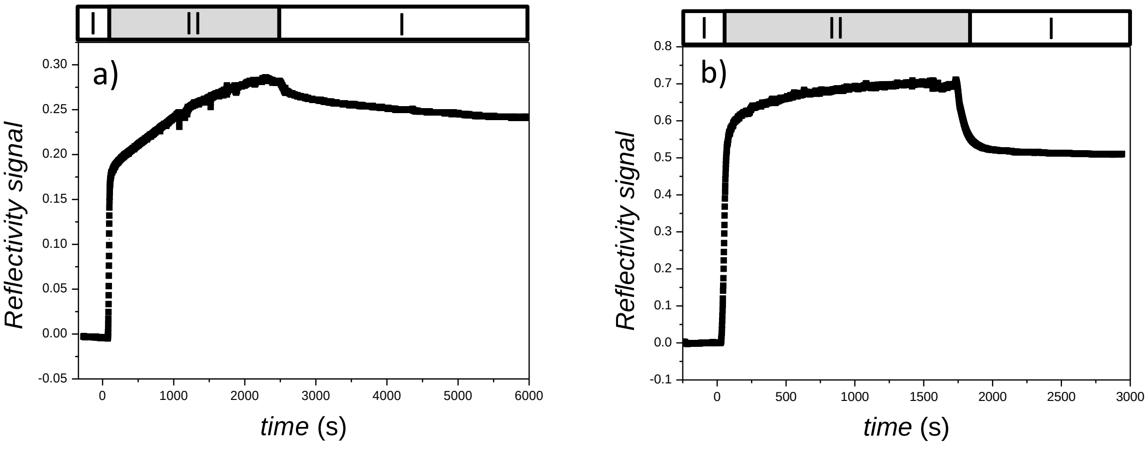

Figure 5-20. Representative time course of the refractive index as measured by reflectometry upon adsorption of the aptamer decorated carriers on a) silica modified with nucleolin (target protein of the aptamer) b) Adsorption of nanocapsules on BSA modified silica. The surface is initially flushed with a 15 mM NaCl buffer solution (I). At time zero, apatamer functionalized capules in 15 mM NaCl is introduced (II) and eventually, the surface is again flushed with the buffer solution.

The same behavior was observed when the PEGylated structures were incubated with the NCL protein. To confirm this phenomenon liquid as well as dry state Atomic Force Microscopy (AFM) were used. As can be seen in the *Figure 5-21a)* and *b)* the AS1411 decorated structures adsorb on both surfaces modified either with nucleolin or BSA (*Figure 5-21 c*) and *d)* (images of surfaces modified with nucleolin and BSA in ESI, *Figure S13 and S14*).

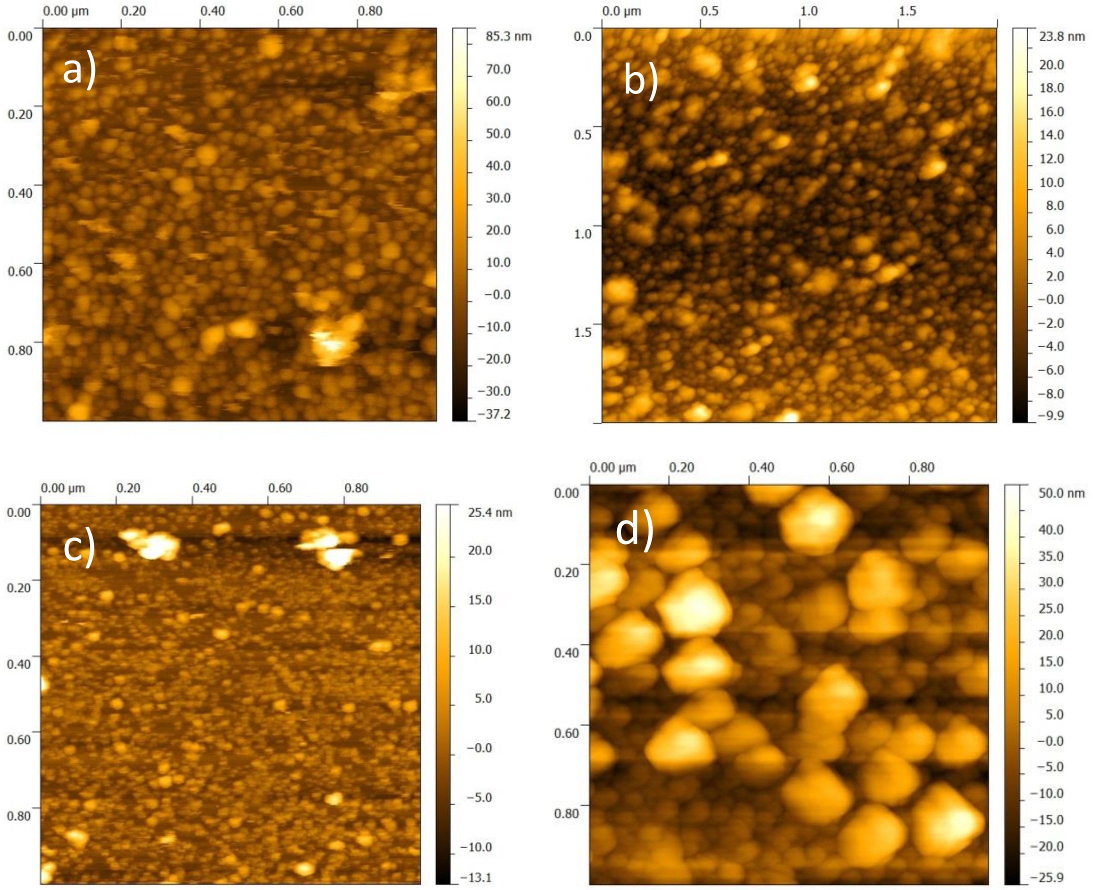

Figure 5-21. Adsorption of the AS1411 decorated structures observed by AFM. a) nucleolin coated silica (imaging in liquid), b) nucleolin coated silica (dry state), c) BSA modified silica (imaging in liquid) d) BSA modified silica (dry state)

Similar adsorption was detected in the case of non-functionalized PEGylated nanocapsules (*Figure S15*). Nevertheless, it was observed that in the case of nonspecific interactions (e.g.AS1411 decorated capsules on BSA modified surface) upon the contact with AFM tip nanocapsules were moving, which could indicate that these capsules were not sufficiently immobilized on the surface. Despite of this fact, these experiments demonstrated that the capsules do not interact specifically with the target protein. This issue could occur due to a low percentage of aptamers on the outer surface (5%). Moreover, DBCO click chemistry is considered as less efficient than conventional azide-alkyl click chemistry which could also lower the number of functional aptameric strands at the capsule surface. Additionally, there is the possibility of electrostatic interactions between the capsule and the protein modified surface since the PEGylation did not completely neutralized the charge (2 mV zeta potential). Negative charge that arises after aptamer grafting might be another reason of unspecific electrostatic interactions with protein.

3. CONCLUSION

Highly potent hybrid nanosized capsules were prepared through the combination of the emulsification, layer-by-layer approaches and convenient functionalization. Well defined morphology, monodispersity of the system as well as possibility of hydrophobic drug high loading make this system attractive. Nevertheless, drug release control as well as specificity of the targeting was far from optimal. To overcome these obstacles further investigations discussed above need to be conducted.

SUPPORTING INFORMATION

General: Chloroform, sodium chloride, ethanol were purchased from Acros Organics (Geel, Belgium).1-ethyl-3-(3-dimethylaminopropyl)carbodiimide hydrochloride, *N*-hydroxysuccinimide, MES buffer, dibenzocyclooctyne-N-hydroxysuccinimidyl ester (DBCO-NHS), hydroxypicolinic acid (3-HPA), diammonium citrate (DAC) and dialysis tube (cut-off 14 kDa M_w) were supplied by Sigma Aldrich (Buchs, Swizerland). 5'-GGTGGTGGTGGTTGTGGTGGTGGTGG-3' modified at the 5' end with an amine group through an hexyl spacer was purchased from Microsynth Laboratory (Balgash, Switzerland). Azido-poly(ethylene glycol)-block-poly(L-glutamic acid sodium salt) (N_3-PEG[5kDa]-b-PLGA[7,5kDa]), methoxy-poly(ethylene glycol)-block-poly(L-glutamic acid sodium salt) (PEG[4.7kDa]-b-PLGA [4.1kDa]), poly(L-lysine hydrochloride) (PLL 16kDa), Poly(L-glutamic acid sodium salt) (PLGA 15kDa) were provided by Alamanda Polymers (Huntsville, USA). DyLight 633 NHS ester, Float-A-LyzerG2 100 kDa and Thermo Scientific Slide-A-Lyzer Dialysis Cassettes 7.5 kDa were supplied by Thermo Scientific (Zug, Switzerland). Paclitaxel was obtained from Taizhou Bolon Pharmachem Co.,Ltd (Taizhou City, China), Nucleolin was provided by Abnova (Taipei, Taiwan). Cellulose membrane for ultrafiltration (100 kDa) was purchased from Milipore (MA, USA). Bovine Serum Albumine (BSA) was provided by Applied Biosystems (Zug, Switzerland). Paclitaxel-Oregon Green® 488 Conjugate was obtained from Invitrogen (Zug, Switzerland). Zeta cells were provided by Instrumat SA (Lausanne, Switzerland). Silicon wafers single side polished, orientation N/Phos <100>, (625 ± 25) µm thickness, 1–50 Ohm cm resistivity were purchased from Silchem (Freiburg, Germany)

Synthesis and Characterization:

Poly[2-(3-butenyl)-2-oxazoline] (PBOX) was prepared as reported earlier.[189] Number-average molecular weight (M_n) of the PBOX sample was equal to 3.5 kDa (corresponding to an average number of 28 repeat units) (^{1}H NMR) and a dispersity index (M_w/M_n) of 1.05 (SEC). *N*-(*tert*-butyloxycarbonyl)-L-cysteine (BocCys) (Merck) was then partially grafted to the alkenyl groups of PBOX via thiol-click chemistry [189]. PBOX/BocCys ^{1}H NMR analysis (*Figure. S1*) revealed 62% functionalization with the *N*-protected amino acid (~17 units per chain) and 38% remained unreacted (~11 units); see the chemical structure in *Scheme 1* (top left).

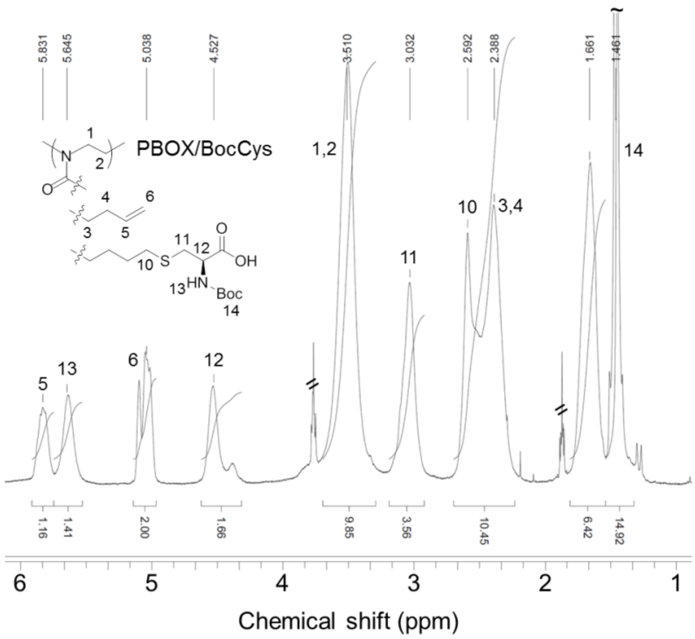

Figure S1: ^{1}H-NMR spectrum (400.1 MHz, $CDCl_3$, r.t.) of the PBOX/BocCys precursor.

PBOX-AS1411 synthesis

In brief, the carboxylic group of Boc-cysteine modified poly[2-(3-butenyl)-2-oxazoline] was activated with EDC/NHS according to a protocol reported earlier.[329] Afterwards the activate ester was coupled with the free 5'-amino group of the 26-mer AS1411 aptamer (sequence 5'- GGTGGTGGTGGTTGTGGTGGTGGTGG-3') modified at the 5' end with an amine group through a hexyl C_6 spacer. The resulting compound was characterised by AUC and UV-Vis spectroscopy.

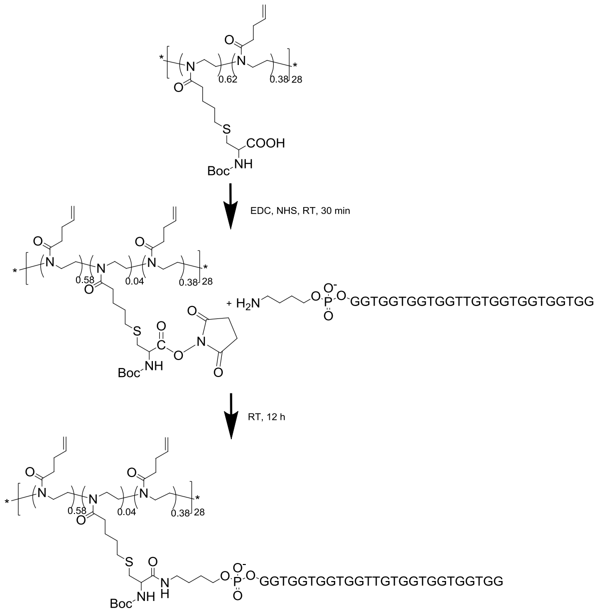

Scheme S2: Schematic representation of the PBOX-AS1411 synthetic route.

Conjugation of amino modified DNA to N-Boc-cysteine modified poly[2-(3-butenyl)-2-oxazoline]. Poly[2-(3-butenyl)-2-oxazoline) modified with Boc-cysteine (0.25 μmol, 1.5 mg, 1 eq), was dissolved in 1 mL of MES (pH=5) in the eppendorf tube. Subsequently 154 μL of EDC (1 mg mL^{-1}, 1 μmol, 0.154 mg, 4 eq) and 114 μL of NHS (1 mg mL^{-1}, 1 μmol, 0.114 mg, 4 eq) was added. Later on, reaction was allowed in a thermoshaker for 30 min at room temperature. Afterwards, 4.2 mg of 5'- GGTGGTGGTGGTTGTGGTGGTGGTGG-3' modified at the 5' end with an amine group through a C_6 spacer (0.5 μmol, 2 eq) was appended to the eppendorf. Closed vail was shaked at room temperature overnight. In order to remove unreacted species as well as side products of the reaction, the reaction mixture was dialysed against water for 5 days (MWCO 14kDa). Final product was obtain subsequent to water removal by freeze-drying.

Instrumentation and microscopy techniques

AUC

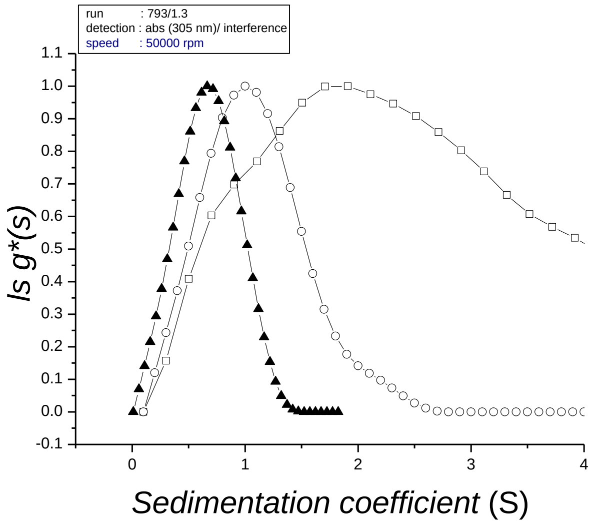

Figure S3. AUC sedimation coefficient distributions of PBOX/BocCys (□), DNA (○), and PBOX-g-AS1411 (▲) in water-ethanol 1:1 (v/v)

UV-Vis grafting density estimation

To determine grafting density oligonucleotide calculator was used (http://www.basic.northwestern.edu/biotools/oligocalc.html)

For a representative quantification of the grafting density(concentration 10μg mL^{-1}), absorbance value at 260 nm was equal to;

A_{260}= 0.157

Thus, from OligoCalc the mass of aptamer is equal to;

$m_{DNA}=4.7\ \mu g$

$M_{PBOX/BocCys} = 12612.5\ g\ mol^{-1}$

$M_{DNA}=8450.5\ g\ mol^{-1}$

$m_{PBOX/BocCys} = 10-4.7 =5.3\ \mu g$

$n_{PBOX/BocCys} =5.3*10^{-6}/ 12612.5= 0.42$ nmol

$n_{DNA} = 4.7*10^{-6}/8450.5= 0.56$ nmol

$n_{DNA} / n_{PBOX/BocCys} = 1.33\approx$ **1** apt strand for one PBOX chain

Emulsification

13.6 mg of PBOX-aptamer along with 10 mg of PTX was dissolved in 300 μL of chloroform and stirred for 24 h. Afterwards, the PTX/copolymer solution was appended to 20 mL of a 15 mM NaCl solution and ultrasonicated for 5 min in order to break the organic phase (Branson Sonifier Digital 450, Zurich, Switzerland), amplitude 35%, max temp; 40 °C, impulse on; 1 s, impulse off; 1 s. To prevent sample overheating the beaker in which sonication was performed was placed in the ice bath. In order to decrease the size and size distribution the resulting emulsion was filtered through 0.2 μm pore size LCR non-protein binding filters prior to the determination of the hydrodynamic radius and zeta potential of the droplets.

Dynamic Light Scatering (DLS)

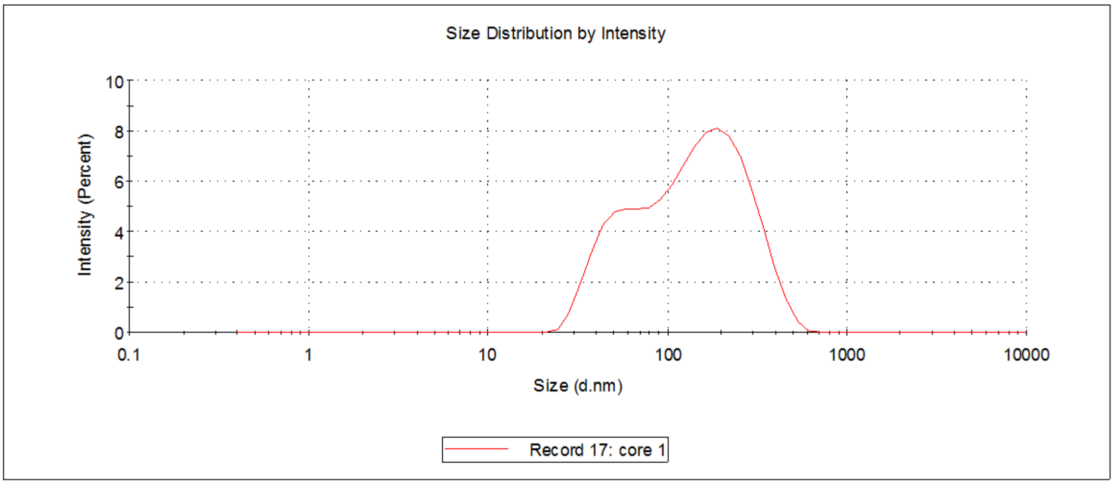

Figure S4. Size distribution of non extruded PBOX-AS1411 copolymer stabilized emulsion (main peaks;187 nm-76.1%, 50 nm-23.9%)

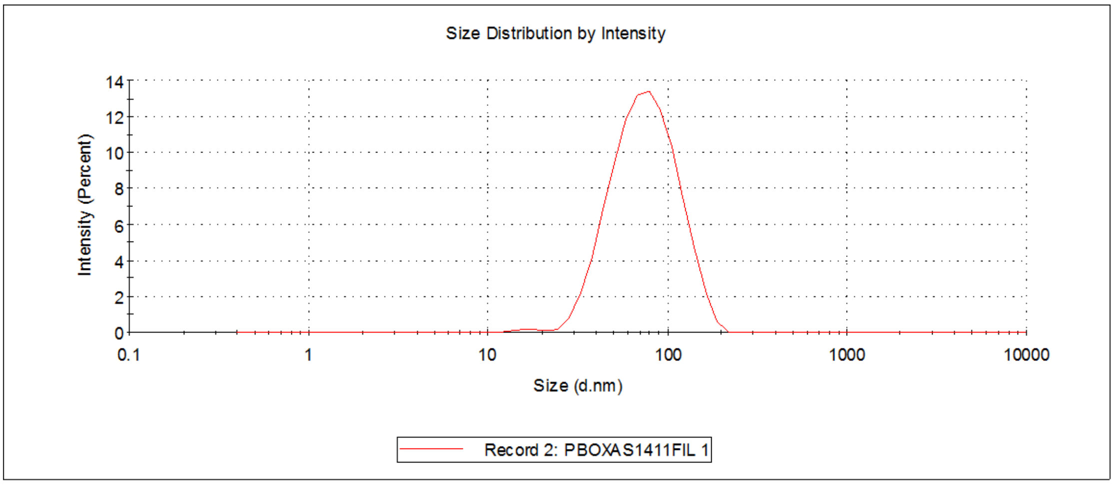

Figure S5. Size distribution of PBOX-AS1411 copolymer stabilized emulsion extruded through 0.22µm (main peak 80nm)

Layer-by-Layer

Deposition was conducted with an *home-made* ultrafiltration cell depicted in *Figure* S6. 10 mL of positively charged polyelectrolyte was placed in the cell chamber added and afterwards 1 mL of emulsion was added dropwise under strirring. The chamber was closed and the polyelectorolyte was let to adsorb on the surface of emulsion droplets for half an hour. Subsequently, gas pressure was applied in order to decrease the volume of the mixture as well as to drain away part of non adsorbed polyelectrolytes. Subsequently 7 mL of milliQ water was poured in the chamber, the cell was closed and the gas pressure was applied to remove excess of the polylectrolyte. This washing step was constantly repeated two times before deposition of the consecutive layer. The capsules suspension was always added to the solution of polyelectrolyte. For the deposition of the subsequent layer the capsules suspension was transferred to another vessel and the chamber was filled with polyelectrolyte solution to which capsules from the previous step were added. Afer few cycles of depositon the membrane had to be exchanged due to filatration slow down caused by the adsorption of the polyelectrolytes on the membrane surface. The deposition cycles were repeated until the capsules with desired number of layers were obtained. In order to PEGylate the surface of the capsules with mPEG-PLGA (as well as N_3-PEG-PLGA), the copolymer was adsorbed on the capules with positively charged outer layer exactly in the same maner as described above (all manipulations were performed in 15 mM NaCl, concentration of polyelectrolytes 2 g L^{-1}).

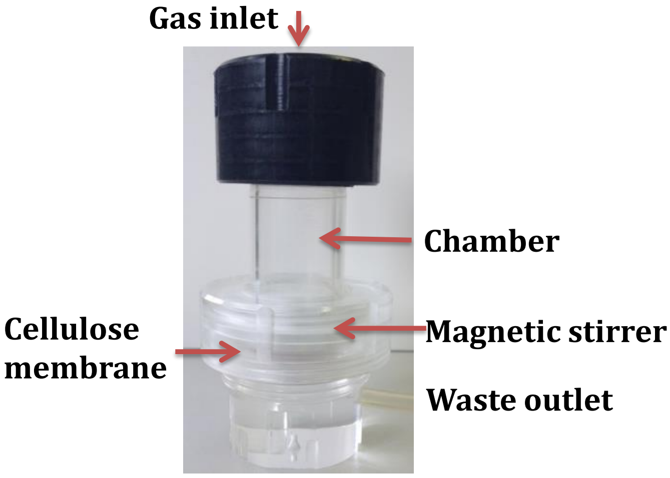

Figure S6. Ultrafiltration cell for LbL deposition. Membrane 100kDa

Zeta potential measurements.

The Zetasizer Nano-Z (Malvern Instruments Ltd, UK) was used to determine the zeta potential of emulsion droplets as well as at every step of layer-by-layer deposition. For every sample 3 measurements were performed from which an average value was extracted.

Transmission electron microscopy (TEM)

Prior to imaging grids were glow discharged for 30 s in order to render the surface of the grids more hydrophilic. Subsequently, on a parafilm foil two droplets of 2% uranyl acetate solution were deposited. 5 μL of fresh sample was transferred on a carbon coated 400-mesh copper grid, and after 30 s which were dedicated to adsorption, liquid was blot off on filter paper by holding it vertically. Later on, the grid was placed on the first uranyl acetate droplet for 1 s and then placed on the second for 30 s. After the second staining the remaining liquid was again removed with the use of filter paper prior to imaging with a Tecnai G2 electron microscope.

__Scanning electron microscopy (SEM)__

5 μL of the 5 layer coated capsules (filled with PTX) was transferred on silicon wafers, and after 3 min of deposition dried with a flow of nitrogen. Subsequently, samples were coated with gold for 20 s in a Jeol JFC-1200 fine coater. SEM images were acquired on a Jeol 6510LV microscope, equipped with a tungsten filament gun, operating at 10.6 mm WD and 10 kV.

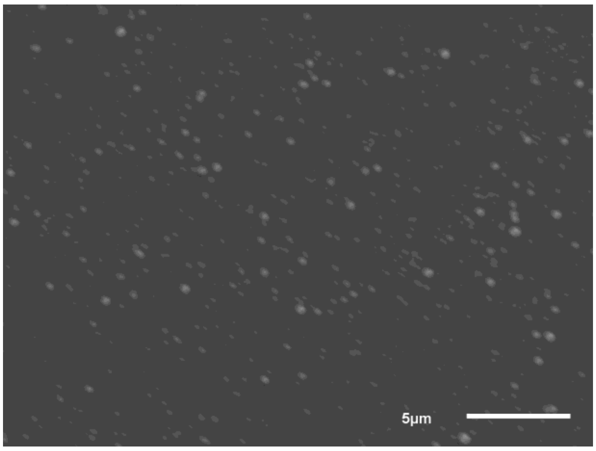

Figure S7. SEM imaging of the capsules with 5 layers deposited.

__PLL-Dylight 633 conjugation.__

To localize the polyelectrolyte layer in the nanocapsule shell poly(L-lysine) was coupled through an amide bond with N-Hydroxysuccinimide (NHS) ester-activated DyLight633. 500 μL of 2 g L^{-1} PLL solution in 15 mM NaCl was transferred to the vial containing 50 μg of NHS-DyLight. Afterwards pH was adjusted to 8 and the solution was left on stirrer for 2 h in the dark. Subsequently dialysis against water was performed for 2 days in the dark (14 kDa MWCO) in order to remove unreacted dye.

Layer localization.

In order to confirm the layer deposition we resorted to Confocal Laser Scanning Microscopy (CLSM). Instead of paclitaxel in the organic phase the Coumarin 6 fluorescent dye was solubilized to reach 100 µM (10 µg) concentration in chloroform. Emulsification was performed as described above. On the resulting emulsion droplets one bilayer of PLL/PLGA was deposited and subsequently the DyLight conjugated polyelectrolyte was adsorbed. Prior to CLSM imaging fluorescently labeled capsules were dialyzed against water (100 kDa) to remove excess of *PLL-Dylight 633.* 10 µL of labeled capsules were spread on a H_2SO_4:H_2O_2 (3:1) cleaned surface. Afterwards, the glass slide was covered by the cover glass and observed simultaneously by CLSM (Zeiss LSM 700 confocal microscope; lens 100× 1.4 NA) at two different excitation wavelengths with suitable filters (Coumarin 6 ex. 488 nm, em. 520 nm; DyLight 633 ex. 639 nm, em. 679 nm).

Release kinetics

Paclitaxel kinetics release protocol was adapted from “Modular Design of Redox-Responsive Stabilizers for Nanocrystals”[330] and “PEG Nanocages as Non-sheddable Stabilizers for Drug Nanocrystals”[331] by K. Fuhrmann et all. However, Oregon green conjugated paclitaxel was used instead of pure drug and UV HPLC detection was replaced by fluorescent spectroscopy. Release of PTX from capsules was performed in the presence of 5% BSA solution which is believed to be the main solubilizing agent of the PTX in vivo. [332] As mentioned above the emulsification was conducted with Oregon green conjugated instead of pure paclitaxel in 20 folds smaller scale (final volume 1 mL) than for regular emulsification experiments. Capsules with varying number of layers were prepared according to the protocol described earlier (1, 3 and 6 bilayers). 0.5mL of capsules solution was mixed with 0.5 mL of 20 mM phosphate buffer (pH 7.4) containing 10% BSA and transferred to a 1 mL Spectra/Por Float-A-LyzerG2 (MWCO100kDa, Thermo Scientific, Zug, Switzerland). Immediately after mixing the 30µL of sample was taken as first point of the drug release (time point 0) as well as to determine the initial concentration of Oregon green conjugated PTX. Afterwards, the Float-A-Lyzer G2 was placed in a 50 mL centrifugation tube filled with 45 mL of 10 mM phosphate buffer (pH 7.4) containing 5% BSA. Subsequently, the tubes were placed for mechanical shaking at 37°C. The samples (30 μL) were taken at following time points; 15 min, 1h, 2h, 4h, 8h and 24h. To each sample 200 μL of a 0.1 M $ZnSO_4$ solution and 500 μL of acetonitrile were added and the samples were vortexed thoroughly. Later on, the samples were centrifuged at 14000 rpm for 15 min in order to remove the BSA precipitate. 0.5 mL of each sample was analyzed by fluorescence emission measurement (FluoroLog®-3, HORIBA, Berlin, Germany), ex. 496 nm, em. 520-600 nm. The concentration of paclitaxel was determined from the calibration curve prepared in the same solvent mixture than the capsules samples.

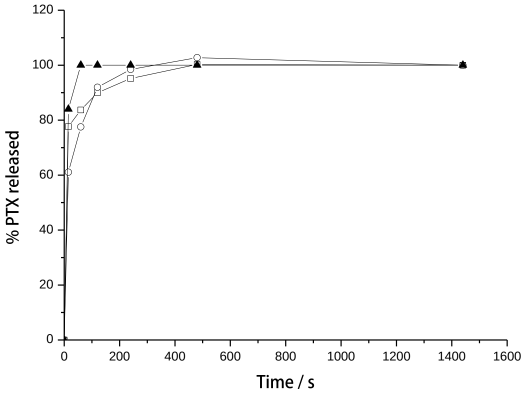

Figure S8. Release kinetics from capsules covered with different layer number; 6 bilayers (□), 3 bilayers (○), 1 bilayer (▲).

Dibenzocyclooctyne- N-Hydroxysuccinimide (DBCO-NHS) conjugation with amine terminated AS1411 aptamer

In order to introduce the DBCO group used for green "click chemistry" to the aptamer, the amine group of the nucleotide sequence was reacted with NHS activated DBCO. To simplify the purification step by dialysis a molar ratio 1:5 of aptamer to DBCO was chosen. 1 mg of 5'-amine terminated AS1411 aptamer was dissolved in 20 μL of miliQ water, 0.3 mg of

DBCO-NHS ester was dissolved in 200 μL of DMSO. The two solutions were mixed together and left for 4h in a thermoshaker. After 4h the crude product was dialyzed against water/DMSO (1.5:1) (Slide-a-Lyzer 7.5kDa MWCO) for 2 days and afterwards dialysis was conducted in pure water to remove DMSO. Subsequently, freeze-drying was performed to obtain solid product. Reaction was followed by MALDI-TOF spectrometry.

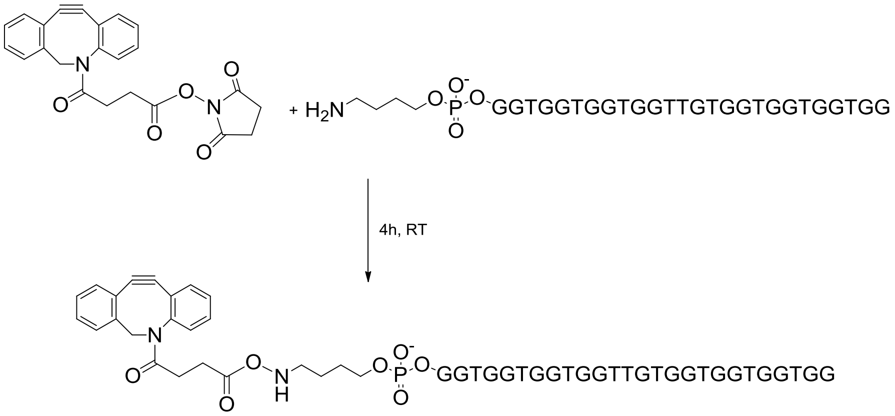

Figure S9. Aptamer functionalization with DBCO group

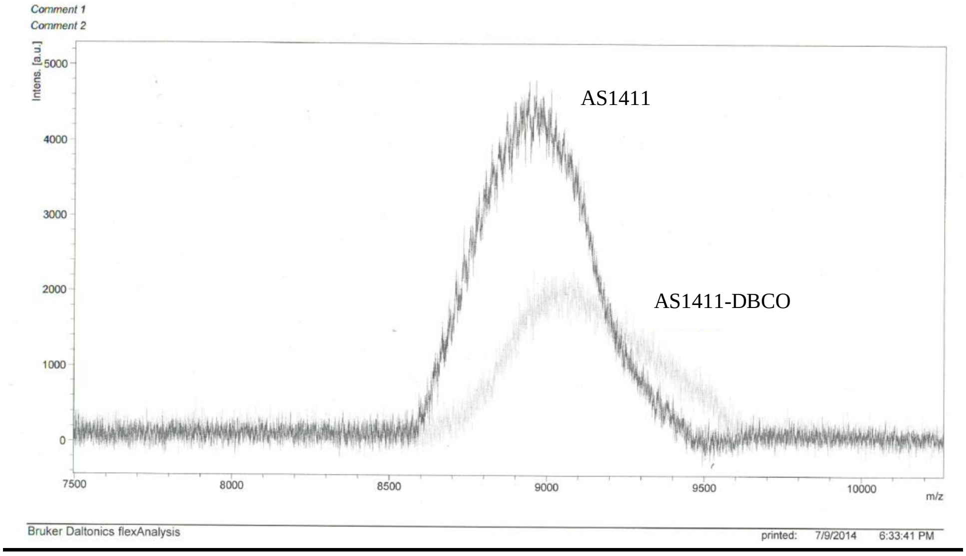

Figure S10. Maldi-tof spectrum of AS1411 aptamer and AS1411-DBCO conjugate (Matrix HPA:DAC).

Aptamer grafting

In order to functionalize the surface of the capsule, the AS1411 aptamer was grafted onto azide modified PEG-PLGA copolymer (500 uL of positively charged capsules and 650 uL of mixed PEG at 2 g L^{-1} concentration). 100 μL of DBCO-AS1411 (1 mg mL^{-1}) aptamer was added to the 700 μL of the PEGylated capsules (all manipulations performed in 15 mM NaCl). Unreacted DBCO modified aptamer was removed by dialysis against water (1 day, Float-A-Lyzer G2 100 kDa MWCO).

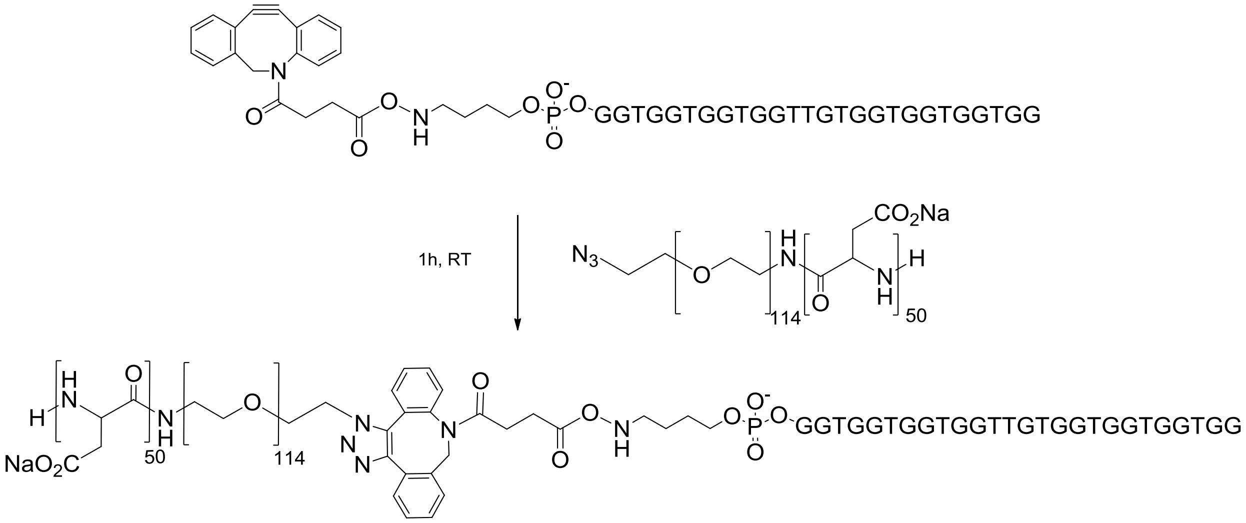

Figure S11. Azido functionalized PEG-PLGA copolymer tagging with DBCO-AS1411 aptamer.

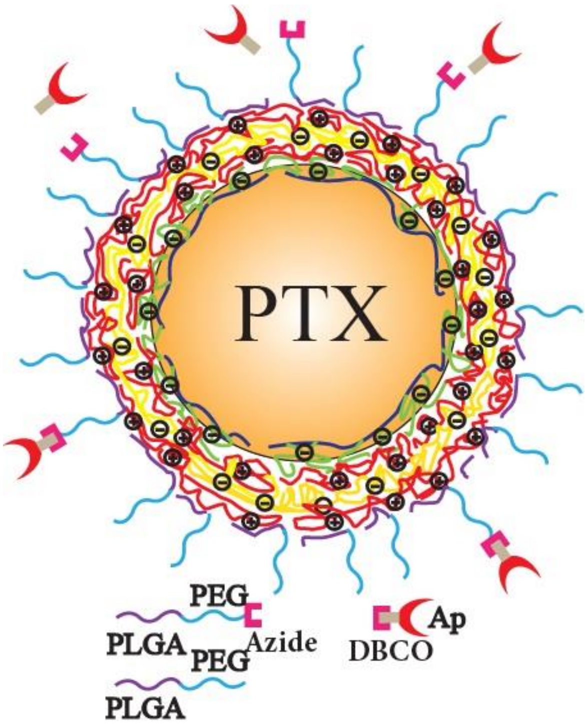

Figure S12. Schematic representation of the PEGylation and «grafting to» functionalization. Azide modified PEG-PLGA (M_w=12.5 kDa) mixed with non-modified PEG-PLGA (M_w=8.8 kDa) copolymer in a 1:20 ratio.

Reflectometry

5×10^{-3} g L^{-1} protein (BSA, NCL) solution were prepared in 15 mM NaCl buffer solution. All substrates (silicon pieces with dimensions of 1.2 × 0.5 cm) were cleaned in a 3:1 solution of concentrated sulphuric acid and 30% hydrogen peroxide for 30 min, washed thoroughly with Milli-Q water and dried under nitrogen. Afterwards, the precise thickness of the native silica layer (average thickness = 2.02 nm) was determined by null ellipsometry (Multiskop, Optrel, Berlin,Germany) [151]. Subsequently, to induce physical adsorption of proteins on the substrates, plates were incubated overnight in the solution of protein. Subsequently, modified plates were extensively washed with buffer solution (15 mM NaCl aqueous solution) in order to remove the excess of protein. Later on, ellipsometry was again employed to measure the thickness of the protein layer (average thickness NCL= 3.95 nm, BSA= 2.53 nm). In order to determine the thickness of the protein layer, a fixed value of refractive index was used, equal to the SiO_2 refractive index. Binding of the aptamer decorated structure to protein was quantitatively assessed by reflectometry measurements, conducted on a home-built fixed-angle reflectometer which allows determination of the adsorbed dry mass [150, 151]. The average sensitivity value was equal to 0.09 m^2 mg^{-1} for NCL and 0.1 m^2 mg^{-1} for BSA. In brief, after protein adsorption, the silicon plate was placed in the cell and the system washed with a buffer solution (solution I). Subsequent to signal stabilization, the solution of the AS1411 decorated (or just PEGylated) structures (solution II) was pumped into the cell and the change of refractivity signal (which is proportional to the adsorbed mass) was measured. Eventually buffer solution was again pumped into the cell (solution I), in order to verify if mass desorption would occur.

Atomic Force Microscopy (AFM)

Samples for AFM were prepared with the same procedure as for reflectometry. However, in order to adsorb the capsules on the substrates the droplet or respective solution was deposited on the silica plate (in a way to cover the whole surface) for 5 min and subsequently gently washed with the buffer solution (10 mL of 15 mM NaCl). AFM imaging in liquid was performed using a Cypher AFM (Asylum Research, Santa Barbara, CA) operating in the AC-mode. Biolever mini AC40TS cantilevers (Olympus, Japan) with a nominal tip radius smaller than 9 nm were used to acquire images in liquid. These probes are characterized with spring constants of around 0.1 N m^{-1} and resonance frequencies in liquid of around 25 kHz. The free oscillation amplitude (FOA) and the scan rate were set to 40 nm and 4.88 Hz respectively. The set point used varied between 60 and 70% of FOA. For the dry state imaging AFM imaging a Nanoscope IIIa scanning probe workstation equipped with a Multimode head using an A-series piezoceramic scanner (Digital Instruments, CA, U.S.) was used. Imaging was performed in the alternating contact mode (AC mode). AFM probes were single-crystal silicon microcantilevers AC240TS (Olympus, Japan) of 70 kHz resonance frequency and 1.8 N m^{-1} spring constant with a nominal tip radius smaller than 9 nm. For imaging in the dry state the surfaces from imaging in liquid were used, subsequent to drying under nitrogen flow.

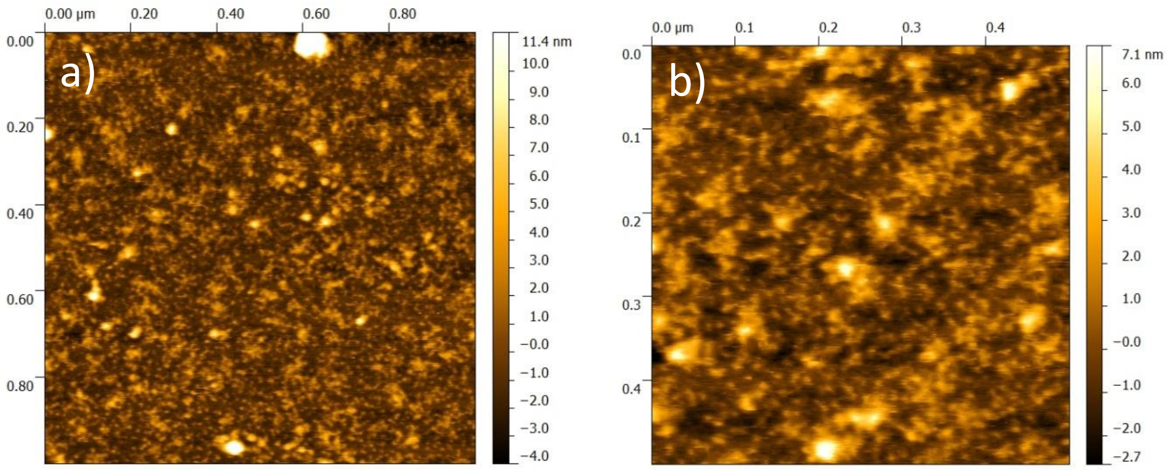

Figure S13. Nucleolin AFM imaging in liquid; a) 1 µm scale, b) 0.5µm scale

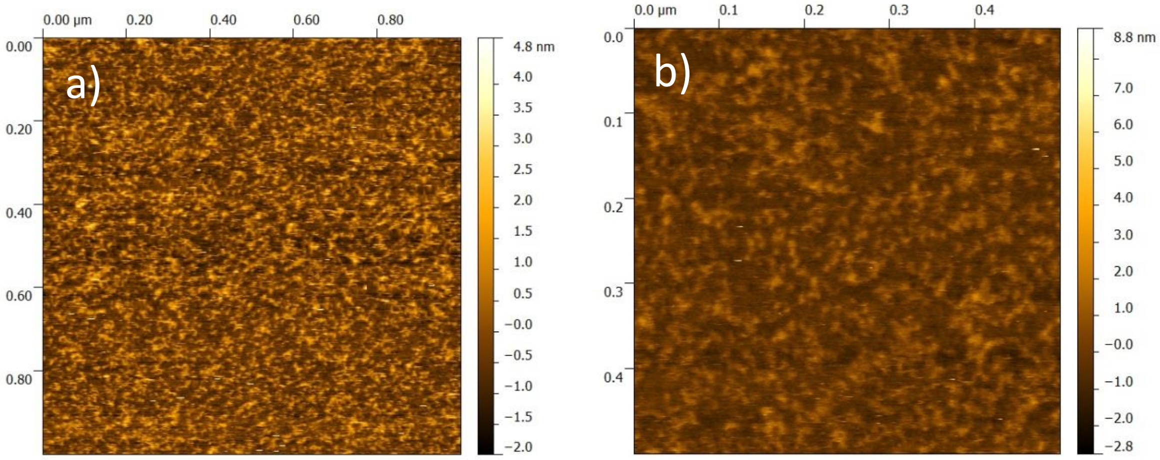

Figure S14. BSA AFM imaging in liquid; a) 1 µm scale, b) 0.5µm scale

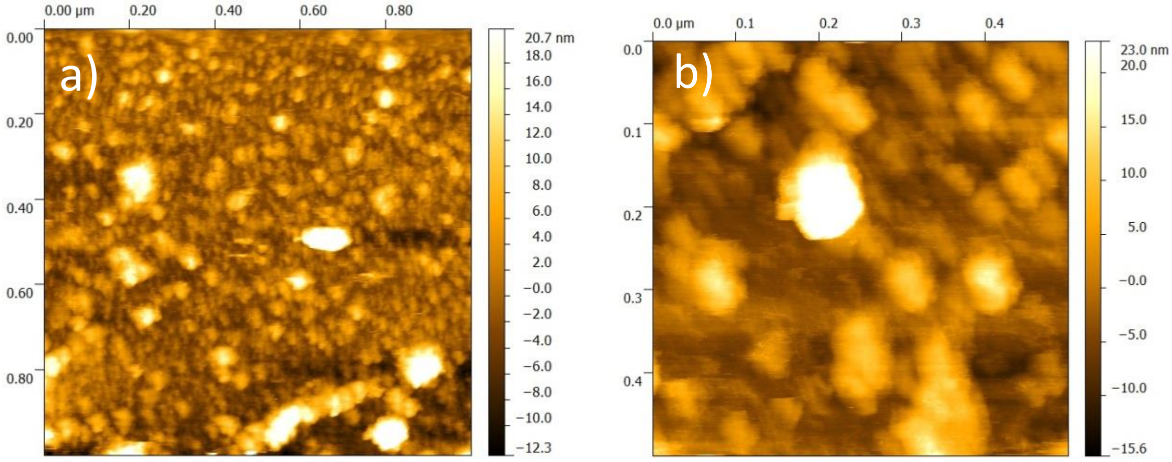

Figure S15. AFM imaging in liquid of PEGylated capsules on nucleolin modified silica surface;a) 1 µm scale, b) 0.5µm scale

6 Conclusions and Outlooks

Self-organization of macromolecules is an appealing, cost effective strategy for generating structures with tailored architecture, size, complexity as well as well-defined localization of functional groups. Along this line, self-assembling molecules based on DNA are especially attractive for the medical and industrial fields due to the functionality originating from the DNA strand. The main aim of this doctoral research was to produce novel DNA “chimeras” and study various modes of structure formation leading to the assembly of different morphologies. Establishment of the mechanisms of organization combined with evaluation of their functionality through simple hybridization assays or more sophisticated specific antibody-antigen like interactions could be evidenced further, which advanced the understanding of DNA-copolymer based structure formation beyond self-assembly.

The amphiphilic chimeras composed of flexible, hydrophilic nucleic acid strands and the hydrophobic poly(oxazoline) were obtained through well-established synthetic routes like solid phase synthesis, solution coupling as well as an innovative approach of taking advantage of polymer crystallization and thiolene “click-chemistry”. These methodologies were used taking into consideration the physical as well as chemical characteristics of both building blocks. The resulting copolymers generated by solid phase synthesis and thiolene “click chemistry” are comb/graft macromolecules along which the grafting density of nucleic acid sequences could be varied. The studies of organization revealed the different formation modes of structure formation according to grafting density, which is inherent to ability of the macromolecule to engage in inter- or intramolecular interactions or both. Conjugation of the hydrophobic pseudo peptide poly(2-oxazoline) with the 12 mer DNA sequence resulted in the formation of an amphiphilic comb/graft copolymer which upon direct dissolution in water organizes into large hollow fibrillar structures what was evidenced through imaging techniques as well as SAXS. Kinetics studies as well as spectroscopic investigations of the secondary structure evidenced a nucleation dependent polymerization mechanism which is characteristic for the amyloid fibers. This copolymer hybrid could thus be considered as a simplified model for elucidating the mechanism of protein fibrillation, which is crucial when considering that amyloid fibers are associated with several neurodegenerative diseases.

Polymer crystallization assisted thiolene photosynthesis of an amphiphilic comb/graft DNA copolymer, consisting of a hydrophobic poly(2-oxazoline) backbone and hydrophilic short single stranded nucleic acid grafts was demonstrated to be considerably more efficient than solid phase synthesis. Due to the significant size of the synthetic polymer crystallites as well as very straightforward and efficient thiolene click chemistry the copolymer-DNA hybrid was obtained without tedious multistep synthesis routes or purification steps. Higher grafting ratio resulted in the formation of sub-micrometer size spherical structures in contrary to the fibers which were achieved with a hybrid of low nucleic acid strands grafting ratio. The structures were further shown to be functional throughout hybridization experiments which also evidenced the mechanical stability of these structures, which is of high potential for application in diagnostic or sensing, in which speciation is required.

The length and function of the nucleic acid grafts were eventually varied through the coupling of an aptamer selected in vitro to target specifically the immunoglobulin E (IgE) protein. The resulting copolymer exhibits surface activity and could thus be regarded as a high molecular weight analogue of a surfactant. It was proven that this copolymer can be used as an emulsifier in an emulsification process which stabilizes efficiently sub-micrometer size oil-in-water emulsion droplets. Functionality of the aptamer strand engaged in the structure formation was assessed by reflectometry, CLSM and AFM imaging. Combination of these advanced analytical techniques demonstrated that the aptamer remains functional subsequent coupling to the synthetic polymer, structure formation and locking of the structure through crosslinking polymerization. The biological-stimulus responsiveness of the structures is extremely appealing for pharmacological applications.

Emulsion templated self-assembly paves the way for encapsulation and delivery of hydrophobic anticancer drugs which in their pure form are very problematic to deliver. In order to control the active agent release and thus increase the therapeutic potential, charged droplets were covered with polyelectrolytes in order to assemble multilayer capsules. To increase the circulation rate, prolonged half-life and decrease of phagocytosis uptake, the outer layer of the capsule was PEGylated. With the purpose of targeted delivery the capsule surface was functionalized with the AS1411 aptamer which specifically recognizes the nucleolin protein overexpressed at the surface of cancer cells. As assessed by imaging and scattering techniques the generated structures were well defined with a size perfectly suited for drug delivery. Despite of the efforts to produce capsules that would delay the drug release as well as target the nucleolin cancer cell surface receptor, further improvements are still needed.

A natural perspective for the work concerning the impact of the grafting ratio on the mode of structure formation and interaction of the DNA-copolymers under investigation would be the synthesis of a wide range of PBOX-*g*-DNA copolymers with various numbers of grafts as well as molecular weight. This manipulation is expected to result in a plethora of exciting bioactive architectures as well as shed more light on the biohybrid self-assembly mechanism.

Emulsion templated self-assembly is an attractive strategy for design of drug delivery systems. However, keeping in mind the obstacles encountered in the project of targeted anticancer drug delivery, the outlook for the use of these structures is quite significant. First of all, the delayed controlled release approach requires drastic improvement. Multilevel crosslinking appears to be the suitable tool to reach this goal. Secondly, targeting failed with the approach described in this thesis. Improvement of the “grafting to” approach has to be implemented, in particular the ratio of aptamer to the non specific, protein repellent poly(ethylene glycol) (PEG) polymer. These issues have to be solved prior to proceed with in vitro and in vivo investigations.

Overall, the described work contributes to the elucidation of fundamental aspects of molecular hybrids self-assembly and evidences the potential for application of the resulting material. Outcomes of this work will be useful for further use of bioactive self-assembled structures in various scientific areas.

List of Publications

- *DNA-polymer conjugates*, In Biosynthetic Polymer Conjugates Advances in Polymer Science, **D. Kedracki**, N. Gour, I. Safir, K. Ngo, and C. Vebert-Nardin, DOI: 10.1007/12_2012_181, Springer-Verlag Berlin Heidelberg 2012
- *Self-Assembling Peptide-Nucleotide Hybrids: Morphological Consequences of Oligonucleotide Grafting to Pathogenic Amyloid Fibrils Forming Peptides*, N. Gour, **D. Kedracki**, I. Safir, K. Ngo, and C. Vebert-Nardin, Chem. Commun., 2012,48, 5440-5442
- *Polymer-aptamer hybrid emulsion templating yields bioresponsive nanocapsules*, **D. Kedracki**, P. Maroni, H. Schlaad and C. Nardin, Advanced Functional Materials (2014), 24(8), 1133-1139
- *Effect of the Interaction of the Amyloid β (1-42) Peptide with Short Single-Stranded Synthetic Nucleotide Sequences: Morphological Characterization of the Inhibition of Fibrils Formation and Fibrils Disassembly*, J.N. Abraham, **D. Kedracki**, E. Prado, C.Gourmel, P. Maroni, C. Nardin
- *Synthesis and Self-Assembly of a DNA Molecular Brush*, **D. Kedracki**, Ch. Mahshid, P. Maroni, H. Schlaad and C. Nardin, Biomacromolecules 2014 , 15 (9), pp 3375–3382
- *Hydrogen bonding induced formation of DNA-copolymer fibrils through amyloid-like nucleation polymerization mechanism*, **D. Kedracki**, S. K. Fillipov, N. Gour, H. Schlaad and C. Nardin, Macromolecular Rapid Communications DOI 10.1002/marc.201400728

Acknowledgments

First of all, I would like to express my deep gratitude to my supervisor prof. Corinne Nardin for accepting me as a PhD student, for her patient guidance, trust, encouragements, help, sympathy and advices during my PhD.

I am grateful to prof. Helmut Schlaad from the University of Potsdam and Dr. Plinio Maroni from the University of Geneva for accepting to be member of the jury for my thesis.

I thank all the former and present members of the group for the warm atmosphere in the lab and especially Annelies Sels, Msc Fabien Chevasson, Dr. Jancy Abraham and Dr. Nidhi Ghour for the fruitful and enjoyable collaboration.

I am grateful to prof. Michal Borkovec for granting me the access to instruments required for my work. I would like to thank Dr. Plinio Maroni for sharing his unique skills regarding the AFM imaging and reflectometry measurements, the very nice collaboration and excellent scientific ideas. I would like to as well acknowledge Dr. Istvan Szilagyi and Dr. Gregor Trefalt for their help concerning light scattering measurement.

I express my deepest gratitude to Magali Cissokho and Anne-Marie Loup for sorting out all the bureaucratic issues as well as to Oliver Vassalli for helping me to resolve technical issue whenever it came to.

I would like to acknowledge members of the Bioimaging Center, especially Dr. Christopher Bauer and Jérôme Bosset for the time invested in showing me imaging techniques, their help and professional attitude.

At the end, great thanks to my family for their encouragement in pursuing a scientific career and special thanks to Anna Polomska for all of her support.

Table of Figures

Table of Equations

References

[1] R. Breslow, Biomimetic Chemistry: Biology as an Inspiration, Journal of Biological Chemistry, 284 (2009) 1337-1342.

[2] R. Breslow, Biomimetic chemistry: a frontier at the chemistry/biology interface, Chemistry & Biology, 5 (1998) R27-R28.

[3] K. Matyjaszewski, N.V. Tsarevsky, Nanostructured functional materials prepared by atom transfer radical polymerization, Nature Chemistry, 1 (2009) 276-288.

[4] J. Rodriguez-Hernandez, F. Checot, Y. Gnanou, S. Lecommandoux, Toward 'smart' nano-objects by self-assembly of block copolymers in solution, Prog. Polym. Sci., 30 (2005) 691-724.

[5] J.H. Kim, M. Lee, J.S. Lee, C.B. Park, Self-Assembled Light-Harvesting Peptide Nanotubes for Mimicking Natural Photosynthesis, Angewandte Chemie International Edition, 51 (2012) 517-520.

[6] Y. Zhao, F. Sakai, L. Su, Y. Liu, K. Wei, G. Chen, M. Jiang, Progressive Macromolecular Self-Assembly: From Biomimetic Chemistry to Bio-Inspired Materials, Advanced Materials, 25 (2013) 5215-5256.

[7] P. Alivisatos, The use of nanocrystals in biological detection, Nature Biotechnology, 22 (2004) 47-52.

[8] J.N. Anker, W.P. Hall, O. Lyandres, N.C. Shah, J. Zhao, R.P. Van Duyne, Biosensing with plasmonic nanosensors, Nature Materials, 7 (2008) 442-453.

[9] R. Thiruvengadathan, V. Korampally, A. Ghosh, N. Chanda, K. Gangopadhyay, S. Gangopadhyay, Nanomaterial processing using self-assembly-bottom-up chemical and biological approaches, Reports on Progress in Physics, 76 (2013).

[10] D.R.T. Jonathan W. Steed, Karl J. Wallace, Core Concepts in Supramolecular Chemistry and Nanochemistry, John Wiley & Sons, (2007).

[11] G. Chen, M. Jiang, Cyclodextrin-based inclusion complexation bridging supramolecular chemistry and macromolecular self-assembly, Chemical Society Reviews, 40 (2011) 2254-2266.

[12] Z. Zhang, R. Ma, L. Shi, Cooperative Macromolecular Self-Assembly toward Polymeric Assemblies with Multiple and Bioactive Functions, Accounts of Chemical Research, 47 (2014) 1426-1437.

[13] M. Sarikaya, Biomimetics: Materials fabrication through biology, Proceedings of the National Academy of Sciences of the United States of America, 96 (1999) 14183-14185.

[14] S. Weiner, H.D. Wagner, The material bone: Structure mechanical function relations, Annual Review of Materials Science, 28 (1998) 271-298.

[15] Y.S. Lee, Self-Assembly and Nanotechnology: A Force Balance Approach, (2007).

[16] Z.-G. Wang, B. Ding, DNA-Based Self-Assembly for Functional Nanomaterials, Advanced Materials, 25 (2013) 3905-3914.

[17] M.J. Hannon, Supramolecular DNA recognition, Chemical Society Reviews, 36 (2007) 280-295.

[18] R.R. Sinden, DNA Structure and Function, Elsevier Academic Press, Inc, (1994).

[19] T. Catherall, D. Huskisson, S. McAdams, A. Vijayaraghavan, Self-assembly of one dimensional DNA-templated structures, Journal of Materials Chemistry C, 2 (2014) 6895-6920.

[20] N. Stephanopoulos, J.H. Ortony, S.I. Stupp, Self-assembly for the synthesis of functional biomaterials, Acta Materialia, 61 (2013) 912-930.

[21] Z.-G. Wang, B. Ding, Engineering DNA Self-Assemblies as Templates for Functional Nanostructures, Accounts of Chemical Research, 47 (2014) 1654-1662.

[22] S.J. Holder, N.A.J.M. Sommerdijk, New micellar morphologies from amphiphilic block copolymers: disks, toroids and bicontinuous micelles, Polymer Chemistry, 2 (2011) 1018-1028.

[23] E.L. Thomas, Templated self assembly of block copolymers: Top down helps bottom up, Abstracts of Papers of the American Chemical Society, 233 (2007).

[24] F.S. Bates, G.H. Fredrickson, Block copolymers - Designer soft materials, Physics Today, 52 (1999) 32-38.

[25] G. Riess, Micellization of block copolymers, Prog. Polym. Sci., 28 (2003) 1107-1170.

[26] S.B. Darling, Directing the self-assembly of block copolymers, Prog. Polym. Sci., 32 (2007) 1152-1204.
[27] N. Hadjichristidis, M. Pitsikalis, H. Iatrou, Synthesis of block copolymers, in: V. Abetz (Ed.) Block Copolymers I, 2005, pp. 1-124.
[28] P.C. Hiemenz, T.P. Lodge, Polymer Chemistry, Second Edition, Taylor & Francis, 2007.
[29] I.W. Hamley, Introduction to soft matter: polymers, colloids amphiphiles, and liquid crystals, Wiley, 2000.
[30] R.J. Hunter, Foundations of Colloid Science, Oxford University Press, 2001.
[31] G.S. Misra, Introductory Polymer Chemistry, J. Wiley & Sons, 1993.
[32] J.W. Goodwin, Colloids and Interfaces with Surfactants and Polymers: An Introduction, Wiley, 2004.
[33] D.J. Shaw, Introduction to Colloid and Surface Chemistry, Butterworth-Heinemann, 1992.
[34] D.F. Evans, H. Wennerström, The Colloidal Domain: Where Physics, Chemistry, Biology, and Technology Meet, Wiley, 1999.
[35] I. Wyman, G. Njikang, G. Liu, When emulsification meets self-assembly: The role of emulsification in directing block copolymer assembly, Prog. Polym. Sci., 36 (2011) 1152-1183.
[36] h. Li Lu, G. Zhao, Theory of microphase separation in block copolymers, Journal of Dalian Institute of Technology, 19 (1980) 1-13.
[37] U. Breiner, U. Krappe, E.L. Thomas, R. Stadler, Structural characterization of the "knitting pattern" in polystyrene-block-poly(ethylene-co-butylene)-block-poly(methylmethacryla te) triblock copolymers, Macromolecules, 31 (1998) 135-141.
[38] D.A. Hajduk, P.E. Harper, S.M. Gruner, C.C. Honeker, G. Kim, E.L. Thomas, L.J. Fetters, The Gyroid: A New Equilibrium Morphology in Weakly Segregated Diblock Copolymers, Macromolecules, 27 (1994) 4063-4075.
[39] T. Hashimoto, T. Kawamura, M. Harada, H. Tanaka, Small-Angle Scattering from Hexagonally Packed Cylindrical Particles with Paracrystalline Distortion, Macromolecules, 27 (1994) 3063-3072.
[40] T.A. Shefelbine, M.E. Vigild, M.W. Matsen, D.A. Hajduk, M.A. Hillmyer, E.L. Cussler, F.S. Bates, Core-shell gyroid morphology in a poly(isoprene-block-styrene-block-dimethylsiloxane) triblock copolymer, J. Am. Chem. Soc., 121 (1999) 8457-8465.
[41] M.W. Matsen, M. Schick, Stable and Unstable Phases of a Linear Multiblock Copolymer Melt, Macromolecules, 27 (1994) 7157-7163.
[42] M.W. Matsen, M. Schick, Microphase separation of star-block copolymer melts, Macromolecules, 27 (1994) 6761-6767.
[43] L. Leibner, Theory of microphase separation in block copolymers, Macromolecules, 13 (1980) 1602-1617.
[44] M.W. Matsen, F.S. Bates, Unifying weak- and strong-segregation block copolymer theories, Macromolecules, 29 (1996) 1091-1098.
[45] G.M. Whitesides, B. Grzybowski, Self-Assembly at All Scales, Science, 295 (2002) 2418-2421.
[46] P. Ball, The Self-Made Tapestry: Pattern Formation in Nature, Oxford University Press, New York, (1999).
[47] D. Philp, J.F. Stoddart, Self-assembly in natural and unnatural systems, Angew. Chem.-Int. Edit., 35 (1996) 1155-1196.
[48] C. Wang, Z. Wang, X. Zhang, Amphiphilic Building Blocks for Self-Assembly: From Amphiphiles to Supra-amphiphiles, Accounts of Chemical Research, 45 (2012) 608-618.
[49] L. Isaacs, Chin, D.N., Bowden, N., Xia, Y., and Whitesides, G.M., Supramolecular Materials and Technologies, John Wiley & Sons Ltd., 1999, 4., (1999).
[50] M. Fialkowski, K.J.M. Bishop, R. Klajn, S.K. Smoukov, C.J. Campbell, B.A. Grzybowski, Principles and Implementations of Dissipative (Dynamic) Self-Assembly, The Journal of Physical Chemistry B, 110 (2006) 2482-2496.
[51] P.A. Kralchevsky, K.D. Danov, E.S. Basheva, Hydration force due to the reduced screening of the electrostatic repulsion in few-nanometer-thick films, Current Opinion in Colloid & Interface Science, 16 (2011) 517-524.

[52] S. Forster, T. Plantenberg, From self-organizing polymers to nanohybrid and biomaterials, Angew. Chem.-Int. Edit., 41 (2002) 689-714.

[53] A. Rösler, G.W.M. Vandermeulen, H.-A. Klok, Advanced drug delivery devices via self-assembly of amphiphilic block copolymers, Advanced Drug Delivery Reviews, 64, Supplement (2012) 270-279.

[54] S. Lim, H.-P. de Hoog, A. Parikh, M. Nallani, B. Liedberg, Hybrid, Nanoscale Phospholipid/Block Copolymer Vesicles, Polymers, 5 (2013) 1102-1114.

[55] Z. Ahmad, A. Shah, M. Siddiq, H.-B. Kraatz, Polymeric micelles as drug delivery vehicles, Rsc Advances, 4 (2014) 17028-17038.

[56] M. Oba, Study on Development of Polymeric Micellar Gene Carrier and Evaluation of Its Functionality, Biological & Pharmaceutical Bulletin, 36 (2013) 1045-1051.

[57] S. Egli, H. Schlaad, N. Bruns, W. Meier, Functionalization of Block Copolymer Vesicle Surfaces, Polymers, 3 (2011) 252-280.

[58] A.T. Nagasamy Venkatesh Dhandapani, Gota Sandip, Ayush Shrestha, Niroj Shresta, Rajan Sharma Bhattrai, Liposomes as novel drug delivery system: A comprehensive review, International Journal Of Pharmaceutical Sciences, 4(2) (2013) 187-193.

[59] Z. Drulis-Kawa, A. Dorotkiewicz-Jach, Liposomes as delivery systems for antibiotics, International Journal of Pharmaceutics, 387 (2010) 187-198.

[60] M.L. Adams, A. Lavasanifar, G.S. Kwon, Amphiphilic block copolymers for drug delivery, Journal of Pharmaceutical Sciences, 92 (2003) 1343-1355.

[61] M. Antonietti, S. Forster, Vesicles and liposomes: A self-assembly principle beyond lipids, Advanced Materials, 15 (2003) 1323-1333.

[62] R.J.R.W. Peters, M. Marguet, S. Marais, M.W. Fraaije, J.C.M. van Hest, S. Lecommandoux, Cascade Reactions in Multicompartmentalized Polymersomes, Angew. Chem.-Int. Edit., 53 (2014) 146-150.

[63] P.V. Pawar, S.V. Gohil, J.P. Jain, N. Kumar, Functionalized polymersomes for biomedical applications, Polymer Chemistry, 4 (2013) 3160-3176.

[64] T. Rosenkranz, A. Katranidis, D. Atta, I. Gregor, J. Enderlein, M. Grzelakowski, P. Rigler, W. Meier, J. Fitter, Observing Proteins as Single Molecules Encapsulated in Surface-Tethered Polymeric Nanocontainers, Chembiochem, 10 (2009) 702-709.

[65] M. Spulber, P. Baumann, S.S. Saxer, U. Pieles, W. Meier, N. Bruns, Poly(N-vinylpyrrolidone)-Poly(dimethylsiloxane)-Based Polymersome Nanoreactors for Laccase-Catalyzed Biotransformations, Biomacromolecules, 15 (2014) 1469-1475.

[66] J.N. Israelachvili, D.J. Mitchell, B.W. Ninham, THEORY OF SELF-ASSEMBLY OF HYDROCARBON AMPHIPHILES INTO MICELLES AND BILAYERS, Journal of the Chemical Society-Faraday Transactions Ii, 72 (1976) 1525-1568.

[67] I.J. N., Intermolecular and surface forces: revised third edition, Academic Press, (2011).

[68] T. Nicolai, O. Colombani, C. Chassenieux, Dynamic polymeric micelles versus frozen nanoparticles formed by block copolymers, Soft Matter, 6 (2010) 3111-3118.

[69] D. J.C. Van Hest, D.A.P., Baars, M.W.P.L., Van Genderen, M.H.P., Meijer, E.W., Polystyrene-dendrimer amphiphilic block copolymers with a generation-dependent aggregation, Science, 268 (1995).

[70] K.J.M. Bishop, C.E. Wilmer, S. Soh, B.A. Grzybowski, Nanoscale Forces and Their Uses in Self-Assembly, Small, 5 (2009) 1600-1630.

[71] G. Foffi, G.D. McCullagh, A. Lawlor, E. Zaccarelli, K.A. Dawson, F. Sciortino, P. Tartaglia, D. Pini, G. Stell, Phase equilibria and glass transition in colloidal systems with short-ranged attractive interactions: Application to protein crystallization, Physical Review E, 65 (2002) 031407.

[72] C.B. Murray, C.R. Kagan, M.G. Bawendi, Self-Organization of CdSe Nanocrystallites into Three-Dimensional Quantum Dot Superlattices, Science, 270 (1995) 1335-1338.

[73] S.A. Harfenist, Z.L. Wang, M.M. Alvarez, I. Vezmar, R.L. Whetten, Highly Oriented Molecular Ag Nanocrystal Arrays, The Journal of Physical Chemistry, 100 (1996) 13904-13910.

[74] M.E. Leunissen, C.G. Christova, A.-P. Hynninen, C.P. Royall, A.I. Campbell, A. Imhof, M. Dijkstra, R. van Roij, A. van Blaaderen, Ionic colloidal crystals of oppositely charged particles, Nature, 437 (2005) 235-240.
[75] B.A. Grzybowski, A. Winkleman, J.A. Wiles, Y. Brumer, G.M. Whitesides, Electrostatic self-assembly of macroscopic crystals using contact electrification, Nat Mater, 2 (2003) 241-245.
[76] A.M. Kalsin, M. Fialkowski, M. Paszewski, S.K. Smoukov, K.J.M. Bishop, B.A. Grzybowski, Electrostatic Self-Assembly of Binary Nanoparticle Crystals with a Diamond-Like Lattice, Science, 312 (2006) 420-424.
[77] S.K. Smoukov, K.J.M. Bishop, B. Kowalczyk, A.M. Kalsin, B.A. Grzybowski, Electrostatically “Patchy” Coatings via Cooperative Adsorption of Charged Nanoparticles, J. Am. Chem. Soc., 129 (2007) 15623-15630.
[78] E. Hao, B. Yang, J. Zhang, X. Zhang, J. Sun, J. Shen, Assembly of alternating TiO2/v\CdS nanoparticle composite films, Journal of Materials Chemistry, 8 (1998) 1327-1328.
[79] D. Lee, M.F. Rubner, R.E. Cohen, All-Nanoparticle Thin-Film Coatings, Nano Letters, 6 (2006) 2305-2312.
[80] A.N. Shipway, M. Lahav, R. Gabai, I. Willner, Investigations into the Electrostatically Induced Aggregation of Au Nanoparticles†, Langmuir, 16 (2000) 8789-8795.
[81] E.J.W. Verwey, Theory of the Stability of Lyophobic Colloids, The Journal of Physical and Colloid Chemistry, 51 (1947) 631-636.
[82] J.F.L. Duval, F.A.M. Leermakers, H.P. van Leeuwen, Electrostatic Interactions between Double Layers: Influence of Surface Roughness, Regulation, and Chemical Heterogeneities, Langmuir, 20 (2004) 5052-5065.
[83] H. Huang, E. Ruckenstein, Interaction force between two charged plates immersed in a solution of charged particles. Coupling between double layer and depletion forces, Langmuir, 20 (2004) 5412-5417.
[84] S.S. Sheiko, B.S. Sumerlin, K. Matyjaszewski, Cylindrical molecular brushes: Synthesis, characterization, and properties, Prog. Polym. Sci., 33 (2008) 759-785.
[85] J.M.H.M. Scheutjens, G.J. Fleer, Interaction between two adsorbed polymer layers, Macromolecules, 18 (1985) 1882-1900.
[86] W.C.K. Poon, The physics of a model colloid-polymer mixture, Journal of Physics-Condensed Matter, 14 (2002) R859-R880.
[87] J. Sharma, R. Chhabra, A. Cheng, J. Brownell, Y. Liu, H. Yan, Control of Self-Assembly of DNA Tubules Through Integration of Gold Nanoparticles, Science, 323 (2009) 112-116.
[88] D. Baranov, A. Fiore, M. van Huis, C. Giannini, A. Falqui, U. Lafont, H. Zandbergen, M. Zanella, R. Cingolani, L. Manna, Assembly of Colloidal Semiconductor Nanorods in Solution by Depletion Attraction, Nano Letters, 10 (2010) 743-749.
[89] A. Nicholls, K.A. Sharp, B. Honig, Protein folding and association: Insights from the interfacial and thermodynamic properties of hydrocarbons, Proteins: Structure, Function, and Bioinformatics, 11 (1991) 281-296.
[90] J.Y. Lehtonen, J.M. Holopainen, P.K. Kinnunen, Evidence for the formation of microdomains in liquid crystalline large unilamellar vesicles caused by hydrophobic mismatch of the constituent phospholipids, Biophysical Journal, 70 (1996) 1753-1760.
[91] T. Yamaguchi, T. Matsuoka, S. Koda, Mode-coupling study on the dynamics of hydrophobic hydration, The Journal of Chemical Physics, 120 (2004) 7590-7601.
[92] T. Yamaguchi, T. Matsuoka, S. Koda, Mode-coupling study on the dynamics of hydrophobic hydration II: Aqueous solutions of benzene and rare gases, Physical Chemistry Chemical Physics, 8 (2006) 737-745.
[93] H.S. Frank, M.W. Evans, Free Volume and Entropy in Condensed Systems III. Entropy in Binary Liquid Mixtures; Partial Molal Entropy in Dilute Solutions; Structure and Thermodynamics in Aqueous Electrolytes, The Journal of Chemical Physics, 13 (1945) 507-532.
[94] J.L. Parker, P.M. Claesson, P. Attard, Bubbles, cavities, and the long-ranged attraction between hydrophobic surfaces, The Journal of Physical Chemistry, 98 (1994) 8468-8480.

[95] J.W.G. Tyrrell, P. Attard, Images of Nanobubbles on Hydrophobic Surfaces and Their Interactions, Physical Review Letters, 87 (2001) 176104.

[96] R. Steitz, T. Gutberlet, T. Hauss, B. Klösgen, R. Krastev, S. Schemmel, A.C. Simonsen, G.H. Findenegg, Nanobubbles and Their Precursor Layer at the Interface of Water Against a Hydrophobic Substrate, Langmuir, 19 (2003) 2409-2418.

[97] T.R. Jensen, M. Østergaard Jensen, N. Reitzel, K. Balashev, G.H. Peters, K. Kjaer, T. Bjørnholm, Water in Contact with Extended Hydrophobic Surfaces: Direct Evidence of Weak Dewetting, Physical Review Letters, 90 (2003) 086101.

[98] P. Ball, Chemical physics: How to keep dry in water, Nature, 423 (2003) 25-26.

[99] K. Abe, Y. Miyamoto, S. Chikazumi, Magnetocrystalline Anisotropy of Low Temperature Phase of Magnetite, Journal of the Physical Society of Japan, 41 (1976) 1894-1902.

[100] T. Steiner, The Hydrogen Bond in the Solid State, Angewandte Chemie International Edition, 41 (2002) 48-76.

[101] J.-M. Lehn, Perspectives in Supramolecular Chemistry—From Molecular Recognition towards Molecular Information Processing and Self-Organization, Angewandte Chemie International Edition in English, 29 (1990) 1304-1319.

[102] S.R. Johnson, S.D. Evans, R. Brydson, Influence of a Terminal Functionality on the Physical Properties of Surfactant-Stabilized Gold Nanoparticles, Langmuir, 14 (1998) 6639-6647.

[103] L. Cusack, R. Rizza, A. Gorelov, D. Fitzmaurice, Self-Assembly and Subsequent Self-Organization of a Semiconductor Nanocrystallite Superlattice, Angewandte Chemie International Edition in English, 36 (1997) 848-851.

[104] M. Kimura, S. Kobayashi, T. Kuroda, K. Hanabusa, H. Shirai, Assembly of Gold Nanoparticles into Fibrous Aggregates Using Thiol-Terminated Gelators, Advanced Materials, 16 (2004) 335-338.

[105] A.K. Boal, F. Ilhan, J.E. DeRouchey, T. Thurn-Albrecht, T.P. Russell, V.M. Rotello, Self-assembly of nanoparticles into structured spherical and network aggregates, Nature, 404 (2000) 746-748.

[106] H. Xiaoge, C. Wenlong, W. Tie, W. Erkang, D. Shaojun, Well-ordered end-to-end linkage of gold nanorods, Nanotechnology, 16 (2005) 2164-2169.

[107] K.G. Thomas, S. Barazzouk, B.I. Ipe, S.T.S. Joseph, P.V. Kamat, Uniaxial Plasmon Coupling through Longitudinal Self-Assembly of Gold Nanorods, The Journal of Physical Chemistry B, 108 (2004) 13066-13068.

[108] Z. Sun, W. Ni, Z. Yang, X. Kou, L. Li, J. Wang, pH-Controlled Reversible Assembly and Disassembly of Gold Nanorods, Small, 4 (2008) 1287-1292.

[109] H. Schlaad, M. Antonietti, Block copolymers with amino acid sequences: Molecular chimeras of polypeptides and synthetic polymers, European Physical Journal E, 10 (2003) 17-23.

[110] H.G. Borner, H. Schlaad, Bioinspired functional block copolymers, Soft Matter, 3 (2007) 394-408.

[111] D. Kedracki, I. Safir, N. Gour, N. Kien Xuan, C. Vebert-Nardin, DNA-Polymer Conjugates: From Synthesis, Through Complex Formation and Self-assembly to Applications, Bio-Synthetic Polymer Conjugates, 253 (2013) 115-149.

[112] Y. Singh, P. Murat, E. Defrancq, Recent developments in oligonucleotide conjugation, Chemical Society Reviews, 39 (2010) 2054-2070.

[113] F.E. Alemdaroglu, N.C. Alemdaroglu, P. Langguth, A. Herrmann, DNA block copolymer micelles - A combinatorial tool for cancer Nanotechnology, Advanced Materials, 20 (2008) 899-+.

[114] M. Kwak, A. Herrmann, Nucleic Acid/Organic Polymer Hybrid Materials: Synthesis, Superstructures, and Applications, Angewandte Chemie International Edition, 49 (2010) 8574-8587.

[115] M. Kwak, A. Herrmann, Nucleic Acid Polymers and DNA Synthetic Polymer Hybrid Materials Generated by Molecular Biology Techniques, in: Materials Science and Technology, Wiley-VCH Verlag GmbH & Co. KGaA, 2006.

[116] M. Kwak, A. Herrmann, Nucleic acid amphiphiles: synthesis and self-assembled nanostructures, Chemical Society Reviews, 40 (2011) 5745-5755.

[117] T. Schnitzler, A. Herrmann, DNA Block Copolymers: Functional Materials for Nanoscience and Biomedicine, Accounts of Chemical Research, 45 (2012) 1419-1430.

[118] A.V. Kachalova, D.A. Stetsenko, M.J. Gait, T.S. Oretskaya, Synthesis of oligonucleotide 2′-conjugates via amide bond formation in solution, Bioorganic & Medicinal Chemistry Letters, 14 (2004) 801-804.

[119] M. Oishi, T. Hayama, Y. Akiyama, S. Takae, A. Harada, Y. Yamasaki, F. Nagatsugi, S. Sasaki, Y. Nagasaki, K. Kataoka, Supramolecular Assemblies for the Cytoplasmic Delivery of Antisense Oligodeoxynucleotide: Polyion Complex (PIC) Micelles Based on Poly(ethylene glycol)-SS-Oligodeoxynucleotide Conjugate, Biomacromolecules, 6 (2005) 2449-2454.

[120] T.S. Zatsepin, T.S. Oretskaya, Synthesis and Applications of Oligonucleotide□Carbohydrate Conjugates, Chemistry & Biodiversity, 1 (2004) 1401-1417.

[121] M. Ballico, S. Drioli, F. Morvan, L. Xodo, G.M. Bonora, Triple, MPEG-Conjugated, Helix-Forming Oligonucleotides (TRIPEGXs): Liquid-Phase Synthesis of Natural and Chimeric "All-Purine" Sequences Linked to High Molecular Weight Poly(ethylene glycols), Bioconjugate Chemistry, 12 (2001) 719-725.

[122] R. Duncan, The dawning era of polymer therapeutics, Nat Rev Drug Discov, 2 (2003) 347-360.

[123] F. Teixeira Jr, P. Rigler, C. Vebert-Nardin, Nucleo-copolymers: oligonucleotide-based amphiphilic diblock copolymers, Chemical Communications, (2007) 1130-1132.

[124] A.H. El-Sagheer, T. Brown, Click chemistry with DNA, Chemical Society Reviews, 39 (2010) 1388-1405.

[125] G. Pourceau, A. Meyer, J.-J. Vasseur, F. Morvan, Synthesis of Mannose and Galactose Oligonucleotide Conjugates by Bi-click chemistry, The Journal of Organic Chemistry, 74 (2009) 1218-1222.

[126] C.J. Yang, M. Pinto, K. Schanze, W. Tan, Direct Synthesis of an Oligonucleotide–Poly(phenylene ethynylene) Conjugate with a Precise One-to-One Molecular Ratio, Angewandte Chemie International Edition, 44 (2005) 2572-2576.

[127] I.P. Beletskaya, G.V. Latyshev, A.V. Tsvetkov, N.V. Lukashev, The nickel-catalyzed Sonogashira–Hagihara reaction, Tetrahedron Letters, 44 (2003) 5011-5013.

[128] S.E. Averick, S.K. Dey, D. Grahacharya, K. Matyjaszewski, S.R. Das, Solid-Phase Incorporation of an ATRP Initiator for Polymer–DNA Biohybrids, Angewandte Chemie, 126 (2014) 2777-2782.

[129] X. Lou, L. He, DNA-Accelerated Atom Transfer Radical Polymerization on a Gold Surface, Langmuir, 22 (2006) 2640-2646.

[130] X. Lou, C. Wang, L. He, Core−Shell Au Nanoparticle Formation with DNA−Polymer Hybrid Coatings Using Aqueous ATRP, Biomacromolecules, 8 (2007) 1385-1390.

[131] P. He, L. He, Synthesis of Surface-Anchored DNA−Polymer Bioconjugates Using Reversible Addition−Fragmentation Chain Transfer Polymerization, Biomacromolecules, 10 (2009) 1804-1809.

[132] T. Owen, Fundamentals of Modern UV-visible Spectroscopy: Primer, Agilent Technologies, 2000.

[133] P. Atkins, J. de Paula, Atkins' physical chemistry, Oxford University Press, 2014.

[134] A. Alvarez-Ordóñez, D.J.M. Mouwen, M. López, M. Prieto, Fourier transform infrared spectroscopy as a tool to characterize molecular composition and stress response in foodborne pathogenic bacteria, Journal of Microbiological Methods, 84 (2011) 369-378.

[135] D.H. Williams, I. Fleming, Spectroscopic Methods in Organic Chemistry, McGraw-Hill, 2008.

[136] G. Ramer, B. Lendl, Attenuated Total Reflection Fourier Transform Infrared Spectroscopy, in: Encyclopedia of Analytical Chemistry, John Wiley & Sons, Ltd, 2006.

[137] http://www.chromacademy.com/lms/sco533/15-infrared-spectroscopy-attenuated-total-reflectance.html?fChannel=14&fCourse=77&fSco=533&fPath=sco533/15-infrared-spectroscopy-attenuated-total-reflectance.html.

[138] D. Clarke, Circular Dichroism and Its Use in Protein-Folding Studies, in: A.F. Hill, K.J. Barnham, S.P. Bottomley, R. Cappai (Eds.) Protein Folding, Misfolding, and Disease, Humana Press, 2011, pp. 59-72.

[139] S.R. Martin, M.J. Schilstra, G. Siligardi, Chapter 7 Circular Dichroism, in: Biophysical Approaches Determining Ligand Binding to Biomolecular Targets: Detection, The Royal Society of Chemistry, 2011, pp. 226-246.

[140] R.W. Woody, [4] Circular dichroism, in: S. Kenneth (Ed.) Method Enzymol., Academic Press, 1995, pp. 34-71.

[141] T. Taniguchi, T. Usuki, Circular Dichroism Spectroscopy, in: Supramolecular Chemistry, John Wiley & Sons, Ltd, 2012.

[142] L.F. Marvin, M.A. Roberts, L.B. Fay, Matrix-assisted laser desorption/ionization time-of-flight mass spectrometry in clinical chemistry, Clinica Chimica Acta, 337 (2003) 11-21.

[143] R. Liyanage, J.O. Lay, An Introduction to MALDI-TOF MS, in: Identification of Microorganisms by Mass Spectrometry, John Wiley & Sons, Inc., 2006, pp. 39-60.

[144] J.K. Lewis, J. Wei, G. Siuzdak, Matrix-Assisted Laser Desorption/Ionization Mass Spectrometry in Peptide and Protein Analysis, in: Encyclopedia of Analytical Chemistry, John Wiley & Sons, Ltd, 2006.

[145] A. Vertes, R.D. Levine, SUBLIMATION VERSUS FRAGMENTATION IN MATRIX-ASSISTED LASER DESORPTION, Chemical Physics Letters, 171 (1990) 284-290.

[146] R.E. Johnson, B.U.R. Sundqvist, LASER-PULSE EJECTION OF ORGANIC-MOLECULES FROM A MATRIX - LESSONS FROM FAST-ION-INDUCED EJECTION, Rapid Communications in Mass Spectrometry, 5 (1991) 574-578.

[147] J.C. Dijt, M.A.C. Stuart, G.J. Fleer, Reflectometry as a tool for adsorption studies, Advances in Colloid and Interface Science, 50 (1994) 79-101.

[148] T. Gao, J. Lu, L.J. Rothberg, Biomolecular Sensing Using Near-Null Single Wavelength Arrayed Imaging Reflectometry, Anal. Chem., 78 (2006) 6622-6627.

[149] E. Özkumur, J.W. Needham, D.A. Bergstein, R. Gonzalez, M. Cabodi, J.M. Gershoni, B.B. Goldberg, M.S. Ünlü, Label-free and dynamic detection of biomolecular interactions for high-throughput microarray applications, Proceedings of the National Academy of Sciences, 105 (2008) 7988-7992.

[150] M. Porus, P. Maroni, M. Borkovec, Highly-sensitive reflectometry setup capable of probing the electrical double layer on silica, Sensors and Actuators B-Chemical, 151 (2010) 250-255.

[151] M. Porus, P. Maroni, M. Borkovec, Structure of Adsorbed Polyelectrolyte Monolayers Investigated by Combining Optical Reflectometry and Piezoelectric Techniques, Langmuir, 28 (2012) 5642-5651.

[152] P.C. Hiemenz, R. Rajagopalan, Principles of Colloid and Surface Chemistry, Third Edition, Revised and Expanded, Taylor & Francis, 1997.

[153] J.W. Steed, P.A. Gale, Supramolecular Chemistry: From Molecules to Nanomaterials, Wiley, 2012.

[154] http://www.soft-matter.uni-tuebingen.de/index.html?dls.html.

[155] T. Zemb, P. Lindner, Neutrons, X-rays and Light: Scattering Methods Applied to Soft Condensed Matter, Elsevier, 2002.

[156] K. Kobayashi, C.-i. Huang, T.P. Lodge, Thermoreversible Gelation of Aqueous Methylcellulose Solutions, Macromolecules, 32 (1999) 7070-7077.

[157] P.A. Hassan, S. Rana, G. Verma, Making Sense of Brownian Motion: Colloid Characterization by Dynamic Light Scattering, Langmuir, (2014).

[158] B. Chu, B.S. Hsiao, Small-Angle X-ray Scattering of Polymers, Chemical Reviews, 101 (2001) 1727-1762.

[159] J. Lipfert, S. Doniach, Small-angle X-ray scattering from RNA, proteins, and protein complexes, in: Annual Review of Biophysics and Biomolecular Structure, Annual Reviews, Palo Alto, 2007, pp. 307-327.

[160] D.I. Svergun, M.H.J. Koch, Small-angle scattering studies of biological macromolecules in solution, Reports on Progress in Physics, 66 (2003) 1735-1782.

[161] M.B. Kozin, V.V. Volkov, D.I. Svergun, ASSA, a Program for Three-Dimensional Rendering in Solution Scattering from Biopolymers, Journal of Applied Crystallography, 30 (1997) 811-815.

[162] M.V. Petoukhov, N.A.J. Eady, K.A. Brown, D.I. Svergun, Addition of Missing Loops and Domains to Protein Models by X-Ray Solution Scattering, Biophysical Journal, 83 (2002) 3113-3125.

[163] M.V. Petoukhov, D.I. Svergun, Global Rigid Body Modeling of Macromolecular Complexes against Small-Angle Scattering Data, Biophysical Journal, 89 (2005) 1237-1250.

[164] J.M.G. Cowie, Polymers: Chemistry and Physics of Modern Materials, 2nd Edition, Taylor & Francis, 1991.
[165] B. Voedisch, H. Thie, Size Exclusion Chromatography, in: R. Kontermann, S. Dübel (Eds.) Antibody Engineering, Springer Berlin Heidelberg, 2010, pp. 607-612.
[166] D.B. Murphy, M.W. Davidson, Confocal Laser Scanning Microscopy, in: Fundamentals of Light Microscopy and Electronic Imaging, John Wiley & Sons, Inc., 2012, pp. 265-305.
[167] S.W. Paddock, Confocal laser scanning microscopy, Biotechniques, 27 (1999) 992-+.
[168] S. Paddock, Principles and practices of laser scanning confocal microscopy, Mol Biotechnol, 16 (2000) 127-149.
[169] S. Paddock, Confocal Laser Scanning Light Microscopy, in: eLS, John Wiley & Sons, Ltd, 2001.
[170] A.R. Hand, Chapter 5 - Electron Microscopy, in: J.A. Glasel, M.P.D.P. Deutscher (Eds.) Introduction to Biophysical Methods for Protein and Nucleic Acid Research, Academic Press, San Diego, 1995, pp. 205-260.
[171] R. Kelsall, I.W. Hamley, M. Geoghegan, Nanoscale Science and Technology, Wiley, 2005.
[172] Y. Mai, A. Eisenberg, Self-assembly of block copolymers, Chemical Society Reviews, 41 (2012) 5969-5985.
[173] A.O. Moughton, M.A. Hillmyer, T.P. Lodge, Multicompartment Block Polymer Micelles, Macromolecules, 45 (2011) 2-19.
[174] M.M. Bloksma, S. Hoeppener, C. D'Haese, K. Kempe, U. Mansfeld, R.M. Paulus, J.-F. Gohy, U.S. Schubert, R. Hoogenboom, Self-assembly of chiral block and gradient copolymers, Soft Matter, 8 (2012) 165-172.
[175] E.B. Zhulina, O.V. Borisov, Theory of Block Polymer Micelles: Recent Advances and Current Challenges, Macromolecules, 45 (2012) 4429-4440.
[176] A.M. Mihut, J.J. Crassous, H. Schmalz, M. Drechsler, M. Ballauff, Self-assembly of crystalline-coil diblock copolymers in solution: experimental phase map, Soft Matter, 8 (2012) 3163-3173.
[177] X. Wang, M. Goswami, R. Kumar, B. G. Sumpter, J. Mays, Morphologies of block copolymers composed of charged and neutral blocks, Soft Matter, 8 (2012) 3036-3052.
[178] F.H. Schacher, P.A. Rupar, I. Manners, Functional Block Copolymers: Nanostructured Materials with Emerging Applications, Angewandte Chemie International Edition, 51 (2012) 7898-7921.
[179] S.A. Meeuwissen, M.F. Debets, J.C.M. van Hest, Copper-free click chemistry on polymersomes: pre- vs. post-self-assembly functionalisation, Polymer Chemistry, 3 (2012) 1783-1795.
[180] R. Novoa-Carballal, A.H.E. Muller, Synthesis of polysaccharide-b-PEG block copolymers by oxime click, Chem. Commun., 48 (2012) 3781-3783.
[181] Z. Zhao, L. Wang, Y. Liu, Z. Yang, Y.-M. He, Z. Li, Q.-H. Fan, D. Liu, pH-induced morphology-shifting of DNA-b-poly(propylene oxide) assemblies, Chem. Commun., 48 (2012) 9753-9755.
[182] A.C. Engler, D.K. Bonner, H.G. Buss, E.Y. Cheung, P.T. Hammond, The synthetic tuning of clickable pH responsive cationic polypeptides and block copolypeptides, Soft Matter, 7 (2011) 5627-5637.
[183] J.W. Robinson, C. Secker, S. Weidner, H. Schlaad, Thermoresponsive Poly(N-C3 glycine)s, Macromolecules, 46 (2013) 580-587.
[184] C. Bonduelle, S. Lecommandoux, Synthetic Glycopolypeptides as Biomimetic Analogues of Natural Glycoproteins, Biomacromolecules, 14 (2013) 2973-2983.
[185] J. Rzayev, Molecular Bottlebrushes: New Opportunities in Nanomaterials Fabrication, ACS Macro Letters, 1 (2012) 1146-1149.
[186] R. Hoogenboom, H. Schlaad, Bioinspired Poly(2-oxazoline)s, Polymers, 3 (2011) 467-488.
[187] K. Kempe, T. Neuwirth, J. Czaplewska, M. Gottschaldt, R. Hoogenboom, U.S. Schubert, Poly(2-oxazoline) glycopolymers with tunable LCST behavior, Polymer Chemistry, 2 (2011) 1737-1743.
[188] H. Schlaad, C. Diehl, A. Gress, M. Meyer, A.L. Demirel, Y. Nur, A. Bertin, Poly(2-oxazoline)s as Smart Bioinspired Polymers, Macromol. Rapid Commun., 31 (2010) 511-525.
[189] A. Gress, A. Volkel, H. Schlaad, Thio-click modification of poly 2-(3-butenyl)-2-oxazoline, Macromolecules, 40 (2007) 7928-7933.

[190] A. Gress, A. Heilig, B.M. Smarsly, M. Heydenreich, H. Schlaad, Hydrogen-Bonded Polymer Nanotubes in Water, Macromolecules, 42 (2009) 4244-4248.
[191] C. Diehl, I. Dambowsky, R. Hoogenboom, H. Schlaad, Self-Assembly of Poly(2-alkyl-2-oxazoline)s by Crystallization in Ethanol–Water Mixtures Below the Upper Critical Solution Temperature, Macromol. Rapid Commun., 32 (2011) 1753-1758.
[192] C. Diehl, H. Schlaad, Polyoxazoline-based Crystalline Microspheres for Carbohydrate-Protein Recognition, Chemistry-a European Journal, 15 (2009) 11469-11472.
[193] D. Kedracki, P. Maroni, H. Schlaad, C. Vebert-Nardin, Polymer-Aptamer Hybrid Emulsion Templating Yields Bioresponsive Nanocapsules, Adv. Funct. Mater., 24 (2014) 1133-1139.
[194] W. Burchard, Light Scattering Techniques, in: S. Ross-Murphy (Ed.) Physical Techniques for the Study of Food Biopolymers, Springer US, 1994, pp. 151-213.
[195] Z.K. Tuzar, P. Matijevic, Surface and colloid Science, Plemum Press: New York, (1993).
[196] J. Vesenka, M. Guthold, C.L. Tang, D. Keller, E. Delaine, C. Bustamante, Substrate preparation for reliable imaging of DNA molecules with the scanning force microscope, Ultramicroscopy, 42–44, Part 2 (1992) 1243-1249.
[197] D.D. Lasic, Liposomes: from physics to applications, Elsevier, 1993.
[198] F.E. Alemdaroglu, K. Ding, R. Berger, A. Herrmann, DNA-Templated Synthesis in Three Dimensions: Introducing a Micellar Scaffold for Organic Reactions, Angewandte Chemie International Edition, 45 (2006) 4206-4210.
[199] D.J. Gravert, K.D. Janda, Organic Synthesis on Soluble Polymer Supports: Liquid-Phase Methodologies, Chemical Reviews, 97 (1997) 489-510.
[200] C. Diehl, Functional Microspheres through Crystallization of Thermoresponsive Poly(2-oxazoline)s., Ph.D. Thesis, Universität Potsdam, (2009) 1-125.
[201] J. Razumovitch, K. de França, F. Kehl, M. Wiki, W. Meier, C. Vebert, Optimal Hybridization Efficiency Upon Immobilization of Oligonucleotide Double Helices, The Journal of Physical Chemistry B, 113 (2009) 8383-8390.
[202] C. Nardin, T. Hirt, J. Leukel, W. Meier, Polymerized ABA triblock copolymer vesicles, Langmuir, 16 (2000) 1035-1041.
[203] I.W. Hamley, Peptide fibrillization, Angew. Chem.-Int. Edit., 46 (2007) 8128-8147.
[204] J.S. Jeong, A. Ansaloni, R. Mezzenga, H.A. Lashuel, G. Dietler, Novel Mechanistic Insight into the Molecular Basis of Amyloid Polymorphism and Secondary Nucleation during Amyloid Formation, Journal of Molecular Biology, 425 (2013) 1765-1781.
[205] N.M. Kad, N.H. Thomson, D.P. Smith, D.A. Smith, S.E. Radford, β2-microglobulin and its deamidated variant, N17D form amyloid fibrils with a range of morphologies in vitro, Journal of Molecular Biology, 313 (2001) 559-571.
[206] J.D. Harper, P.T. Lansbury, Models of amyloid seeding in Alzheimier's disease and scrapie: Mechanistic truths and physiological consequences of the time-dependent solubility of amyloid proteins, Annu. Rev. Biochem., 66 (1997) 385-407.
[207] J. Adamcik, J.-M. Jung, J. Flakowski, P. De Los Rios, G. Dietler, R. Mezzenga, Understanding amyloid aggregation by statistical analysis of atomic force microscopy images, Nat Nano, 5 (2010) 423-428.
[208] T. Koga, K. Taguchi, Y. Kobuke, T. Kinoshita, M. Higuchi, Structural regulation of a peptide-conjugated graft copolymer: A simple model for amyloid formation, Chemistry-a European Journal, 9 (2003) 1146-1156.
[209] J.W. Kelly, The alternative conformations of amyloidogenic proteins and their multi-step assembly pathways, Current Opinion in Structural Biology, 8 (1998) 101-106.
[210] C.M. Dobson, Protein folding and misfolding, Nature, 426 (2003) 884-890.
[211] J.M. Andreu, S.N. Timasheff, THE MEASUREMENT OF COOPERATIVE PROTEIN SELF-ASSEMBLY BY TURBIDITY AND OTHER TECHNIQUES, Method Enzymol., 130 (1986) 47-59.
[212] W.A. Eaton, J. Hofrichter, THE BIOPHYSICS OF SICKLE-CELL HYDROXYUREA THERAPY, Science, 268 (1995) 1142-1143.

[213] S. Asakura, Polymerization of flagellin and polymorphism of flagella, Advances in biophysics, 1 (1970) 99-155.
[214] J.T. Jarrett, P.T. Lansbury Jr, Seeding “one-dimensional crystallization” of amyloid: A pathogenic mechanism in Alzheimer's disease and scrapie?, Cell, 73 (1993) 1055-1058.
[215] J. Hofrichter, P.D. Ross, W.A. Eaton, KINETICS AND MECHANISM OF DEOXYHEMOGLOBIN-S GELATION - NEW APPROACH TO UNDERSTANDING SICKLE-CELL DISEASE, Proc. Natl. Acad. Sci. U. S. A., 71 (1974) 4864-4868.
[216] J.T. Jarrett, E.P. Berger, P.T. Lansbury, THE CARBOXY TERMINUS OF THE BETA-AMYLOID PROTEIN IS CRITICAL FOR THE SEEDING OF AMYLOID FORMATION - IMPLICATIONS FOR THE PATHOGENESIS OF ALZHEIMERS-DISEASE, Biochemistry, 32 (1993) 4693-4697.
[217] H. Naiki, K. Nakakuki, First-order kinetic model of Alzheimer's beta-amyloid fibril extension in vitro, Laboratory Investigation, 74 (1996) 374-383.
[218] W.P. Esler, E.R. Stimson, J.R. Ghilardi, Y.A. Lu, A.M. Felix, H.V. Vinters, P.W. Mantyh, J.P. Lee, J.E. Maggio, Point substitution in the central hydrophobic cluster of a human beta-amyloid congener disrupts peptide folding and abolishes plaque competence, Biochemistry, 35 (1996) 13914-13921.
[219] J.T. Jarrett, P.T. Lansbury, AMYLOID FIBRIL FORMATION REQUIRES A CHEMICALLY DISCRIMINATING NUCLEATION EVENT - STUDIES OF AN AMYLOIDOGENIC SEQUENCE FROM THE BACTERIAL PROTEIN OSMB, Biochemistry, 31 (1992) 12345-12352.
[220] H. Tsutsumi, H. Mihara, Soft materials based on designed self-assembling peptides: from design to application, Molecular Biosystems, 9 (2013) 609-617.
[221] A. Gress, B. Smarsly, H. Schlaad, Formation of glycopolyamide nanofibers, Macromol. Rapid Commun., 29 (2008) 304-308.
[222] A. Patwa, A. Gissot, I. Bestel, P. Barthelemy, Hybrid lipid oligonucleotide conjugates: synthesis, self-assemblies and biomedical applications, Chemical Society Reviews, 40 (2011) 5844-5854.
[223] Y.H. Roh, R.C. Ruiz, S. Peng, J.B. Lee, D. Luo, Engineering DNA-based functional materials, Chem Soc Rev, 40 (2011) 5730-5744.
[224] T. Torring, N.V. Voigt, J. Nangreave, H. Yan, K.V. Gothelf, DNA origami: a quantum leap for self-assembly of complex structures, Chemical Society Reviews, 40 (2011) 5636-5646.
[225] J.I. Cutler, K. Zhang, D. Zheng, E. Auyeung, A.E. Prigodich, C.A. Mirkin, Polyvalent Nucleic Acid Nanostructures, J. Am. Chem. Soc., 133 (2011) 9254-9257.
[226] K. Lu, Q.-P. Duan, L. Ma, D.-X. Zhao, Chemical Strategies for the Synthesis of Peptide-Oligonucleotide Conjugates, Bioconjugate Chemistry, 21 (2010) 187-202.
[227] J.J. Storhoff, C.A. Mirkin, Programmed materials synthesis with DNA, Chemical Reviews, 99 (1999) 1849-1862.
[228] C.A. Mirkin, Programming the assembly of two- and three-dimensional architectures with DNA and nanoscale inorganic building blocks, Inorganic Chemistry, 39 (2000) 2258-2272.
[229] Z. Li, Y. Zhang, P. Fullhart, C.A. Mirkin, Reversible and chemically programmable micelle assembly with DNA block-copolymer amphiphiles, Nano Letters, 4 (2004) 1055-1058.
[230] J.H. Jeong, T.G. Park, Novel Polymer−DNA Hybrid Polymeric Micelles Composed of Hydrophobic Poly(d,l-lactic-co-glycolic Acid) and Hydrophilic Oligonucleotides, Bioconjugate Chemistry, 12 (2001) 917-923.
[231] H.M. Koenig, A.F.M. Kilbinger, Learning from nature: beta-sheet-mimicking copolymers get organized, Angew. Chem.-Int. Edit., 46 (2007) 8334-8340.
[232] C.G. Glabe, Common mechanisms of amyloid oligomer pathogenesis in degenerative disease, Neurobiology of Aging, 27 (2006) 570-575.
[233] H.A. Lashuel, D. Hartley, B.M. Petre, T. Walz, P.T. Lansbury, Neurodegenerative disease - Amyloid pores from pathogenic mutations, Nature, 418 (2002) 291-291.
[234] N. Gour, D. Kedracki, I. Safir, K.X. Ngo, C. Vebert-Nardin, Self-assembling DNA-peptide hybrids: morphological consequences of oligonucleotide grafting to a pathogenic amyloid fibrils forming dipeptide, Chem. Commun., 48 (2012) 5440-5442.
[235] J. Kypr, I. Kejnovska, D. Renciuk, M. Vorlickova, Circular dichroism and conformational polymorphism of DNA, Nucleic Acids Res., 37 (2009) 1713-1725.

[236] N. Gour, J.N. Abraham, M. Chami, A. Castillo, S. Verma, C. Vebert-Nardin, Label-free, optical sensing of the supramolecular assembly into fibrils of a ditryptophan-DNA hybrid, Chem. Commun., 50 (2014) 6863-6865.

[237] D.P. Smith, S.E. Radford, Role of the single disulphide bond of beta(2)-microglobulin in amyloidosis in vitro, Protein Science, 10 (2001) 1775-1784.

[238] C.M. Kedracki D, Maroni P, Schlaad H, Nardin C, Synthesis and Self-assembly of a DNA Molecular Brush, Biomacromolecules, DOI: 10.1021/bm5008713 (2014).

[239] S.K. Mehta, G. Kaur, Microemulsions: Thermodynamic and Dynamic Properties, 2011.

[240] M. Kuentz, Oral self-emulsifying drug delivery systems, from biopharmaceutical to technical formulation aspects, Journal of Drug Delivery Science and Technology, 21 (2011) 17-26.

[241] D.J. McClements, Edible nanoemulsions: fabrication, properties, and functional performance, Soft Matter, 7 (2011) 2297-2316.

[242] D.J. McClements, Advances in fabrication of emulsions with enhanced functionality using structural design principles, Current Opinion in Colloid & Interface Science, 17 (2012) 235-245.

[243] U.K.S. F. Muzzafar, L. Chauhan, Review on microemulsion as futuristic drug delivery, International Journal of Pharmacy and Pharmaceutical Sciences, 5 (2013).

[244] J.T.G. Overbeek, The First Rideal Lecture. Microemulsions, a field at the border between lyophobic and lyophilic colloids, Faraday Discussions of the Chemical Society, 65 (1978) 7-19.

[245] T.F. Tadros, Emulsion Science and Technology, (2009).

[246] D.J. McClements, Design of Nano-Laminated Coatings to Control Bioavailability of Lipophilic Food Components, Journal of Food Science, 75 (2010) R30-R42.

[247] G. Decher, Fuzzy nanoassemblies: Toward layered polymeric multicomposites, Science, 277 (1997) 1232-1237.

[248] M. Freemantle, Polyelectrolyte multilayers - Thin-film properties can be finely tuned through layer-by-layer assembly, Chemical & Engineering News, 80 (2002) 44-48.

[249] C.S. Peyratout, L. Dähne, Tailor-Made Polyelectrolyte Microcapsules: From Multilayers to Smart Containers, Angewandte Chemie International Edition, 43 (2004) 3762-3783.

[250] G.B. Sukhorukov, A. Fery, M. Brumen, H. Mohwald, Physical chemistry of encapsulation and release, Physical Chemistry Chemical Physics, 6 (2004) 4078-4089.

[251] D. Lee, M.F. Rubner, R.E. Cohen, Formation of Nanoparticle-Loaded Microcapsules Based on Hydrogen-Bonded Multilayers, Chemistry of Materials, 17 (2005) 1099-1105.

[252] G. Ladam, P. Schaad, J.C. Voegel, P. Schaaf, G. Decher, F. Cuisinier, In Situ Determination of the Structural Properties of Initially Deposited Polyelectrolyte Multilayers, Langmuir, 16 (1999) 1249-1255.

[253] M. Lösche, J. Schmitt, G. Decher, W.G. Bouwman, K. Kjaer, Detailed Structure of Molecularly Thin Polyelectrolyte Multilayer Films on Solid Substrates as Revealed by Neutron Reflectometry, Macromolecules, 31 (1998) 8893-8906.

[254] F. Caruso, D.N. Furlong, K. Ariga, I. Ichinose, T. Kunitake, Characterization of Polyelectrolyte−Protein Multilayer Films by Atomic Force Microscopy, Scanning Electron Microscopy, and Fourier Transform Infrared Reflection−Absorption Spectroscopy, Langmuir, 14 (1998) 4559-4565.

[255] J.-i. Anzai, Y. Kobayashi, N. Nakamura, M. Nishimura, T. Hoshi, Layer-by-Layer Construction of Multilayer Thin Films Composed of Avidin and Biotin-Labeled Poly(amine)s, Langmuir, 15 (1998) 221-226.

[256] J. Hodak, R. Etchenique, E.J. Calvo, K. Singhal, P.N. Bartlett, Layer-by-Layer Self-Assembly of Glucose Oxidase with a Poly(allylamine)ferrocene Redox Mediator, Langmuir, 13 (1997) 2708-2716.

[257] M. Onda, Y. Lvov, K. Ariga, T. Kunitake, Sequential actions of glucose oxidase and peroxidase in molecular films assembled by layer-by-layer alternate adsorption, Biotechnology and Bioengineering, 51 (1996) 163-167.

[258] H. Ai, S. Jones, Y. Lvov, Biomedical applications of electrostatic layer-by-layer nano-assembly of polymers, enzymes, and nanoparticles, Cell Biochem Biophys, 39 (2003) 23-43.

[259] K. Ariga, Y. Lvov, T. Kunitake, Assembling Alternate Dye−Polyion Molecular Films by Electrostatic Layer-by-Layer Adsorption, Journal of the American Chemical Society, 119 (1997) 2224-2231.

[260] S. Das, A.J. Pal, Layer-by-Layer Self-Assembling of a Low Molecular Weight Organic Material by Different Electrostatic Adsorption Processes, Langmuir, 18 (2001) 458-461.

[261] N.A. Kotov, I. Dekany, J.H. Fendler, Layer-by-Layer Self-Assembly of Polyelectrolyte-Semiconductor Nanoparticle Composite Films, The Journal of Physical Chemistry, 99 (1995) 13065-13069.

[262] N. Malikova, I. Pastoriza-Santos, M. Schierhorn, N.A. Kotov, L.M. Liz-Marzán, Layer-by-Layer Assembled Mixed Spherical and Planar Gold Nanoparticles: Control of Interparticle Interactions, Langmuir, 18 (2002) 3694-3697.

[263] S.K. Ghosh, Functional Coatings: By Polymer Microencapsulation, Wiley, 2006.

[264] A. Izquierdo, S.S. Ono, J.C. Voegel, P. Schaaf, G. Decher, Dipping versus Spraying: Exploring the Deposition Conditions for Speeding Up Layer-by-Layer Assembly, Langmuir, 21 (2005) 7558-7567.

[265] G. Decher, J.B. Schlenoff, Multilayer Thin Films: Sequential Assembly of Nanocomposite Materials, Wiley, 2012.

[266] S.L.R. Barker, D. Ross, M.J. Tarlov, M. Gaitan, L.E. Locascio, Control of Flow Direction in Microfluidic Devices with Polyelectrolyte Multilayers, Analytical Chemistry, 72 (2000) 5925-5929.

[267] F. Caruso, K. Niikura, D.N. Furlong, Y. Okahata, 2. Assembly of Alternating Polyelectrolyte and Protein Multilayer Films for Immunosensing, Langmuir, 13 (1997) 3427-3433.

[268] K. Sirkar, A. Revzin, M.V. Pishko, Glucose and Lactate Biosensors Based on Redox Polymer/Oxidoreductase Nanocomposite Thin Films, Analytical Chemistry, 72 (2000) 2930-2936.

[269] J.F. Rusling, L. Zhou, B. Munge, J. Yang, C. Estavillo, J.B. Schenkman, Applications of polyion films containing biomolecules to sensing toxicity, Faraday Discussions, 116 (2000) 77-87.

[270] H. Hattori, Anti-Reflection Surface with Particle Coating Deposited by Electrostatic Attraction, Advanced Materials, 13 (2001) 51-54.

[271] T.R. Farhat, J.B. Schlenoff, Corrosion Control Using Polyelectrolyte Multilayers, Electrochemical and Solid-State Letters, 5 (2002) B13-B15.

[272] T. Cassagneau, J.H. Fendler, High Density Rechargeable Lithium-Ion Batteries Self-Assembled from Graphite Oxide Nanoplatelets and Polyelectrolytes, Advanced Materials, 10 (1998) 877-881.

[273] R. Gref, Y. Minamitake, M.T. Peracchia, V. Trubetskoy, V. Torchilin, R. Langer, BIODEGRADABLE LONG-CIRCULATING POLYMERIC NANOSPHERES, Science, 263 (1994) 1600-1603.

[274] D.E. Discher, A. Eisenberg, Polymer vesicles, Science, 297 (2002) 967-973.

[275] B.M. Discher, Y.-Y. Won, D.S. Ege, J.C.-M. Lee, F.S. Bates, D.E. Discher, D.A. Hammer, Polymersomes: Tough Vesicles Made from Diblock Copolymers, Science, 284 (1999) 1143-1146.

[276] E. Lorenceau, A.S. Utada, D.R. Link, G. Cristobal, M. Joanicot, D.A. Weitz, Generation of Polymerosomes from Double-Emulsions, Langmuir, 21 (2005) 9183-9186.

[277] A.S. Utada, E. Lorenceau, D.R. Link, P.D. Kaplan, H.A. Stone, D.A. Weitz, Monodisperse Double Emulsions Generated from a Microcapillary Device, Science, 308 (2005) 537-541.

[278] R.C. Hayward, A.S. Utada, N. Dan, D.A. Weitz, Dewetting Instability during the Formation of Polymersomes from Block-Copolymer-Stabilized Double Emulsions, Langmuir, 22 (2006) 4457-4461.

[279] R. Zheng, G. Liu, Water-Dispersible Oil-Filled ABC Triblock Copolymer Vesicles and Nanocapsules, Macromolecules, 40 (2007) 5116-5121.

[280] K. Letchford, H. Burt, A review of the formation and classification of amphiphilic block copolymer nanoparticulate structures: micelles, nanospheres, nanocapsules and polymersomes, European Journal of Pharmaceutics and Biopharmaceutics, 65 (2007) 259-269.

[281] J.P. Jain, N. Kumar, Self Assembly of Amphiphilic (PEG)3-PLA Copolymer as Polymersomes: Preparation, Characterization, and Their Evaluation As Drug Carrier, Biomacromolecules, 11 (2010) 1027-1035.

[282] N. Cottenye, K. Anselme, L. Ploux, C. Vebert-Nardin, Vesicular Structures Self-Assembled from Oligonucleotide-Polymer Hybrids: Mechanical Prevention of Bacterial Colonization Upon their Surface Tethering Through Hybridization, Adv. Funct. Mater., 22 (2012) 4891-4898.

[283] N. Cottenye, F. Teixeira, A. Ponche, G. Reiter, K. Anselme, W. Meier, L. Ploux, C. Vebert-Nardin, Oligonucleotide Nanostructured Surfaces: Effect on Escherichia coli Curli Expression, Macromolecular Bioscience, 8 (2008) 1161-1172.

[284] E. Peyrin, Nucleic acid aptamer molecular recognition principles and application in liquid chromatography and capillary electrophoresis, Journal of Separation Science, 32 (2009) 1531-1536.

[285] S.E. Osborne, I. Matsumura, A.D. Ellington, Aptamers as therapeutic and diagnostic reagents: problems and prospects, Current Opinion in Chemical Biology, 1 (1997) 5-9.

[286] D. Proske, M. Blank, R. Buhmann, A. Resch, Aptamers—basic research, drug development, and clinical applications, Applied Microbiology and Biotechnology, 69 (2005) 367-374.

[287] S.M. Nimjee, C.P. Rusconi, B.A. Sullenger, Aptamers: An emerging class of therapeutics, in: Annual Review of Medicine, Annual Reviews, Palo Alto, 2005, pp. 555-+.

[288] N.t. Brummelhuis, H. Schlaad, Stimuli-responsive star polymers through thiol-yne core functionalization/crosslinking of block copolymer micelles, Polymer Chemistry, 2 (2011) 1180-1184.

[289] K. Szczepanowicz, D. Dronka-Gora, G. Para, P. Warszynski, Encapsulation of liquid cores by layer-by-layer adsorption of polyelectrolytes, Journal of Microencapsulation, 27 (2010) 198-204.

[290] A.P.R. Johnston, G.K. Such, F. Caruso, Triggering Release of Encapsulated Cargo, Angewandte Chemie International Edition, 49 (2010) 2664-2666.

[291] M. Delcea, H. Möhwald, A.G. Skirtach, Stimuli-responsive LbL capsules and nanoshells for drug delivery, Advanced Drug Delivery Reviews, 63 (2011) 730-747.

[292] J. Cui, Y. Wang, A. Postma, J. Hao, L. Hosta-Rigau, F. Caruso, Monodisperse Polymer Capsules: Tailoring Size, Shell Thickness, and Hydrophobic Cargo Loading via Emulsion Templating, Adv. Funct. Mater., 20 (2010) 1625-1631.

[293] U. Bazylinska, R. Skrzela, K. Szczepanowicz, P. Warszynski, K.A. Wilk, Novel approach to long sustained multilayer nanocapsules: influence of surfactant head groups and polyelectrolyte layer number on the release of hydrophobic compounds, Soft Matter, 7 (2011) 6113-6124.

[294] P. van Rijn, N.C. Mougin, D. Franke, H. Park, A. Boker, Pickering emulsion templated soft capsules by self-assembling cross-linkable ferritin-polymer conjugates, Chem. Commun., 47 (2011) 8376-8378.

[295] F. Cavalieri, A. Postma, L. Lee, F. Caruso, Assembly and Functionalization of DNA−Polymer Microcapsules, ACS Nano, 3 (2009) 234-240.

[296] C. Cortez, E. Tomaskovic-Crook, A.P.R. Johnston, A.M. Scott, E.C. Nice, J.K. Heath, F. Caruso, Influence of Size, Surface, Cell Line, and Kinetic Properties on the Specific Binding of A33 Antigen-Targeted Multilayered Particles and Capsules to Colorectal Cancer Cells, ACS Nano, 1 (2007) 93-102.

[297] M. Delcea, H. Moehwald, A.G. Skirtach, Stimuli-responsive LbL capsules and nanoshells for drug delivery, Advanced Drug Delivery Reviews, 63 (2011) 730-747.

[298] H. Holthoff, S.U. Egelhaaf, M. Borkovec, P. Schurtenberger, H. Sticher, Coagulation Rate Measurements of Colloidal Particles by Simultaneous Static and Dynamic Light Scattering, Langmuir, 12 (1996) 5541-5549.

[299] I. Szilagyi, A. Polomska, D. Citherlet, A. Sadeghpour, M. Borkovec, Charging and aggregation of negatively charged colloidal latex particles in the presence of multivalent oligoamine cations, Journal of Colloid and Interface Science, 392 (2013) 34-41.

[300] R.H. Muller, C. Jacobs, O. Kayser, Nanosuspensions as particulate drug formulations in therapy Rationale for development and what we can expect for the future, Advanced Drug Delivery Reviews, 47 (2001) 3-19.

[301] M. Porus, P. Maroni, M. Borkovec, Highly-sensitive reflectometry setup capable of probing the electrical double layer on silica, Sensors and Actuators B: Chemical, 151 (2010) 250-255.

[302] L. Li, J. Hou, X. Liu, Y. Guo, Y. Wu, L. Zhang, Z. Yang, Nucleolin-targeting liposomes guided by aptamer AS1411 for the delivery of siRNA for the treatment of malignant melanomas, Biomaterials, 35 (2014) 3840-3850.

[303] J. Guo, X. Gao, L. Su, H. Xia, G. Gu, Z. Pang, X. Jiang, L. Yao, J. Chen, H. Chen, Aptamer-functionalized PEG–PLGA nanoparticles for enhanced anti-glioma drug delivery, Biomaterials, 32 (2011) 8010-8020.

[304] S.V. Lale, A. R. G, A. Aravind, D.S. Kumar, V. Koul, AS1411 Aptamer and Folic Acid Functionalized pH-Responsive ATRP Fabricated pPEGMA–PCL–pPEGMA Polymeric Nanoparticles for Targeted Drug Delivery in Cancer Therapy, Biomacromolecules, 15 (2014) 1737-1752.
[305] W.H. Zhou, Y.B. Zhou, J.P. Wu, Z.B. Liu, H.Z. Zhao, J.W. Liu, J.S. Ding, Aptamer-nanoparticle bioconjugates enhance intracellular delivery of vinorelbine to breast cancer cells, Journal of Drug Targeting, 22 (2014) 57-66.
[306] T. Lammers, Improving the efficacy of combined modality anticancer therapy using HPMA copolymer-based nanomedicine formulations, Advanced Drug Delivery Reviews, 62 (2010) 203-230.
[307] A. Aravind, P. Jeyamohan, R. Nair, S. Veeranarayanan, Y. Nagaoka, Y. Yoshida, T. Maekawa, D.S. Kumar, AS1411 aptamer tagged PLGA-lecithin-PEG nanoparticles for tumor cell targeting and drug delivery, Biotechnology and Bioengineering, 109 (2012) 2920-2931.
[308] V. Vergaro, F. Scarlino, C. Bellomo, R. Rinaldi, D. Vergara, M. Maffia, F. Baldassarre, G. Giannelli, X. Zhang, Y.M. Lvov, S. Leporatti, Drug-loaded polyelectrolyte microcapsules for sustained targeting of cancer cells, Advanced Drug Delivery Reviews, 63 (2011) 847-864.
[309] T.S. Shim, S.-H. Kim, S.-M. Yang, Elaborate Design Strategies Toward Novel Microcarriers for Controlled Encapsulation and Release, Particle & Particle Systems Characterization, 30 (2013) 9-45.
[310] P.R. Gil, L.L. del Mercato, P. del_Pino, A. Muñoz_Javier, W.J. Parak, Nanoparticle-modified polyelectrolyte capsules, Nano Today, 3 (2008) 12-21.
[311] D.E. Owens Iii, N.A. Peppas, Opsonization, biodistribution, and pharmacokinetics of polymeric nanoparticles, International Journal of Pharmaceutics, 307 (2006) 93-102.
[312] F. Alexis, E. Pridgen, L.K. Molnar, O.C. Farokhzad, Factors Affecting the Clearance and Biodistribution of Polymeric Nanoparticles, Molecular Pharmaceutics, 5 (2008) 505-515.
[313] Y. Malam, M. Loizidou, A.M. Seifalian, Liposomes and nanoparticles: nanosized vehicles for drug delivery in cancer, Trends in Pharmacological Sciences, 30 (2009) 592-599.
[314] J.W. Park, Liposome-based drug delivery in breast cancer treatment, Breast cancer research : BCR, 4 (2002) 95-99.
[315] F. Bensaid, O. Thillaye du Boullay, A. Amgoune, C. Pradel, L. Harivardhan Reddy, E. Didier, S. Sablé, G. Louit, D. Bazile, D. Bourissou, Y-Shaped mPEG-PLA Cabazitaxel Conjugates: Well-Controlled Synthesis by Organocatalytic Approach and Self-Assembly into Interface Drug-Loaded Core–Corona Nanoparticles, Biomacromolecules, 14 (2013) 1189-1198.
[316] H. Maeda, The enhanced permeability and retention (EPR) effect in tumor vasculature: the key role of tumor-selective macromolecular drug targeting, Advances in Enzyme Regulation, 41 (2001) 189-207.
[317] R.A. Petros, J.M. DeSimone, Strategies in the design of nanoparticles for therapeutic applications, Nat Rev Drug Discov, 9 (2010) 615-627.
[318] F. Danhier, B. Vroman, N. Lecouturier, N. Crokart, V. Pourcelle, H. Freichels, C. Jerome, J. Marchand-Brynaert, O. Feron, V. Preat, Targeting of tumor endothelium by RGD-grafted PLGA-nanoparticles loaded with Paclitaxel, Journal of Controlled Release, 140 (2009) 166-173.
[319] S.-s. Feng, G. Huang, Effects of emulsifiers on the controlled release of paclitaxel (Taxol®) from nanospheres of biodegradable polymers, Journal of Controlled Release, 71 (2001) 53-69.
[320] A.K. Singla, A. Garg, D. Aggarwal, Paclitaxel and its formulations, International Journal of Pharmaceutics, 235 (2002) 179-192.
[321] W.J. Gradishar, S. Tjulandin, N. Davidson, H. Shaw, N. Desai, P. Bhar, M. Hawkins, J. O'Shaughnessy, Phase III Trial of Nanoparticle Albumin-Bound Paclitaxel Compared With Polyethylated Castor Oil–Based Paclitaxel in Women With Breast Cancer, Journal of Clinical Oncology, 23 (2005) 7794-7803.
[322] M. Srivastava, H.B. Pollard, Molecular dissection of nucleolin’s role in growth and cell proliferation: new insights, The FASEB Journal, 13 (1999) 1911-1922.
[323] D. Guzey, D.J. McClements, Formation, stability and properties of multilayer emulsions for application in the food industry, Advances in Colloid and Interface Science, 128–130 (2006) 227-248.
[324] E.M. Shchukina, D.G. Shchukin, Layer-by-layer coated emulsion microparticles as storage and delivery tool, Current Opinion in Colloid & Interface Science, 17 (2012) 281-289.

[325] A.P.R. Johnston, C. Cortez, A.S. Angelatos, F. Caruso, Layer-by-layer engineered capsules and their applications, Current Opinion in Colloid & Interface Science, 11 (2006) 203-209.

[326] G. Zhang, H. Yan, S. Ji, Z. Liu, Self-assembly of polyelectrolyte multilayer pervaporation membranes by a dynamic layer-by-layer technique on a hydrolyzed polyacrylonitrile ultrafiltration membrane, Journal of Membrane Science, 292 (2007) 1-8.

[327] G. Zhang, W. Gu, S. Ji, Z. Liu, Y. Peng, Z. Wang, Preparation of polyelectrolyte multilayer membranes by dynamic layer-by-layer process for pervaporation separation of alcohol/water mixtures, Journal of Membrane Science, 280 (2006) 727-733.

[328] L. Richert, F. Boulmedais, P. Lavalle, J. Mutterer, E. Ferreux, G. Decher, P. Schaaf, J.-C. Voegel, C. Picart, Improvement of Stability and Cell Adhesion Properties of Polyelectrolyte Multilayer Films by Chemical Cross-Linking, Biomacromolecules, 5 (2003) 284-294.

[329] Y. Wang, J. Su, W. Cai, P. Lu, L. Yuan, T. Jin, S. Chen, J. Sheng, Hepatocyte-targeting gene transfer mediated by galactosylated poly(ethylene glycol)-graft-polyethylenimine derivative, Drug Design Development and Therapy, 7 (2013) 211-221.

[330] K. Fuhrmann, A. Połomska, C. Aeberli, B. Castagner, M.A. Gauthier, J.-C. Leroux, Modular Design of Redox-Responsive Stabilizers for Nanocrystals, ACS Nano, 7 (2013) 8243-8250.

[331] K. Fuhrmann, J.D. Schulz, M.A. Gauthier, J.-C. Leroux, PEG Nanocages as Non-sheddable Stabilizers for Drug Nanocrystals, ACS Nano, 6 (2012) 1667-1676.

[332] K. Letchford, R. Liggins, K.M. Wasan, H. Burt, In vitro human plasma distribution of nanoparticulate paclitaxel is dependent on the physicochemical properties of poly(ethylene glycol)-block-poly(caprolactone) nanoparticles, European Journal of Pharmaceutics and Biopharmaceutics, 71 (2009) 196-206.